



**UNIVERSITÀ
DEGLI STUDI
DI TRIESTE**

UNIVERSITÀ DEGLI STUDI DI TRIESTE

**XXXV ciclo del Dottorato di Ricerca in
FISICA**

**Mono- and bi-metallic tetra-pyridyl porphyrin
monolayers from UHV to near-ambient conditions**

Settore scientifico-disciplinare: FIS/03

**DOTTORANDO/A:
FRANCESCO ARMILLOTTA**

**COORDINATORE:
PROF. FRANCESCO LONGO**

**SUPERVISORE DI TESI:
PROF. ERIK VESSELLI**

ANNO ACCADEMICO 2021/2022

ABSTRACT

Bi-dimensional metal-organic frameworks (2D-MOF) are a relatively new class of materials that are gaining particular interest in surface science. Their dimensionality naturally allows the exploitation of many surface-sensitive techniques, beneficial to study with great detail their geometry, electronic structure, and chemical reactivity. On the other hand, the well-defined chemical environment of the active sites makes them ideal single-atom catalysts for heterogeneous catalysis. In this thesis, we focus on the Ultra High Vacuum (UHV) growth and characterization, and on the investigation of the reactivity from UHV to Near Ambient Pressure (NAP) of M_1 TPyPM₂ 2D Metal-organic Frameworks (MOFs, with $M_{1,2} = \text{Fe, Co}$, TpyP = Tetra Pyridyl-Porphyrin) self-assembled on almost free-standing Graphene/Ir(111). In the first part, some selected monolayers have been investigated in UHV with a combination of vibrational- (IR-Vis SFG), real-space imaging and spectroscopy (STM/STS), and electronic- (NEXAFS, XPS) sensitive techniques, and the results compared with the literature and *ab initio* DFT. In the second part, we exposed a CoTPyP/Gr/Ir(111) monolayer to a mixture of water and oxygen gases (up to fractions of mbar), and an intense bending mode appeared at 1712 cm^{-1} in Sum Frequency Generation spectra collected *in situ*: this is associated with the hydroperoxyl molecule, an important reaction intermediate for the Oxygen Reduction Reaction. NAP-XPS measurements confirmed our thesis through O 1s and Co 2p core levels analysis, while pump-probe SFG allowed us to directly inspect the coupling between the hydroperoxyl and the surrounding water molecules representing the solvent. In the last part, carbon monoxide has been exploited as a probe to investigate the CoTPyPCo/Gr/Ir(111) local sites' electronic structure and coordination. The IR-Vis SFG spectra collected *in situ* showed evidence of both long-range MOF-driven interactions, including the anti-cooperativity of the CO adsorption process, provided that active sites are sufficiently close to each other. This experiment has been revealed to be an effective approach to investigate subtle effects in the MOF chemical affinity, possibly responsible for the remarkable non-linear increase of the electrocatalytic performances of such M_1 TPyPM₂ compounds, which is one of the scientific interests at the basis of this thesis.

CONTENTS

Abstract	i
1 Introduction	1
1.1 Challenges and solutions	1
1.2 Single-Atom Catalysts based on Metal-organic Frameworks	2
1.2.1 Two-dimensional Metal-organic Frameworks	6
1.3 Secondary batteries and bifunctional materials	6
1.4 Porphyrin-based MOFs for ORR/OER	9
1.5 Mind the gap - a quest for <i>in situ</i> and <i>operando</i> approaches	14
1.6 Aim of this thesis	15
1.7 <i>Ab initio</i> calculations	17
1.7.1 Computational details	17
2 Experimental Methods	20
2.1 IR-Vis Sum-Frequency Generation Spectroscopy	20
2.1.1 Theoretical background	20
2.1.2 Time-resolved IR-Vis SFG	26
2.1.3 Lineshape modeling	28
2.1.4 Experimental setup	29
2.2 STM and STS	33
2.3 Single-photon Photoemission Spectroscopies	35
2.3.1 XPS	36
2.3.2 NAP-XPS	43
2.3.3 UPS	47
2.3.4 NEXAFS	47
2.3.5 ARPES	51
2.4 Two-photon Photoemission Spectroscopies	53
2.4.1 Time-resolved 2PPE	54
2.4.2 ANCHOR-SUNDYN setup	54
3 UHV Characterization	56
3.1 Gr/Ir(111)	56
3.1.1 Sample Preparation	56
3.1.2 SFG	56
3.1.3 LEED	56
3.2 Mono-metallic MOFs: CoTPyP and FeTPyP	59
3.2.1 MOF growth	59
3.2.2 STM - CoTPyP	59
3.2.3 STS - CoTPyP	61

3.2.4	DFT - CoTPyP	64
3.2.5	XPS - CoTPyP and FeTpyP	66
3.2.6	NEXAFS - CoTPyP and FeTpyP	68
3.2.7	SFG - CoTPyP and FeTpyP	72
3.3	Bi-metallic MOF: CoTPyPCo, CoTPyPFe, and FeTPyPFe	78
3.3.1	STM - CoTPyPCo	78
3.3.2	STS - CoTPyPCo	85
3.3.3	DFT - CoTPyPCo	87
3.3.4	XPS - CoTPyPCo, CoTPyPFe, and FeTpyPFe	93
3.3.5	NEXAFS - CoTPyPFe, and FeTpyPFe	95
3.3.6	SFG - CoTPyPCo	95
3.4	Additional Measurements	98
3.4.1	UPS and Work Function	98
3.4.2	ARPES	99
3.4.3	Tr-2PPE	101
3.5	Main Results	103
4	O ₂ +H ₂ O on CoTPyP/Gr/Ir(111)	104
4.1	Results and Discussion	108
4.2	Exposure to O ₂ and H ₂ O	109
4.3	The time-resolved IR-Vis SFG experiment	111
4.4	<i>Ab initio</i> calculations	113
4.5	Main Results	113
5	CO at NAP on CoTPyPCo	118
5.1	CO adsorption in CoTPyPCo	118
5.2	CO uptakes at NAP	122
5.2.1	CO uptake with CoTPyP _{0.5} Co _{0.12}	122
5.2.2	CO uptake with CoTPyP _{0.5} Co _{1.4}	126
5.3	Final Remarks	133
5.3.1	Comparison with DFT	133
5.3.2	Absence of Förster transfer	133
5.3.3	Polarization dependence	135
5.3.4	χ_e dependence on IR-Vis impulses delay	135
5.4	Main Results	135
6	Conclusions and future perspectives	137
A	Appendix	139
A.1	UHV	139
A.1.1	XPS	139
A.1.2	XPS stepwise annealing	139
A.1.3	SFG coverage dependent experiment	144
A.1.4	SFG CoTPyP/Gr/Ir(111) Thermal Annealing	152

A.1.5	SFG CoTPyPCo/Gr/Ir(111)	152
A.1.6	STM CoTPyPCo/Gr/Ir(111)	156
A.2	O ₂ +H ₂ O on CoTPyP/Gr/Ir(111)	157
A.3	CO on CoTPyPCo	164
	Acronyms	170
	List of publications	172
	Ringraziamenti	173
	Bibliography	175

1 | INTRODUCTION

1.1 CHALLENGES AND SOLUTIONS

The 21st century needs to deal with multiple and interconnected challenges, which involve complex scientific, technological, geopolitical, economic, social, and ethical facets that shall be solved in multiple and synergic solutions [1]. Global warming, the related clean energy transition, and the urgency of global energy supply will partially change our currently unsustainable technological and economic model. In every scenario, the supply of raw materials is an important problem that must be taken into account.

Indeed, in the last years, the European Commission listed 27 “critical raw materials” that cover a major role in industry, modern technology (a single smartphone contains up to 50 different kinds of metals), and environmental-related technologies (solar panels, wind turbines, electric vehicles, and energy-efficient lighting) [2, 3], both for their economic importance and supply risk (Fig. 1.1). To give an example, it is estimated that by 2050 the world’s wind turbines will require 300% more metals than they do today, solar panels 200% more, and energy storage devices 1000% more [4].

The need for raw metals tackles economic problems (price trend, the concentration of production, economical monopoly...) [5–7], socio-ethical problems (international agreements, child labor in mining...) [7], and concurrent problems such as the large footprint caused by the extraction and refining processes [5].

One path which is logical to follow is the enhancement of the recycling process and the use of “smart” technologies that minimize the use and maximize the efficiency of raw metals. The last goal, in particular, will be achieved if fundamental research will succeed to understand and engineer the intricate mechanisms that underly even currently available technologies [1]. For instance, it is astonishing how little is known of the fundamentals of catalysis, which is involved in virtually any energy-related process (Fig. 1.2A): in the processing of crude oil into fuels, in all of the biological reactions involved in photosynthesis, in fixing CO₂, in biodegradation, in the hydration of CO₂ to carbonate, in the displacement of electrons in batteries, in the operation of fuel cells, in the cleanup of exhaust gases from internal combustion engines, and many others [1].

In this perspective, nanoscience and surface science offer today a new approach to the problem since we can synthesize and control catalysts with very well defined active sites, investigate the system with atomic resolution *in situ* and *operando*, and even mimic the enzymatic active site within a biomimetic approach [8–10].

To give an example, the oxygen reduction reaction (ORR) is at the basis of the fuel cell working principle, since we can extract energy by reducing molecular oxygen to water (by combination with hydrogen). To work, this process involves the transfer of four electrons, which is a sluggish process and reduces the overall performance of the cell [1]. It is evident that a deep understanding of the electron transfer mechanisms and the role of the intermediate species are necessary requisites to develop novel and more efficient fuel cell devices or (in the case of the reverse process) electrolyzers to produce H₂ from water. Also, the chemistry of CO₂ is a key knowledge for the challenges of this century, playing a major role in global warming [1].

To conclude, even photosynthesis, a ubiquitous process at the foundation of Life as we know it today, is not “an optimized marvel” [1]: some steps are thermodynamically inefficient and several key reactions have a poor yield. Nevertheless, this means a technological opportunity for re-engineering biological photosynthesis for greater efficiency, with the goal, for example, of photochemical production of fuels or energy storage [1, 9].

1.2 SINGLE-ATOM CATALYSTS BASED ON METAL-ORGANIC FRAMEWORKS

As depicted above, catalysts play a major role in 21st-century challenges. Indeed, they are widely used for the synthesis of chemicals and energy vectors (Fig. 1.2A). By definition, catalytic materials are able to speed up the rate of a chemical reaction, by lowering, without being consumed, the activation energy (or energies) of the corresponding reaction path. They can be divided into two big families: homogeneous catalysts and heterogeneous catalysts. In the first class, the catalyst and the reactants are in the same phase, principally in solution; generally, homogeneous catalysts show a higher selectivity, and are easier to study, but more difficult to separate from the reaction products at the end of the process. Also, for the latter reason, heterogeneous catalysts, where the catalytic material and the reactants are in distinct phases (such as solid-gas or solid-liquid), are largely employed. Henceforth, we'll focus on heterogeneous catalysts only.

Supported metal nanostructures play a major role in heterogeneous catalysis. It is well established that the size of the metal cluster is a crucial parameter of the catalyst's specific activity (activity per active site) (Fig. 1.2B-C). The reason is that low-coordinated metal atoms often function as catalytically active sites [12], thus only a fraction of the atoms in a nano- or sub-nanoparticle are catalytically active. A striking example is the chemically inert gold, which exhibits extraordinary catalytic performance in many heterogeneous reactions upon downsizing bulk gold to nanoparticles or even to sub-nanoclusters [13, 14]. In general, the reduction of size implies not only a larger fraction of active sites (because of the increase of the surface-to-volume ratio) but also quantum effect size (as the discretization of the energy levels) and a different (usually stronger) interaction with

A

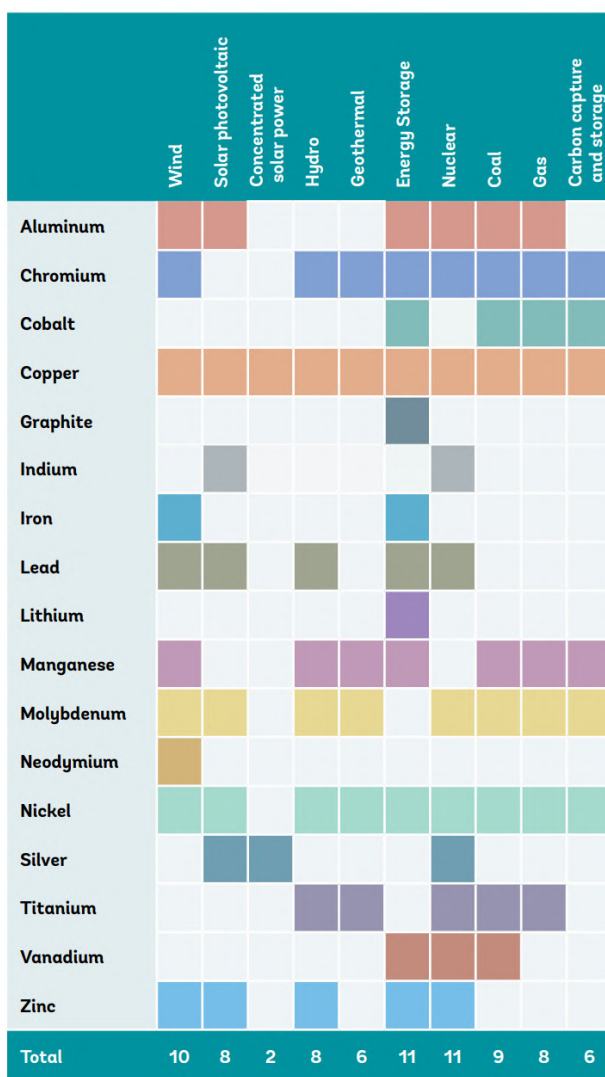
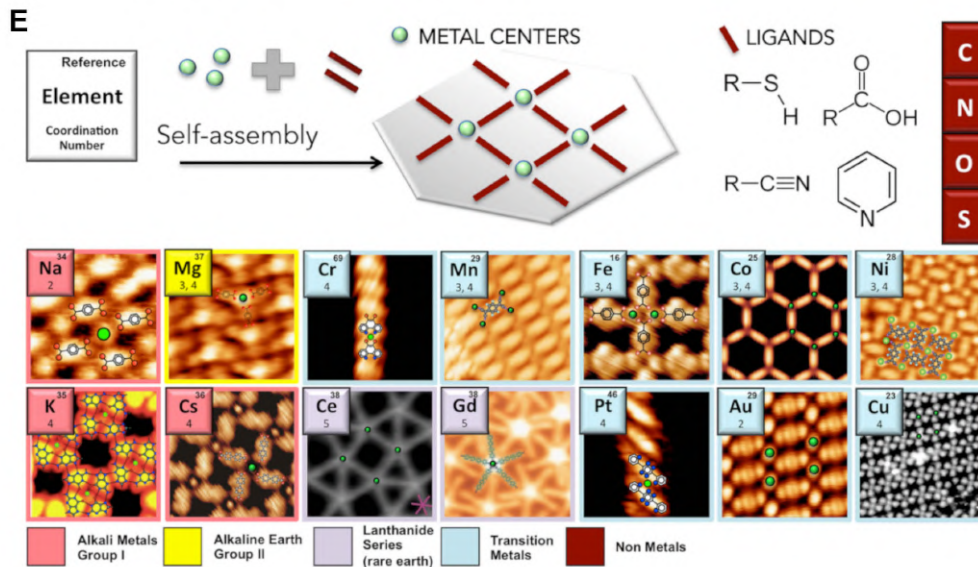
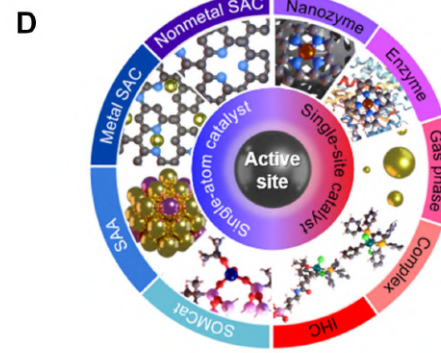
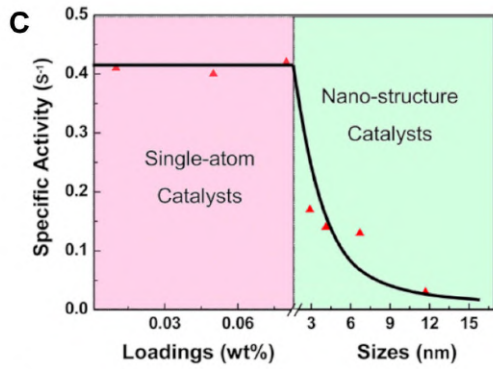
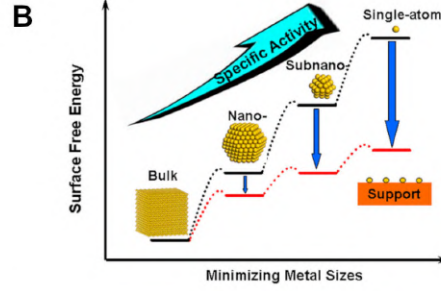
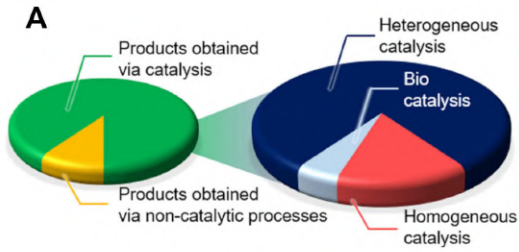


Figure 1.1: Mapping minerals with relevant applications in the fields of energy production and storage technologies [3]



the support (charge transfer, magnetic coupling...). Furthermore, nano- and subnano-clusters are intrinsically composed, despite their tiny size, by non-equivalent active sites which, from one side, makes them very challenging to study, and from the other side, lowers their selectivity, yielding unwanted products for the specific process. In addition, pressure and temperature induced sintering hinders their study in *operando*.

In this perspective, the ideal limit for a metal nanostructured catalyst is the single-atom catalyst (SAC), i.e. isolated metal atoms dispersed on a suitable support, that prevent their clustering (Fig. 1.2D). Indeed, the reduction of the size implies also an increase in the particle's free energy and, hence, their tendency to aggregate (Fig. 1.2B). Hence, the presence of a single metal species optimizes the metal usage and its specific activity, improves the fine-tuning control at a fundamental level, and makes the active sites all identical.

As mentioned, a major challenge in the preparation of SACs is that single metal atoms tend to aggregate. There are many solutions to the problem, from wet chemistry to mass selection starting from bulk materials [12], but a promising method is the stabilization of the metal center by an organic matrix or cage, with the subsequent formation of a so-called metal-organic framework (MOF). These compounds, characterized by a high degree of crystallinity, due to the highly anisotropic bonding nature of the organic linkers, offer multiple advantages such as high surface area, solid bonding of the metal, a well-defined structure, and a high degree of engineering possibilities, which comes from the choice of the cation center or organic linker, and the interaction with the substrate. Furthermore, the embedding of different metals and/or the presence of non-equivalent active sites offer a degree of flexibility for different catalytic preferences.

Figure 1.2 (preceding page): *A) Relevance of catalysis for the chemical industry. Over 90% of the world's manufactured consumer goods involve catalysis at one or more stages. Approximately 80% of all catalytic processes require heterogeneous catalysts, 15% homogeneous catalysts, and 5% biocatalysts [11]; B) Schematic illustrate the changes of surface free energy and specific activity per metal atom with metal particle size and the support effects on stabilizing single atoms [12]; C) Specific activity as a function of metal loadings/sizes [12]; D) Overview of subclasses of catalysts comprising an isolated atom as the active site (SAC= single- atom catalysts; SAA= single-atom alloy; SOMCats= surface organometallic catalysts) [11]; E) Table showing STM images of metal-organic networks incorporating different metal centers. Typical functional groups of the most common ligands are listed at the bottom [9]*

1.2.1 Two-dimensional Metal-organic Frameworks

Surface coordination chemistry can be exploited for the synthesis of very thin MOFs at the very well-defined metal facets, down to the single atom thickness. For this reason, we refer to them as two-dimensional metal-organic frameworks (2D MOFs). They can be self-assembled starting from relatively simple organic ligands and co-deposited metal atoms [9]. The modular approach allows the combination of multiple metals and ligands, enriching the chemistry of the system and yielding ideal platforms to model the reactive sites of enzymes (Fig. 1.2E) [9, 15]. As in their 3D counterpart, the electronic structure and consequently the chemical reactivity are determined by the elementary type of the metal, the number and the geometry of the coordinating molecular functional groups, and the electron affinity of the organic molecules. But the true advantage resides in the presence of open coordination sites, which makes the network highly reactive toward binding of ligands or reactants from gas/liquid phase at these positions, together with the stronger interaction with the supporting metal surface, which strongly affects the electronic structure. In addition, the presence of the substrate can modify the MOF adsorption properties through the so-called surface trans effect, accounting for the competition for the electronic charge between the surface and the potential ligand, at the opposite sides of the metalorganic plane.

Another benefit of working with 2D MOFs is the possibility of taking full advantage of the powerful surface science growth and characterization techniques, which nowadays offer an incredible level of insight on the geometry, electronic and magnetic structure of the layer with the possible presence of adsorbates, with techniques running even *in situ* and *operando* conditions, and compare the results with *ab initio* methods. The effectiveness of these techniques is combined with the high level of control regarding the growth and the contamination of the sample, since many of these 2D MOFs can be synthesized directly in ultra-high vacuum (UHV) conditions, as in this thesis work.

1.3 SECONDARY BATTERIES AND BIFUNCTIONAL MATERIALS

As we shall see in this paragraph, MOF-based catalysts can be technologically relevant in the field of energy storage. Indeed, the transition from fossil fuels to renewable but intermittent energy sources, like wind and sun, fosters the production of new, cheap, and efficient energy storage devices [16, 17]. In particular, rechargeable (secondary) batteries allow re-using the same device over thousands of cycles, saving materials and energy. At present, lithium-based secondary batteries are the most widespread energy storage devices available on the market (Fig. 1.3A). However, lithium supply is limited and its cost is high, besides the serious issues concerning safety and environmental unfriendliness [18].

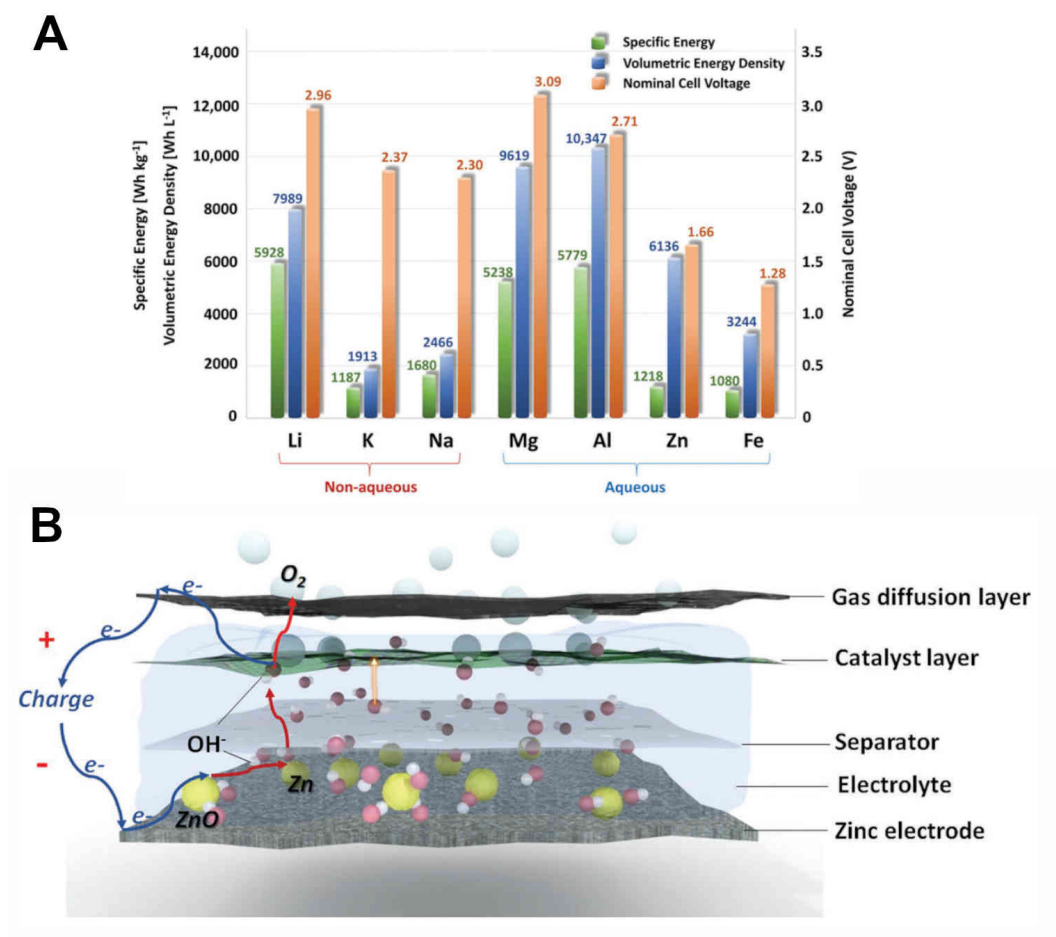


Figure 1.3: A) Theoretical specific energies, volumetric energy densities, and nominal cell voltages for various metal anodes in aqueous and non-aqueous metal-air batteries. Specific energy values account for oxygen uptake in the battery by numeric integration between the fully charged and fully discharged states [16]; B) Schematic of an aqueous rechargeable zinc-air battery at charging status [16].

Recently, metal-air batteries have been proposed as a possible alternative to Li-ion batteries, with several advantages [16]. The main constituting elements of a metal-air battery, schematized in Fig. 1.3B, are the metal-electrode (where the metal is stored), the electrolyte (which allows ion current), the separator (which denies the metal to pass through), the catalyst layer, the gas diffusion layer, and the external air. The gas diffusion layer, in the air electrode, allows oxygen to reach the internal layer and at the same time prevents electrolyte leaks. On the catalyst layer, during the discharge, molecular oxygen (coming from the external air) is reduced to water, combining with hydroxide (OH^-) species in the electrolyte. For this reason, the reaction is called Oxygen Reduction Reaction (ORR), described by the equation:



During charging, the opposite reaction occurs, called the Oxygen Evolution Reaction (OER): in this case, di-oxygen is released again into the air and the OH^- species solvate the metallic electrode, after crossing the separator layer. It is important to underline that both reactions occur on the same catalyst.

Metal-air batteries display considerably high energy densities (WhKg^{-1}) because oxygen is used as the reactant at the positive electrode and is stored outside of the battery (i.e. in the atmosphere) [16]. A high volumetric energy density is particularly desirable for mobile and portable devices because there is a limited volume for mounting the batteries in these applications [19]. The energy storage density of Li-ion batteries (265 WhKg^{-1}) is relatively low if compared to the Li-air (3458 WhKg^{-1}) or Zn-air (1086 WhKg^{-1}) ones [18]. For secondary metal-air batteries, lithium is still considered to be a valid anode candidate since it has the highest theoretical specific energy. However, lithium in the metallic form is plagued by its inherent instability when exposed to air and aqueous electrolytes [20], so research efforts are focusing on alternative elements, in particular zinc. Compared with lithium, zinc is inexpensive and more abundant in the earth's crust, readily available in many regions of the world. In addition, Zn as a metal is safer than Li and can be fully recycled. It is worth noting that even though Li, Ca, Mg, and Al have higher specific energies than Zn, they exhibit significantly more negative electrode potentials and therefore are more prone to self-discharge, making rechargeable schemes more demanding [21, 22].

Despite all recent years efforts, the development of rechargeable Zn-air batteries is still a challenge, due to irregular dissolution and re-deposition of Zn on the anode, corrosion of Zn electrode materials, formation of deposits from side reactions products, and the sluggish ORR/OER reactions occurring on the catalyst. Currently, catalysts are optimized for just one or another reaction, including carbon nanostructures, metal clusters, transition metal oxides, and metal-organic frameworks [23]. The most diffused catalysts are noble metals and alloys, in particular, carbon-supported platinum (Pt/C) for ORR and noble- or transition metal oxides for OER, such as RuO_2 or IrO_2 [18]. However, these catalysts are really expensive and are usually active towards only one of the two reactions [23]. Currently, the "solution" is the mixture of separately optimized catalysts on an engi-

neered substrate, which supports the active medium and avoids aggregation [24]. A much better solution would be to develop a bifunctional, cheap, efficient, and stable catalyst for ORR/OER to take place alternately on the same electrode material [16–18, 23].

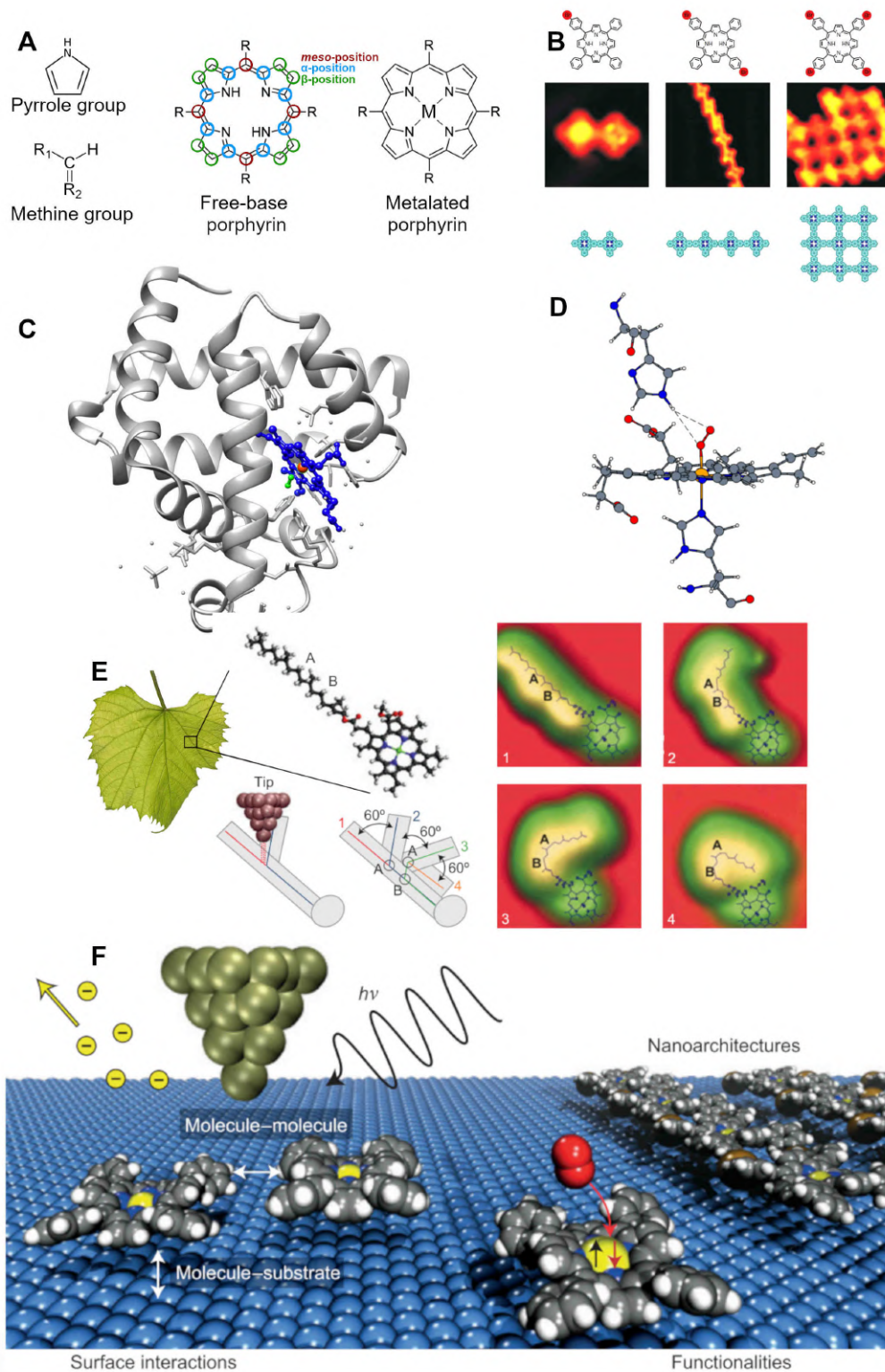
An example of monophasic bifunctional catalyst is based on single-atom cobalt, considered a low precious metal, in an N-doped graphene-like carbon support, which performed as a good catalyst for both ORR and OER when used at the air electrode of a Zn-air battery [25]. Thanks to their crystalline porous structure, high surface area, well-defined structure, accurate designability [26], smooth electron and mass transfer pathways, and active sites with different catalytic preferences, MOF-based SACs emerge as a novel and interesting solution to bifunctionality. Besides, they are relatively easy to study, meaning that the most crucial features can be understood and fine-tuned.

1.4 PORPHYRIN-BASED MOFS FOR ORR/OER

Recently, 2D MOFs based on self-assembled porphyrins have attracted attention due to their interesting ORR/OER electrocatalytic activity. Before entering into the details of these findings, it is useful to provide the reader with a brief description of such molecules.

Porphyrins belong to the big family of tetrapyrroles that, as the name suggests, are quasi-planar molecules formed by the cyclic junction of four pyrrole groups through four methine bridges [27] (Fig. 1.4A). This stiff organic backbone, called macrocycle, is responsible for the porphyrins' high thermal and chemical stability [30]. The four pyrrolic nitrogen atoms, internal to the macrocycle, allow the hosting of a single metal atom, typically a transition metal in a formal +II oxidation state when no other ligand is bound (Fe, Co or Mg prevail in biological systems [30]). The metalation of a porphyrin represents a primary “dial” for the tuning of its electronic, photochemical, catalytic, optical, magnetic, chiral, and adsorption properties [27, 30–36]. Moreover, it is possible to attach flexible residues to the carbon atoms of the methine bridges (C_{β}), affecting in this way especially the molecule-molecule and the molecule-substrate interaction and fine-tuning the electronic configuration of the macrocycle (Fig. 1.4B) [37–40].

Porphyrins, together with other caged single atoms embedded in a protein backbone [41], cover fundamental biological tasks, and often constitute the prosthetic group of a protein: to give an example, hemoproteins alone, containing a heme-prosthetic group with a central Fe atom in a porphyrinic cage (Fig. 1.4C), are responsible for the oxygen transport and storage (Fig. 1.4D) (hemoglobin, myoglobin, neuroglobin, cytoglobin), catalysis (cytochrome P450s, cytochrome c oxidase, peroxidases), electron transfer (cytochromes a, b, and c) and defense (catalase) [27]. Indeed, metalloenzymes constitute about one-third of the known enzymes [42]. Another striking example is chlorophyll (Fig. 1.4E), an Mg-based porphyrinoid, notoriously responsible for photosynthesis. It is not a case, indeed, that the study of porphyrins started to answer the question of why leaves are green or blood is red and, both for their dyeing properties and their essential role in



biochemistry, porphyrins are also called “the pigment of life” [30]. The functionality of the porphyrinic active site in the protein environment is given by a complex interplay between the chemical identity of the metal, the peripheral structure of the tetrapyrrolic cage, the nature of the axial ligand, and the distal superstructure of the hosting protein [42–44]. Indeed, during the enzymatic reaction, the reactant¹ binds coordinatively to the metal within the three-dimensional organic pocket of the enzyme, ensuring substrate selectivity, reaction selectivity, and stereoselectivity [9, 45]. Sometimes, even the organic cage itself plays an active role, as in the case of P450 that favors benzene hydroxylation [46]. Another example is myoglobin (Fig. 1.4D), a heme prosthetic group with a central Fe atom, that tunes the binding of a dioxygen molecule by means of the (proximal) imidazole ring of a histidine residue in trans-configuration, together with a (distal) histidine [29]: while the latter is involved in a simple hydrogen bonding, the proximal ligand exploits the molecular trans-effect, i.e. the competition between two ligands in trans position binding to the same metal center. In general, the presence of an additional axial ligand weakens

¹ The “reactant” is called “substrate” in biochemistry

Figure 1.4 (preceding page): A) Structure of a porphyrin. Adapted from [27]; B) Covalent bond formation between Br-substituted tetra-phenylporphyrins adsorbed on Au(111). As it can be noticed, the shape of the nanostructure strongly depends on the number and the position of the Br substitutions; C) Schematics of an oxygenated myoglobin protein: the heme prosthetic group is encapsulated in the complex protein scaffold. Atoms color legend: green-oxygen, red-iron, blue-heme group [28]; D) Detail of the O₂ binding in the myoglobin active site: the ligation is affected by the molecular trans-effect of the proximal histidine and the H-bonding of the distal His64 residue. Atoms color legend: red-oxygen, grey-carbon, blue-nitrogen, white-hydrogen, yellow-iron [29]; E) Different structural conformations induced by the STM tip in the chlorophyll a phytyl chain, immobilized under cryogenic conditions on Au(111) [30]; F) Schematic characteristics of porphyrins and their control at surfaces: typical investigation methods involving tip, photon, and/or electron spectroscopies/microscopies; control by lateral and vertical interaction; adsorption of ligands with a possible consequent change of the molecule magnetic properties; formation of low-dimensional nanostructures via supramolecular engineering [30].

the adsorption of the other ligand, because the same metal orbitals are involved in both covalent bondings [47].

In the last decades, great attention has been devoted to porphyrins adsorbed at surfaces, with multiple advantages (Fig. 1.4F):

- The quasi-planar configuration that gives almost parallel adsorption of the macro-cycle [30], which is ideal for a surface scientist;
- The possibility of using them as tectons for creating two-dimensional nanomaterials via supramolecular assembly, which is mainly determined by the molecule-molecule and the molecule-substrate interaction; [30, 36, 39, 48, 49]
- Altering the porphyrin's chemical, electronic, geometric, and magnetic properties by means of metalation, choice of the substrate, lateral interaction, gas exposure, or tip-manipulation (Fig. 1.4E) [30, 32, 33, 50–54];
- In a biomimetic approach, tuning the adsorption capabilities by exploiting the molecular trans-effect, in particular by using the surface as the proximal ligand and, for this reason, called surface trans-effect [30, 33, 47, 51, 55];
- The conformational changes possibly induced by the strong interaction with substrate or ligands, that often play an important role in the porphyrin's functionality [44, 56].

In this thesis, we will give particular focus to tetra-pyridyl-porphyrins (TPyPs), in the perspective of their potential role in the assembly of effective, promising ORR/OER catalysts, as we shall see in a moment. The TPyP molecule is a porphyrin with four pyridine residues attached at the meso-positions. They usually exhibit attractive lateral interactions, and they typically form near-hexagonal or near-square 2D lattices when deposited on relatively weakly interacting metals, such as Ag(111) or Au(111), where large islands are formed [32, 39]. The interest in these molecules resides in the 4 N atoms of the pyridinic terminations that can easily form extra coordinative sites [9]. In this way, by co-depositing extra metal atoms, two-dimensional bimetallic frameworks can be easily grown at surfaces *in vacuo* [32], or even sub-micron monolayers at the liquid/air interface using Langmuir–Blodgett methods [57], the latter being of extreme interest for practical bottom-up MOF growth methods [58].

D. Hötger *et al.* have demonstrated how FeTPyP and CoTPyP self-assembled on Au(111) show good electrocatalytic performance and stability with respect to the ORR reaction (CoTPyP is even more active than Co nanoclusters), while both MOFs quickly deteriorate under OER conditions [59]. B. Wurster *et al.* performed ORR and OER reactions with all combinations of M1TPyPM2/Au(111) (M1,2=Co, Fe) where M2 is the metal co-deposited in UHV which coordinates to the four adjacent molecules at the pyridinic N atoms of (Fig. 1.5A). The results show a non-linear increment of the catalytic conversion of about two orders of magnitude for the bimetallic systems, with a maximum yield for CoTPyPCo [32]

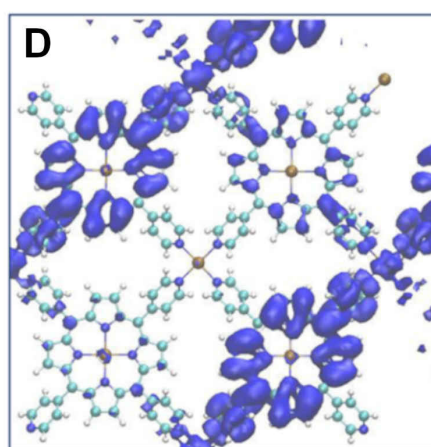
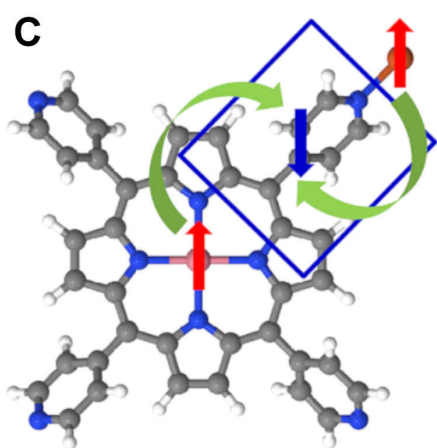
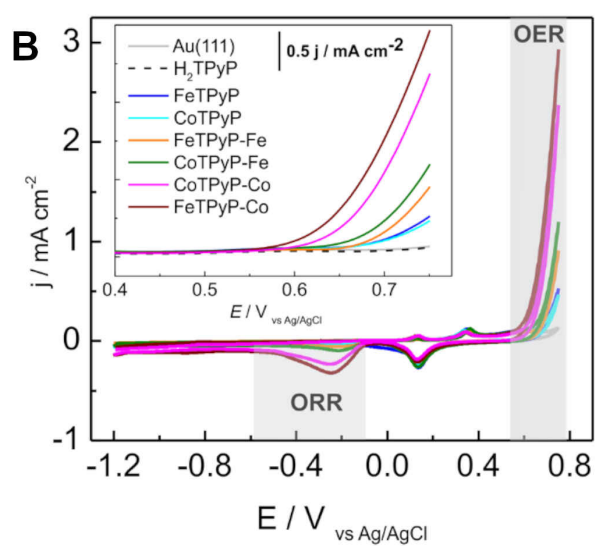
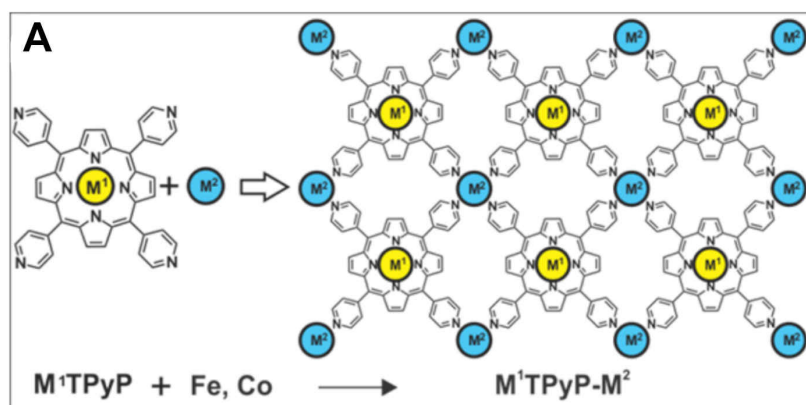


(Fig. 1.5B). They suggest that this cooperative behavior “stems from more fundamental properties such as changes in the electronic structure of the metals in mono- vs bimetallic catalysts as a result of synergetic effects of the two metal centers” [32, 60]. Insight in this sense is provided by the *ab initio* simulation of Mandal *et al.*, who showed how the two metals can be magnetically coupled even at 7 Å of distance (Fig. 1.5C) thanks to the polarization of the organic matrix, for the free-standing Fe- and Co- bimetallic TPyP frameworks [54]. Furthermore, they found that coordination of the second metal provides further stability to the structure, because of the electrostatic interaction, and their simulations show the presence of Bloch states with linear dispersion (Fig. 1.5D), delocalized throughout the molecules, that could aid the 4-electron transfer in the OER, thus explaining the increase of the catalytic activity [54]. Baranowski *et al.* have proven that NiTPP π -conjugated molecular networks can have a dispersive character, indicating that delocalized block states can be effectively established through the molecular network [61].

1.5 MIND THE GAP – A QUEST FOR *IN SITU* AND *OPERANDO* APPROACHES

At this point, it is worth pointing out that most of the discussed investigations have been conducted in UHV or *ex situ*. The issue with the first is the huge pressure gap (10^{13} orders of magnitude) with the ambient pressure, where real-life applications take place. Besides, some studies are even conducted at cryogenic temperatures, which constitutes also an extra gap from the real-working conditions. It is well known that some phenomena, crucial for the catalyst activity (or inactivity), are triggered exactly from those high-pressure/temperature conditions, such, for example, the formation of active phases, structural changes, or bonding cleavage/formation [8, 62]. Moreover, the issue with the

Figure 1.5 (preceding page): A) 2D MOF based on tetra-pyridyl porphyrin self-assembled on Au(111): the additional extra metal (M2) forms a tetravalent bonding with the N atoms of the pyridyl endgroups [32]; B) Cyclic voltammetry at 0.05 V s^{-1} in NaOH 0.1 M Ar saturated solution for all combination of the molecular catalysts depicted in panel (A): the bimetallic compounds show better catalytic performance [32]; C) Schematic diagram showing through-bond spin polarization in CoTPyPFe and FeTPyPCo [54]; D) The plot of charge density around 0.25 eV above the Fermi level (isovalue=0.01) in CoTPyPCo reveals the extension of the electronic state over many molecular units [54].

second (i.e. *ex situ* measurements) is the missing of possible changes that occur only during a catalytic reaction at ambient pressure, such as the formation of metastable chemical species, phase changes, or reaction pathways that strongly depend on the partial pressure of the reactants, temperature, time on-stream, etc. [8]. Many orders of magnitude of difference in pressure create a fundamental uncertainty in how far the phenomena observed *in vacuo* can be transferred to other environments. Thus, it is of utmost importance the necessity to investigate the reaction *in situ* and *operando*, meaning at the conditions of interest as the evolution is proceeding.

Working *in situ* and *operando* is a challenge for most standard surface science techniques, due to contamination, the probes mean free path, change of work function, pumping systems, and filament burning, just to name a few issues. For this reason, experimental techniques that offer atom-detailed information beyond UHV are needed. Currently, sophisticated and constantly improved methods allow the extension of Scanning Tunneling Microscopy (STM) [63–65], Transmission Electron Microscopy (TEM), and X-Ray Photoemission Spectroscopy [66] to the near ambient pressure regimes (~ 1 mbar), while vibrational information can be extracted from Polarization-Modulation InfraRed Reflection Adsorption Spectroscopy (PM-IRRAS) [67] and Infrared-Visible Sum-Frequency Generation Vibrational Spectroscopy (IR-Vis SFG) [44, 67]. The latter, in particular, represents the main technique used in this thesis, exploiting non-linear optics and symmetry arguments to collect information only and directly from interfaces.

1.6 AIM OF THIS THESIS

In this thesis, we focused on the growth, UHV characterization, and reactivity to small gases at near ambient pressure of TPyP-based mono- and bi-metallic 2D MOFs self-assembled on almost free-standing graphene on Ir(111). For this purpose, we exploited a combination of standard (STM, NEXAFS, ARPES, XPS, 2PPE, UPS) and non-standard (IR-Vis SFG, NAP-XPS) experimental and *ab initio* (DFT) techniques, yielding atomic-resolution insight into the electronic, magnetic, and geometrical structure of the layer.

The choice of using the almost free-standing [68] graphene, grown at the (111) termination of an iridium single-crystal, lies in a multitude of reasons: firstly, the majority of the literature deals with 2D MOFs assembled at “weakly” interacting metal surfaces, also because of the relatively easy experimental constraints of such specimens, for instance, Au(111) or Ag(111). But even if they are often considered as “weakly” interacting substrates, it is well established that their interaction with the MOF is not at all negligible, because a direct covalent bonding is often formed between the bare metallic substrate and the single metal of the MOF [33, 69, 70]. Thus, it is impossible to discuss an isolated single metal atom without accounting for the support, unless the latter is really “weakly” interacting and, in this sense, Gr/Ir(111) is a good candidate. The second reason is the graphene chemical passivation of the substrate, which comes very useful when studying

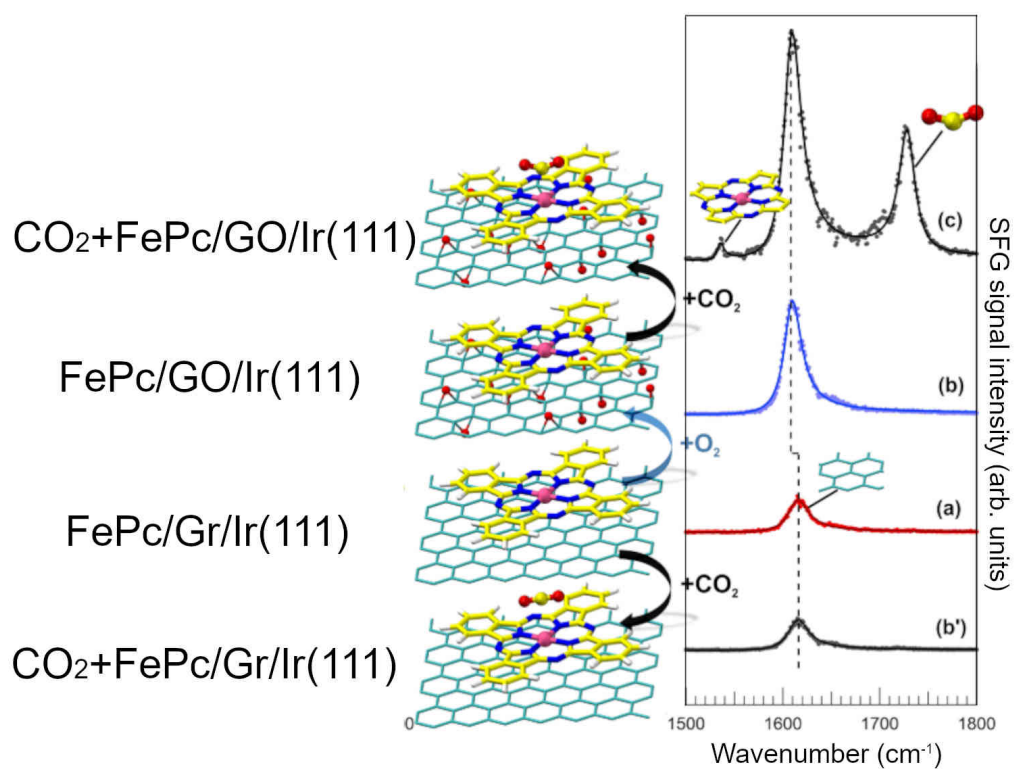


Figure 1.6: The surface trans-effect, allowing adsorption of carbon dioxide at near ambient pressure, is triggered, in a FePc monolayer, by graphene oxidation [55].

the system at near ambient pressure, focusing in this way only on the MOF active sites. The third reason comes from the – already mentioned – surface trans effect, i.e. the competition for the transition metal orbitals between the surface and the axial ligand [47]. In addition, a strongly interacting surface could drain electrons from the MOF, at the expense of its activity towards ligation: for example (Fig. 1.6), it has been demonstrated that an adsorbed Fe-Phthalocyanine can activate the notoriously stable CO₂ upon oxidation of the graphene support[55], driving the injection of extra charge into the phthalocyanine plane. Although graphene doping is not assessed in this thesis, this is still an interesting and powerful perspective to investigate. In conclusion, the weakening of the molecule-substrate interaction strengthens the tectons' lateral coupling, yielding the growth of ordered layers and charge delocalization for excitonic fission, energy funneling, or efficient charge conductivity. . .

1.7 AB INITIO CALCULATIONS

In this thesis, novel results from *ab initio* calculations are reported to corroborate the experimental data and gain a deeper insight in the physics of the system under examination. The method used is Density Functional Theory (DFT), and the computational results are the fruit of the work of a colleague Ph.D. student, Davide Bidoggia, under the supervision of prof. Maria Peressi, both affiliated with the University of Trieste. **The author of this thesis did not give any active contribution to such theoretical work.** We now report the essential computational details.

1.7.1 Computational details

Because of the small interaction between Gr and the Ir(111) substrate, the latter was always neglected in order to minimize the computational effort. However, the CoTPyP-Gr interaction could not be ignored, yielding an adsorption energy of 1.95 eV/molecule and determining the CoTPyP geometric and electronic structures.

All DFT calculations were performed using the open source Quantum ESPRESSO package[71–73], based on plane waves and pseudopotentials approach. The exchange correlation energy was described by the Perdew-Burke- Ernzerhof (PBE) functional within the generalized gradient approximation (GGA) method. Vanderbilt ultrasoft pseudopotentials were employed except for the Co atom, for which a Rappe-Rabe-Kaxiras-Joannopoulos ultrasoft pseudopotential was used, instead [74]. For an efficient treatment of the Co 3d states we used the Hubbard-U correction [75] with an U parameter of 3.5 eV in order to recover the 5.5 eV distance between occupied and unoccupied 3d_{z²} levels in CoTPyP, as suggested in the literature [76]. Van der Waals interactions were included through the Grimme DFT-D3 approach [77]. A plane-wave basis set with energy cutoff of 60 Ry was

used for the wave functions, together with a 240 Ry cutoff for the charge density. The lattice parameters and the choice of the Monkhorst-Pack k-point sampling grid for the Brillouin zone integration is specific for the treated system:

- In Chapters 3 and 5, where close-packed CoTPyP and CoTPyPCo are treated, Brillouin zone integration was performed with a Monkhorst-Pack $4 \times 2 \times 1$ k-points sampling grid for self-consistent field (SCF), while $8 \times 4 \times 1$ is used for nonself-consistent field (NSCF). The CoTPyP molecules are close-packed in a triangular lattice with $d_{Co-Co} \approx 1.5$ nm (distance between adjacent macrocyclic cobalt atoms), while a square lattice with a $d_{Co-Co} \approx 1.4$ nm has been used for CoTPyPCo, according to the experimental data.
- In Chapter 4, where isolated CoTPyPs are simulated, the triangular lattice is characterized by a larger distance ($d_{Co-Co} \approx 1.7$ nm), and the Brillouin zone is integrated on a $4 \times 4 \times 4$ and a $8 \times 8 \times 8$ k-point sampling grid for SCF and NSCF calculations, respectively. In order to investigate the bonding nature of the O₂H-H₂O/Co system, different postprocessing tools were used in this chapter. All the plots showing electron density rearrangement due to adsorption of component B on component A were calculated as the difference in electron density distribution between the full system (A+B) and the individual, separated components in the positions assumed in the total system:

$$\Delta n(r) = n_{A+B}(r) - (n_A + n_B)(r).$$

In order to identify the character and the strength of the interaction, the reduced density gradient (RDG) ($s(r) = \frac{|\nabla n(r)|}{2(3\pi^2)^{1/3}n^{4/3}}$) was calculated together with the electron density multiplied by the sign of the second Hessian eigenvalue, following [78]. Spatially resolved energy-integrated local density of states (ILDOS) was calculated in order to visualize charge density in bonding regions. Interesting energy regions to calculate ILDOS were identified by comparing the projected density of states (PDOS) of a bonding configuration with respect to the PDOS of the individual, separated constituents. After full optimization of the CoTPyP/Gr system, which leads to an almost flat Gr layer, the optimization of the structures with adsorbed O₂H and, subsequently, H₂O, was made keeping Gr fixed. Oxygen core level shifts were obtained from total energy differences between SCF calculations, in which one O atom at a time was described by a pseudopotential taking into account a full core hole in 1 s state, using the final state approximation [79].

Because of the metallic behavior of the system, a Methfessel-Paxton scheme [80] was used for the occupation of the electronic states, with a smearing of 0.01 Ry. Optimized structures were obtained using the Broyden, Fletcher, Goldfarb, and Shanno algorithm with energy and force convergence threshold of 1.0×10^{-6} Ry and 1.0×10^{-3} a.u. respectively. Oxidation states for the Co metal center were determined according to the literature

[81], counting the number of valence electrons to be assigned to the atom as the number of its fully occupied 3d-orbitals (i.e., Löwdin population of the orbital=1).

2 | EXPERIMENTAL METHODS

In this thesis, several techniques are complementarily exploited to characterize the systems in UHV and probe their reactivity at near ambient pressure. In particular, Infrared-Visible Sum-Frequency Generation Spectroscopy (IR-Vis SFG), Near-Ambient Pressure X-Ray Photoemission Spectroscopy (NAP-XPS), Scanning Tunneling Microscopy (STM) and Spectroscopy (STS) are the principal methods used in this work. Useful additional information can be extracted also from UV Photoemission Spectroscopy (UPS) and time-resolved 2 Photon Photoemission Spectroscopy (tr-2PPE), for which a brief description is also provided in this chapter.

2.1 IR-VIS SUM-FREQUENCY GENERATION SPECTROSCOPY

IR-Vis SFG is a surface-sensitive photon-in photon-out technique that provides both vibrational and electronic information about interfaces. Being a second-order optical technique, the SF signal can only be generated from non-centrosymmetric materials, therefore it is an intrinsically surface-sensitive technique. These second-order processes have typically a low yield, thus pulsed laser radiation is required to have the high peak power necessary to obtain a detectable output signal [82]. Surface sensitivity, combined with the long mean free path of photons in the gas phase, makes this technique suitable for the investigation of many interfaces (such as solid-vacuum, solid-liquid, solid-gas, liquid-gas) both in UHV and at NAP conditions. For the system to be SF active for a specific normal mode at a metal surface, the corresponding dipole must have a net component normal to the surface and a net orientation on a range of a few hundred nanometers, which is the typical wavelength of a visible photon [83, 84].

2.1.1 Theoretical background

The IR-Vis SFG signal is generated at an interface using two laser beams, one in the visible light region and the other in the IR region: in our setup, the visible beam is green with 532 nm wavelength, and the one in the infrared region is tunable between 2300 and 10000 nm. In order to generate SFG radiation IR and visible laser pulses need to overlap at the surface, both spatially and temporally. The visible beam induces an electronic transition to an excited virtual state, while the tunable IR beam can excite a vibrational transition when the radiation energy matches the energy of a vibrational resonance of the system.

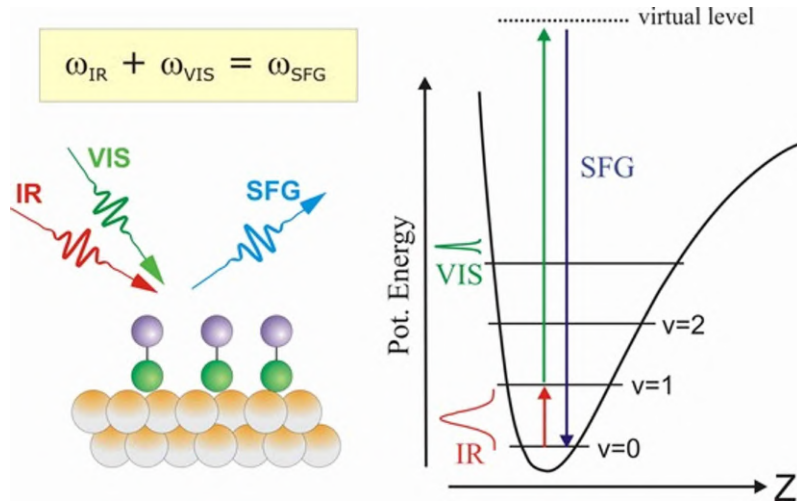


Figure 2.1: The SFG signal is generated from two laser beams, IR and visible, impinging on a surface (left). Schematic representation of SFG transitions (right). Image taken from [85]

Both the IR or the Vis photons can be first absorbed, but since the vibrational excited state has a longer lifetime than the electronic one, usually the anti-stokes process where the IR photon is absorbed prior to the Vis photon is generally favored.

The relaxation of this excited state generates the emission of radiation with energy given by the sum of the visible and infrared energies

$$\omega_{SFG} = \omega_{VIS} + \omega_{IR} \quad (2.1)$$

A schematic representation of the process is reported in Fig. 2.1. SFG radiation intensity is measured as a function of the IR energy to identify molecules and gas adsorbates through their specific vibrational energies.

SFG as a non-linear optical process

In the description of a material's response to an oscillating external electric field, it is easier to start from a scalar electric field $E(t)$ that generates a polarization $P(t)$. In linear optics processes, the polarization dependence on the electric field is usually expressed by

$$P(t) = \epsilon_0 \chi^{(1)} E(t) \quad (2.2)$$

where ϵ_0 is the vacuum dielectric constant and $\chi^{(1)}$ is the first order susceptibility of the material. This relation is valid for weak fields.

In the presence of strong external fields ($E \sim 10^6$ V/m) this relation is no longer valid and it is necessary to expand the polarization as a power series in $E(t)$: using the formalism of [86] the expression for the polarization becomes

$$\begin{aligned} P(t) &= \epsilon_0 [\chi^{(1)} E(t) + \chi^{(2)} E^2(t) + \chi^{(3)} E^3(t) + \dots] \\ &\equiv P^{(1)}(t) + P^{(2)}(t) + P^{(3)}(t) + \dots \end{aligned} \quad (2.3)$$

where the coefficients are now given by higher orders susceptibilities. It is possible to generalize this description to take into account the vectorial nature of $\mathbf{E}(t)$ and $\mathbf{P}(t)$ using tensorial notation for the susceptibilities: $\chi^{(1)}$ becomes a second-order tensor and $\chi^{(2)}$ a third order tensor.

If the external impinging electric field is given by the sum of two different components, oscillating at different frequencies, it can be written in the form

$$\mathbf{E}(\mathbf{r}, t) = \mathbf{E}_1(\omega_1)e^{-i(\omega_1 t - \phi_1)} + \mathbf{E}_2(\omega_2)e^{-i(\omega_2 t - \phi_2)} + c.c. \quad (2.4)$$

where $\mathbf{E}_n(\omega_n) \equiv \frac{1}{2}\mathbf{E}_n e^{i\mathbf{k}_n \cdot \mathbf{r}}$ and \mathbf{E}_n is the product of the amplitude and the polarization vector. Using the relation $\mathbf{E}_n(-\omega_n) = \mathbf{E}_n^*(\omega_n)$ a more compact form of (2.4) can be written:

$$\mathbf{E}(\mathbf{r}, t) = \sum_n \mathbf{E}_n(\omega_n) e^{-i(\omega_n t - \phi_n)}, \quad n = -2, -1, 1, 2 \quad (2.5)$$

where the sum extends over positive and negative frequencies, with $\omega_{-n} = -\omega_n$, taking into account the complex conjugate. It is now possible to write a cartesian component of the second order polarization as

$$P_i^{(2)}(\mathbf{r}, t) = \varepsilon_0 \sum_{jk} \sum_{nm} \chi_{ijk}^{(2)}(\omega_n + \omega_m; \omega_n, \omega_m) E_j(\omega_n) E_k(\omega_m) e^{-i[(\omega_n + \omega_m)t - (\phi_n + \phi_m)]} \quad (2.6)$$

where it is easy to see that the resulting components of the second order polarization oscillate at different frequencies $\omega_n + \omega_m$ with respect to the oscillation frequencies of the field components. The sum over n and m produces different components: second harmonic generation (SHG) at $2\omega_1$ and $2\omega_2$, difference frequency generation (DFG) at $\omega_1 - \omega_2$, sum frequency generation (SFG) at $\omega_1 + \omega_2$ and optical rectification (OR) that is a non-oscillating term.

We can now focus on the SFG component, with $\omega_3 = \omega_1 + \omega_2$, that becomes

$$P_i^{(SFG)}(\mathbf{r}, t) = \varepsilon_0 \sum_{jk} [\chi_{ijk}^{(2)}(\omega_3; \omega_1, \omega_2) E_j(\omega_1) E_k(\omega_2) + \chi_{ijk}^{(2)}(\omega_3; \omega_2, \omega_1) E_j(\omega_2) E_k(\omega_1)] e^{-i(\omega_3 t - \phi_3)} + c.c. \quad (2.7)$$

using the relation $\chi_{ijk}^{(2)}(-\omega_3; -\omega_1, -\omega_2) = \chi_{ijk}^{(2)}(\omega_3; \omega_1, \omega_2)^*$. Assuming that the nonlinear susceptibility has intrinsic permutation symmetry $\chi_{ijk}^{(2)}(\omega_3; \omega_1, \omega_2) = \chi_{ikj}^{(2)}(\omega_3; \omega_1, \omega_2)$ [86] the dummy indexes j and k can be interchanged, thus SFG polarization can be expressed by

$$\begin{aligned} P_i^{(SFG)}(\mathbf{r}, t) &= 2\varepsilon_0 \sum_{jk} \chi_{ijk}^{(2)}(\omega_3; \omega_1, \omega_2) E_j(\omega_1) E_k(\omega_2) e^{-i(\omega_3 t - \phi_3)} + c.c. \\ &= \frac{1}{2} \varepsilon_0 \sum_{jk} \chi_{ijk}^{(2)}(\omega_3; \omega_1, \omega_2) E_{1,j} E_{2,k} e^{i(\mathbf{k}_3 \cdot \mathbf{r} - \omega_3 t + \phi_3)} + c.c. \end{aligned} \quad (2.8)$$

and neglecting the spatial and temporal dependence a more compact form is obtained

$$P_i^{(SFG)} = \varepsilon_0 \sum_{jk} \chi_{ijk}^{(2)} E_{1,j} E_{2,k} \quad (2.9)$$

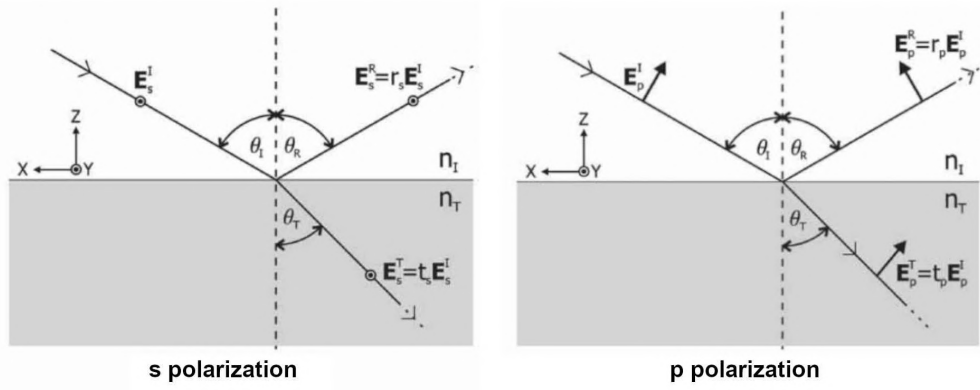


Figure 2.2: Reflection at an interface for p and s polarized radiation. Image taken from [83].

Equation (2.9) is useful to derive a fundamental property of the SFG signal that is the interface specificity, due to the fact that $\chi^{(2)}$ vanishes for centrosymmetric materials. When parity symmetry is applied to the polarization and electric field vectors they change sign (because they are polar vectors), while $\chi_{ijk}^{(2)}$ does not change sign because a centrosymmetric material is identical under inversion, thus $\chi_{ijk}^{(2)} = \chi_{-i-j-k}^{(2)}$. It is possible to write

$$\begin{aligned} -P_i^{(SFG)} &= \epsilon_0 \sum_{jk} \chi_{ijk}^{(2)} (-E_{1,j}) (-E_{2,k}) \\ &= \epsilon_0 \sum_{jk} \chi_{ijk}^{(2)} E_{1,j} E_{2,k} \end{aligned} \quad (2.10)$$

that for a centrosymmetric materials only holds when $\chi_{ijk}^{(2)}$ vanishes.

This property is largely exploited in SFG spectroscopy experiments: due to the fact that gas phases and many bulk materials are centrosymmetric, they are not SFG active and they don't contribute to the SFG signal. Therefore, SFG spectroscopy is the perfect technique to obtain vibronic information about surfaces and interfaces that are intrinsically non-centrosymmetric media.

SFG in reflection geometry

In our case, the imping electric fields consist of a visible beam and a tunable infrared beam. The visible beam is green and couples with the HOMO-LUMO gap of molecules; this choice is functional because detection is more efficient in the visible range and at this frequency radiation is not ionizing, thus limiting beam damage [83]. In the description of reflection at a surface, it is useful to decompose an incident field E_I into components polarized parallel (p) and perpendicular (s) to the incidence plane as follows:

$$\begin{aligned} E_{I,x} &= -E_p \cos\theta \\ E_{I,y} &= E_s \\ E_{I,z} &= E_p \sin\theta \end{aligned} \quad (2.11)$$

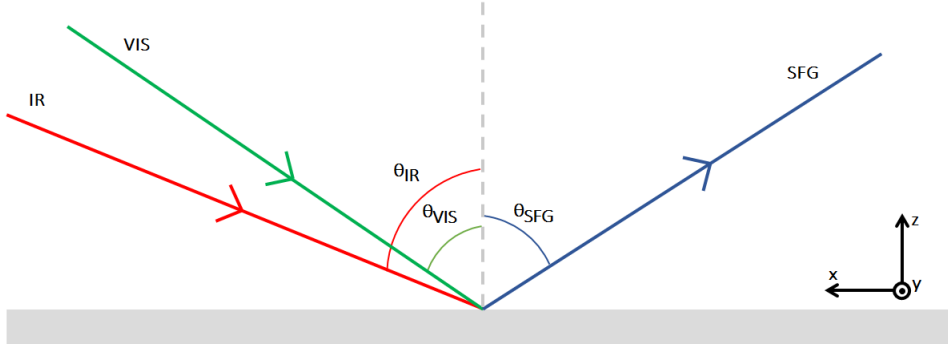


Figure 2.3: Generation of an SFG signal on a surface from IR and visible laser beams in reflection geometry. Image taken from [83].

where θ and the coordinate convention refer to Fig. 2.2. The total electric field at the surface is given by the sum of the incident and reflected beams. If we define the Fresnel amplitude coefficients for reflection (r_p, r_s) as in [83], the components of the total electric field at the surface can be written as

$$\begin{aligned} E_x &= -(1 - r_p)E_p \cos\theta \equiv K_x E_p \\ E_y &= (1 + r_s)E_s \equiv K_y E_s \\ E_z &= (1 + r_p)E_p \sin\theta \equiv K_z E_p \end{aligned} \quad (2.12)$$

Exploiting equation (2.12), the SFG polarization in (2.9) can now be expressed in term of the amplitude of the incident fields $E_{I,1} = E_{IR}$ and $E_{I,2} = E_{VIS}$:

$$P_i^{(SFG)} = \epsilon_0 \sum_{jk} \chi_{ijk}^{(2)} K_{IR,j} E_{IR} K_{VIS,k} E_{VIS} \quad (2.13)$$

The nonlinear polarization generates a surface bound SFG electric field. The emission angle of the SFG signal is determined by the phase-matching condition [83] that expresses the momentum conservation at the interface:

$$n_{SFG} k_{SFG} \sin\theta_{SFG} = n_{IR} k_{IR} \sin\theta_{IR} + n_{VIS} k_{VIS} \sin\theta_{VIS} \quad (2.14)$$

where n is the refractive index of the propagation medium, k the wavevector and θ the angle between the beam and the normal to the surface. In our case all the beams propagate in the same medium, thus refractive indexes can be neglected. Angle notation refers to Fig. 2.3

It is possible to express the SFG electric field in term of the induced polarization introducing the nonlinear SFG Fresnel factors (L factors) defined in [83] and not reported here

$$E_{i,SFG} = L_i P_i^{(SFG)} \quad (2.15)$$

The intensity of the SFG signal depends on the square modulus of the electric field, therefore the following relations hold:

$$\begin{aligned}
 I_{SFG} &\propto \left| \sum_i E_{i,SFG} \right|^2 \\
 &\propto \left| \sum_i L_i P_i^{(SFG)} \right|^2 \\
 &\propto \left| \epsilon_0 \sum_{ijk} L_i \chi_{ijk}^{(2)} K_{IR,j} E_{IR} K_{VIS,k} E_{VIS} \right|^2
 \end{aligned} \tag{2.16}$$

Using the convention of Fig. 2.2 we note that p polarization can have x and z components, while s polarization only has y components. The polarization of the incident beams determines the susceptibility tensor's components that can be measured, thus it is important to have the control over polarizations in SFG experiments.

Microscopic approach

The relation between SFG signal intensity and $\chi^{(2)}$, that is the macroscopic average of molecular polarizabilities, has been found in the previous paragraph. Microscopic molecular polarization $\boldsymbol{\mu}$ and imping electric field \boldsymbol{E} are linked by the relation

$$\boldsymbol{\mu} = \boldsymbol{\mu}_0 + \alpha \boldsymbol{E} + \beta \boldsymbol{E}^2 + \gamma \boldsymbol{E}^3 + \dots \tag{2.17}$$

which includes non-linear effects. β and γ are the first and second order hyperpolarizabilities of the molecules adsorbed on the surface [87]. The tensor β is a third-rank tensor, the same dimension of $\chi^{(2)}$, describing the nonlinear response of molecules on the surface to incident electric fields: different components refer to different vibrational modes. The second-order susceptibility tensor is the macroscopic average of β : hyperpolarizability β undergoes substantial changes when IR radiation is tuned through a resonance that is observed, through SFG measurements, as a change in $\chi^{(2)}$.

We can use a molecular bound coordinate system identified with indexes (a, b, c) instead of the surface one (i, j, k) : an example is reported in Fig. 2.4 where a molecule adsorbed on the surface is tilted of a θ angle. The molecular coordinate system is simply related to the surface one by three rotational matrixes $R(\psi)R(\theta)R(\phi)$ that refer to the Euler angles (ψ, θ, ϕ) . The hyperpolarizability tensor becomes $R(\psi)R(\theta)R(\phi)\beta$ and its macroscopic averaging can be written as:

$$\chi_{ijk}^{(2)} = \frac{N}{\epsilon_0} \sum_{abc} \langle R(\psi)R(\theta)R(\phi)\beta_{abc} \rangle \tag{2.18}$$

where N is density of adsorbed molecules and the matrix element represents an orientational averaging. A quantum mechanical expression for β_{abc} can be derived using perturbation theory [88]. In the case of visible radiation ω_{VIS} far from electronic res-

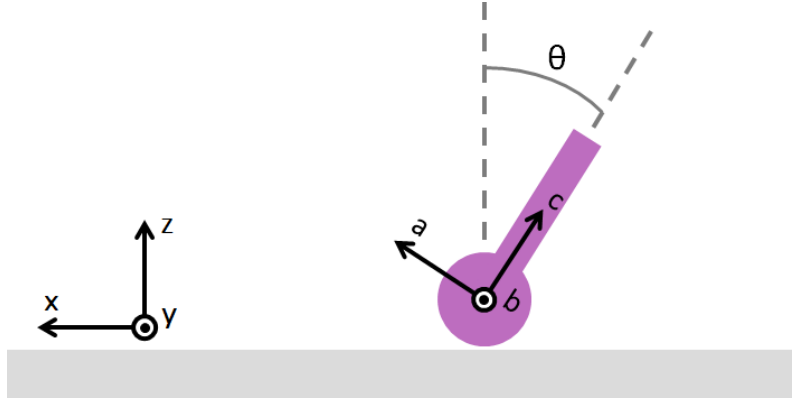


Figure 2.4: A molecule adsorbed on a surface, tilted of an angle θ . The two coordinate systems are related by a rotation matrix $R(\theta)$. Image taken from [83].

onances and infrared radiation ω_{IR} close to a vibrational resonance ω_0 , the following simplified version can be used:

$$\beta_{abc} = \frac{1}{2-\hbar} \frac{M_{ab} T_c}{\omega_0 - \omega_{IR} - i\Gamma} \quad (2.19)$$

where Γ^{-1} is the relaxation time of the vibrational excited state, M_{ab} and T_c are the Raman and infrared transition moments respectively, defined in [87]. A selection rule is immediately derived from (2.19): a resonance must be both Raman and infrared active in order to be observed through an SFG transition [89]. Eq. (2.19) has the shape of a Lorentzian resonance and when inserted in (2.18) it reveals the origin of the SFG signal intensity changing when the energy of the infrared laser approaches the energy of a vibrational resonance on the surface.

If we imposed a generic cylindrical symmetry, which is a reasonable assumption since we're dealing with surfaces, we would notice that many of the 27 $\chi_{ijk}^{(2)}$ components vanish (see. ref. [83] for more details). The non-zero components, and corresponding polarizations, are reported in Tab. 2.1. With dielectric surfaces such as silica, both s and p incident laser polarizations result in substantial surface electric fields and all the shown combinations, therefore, achievable. However, for metallic substrates, the reflectivity in the infrared wavelength region is often particularly high and it may be shown that the incident beam results in a large surface E field in the z direction, but negligible fields in the x and y direction [83]. Thus, for a metallic substrate, where almost all of the incident infrared beam is reflected from the surface, only resonant susceptibilities with a z infrared component generate a substantial SF signal, as listed in the last column of Tab. 2.1.

2.1.2 Time-resolved IR-Vis SFG

Ideally, one should use three different pulses to perform a proper time-resolved IR-Vis SFG experiment: one pump and two probes. Their duration should be short enough to

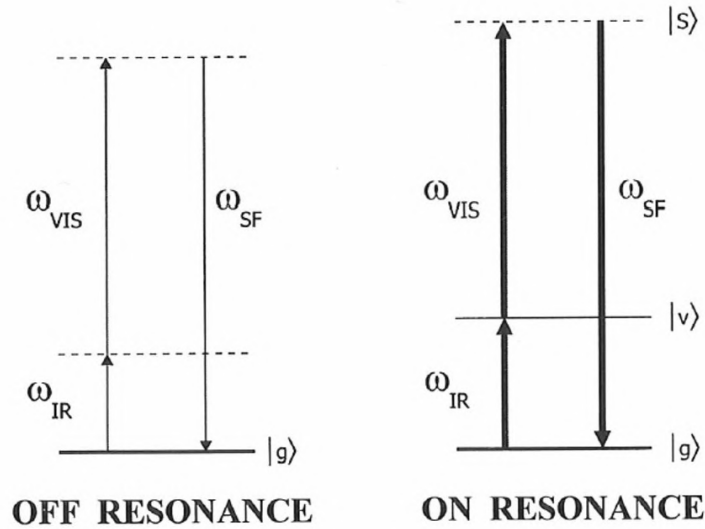


Figure 2.5: Graphic comparison between non-resonant and resonant SFG transitions: when the infrared energy matches the energy difference between the ground and vibrationally excited state the SFG signal is enhanced. Image taken from [83].

Polarization combinations	Non-vanishing $\chi_{ijk}^{(2)}$ components by C_{∞}	Non-vanishing $\chi_{ijk}^{(2)}$ components on metals surfaces
pss	zyy	
sps	zyz	
ssp	yyz	yyz
ppp	zzz, zxx, xzx, xxz	zzz, xxz

Table 2.1: All possible polarisation combinations and the elements of $X_{ijk}^{(2)}$ that contribute to the spectrum [83]

set the limit for the time resolution required for the experiment. The energy of the pump depends on the kind of experiment. In our case, we used an IR pulse of about 1700 cm^{-1} (see section Fig. 4.3). The two probes should be the IR and Vis spatially and temporally overlapped pulses which generate the SF signal. The time delay τ between the pump and the probes should be tunable in order to collect the spectra as a function of τ .

Unfortunately, our setup is equipped with only two delayable pulses (IR and Vis). Given this restriction, we exploited their intrinsic time-width (FWHM $\sim 30 \text{ ps}$) as depicted in Fig. 2.6, which shows the intensities of the IR and Vis pulses, delayed by τ , as a function of time: the time-resolved experiment, discussed in the following chapters, is thus performed with the pumping pulse (IR in this case) initially exciting the system and at a later time, when

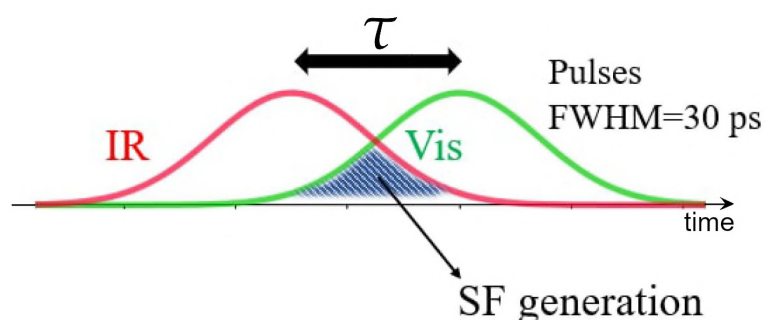


Figure 2.6: Intensity of delayed IR and Vis pulses as a function of time. As shown, the two pulses need to overlap in order to generate a SF signal (colored area). Our setup produces pulses with a FWHM of ~ 30 ps.

both the Vis and the same IR still have a nonnegligible overlap, also the SF signal can be generated from the excited state.

Of course, the SF signal can be also directly generated from the ground state. For this reason, if no physical evolution is occurring, one would notice just a general decrease of the SF signal due to the diminishing of the time overlap of the IR and Vis pulses. On the contrary, if there is an actual time evolution of the system, one would expect an important change in the SFG spectra collected at the different delays. The intensity of the non-resonant background can be readily used to normalize the spectra taking into account the different overlap at the considered delay τ .

In conclusion, the limitations of our time resolved SFG experiment are:

- 1) The range in which τ can be varied is limited by the pulse duration: in order to generate the SFG signal it is necessary to have both spatial and temporal overlap between the IR and visible pulses, and the resulting SFG intensity depends on their overlap area (Fig. 2.6);
- 2) A proper pump-probe experiment is performed by means of a fixed-energy pump beam and a probe beam with variable energy. In our setup the IR pump and probe beams are necessarily the same, thus the pump wavelength also varies as the probe is changed. Nevertheless, we adopted this approach that allowed the investigation of relevant relaxation dynamics of the porphyrin layers.

2.1.3 Lineshape modeling

The description that led us to eq. (2.19) is based on an oversimplification of real systems: a generic system composed of molecules adsorbed on a surface produces an SFG signal that is the combination of both the molecular and substrate contribution. The molecular contribution to the susceptibility tensor $\chi_{RES}^{(2)}$ varies sensibly as the infrared radiation is

tuned through the vibrational resonances. The substrate contribution doesn't change, in a first approximation, with the infrared tuning and, together with the constant part of the molecular susceptibility, it contributes to the non-resonant $\chi_{NR}^{(2)}$ susceptibility, usually approximated with a constant value. The total susceptibility is therefore

$$\chi^{(2)} = \chi_{RES}^{(2)} + \chi_{NR}^{(2)} \quad (2.20)$$

For dielectric materials $\chi_{NR}^{(2)}$ contribution is small compared to the resonant part. When the substrate is metallic $\chi_{NR}^{(2)}$ contribute is significant, due to the presence of surface plasmon resonances [83].

To a practical extent, it is common to replace the susceptibility tensor introducing an effective scalar susceptibility [82] shaped as

$$\begin{aligned} \chi^{(2)}(\omega_{IR}) &= A_{NR} e^{i\phi_{NR}} + \sum_n \frac{A_n e^{i\phi_n}}{\omega_{IR} - \omega_n + i\Gamma_n} \\ &= e^{i\phi_{NR}} \left[A_{NR} + \sum_n \frac{A_n e^{i\Delta\phi_n}}{\omega_{IR} - \omega_n + i\Gamma_n} \right] \end{aligned} \quad (2.21)$$

where the sum runs over the various resonances of the system. The parameters are real-valued amplitudes A_n , phases ϕ_n , resonance frequencies ω_n and resonance broadenings Γ_n related to their lifetimes. In the second line of eq. (2.21) the non-resonant phase has been factorized and the phase differences $\Delta\phi_n$ have been introduced: these represent the relative phase-shift of the n^{th} resonance to the non-resonant background. The amplitudes A_n depend on the density of molecules N and the electronic and vibrational transition moments, respectively M_n and T_n as

$$A_n \propto NM_n T_n \delta\rho_n \quad (2.22)$$

and the population difference between the ground and excited state $\delta\rho_n$ [67]. As said, SFG spectra can be modeled exploiting an effective scalar susceptibility, and combining equation (2.21) with (2.16) we obtain an expression for the SFG signal intensity as a function of the infrared frequency

$$I_{SFG}(\omega_{IR}) \propto \left| A_{NR} + \sum_n \frac{A_n e^{i\Delta\phi_n}}{\omega_{IR} - \omega_n + i\Gamma_n} \right|^2 I_{VIS} I_{IR}(\omega_{IR}) \quad (2.23)$$

Frequency dependence has been explicitated in the infrared intensity to emphasize that, while visible radiation intensity is constant (except for laser instabilities), I_{IR} varies with the IR tuning: it is thus important to normalize the measured SFG intensity taking into account for this effect.

2.1.4 Experimental setup

SFG measurements were performed at the Visible and Infrared Spectroscopy Laboratory (VISpLab, University of Trieste) exploiting a customised setup purchased from the

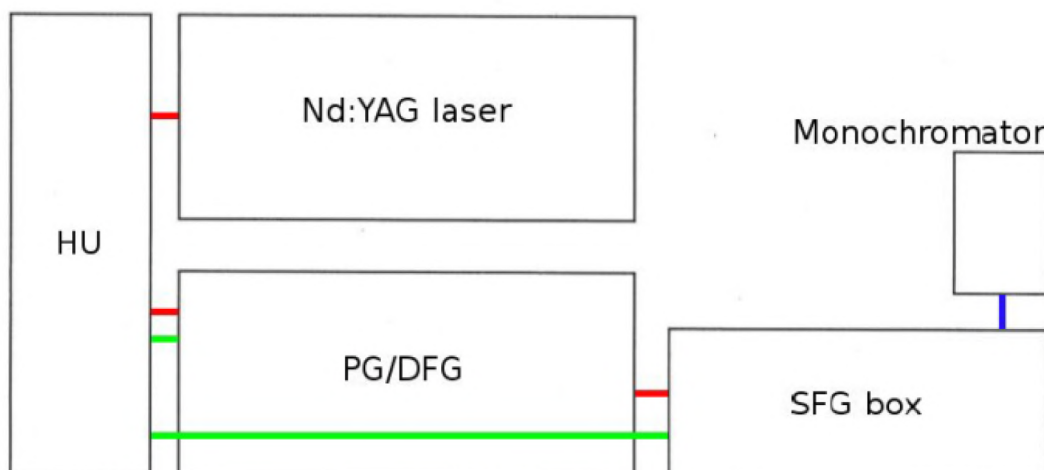


Figure 2.7: Scheme of the experimental setup (top view). The fundamental IR beam is generated in the laser unit, then enters HU to generate the second harmonics, tunable IR radiation is provided by the PG/DFG unit and the final IR and VIS beams are conveyed to the sample in the SFG box. The SFG radiation thus generated reaches the monochromator before being detected.

Lithuanian laser manufacturing company EKSPLA. All the components are controlled via LabVIEW software. Samples are prepared in a UHV chamber and SFG spectra are taken in a high-pressure cell. In this section the setup is described, in order to give a clear picture of how SFG signal is generated and understand some features that will be important to understand the experimental data analysis.

SFG setup

SFG measurements are performed using pulsed laser radiation: green light at 532 nm and infrared radiation in the range 2300 – 10000 nm are generated in the laser setup, overlap at the sample surface and then SFG output signal is measured. The principal components of the setup are:

- a fourth class PL2230 Series Laser, generating the fundamental infrared pulsed radiation at 1064 nm. The pulses are ~ 30 ps long with a repetition rate of 50 Hz and maximum pulse energy of 25 mJ. The peak power of the fundamental radiation, defined as $P = E/\Delta t$ (E being the maximum pulse energy and Δt the pulse duration) is ~ 1 GW; the mean power is therefore ~ 1.25 W. The beam diameter is ~ 6 mm;
- a Harmonic Unit H500 where second harmonics radiation at 532 nm (green) is generated. Three outputs are produced at this stage: a beam at the fundamental wavelength (1064 nm) with maximum pulse energy of 15 mJ and two visible beams. One of the visible beams, with 1 mJ maximum energy per pulse, is directly used to produce SFG radiation; the other, with 10 mJ maximum energy per pulse, is

exploited to generate the tunable infrared radiation. In this unit the temporal overlap of IR and visible pulses can be modified by means of a delay line;

- an Optical Parametric Generator PG501/DFG1P where the 2300 – 10000 nm tunable mid-IR radiation is generated using the fundamental radiation and one of the visible beams. The measured pulse average energy is ~ 200 mJ;
- the SFG box: here the polarizations of the tunable mid-IR and visible beams are selected and the beams are spatially overlapped on the sample, generating a SFG signal in the range 432 – 505 nm.

Fig. 2.7 is a schematic top view of the laser setup and SFG spectrometer where the different sections described above can be identified. Information about the laser setup and SFG spectrometer can be found in [90].

Experimental chamber

We are interested in the investigation of different metal-organic systems, focusing on the surface characterization. In order to obtain a reliable surface characterization, it is important to prepare the samples in a controlled environment to prevent contamination both during the preparation and the measurements. For this reason the SFG setup is coupled to a UHV chamber (the preparation chamber) where samples are loaded and prepared. The presence of a LEED setup is helpful to obtain information about the surface structure and quality of the sample, and Auger electron spectroscopy gives chemical information about the surface composition.

The experimental chamber (see. Fig. 2.8) consists of a cylindrical diamagnetic stainless steel UHV chamber with 30 cm diameter, a pumping section and a high-pressure cell (HP cell) designed for the SFG experiments. The three sections are made independent through gate valves. The pumping section is located below the preparation chamber and hosts a cryogenic pump (10) coupled with a titanium sublimation pump, and an ion pump (12). The preparation chamber is also pumped by a turbo molecular pump (4), prepumped by a diaphragm pump. When the gate valve between the preparation chamber and the pumping section is opened, a background pressure of 5×10^{-11} mbar can be achieved. The presence of a fast entry lock loading system (5) allows the sample loading into the UHV system without breaking the vacuum. It is independently pumped by a turbomolecular pump coupled with a backing pump (11) for the pre-pumping (we will refer to this pumping group as turbo pumping station), that grants a background pressure lower than 10^{-8} mbar.

A magnetic transfer arm (7) is employed to load (or unload) the sample-holder from the fast entry lock and the two manipulators (the preparation chamber's one and the one present in the HP cell). The sample-holder allows to heat the sample up to 1300 K in UHV and 700 K at 1 bar by means of resistive heating. The sample is caged by a tantalum wire (0.2 mm diameter) fitting in a slot on the sample's side. Such configuration minimizes

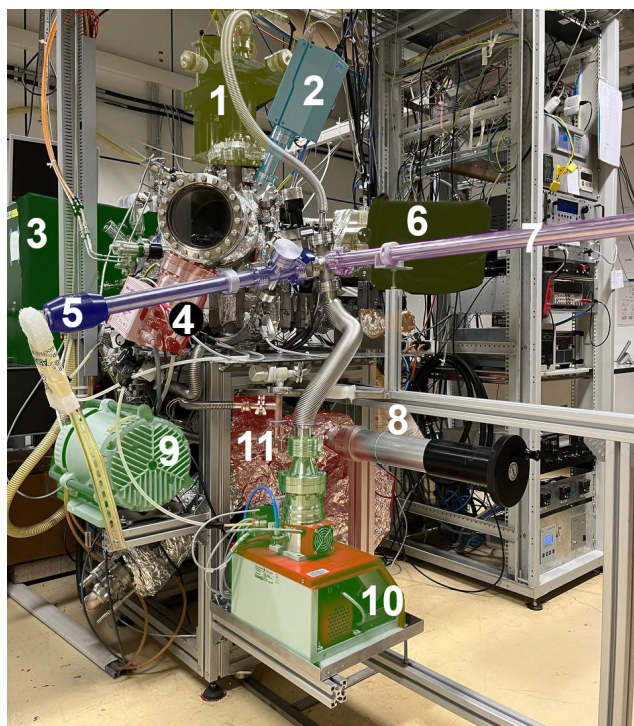


Figure 2.8: Overview of the preparation chamber, equipped with: (1) a manipulator, (2) a mass spectrometer, (4) a turbo molecular pump, (5) a fast entry lock loading system, (6) a LEED setup, (7) a transfer arm, (8) a gas line, (9) a scroll pump, (10) a cryogenic pump, (11) a turbo pumping station and (12) a ionic pump. The SFG box (3) can be seen.

the mechanical stress due to the wire thermal expansion and contraction, thus reducing the probability of sample damage during heating and cooling. The sample's temperature is measured via a K-type chromel-alumel thermocouple spot-welded at the back of the sample.

The HP cell is located behind the preparation chamber and coupled with the SFG box. It consists of a steel cylinder (6 cm diameter) and two barium fluoride (BaF_2) windows that allow the transmission of the visible, IR and SFG radiation with nearly 100% efficiency. They can sustain a pressure difference up to 1 bar. IR and visible beams are not at normal incidence with respect to the window, in order to avoid back reflection into the SFG setup (that may damage the optics). The cell is equipped with its own manipulator that provides (x,y,z) translations, polar rotation and the possibility to tilt the sample. Pressure is measured through a full range gauge (FRG) working in the $5 \times 10^{-9} - 10^3$ mbar range, that is made of a cold cathode gauge and a pirani gauge connected in series. A gas line, which can handle up to three different gases, is present. The SFG cell can be independently pumped by the scroll pump (9) and by the turbo pumping station (11).

As said before, the preparation chamber is dedicated to the preparation and characterization of samples. It is equipped with a LEED (low energy electron diffraction) setup (6)

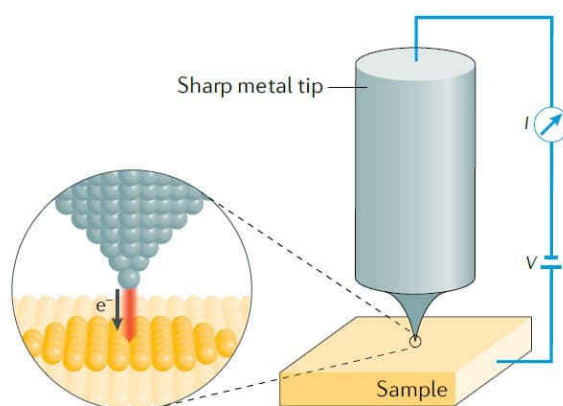


Figure 2.9: Schematic diagram of an STM setup: a bias is applied between the tip and the sample and electrons can tunnel, producing a tunneling current I (adapted from [91]).

and an Auger electron spectroscopy setup. A mass spectrometer (2), an ion gun (used to sputter the sample) and a gas line (8) are also present. The pressure is measured using an ion gauge working in the range $3 \times 10^{-11} - 10^{-3}$ mbar. An evaporator is included in the chamber: the molecules are contained in a quartz crucible and evaporated by resistive heating of the surrounding tungsten filament; a Co (or Fe) filament is also mounted on the evaporator and metal atoms are evaporated by means of Joule effect. The deposition rate can be calibrated using a retractable quartz balance. The top part of the preparation chamber ends with the manipulator (1) that provides four degrees of freedom: the three translations (x,y,z) and the polar rotation.

2.2 STM AND STS

A Scanning Tunneling Microscope has been used for the first time by Binnig and Rohrer in 1982 [92]. This technique consists in scanning a surface while locally probing it with a metal tip in order to investigate the topological and electronic structure of such surface. Using this method, samples are directly explored in real space with atomic resolution, and fundamental information such as the unitary cell shape, distribution and deformation of molecules inside the cell, and long-range structures (for example the moiré pattern in graphene) are observed.

STM measurements consist in applying a voltage between a sharp metallic tip and the sample and scanning the surface along x and y coordinates: there are two possible ways to map the sample, measuring the resulting tunnelling current I or the sample-tip distance d . In the first case, the vertical coordinate z is fixed and the tunneling current (that depends on d) is measured. In the second case I is held at a constant value: z is constantly adjusted by means of a feedback loop circuit in order to keep the current constant. The

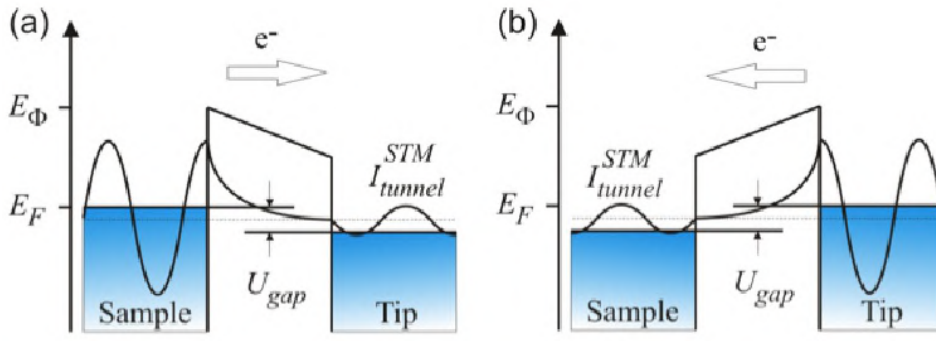


Figure 2.10: Fermi levels of two grounded metals (one represents the sample, the other the tip) when a bias U_{gap} is applied and their Fermi levels are shifted by $+eU_{gap}$ (a) and $-eU_{gap}$ (b). An electron tunneling current can flow from occupied states of the one with higher E_F to unoccupied states of the other. Image taken from [95].

set of measured I or z respectively, is used to create a 2D map that represents the sample's surface structure [93]. The tunnelling current depends not only on the sample-tip distance but also on the chemical species that the tip is probing, through the density of states.

Typical distances are $z \sim 1$ nm, current and bias typical values are of the order of $I \sim 1$ pA – 10 nA and $V \sim 1$ V [93, 94]. In Fig. 2.9 a bias is applied between the metallic tip and the sample, and the tunneling current is measured.

If we consider a metal tip and a metal surface that are placed close to each other, they have different Fermi levels and work functions. Their work function difference gives the Fermi levels offset:

$$\Phi_c = E_F^L - E_F^R \quad (2.24)$$

where $E_F^{L,R}$ refer to the Fermi levels and Φ_c is the work function difference. When the metals are grounded together their Fermi levels coincide and no electrons can flow from one side of the potential barrier to the other. When a potential U is applied, as in Fig. 2.10a,b, their Fermi levels shift up or down of $\pm eU$, depending on the direction of the applied potential difference: if the potential is inverted the current flows in the opposite direction.

If the two metals are brought sufficiently close together, their wavefunctions overlap and there is a non zero probability of tunneling: the tunneling current I depends on the distance as

$$I \propto e^{-2\alpha z} \quad (2.25)$$

where $\alpha^2 = \frac{2m}{\hbar^2} (eU_B - E)$ with U_B the potential barrier and E the energy of the state from which the tunnelling occurs. Typical values of α are $\sim 1 \text{ \AA}^{-1}$, thus the current intensity is extremely sensitive to distance changes of the order of the \AA or less [96].

Electrons flow from occupied states of the component at higher Fermi energy to the unoccupied states of the other and the probability of transition depends on the density

of states of both the tip and the sample: STM images represent the convolution of their density of states.

Often, adsorbates (such as porphyrins in our case) are highly mobile at room temperature, due to the weak coupling with the substrate (i.e. graphene); in these cases, low temperature is used to freeze the kinetics, yielding more stable measuring conditions. For the very same reason, also the tip is more stable at low temperature, and its atomic configuration changes less frequently: in this way, all the differences measured in an STM image are physical and can be attributed to the sample-tip system [97].

Information about the electronic Density of States (DOS) can also be obtained from a scanning tunneling setup (Scanning Tunneling Spectroscopy or STS). As tunneling current I is proportional to the integral of the density of states from Fermi level to eV , taking a numerical derivative yields DOS of the sample at a given energy eV :

$$\frac{dI}{dV} \propto \rho_s(eV)$$

Depending on the sign of the voltage bias, occupied and unoccupied states can be revealed: by convention, negative bias corresponds to electrons going from the sample to the tip (occupied states), and vice versa. From a practical standpoint, taking directly the numerical derivative of the I/V profile yields extremely noisy data. For this reason, a lock-in amplifier is commonly used. During the acquisition of a dI/dV spectrum, the feedback loop (which determines the tip-sample distance) is turned off, and the voltage is swept while the lock-in signal is recorded. Afterward, one can calibrate the conductance scale ($[dI/dV]=\text{siemens}$) by matching with the numerical derivative of the I/V profile, which is also recorded during the measurement.

If the dI/dV signal is collected, at a certain voltage bias, while scanning the surface at a constant height, the spatial distribution of the density of states is revealed (dI/dV maps). As shown in Fig. 2.11, one can collect dI/dV maps at different biases, thus obtaining the 3D DOS map of the system.

Our STM measurements have been performed in the laboratories of the University of Trieste at the CNR-IOM (TASC laboratory, Trieste), in the groups of prof. S. Modesti and prof. G. Comelli. All the STM images have been acquired in UHV. The experimental setup consist of a vacuum chamber in which samples are prepared, and and the presence of a cryostat allows to measure at low temperature (typically with liquid nitrogen or helium).

2.3 SINGLE-PHOTON PHOTOEMISSION SPECTROSCOPIES

A one-photon photoemission experiment consists in exposing the sample to monochromatic radiation, of energy $h\nu$, and measuring the kinetic energy distribution of the pho-

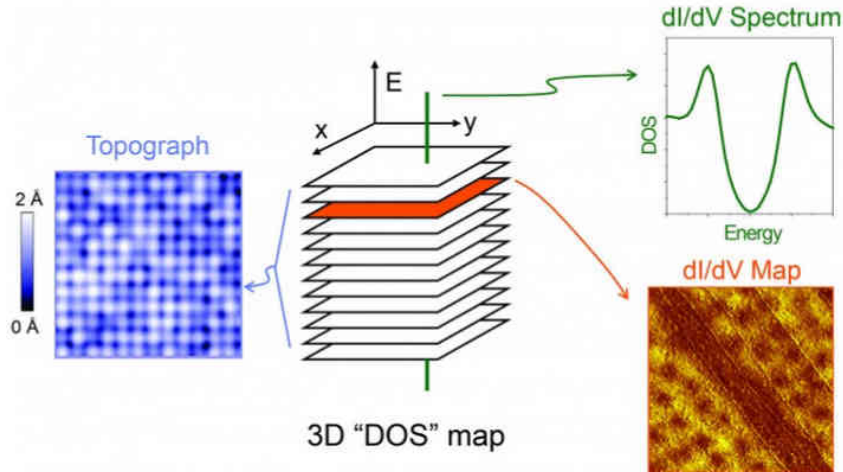


Figure 2.11: Schematic of 3-dimensional data sets obtained on a pixel grid (3D “DOS” maps) and main types of STM measurements. Image taken from [98]

toemitted electrons. Using laser sources or tunable synchrotron radiation, electrons are emitted and detected through an electron analyser. Their kinetic energy E_k is given by

$$E_k = h\nu - E_B - \Phi_S \quad (2.26)$$

where E_B is the binding energy and Φ_S the work function of the sample, with E_F the Fermi level and E_{VAC} the vacuum level (Fig. 2.13). Electrons have a short mean free path in gas phase: photoelectrons should travel from the sample surface to the analyser and through the analyser to the detector. For this reason, standard photoemission experiments are carried out in UHV.

Typical photon energies for X-ray photoemission spectroscopy (XPS) are in the range $10^2 - 10^3$ eV. Quantitative information about the chemical identity of the surface species can be inferred by the energy of the atomic core level. Binding energies are affected by the surrounding environment and it is possible to distinguish bulk from surface atoms, gas phase from adsorbed species or identical elements involved in different chemical bonding.

Photon energies in the UV range 10 – 100 eV (UPS) are employed to map the valence band. A schematic representation of the photoemission process is reported in Fig. 2.12 where UPS and XPS features are distinguished: the first explores the valence band and the second refers to core levels.

2.3.1 XPS

X-ray Photoelectron Spectroscopy (XPS) is a photon-in-electron-out surface science technique. Besides having element sensitivity, XPS allows gaining information about the chemical environment of an atom, structural dishomogeneities, lifetime of the excited state induced by photoemission process and metallicity. It is based upon the study of the

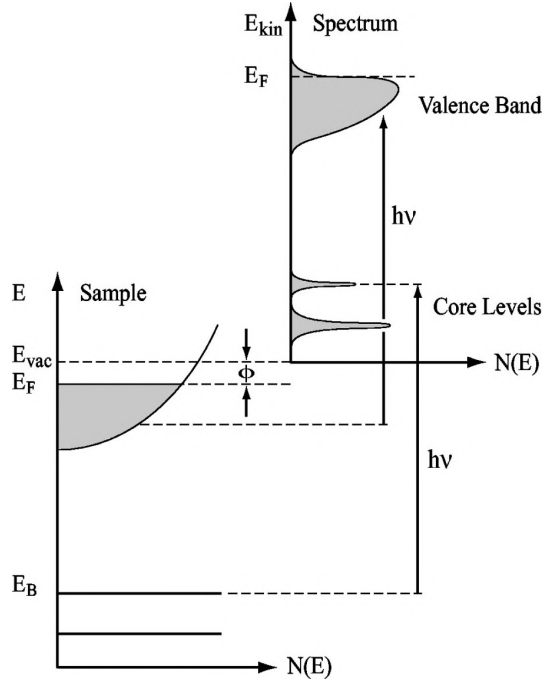


Figure 2.12: Schematic representation of the photoemission process. On the left the density of states of the sample; on the right the corresponding spectrum with both core levels and valence band features (from [99]).

core-level photoelectrons, extracted by X-rays via photoelectric effect from the sample and retrieves information through analysis of their core-level's spectrum lineshape, binding energy and intensity. Due to the short mean free path of electrons through a gas phase, XPS is commonly employed in vacuum up to $\sim 10^{-6}$ mbar. In order to work with near ambient pressure (NAP) (\sim mbar) systems, it is necessary to modify the electron energy analyser as described in the following paragraphs.

From a theoretical point of view, the photoemission process can be treated with time-dependent perturbation theory. A semiclassical approach is conventionally adopted, meaning that apart from the electromagnetic field, which is treated classically, the theory is developed in the quantum mechanical framework [101]. The unperturbed system (electrons in a time-independent potential) is subject to the time-independent Hamiltonian H_0 and, at the instant $t_0 = 0$, it is perturbed by a monochromatic electromagnetic field (with oscillation frequency ω , with $\omega = 2\pi\nu$). As a consequence, the Hamiltonian is given by the sum of H_0 with a time-dependent term $H_I(t)$ that describes the perturbation (\mathbf{r} indicates the position of the electron):

$$H(\mathbf{r}, t) = H_0(\mathbf{r}) + H_I(\mathbf{r}, t) \quad (2.27)$$

Using minimal coupling $\mathbf{p} \rightarrow \mathbf{p} - \frac{e}{c} \mathbf{A}$, the interaction Hamiltonian can be written as follows:

$$H_I(\mathbf{r}, t) = \frac{e}{2mc} (\mathbf{A} \cdot \mathbf{p} + \mathbf{p} \cdot \mathbf{A}) - e\phi + \frac{e^2}{2mc^2} (\mathbf{A} \cdot \mathbf{A}) \quad (2.28)$$

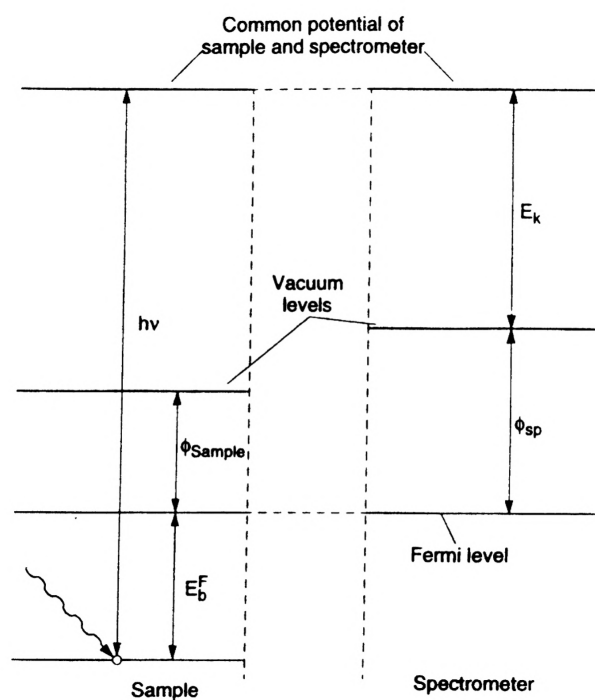


Figure 2.13: Connected sample and analyzer have the same Fermi level but different work functions. The photoemitted electrons have kinetic energy ranging from 0 to $h\nu - \Phi$: when a negative bias is applied to the sample all the photoelectrons can be detected. Adapted from [100]

where $\mathbf{A} = \mathbf{A}(\mathbf{r}, t)$ and $\phi = \phi(\mathbf{r}, t)$ are the vector and scalar potential. \mathbf{p} is the momentum operator [102]. The perturbation depends explicitly on time through \mathbf{A} . If the Coulomb gauge is chosen, then $\nabla \cdot \mathbf{A} = 0$. Maxwell equation for the potentials can be solved by choosing $\phi = 0$. \mathbf{A}^2 , which represents the two photon scattering, can be neglected, being a second-order term in \mathbf{A} . Eventually, considering that $\{A, p\} = 2\mathbf{A} \cdot \mathbf{p} + i\hbar \nabla \cdot \mathbf{A}$, $H_I(\mathbf{r})$ can be simplified as follows:

$$H_I(\mathbf{r}, t) = \frac{e}{mc} \mathbf{A}(\mathbf{r}, t) \cdot \mathbf{p}. \quad (2.29)$$

Starting from here, it is possible to calculate, using Fermi's golden rule, the photoionization probability per unit time w for a transition. In the case of XPS, this transition starts from a N-electron initial state ψ_i , to a final state ψ_f in which a core electron has been ejected. The resulting expression for w is

$$w \propto \frac{2\pi}{\hbar} |\langle \psi_i | H_I(\mathbf{r}) | \psi_f \rangle|^2 \delta(E_f - E_i - \hbar\omega), \quad (2.30)$$

where $H_I(\mathbf{r})$ is only the space-dependent part of equation 2.29. Because of the delta function in equation (2.30), the transition may occur only when the photon energy matches the energy difference between the final and the initial state of the system. Supposing that $\mathbf{A}(\mathbf{r}, t)$ generates a monochromatic radiation, $H_I(\mathbf{r})$ in equation (2.30) is equal to (q_e =electron charge):

$$H_I(\mathbf{r}) = \cos t \cdot q_e A_0 \cdot \mathbf{p} e^{ik \cdot \mathbf{r}} : \quad (2.31)$$

since the relevant integration domain in equation (2.30) is given by the minimum extension between the two wavefunction ψ_i and ψ_f , in this region of space the term $e^{ik \cdot \mathbf{r}}$ can be considered constant if the radiation's wavelength is sufficiently large. In our case, ψ_i represents the core levels with extension of few angstroms; so, it is sufficient to use radiation with energy $h\nu \leq 800$ eV, with a corresponding wavelength of ~ 1.5 nm. This assumption allows to take just the first term of the expansion of the exponential, namely 1. Using the commutation relation

$$[\mathbf{r}, H_0] = \frac{i\hbar}{m_e} \mathbf{p} \quad (2.32)$$

the matrix element in (2.30) can be written as (neglecting constants):

$$\langle \psi_i | H_I(\mathbf{r}) | \psi_f \rangle \sim \langle \psi_i | q_e \mathbf{p} | \psi_f \rangle \sim \langle \psi_i | q_e [\mathbf{r}, H_0] | \psi_f \rangle \sim (E_f - E_i) \langle \psi_i | q_e \mathbf{r} | \psi_f \rangle. \quad (2.33)$$

This is the so called *Dipole Approximation*. It is important to point out that the cross sections (which are proportional to the probability of photoionization w) depend on the integral of the radial part of the wave function, which is directly defined by the value assumed by the quantum numbers n and l , since the wavefunction can be written as follows (in spherical coordinates):

$$\psi_{n,l,m}(r, \theta, \phi) = R_{n,l}(r) Y_{l,m}(\theta, \phi). \quad (2.34)$$

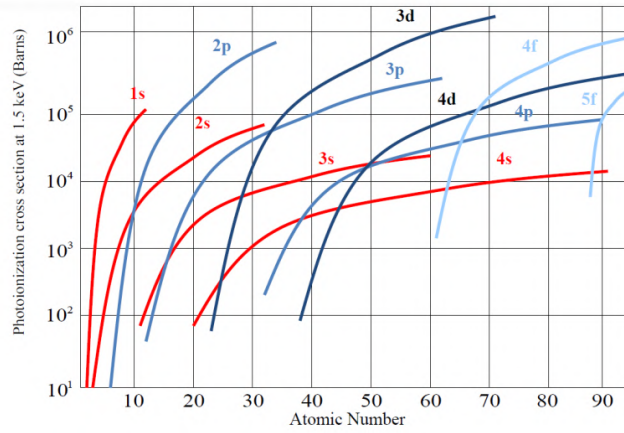


Figure 2.14: Photoionization cross-section at 1.5 keV as a function of the atomic number. Image from [102]

In Fig. 2.14 it is clearly demonstrated that, given a photon energy, the cross section is different for each shell within the same atom. Of course the cross section is also dependent on the atomic number of the element considered. Working with synchrotron radiation, which has the advantage of having a tunable energy, this fact can be exploited choosing the right photon energy in order to maximise the photoelectron signal.

INTERATOMIC RELAXATION SHIFT When the energies of core levels are investigated with high energy resolution, it is found that differences in binding energy between two non-equivalent atoms of the same species can be detected. These energy differences are called chemical shifts and depend on the bonding environment around the atom and, in particular, on its oxidation state. To explain chemical shifts, further understanding of the relation between the binding energy and the electronic configuration of a photoionized atom is necessary.

The binding energy E_b of an electron k undergoing photoemission from a n -electron atom within a solid is given by the difference in energy between the final and initial states of the atom, that is

$$E_b(k) = E_f(n-1) - E_i(n) \quad (2.35)$$

If there were no rearrangement of all of the spectator electrons, Koopmans' approximation would hold. In this case, the initial state atomic wavefunction ψ_i could be written as

$$\psi_i(n) = \varphi_j \Psi_j(n-1) \quad (2.36)$$

where φ_j is the wavefunction of the electron that will be removed and Ψ_j is the wavefunction on the $(n-1)$ -electron ion. Instead, the final state wavefunction ψ_f of the ion would be

$$\psi_f(n-1) = \Psi_j(n-1). \quad (2.37)$$

Consequently, the binding energy of the electron that gets photoemitted would be given by the unique value $E_b = -\epsilon_j$, where ϵ_j is the energy of the j -th energy level of the initial state, and only one peak would be expected in the photoelectron spectrum.

Yet, this approximation is too rough, since electrons cannot be treated as frozen in their configuration; a more sophisticated picture is required. The final state, achieved by removing one electron, corresponds to an ionic state in which a hole exists in place of the ejected photoelectron. This does not correspond to the ground state of the final ionic state. The electrons in the ionized atom, but also those on neighbouring atoms, can relax in response to the ionization event and, thereby, lower the energy of the final state wavefunction. In fact, it should be written in terms of the s eigenstates of the ion with a core hole in the j -th orbital

$$\psi_f(n-1) = \Phi_{js}(n-1) \quad (2.38)$$

The fact that a relaxation of the ion core occurs in the final state, means that the wavefunction $\Psi_j(n-1)$ is not an eigenstate of the ion. Therefore, it must be projected onto the actual eigenstate of the ion $\Phi_{js}(n-1)$. This results in the formation of one or more possible final state wavefunctions, yielding therefore to multiple eigenvalues and final state energy values. In terms of photoelectron spectrum this means that there will be a main peak, but also additional ones, called *satellite lines*.

From the above discussion, it is clear that both the initial state and final state effects influence the binding energy. Initial state effects are caused by chemical bonding, which influences the electronic configuration in and around the atom. For this reason, the energetic shift caused by initial state effects is known, as mentioned before, as chemical shift. This energy shift strongly depends on the oxidation state of the atom, and, usually, the binding energy increases with the oxidation state; in fact the greater the electronegativity of an atom, the higher the binding energy. This can be understood on the basis of simple electrostatics. The first ionization energy of an atom is always lower than the second, as the higher the effective positive charge on the atom, the higher the binding energy of the photoelectron. Most of the atomic relaxation results from the rearrangement of outer shell electrons, while the inner ones, possessing higher binding energy, scarcely contribute. The material's conductivity determines the extra-atomic relaxation. In a conducting material such as a metal, valence electrons are free to move from one atom to a neighboring one and screen the hole created by photoionization. In an insulator, the electrons do not possess such mobility, so they react by being polarized by the core hole. Hence, the magnitude of the extra-atomic relaxation in metals is greater than that of insulators.

SURFACE SENSITIVITY Photoemission-spectroscopy gains its surface sensitivity from the fact that electrons have a high cross section for inelastic scattering with matter. This is shown in the graph in Fig. 2.15, which reports the inelastic mean free path of electrons in a solid as a function of the electrons energy. This curve is known as the universal curve because its shape does not depend strongly on the chemical composition of the solid.

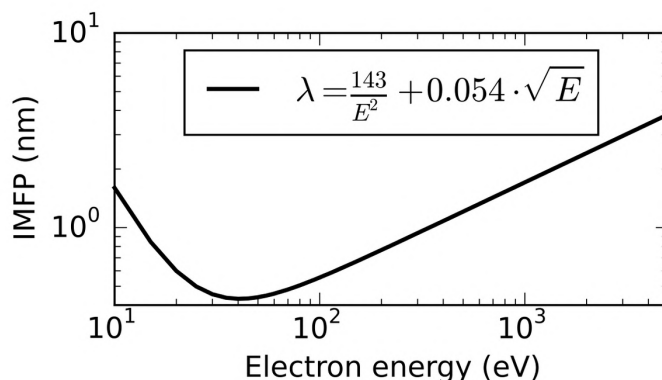


Figure 2.15: The universal curve of electron mean free path in solid matter based on the equation in [103].

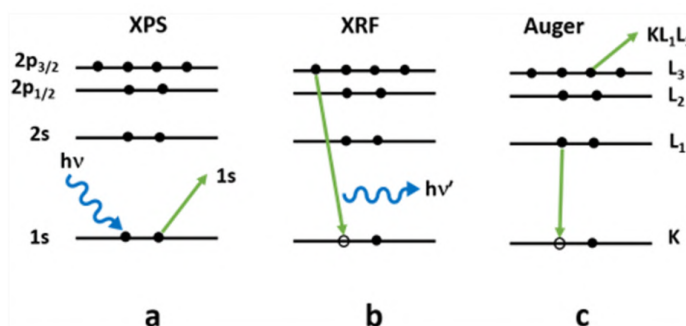


Figure 2.16: Energy level diagram showing the filling of a core hole, giving rise to (a) direct photoemission, (b) X-Ray Fluorescence, and (c) non-radiative Auger electron emission. Image taken from [105]

Photoelectrons emitted with a kinetic energy between 10 and 1000 eV are particularly suitable for surface elemental analysis, as their mean free path is below $\sim 10 \text{ \AA}$.

XPS Lineshape and data analysis

LINESHAPE The basic lineshape of a photoemission process is given by a Lorentzian function [104]. The natural line width is determined by the lifetime of the core hole generated by the photoelectron in the ionized atom, which is related, via the Heisenberg principle, to the probability of the core hole to be filled by an electron in a lower binding energy level. The more decay channels through which electrons can fill the core hole, the shorter is the life time. As schematically pictured in Fig. 2.16, decay channels can be, for instance, Auger or radiative processes.

Given Γ the intrinsic peak width, and τ the core hole lifetime, the uncertainty relation states that

$$\Gamma = \frac{h}{\tau} \quad (2.39)$$

where h is the Planck constant. By means of Fermi's golden rule for matter-radiation interaction, the X-ray photoemission cross section can be evaluated, considering the metal ground state and the Fermi sea + a hole + the photoelectron in the initial and final states, respectively [106]. The photoemission peak lineshape is therefore generally expressed as

$$I_{Lor}(E_{kin}) = I_0 \frac{\Gamma/2\pi}{(E_{kin} - E_0)^2 + \Gamma^2/4} \quad (2.40)$$

where the Full Width at Half Maximum (FWHM) is denoted by Γ and E_0 is the position for the maximum intensity I_0 . The experimental energy resolution (related to both the photon source and the energy analyser), the excitation of phonons in the solid, and the intrinsic sample inhomogeneity contribute to a Gaussian broadening of the photoemission peak. Moreover shake-up and shake-off events may impact on the lineshape with an asymmetry contribution: when ejected, a photoelectron may cease part of its energy to other electrons. In metals, for example, photoelectrons may create electron-hole pairs at the Fermi level or may excite plasmons (shake-up event). In a generic system, other electrons can be emitted as a consequence of core ionization (shake-off event). In both cases the actual photoelectron kinetic energy is lowered, thus the XPS peak has an asymmetric tail at higher binding energy. The most common parametrization for the core-level lineshape in photoemission spectra, including all the previously mentioned physical effects, is a Doniach-Šunjić function convoluted with a gaussian function [106]. The mathematical expression for a Doniach-Šunjić is basically a Lorentzian function with an asymmetry parameter α :

$$I_{DS}(E_{kin}) = I_0 \frac{\Gamma_E(1-\alpha)}{((E_{kin} - E_0)^2 + \Gamma^2/4)^{(1-\alpha)/2}} \xi(E_{kin}) \quad (2.41)$$

where α is the asymmetry parameter, Γ_E is the Euler Gamma function, and

$$\xi(E) = \cos \left[\frac{\pi\alpha}{2} + (1-\alpha) \tan^{-1} \left(\frac{E_0 - E}{\Gamma/2} \right) \right] \quad (2.42)$$

In our experiments, the energy scale of the XPS spectra has been calibrated by taking the bulk component of Ir $4f_{7/2}$ core level as reference (@60.87 eV). The absolute error associated with the binding energy calibration is about 50 meV.

DATA FITTING The spectra were analysed with a fitting procedure based on χ^2 minimisation. As explained earlier, the fitting function is a Doniach-Šunjić profile convoluted with a Gaussian. Each peak is described by five parameters: the Lorentzian linewidth (Γ), the asymmetry parameter (α), the Gaussian linewidth (G), the intensity (I_0), and the binding energy position (E_0).

2.3.2 NAP-XPS

As it was reported above, X-ray photoelectron spectroscopy is a surface-sensitive technique. XPS spectra are obtained by irradiating a material with a beam of X-rays, while

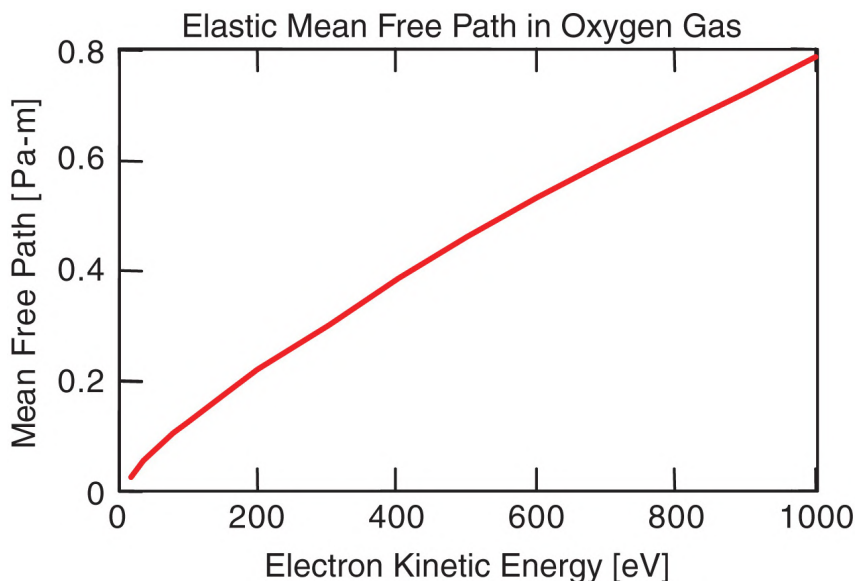


Figure 2.17: Electron elastic mean free path through an oxygen gas environment as a function of kinetic energy. At 100 Pa (1 mbar) a 400 eV electron travels approximately 4 mm before suffering an inelastic collision. Ten Pa-meter represents the same number of molecules as approximately 1 monolayer, if projected on a surface. Image from [107].

simultaneously measuring the flux and the kinetic energy of electrons that escape from the surface of such material. The electron energy analyser requires ultra high vacuum conditions in the analysis chamber ($P \leq 10^{-8}$ mbar). In fact, once photoelectrons are emitted from the sample surface, they undergo elastic and inelastic collisions from atoms or molecules in the gas-phase [107]. The electron mean free path λ_e , or the average distance between collisions, depend on its energy and on the gas pressure P in the chamber. There are very scarce available experimental data about the relation between pressure and λ_e , and from a theoretical point of view there are some difficulties in the modeling, nevertheless they present a linear relationship on a log-log scale, of the order of 100 μm at 1 mbar and 10 m at 10^{-5} mbar [108, 109]. Fig. 2.17 reports the variation of λ_e as a function of the electron energy in an oxygen gas environment. For electrons of 400 eV kinetic energy, λ_e is about 4 mm when the oxygen pressure is ~ 1 mbar (similar values are found for other gases).

Since λ_e is inversely proportional to P , its value decreases to about 30 μm at 100 mbar, which makes the collection of unscattered electrons very challenging. The count rate of detected photoelectrons decreases exponentially with sample-analyser distance. Therefore, λ_e at high pressure needs to be maximised in order to limit XPS signal loss. For these reasons, it is difficult to conduct investigations of surfaces under applicative conditions, namely in the presence of gases, such as in the case of interfacial chemical reactions in electrochemistry or catalysis. With Near Ambient Pressure XPS (NAP-XPS), some issues in the experimental set-up are addressed, allowing to operate even in near ambient pressure

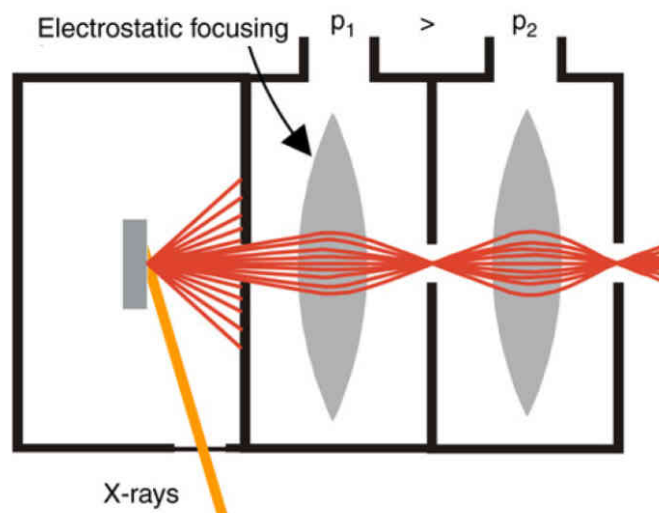


Figure 2.18: Schematic representation of the differential pumping system used for photoelectron spectroscopy in ambient gas pressures. Electrostatic lenses refocus the electron trajectories into the apertures connecting the differential pumping stages. Image from [107].

(up to a few tens of mbar). Inside the NAP cell, an analyser is equipped with a skimmer which acts as passage channel for the generated photoelectrons. Then, these electrons pass through differential pumping stages (see Fig. 2.18) which reduce the pressure by several orders of magnitude, so to diminish electron scattering. The skimmer opening diameter must meet both the necessity of high photoelectron flux and low pressure in the energy analyser chamber while maintaining the desired pressure on the sample. Accounting for gas flow and pressure distribution conditions in the geometry of a commercial setup, the aforementioned constraints are satisfied with a skimmer opening of about ~ 0.3 mm, and a skimmer-sample distance of ~ 0.3 mm.

THE HIPPIE BEAMLINE @MAX IV The NAP-XPS data presented in this manuscript were collected at the HIPPIE beamline of Lund 3 GeV Synchrotron. HIPPIE is a soft X-ray beamline equipped with a novel ambient pressure X-Ray photoelectron spectroscopy instrument. Here follows a brief description of the endstation characteristics [66].

The source of the beamline is an APPLE-II-type elliptically polarizing undulator, with a period of 53 mm for a total length of 3.9398 m. It was chosen to satisfy the requirement of full polarization control at a minimum energy of 250 eV, which corresponds to a minimum undulator gap of 11 mm. The optical apparatus is constituted by (going downstream): a toroidal mirror, a plane mirror, a monochromator (blazed profile, 1200 lines/mm), a cylindrical mirror to focus vertically the photons dispersed by the monochromator, and finally the beam is refocused by a single toroidal mirror. The described configuration allows a beam size of about $100 \times 25 \mu\text{m}$ on the sample. The endstation (Fig. 2.19) is

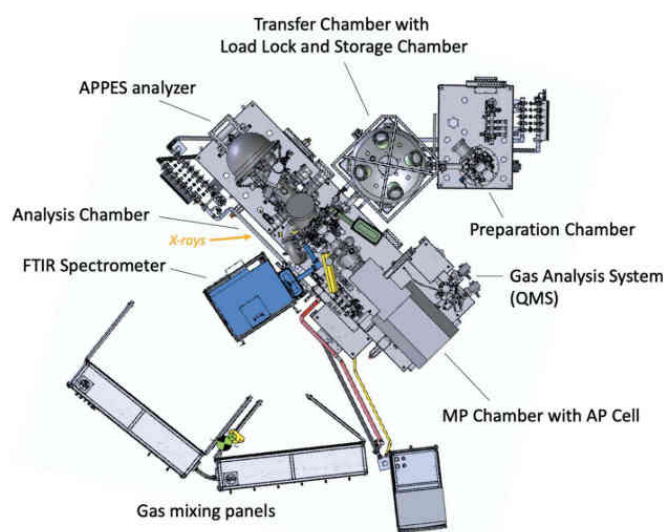


Figure 2.19: Top view of the Ambient Pressure XPS setup at the HIPPIE endstation. Image from [66].

provided with a preparation chamber, an analysis chamber, a radial distribution chamber (UFO), and a load lock. The preparation chamber has a base pressure of 1×10^{-10} mbar and is pumped by a turbomolecular and an ion getter pump. Common surface science instruments are available, such as a LEED, a quadrupole mass spectrometer, a quartz crystal microbalance, an ion source, and spare ports for the user equipment. The sample can be heated with an e-beam up to 1200 °C. The analysis vacuum vessel is similar to the preparation chamber, with a similar pumping system and base pressure. It is equipped with a ScientaOmicron HiPP-3 analyzer which can work up to 30 mbar. The nozzle diameter is about 0.3 mm. Inside the chamber, the ambient pressure regime is achieved through a cell-in-cell configuration. The gas inlet contains eight gas lines equipped with individual mass flow controllers. The pre-defined gas mixture is dosed into the ambient pressure cell, either directly or via an adjustable leak valve (as was done with water, in our experiment). In this way, it is possible to reach any total pressure between 1×10^{-8} and 30 mbar. The pressure is read directly into the ambient cell either with a Pirani (1×10^{-4} -30 mbar) or a capacitance manometer (1.3×10^{-2} -133 mbar). In our experiment, the additional full-range gauge was kept off, to avoid chemical contamination from the cold cathode gauge. The composition of the gas mixture is monitored with a quadrupole mass spectrometer located in the first pumping stage of the analyzer. Finally, the experiment is performed in a dynamic flow of gas, with a continuous pumping via a 4 mm tube partly open.

2.3.3 UPS

Photon energies in the range 10 – 100 eV are appropriate to study the valence band of solids by photoemission spectroscopy. UPS measurements have been performed at the ANCHOR endstation at the Elettra synchrotron in Trieste, exploiting an helium lamp as UV radiation source: the used energies are He I (21.2 eV) and He II (40.8 eV) emission lines.

Complementary information obtained by UPS in our case are the valence band spectroscopy and the sample's work function. A negative bias has been applied to the sample in order to measure the value of Φ . Work function values are extracted from UPS spectra considering that in Fig. 2.13 extracted electrons have binding energies ranging from 0 to $h\nu - \Phi$: the applied bias ensures that all extracted electrons reach the analyzer, and are not partially blocked by the detector's work function. Thus, the energy difference between the electrons with maximum and minimum kinetic energy corresponds to

$$\Delta E = h\nu - \Phi \quad (2.43)$$

from which the value of Φ is easily obtained.

2.3.4 NEXAFS

Near-edge X-ray absorption fine structure spectroscopy (NEXAFS) is a spectroscopic technique, initially devised in the 1980s with the goal of investigating the structure of molecules bonded to surfaces. The technique constantly developed during the following decades [110] and now is routinely exploited in surface science. Despite the technical requirements, first of all the need for a high performance synchrotron source, NEXAFS spectroscopy is a major method in order to achieve reliable information about the geometric and electronic structure at surfaces. This section contains a concise but as far as possible complete description of NEXAFS principles and methods, without any claim to be exhaustive, referring eventually to Stöhr's book [110] for a more detailed discussion. The NEXAFS data discussed in this thesis have been acquired at the CNR-IOM ALOISA beamline at the Elettra synchrotron facility in Trieste.

Principles and Physics

As already seen in section 2.3.1, the transition probability w describing the absorption of a photon by an electron excited from an initial state $|\psi_i\rangle$ to a final state $|\psi_f\rangle$ is proportional to:

$$w \propto |\langle \psi_f | \mathbf{e} \cdot \mathbf{p} | \psi_i \rangle|^2. \quad (2.44)$$

The cross section expressed in this way is relative to a single transition: in order to obtain the total one, all possible initial and final states must be summed. In general all shells must

be considered, but working at photon energies close to a specific core level edge allows to neglect contributions from other shells, because the energy-dependent contribution of their absorption is smooth in this range and orders of magnitude smaller. Final states can be bound, like molecular orbitals (MO) or Rydberg states, or in the continuum, like when the electron is photoemitted above the vacuum level (VL) or excited in a continuous level close to Fermi (FL), as it takes place in metals.

Whether the electron is excited in a vacuum state or not, a hole is created in the inner shell, with a finite lifetime. There are two major ways for the hole to be filled: X-ray fluorescence and Auger electron emission (See Fig. 2.16). In the first one, the recombination creates a photon with energy correspondent to the electron transition, while in the second one the exceeding energy is transferred to another electron that is emitted from the atom. The latter is called an Auger electron. These two different possibilities of recombination allow to investigate x-ray absorption by detecting either photons or electrons. Auger electrons detection is usually preferred because Auger emission has larger probability with respect to fluorescence in low Z atoms, mainly present in biological molecules. In addition, Auger signal detection offers a better surface sensitivity because electrons have a way smaller inelastic mean free path in solids with respect to fluorescence photons.

The NEXAFS experiments discussed in this work were performed in the so-called Partial Electron Yield (PEY) mode, consisting in suppressing lower kinetic energy electrons, emerging from the sample, by applying a retarding voltage. In fact, this mode is frequently exploited for the investigation of adsorbates at surfaces because the surface sensitivity is considerably enhanced, allowing only those electrons that emerge from the outermost surface region to be detected. Further available options are the total electron yield (TEY) mode, where all electrons that emerge from the surface are detected and the Auger Electron Yield (AEY) mode, where electrons are selected in energy in order to collect only Auger electrons.

Dichroism

Through NEXAFS it is possible to obtain important information on the geometric structure of the molecules absorbed on a surface. In particular, investigation of transitions to MO is usually revealing. In fact, one important feature of molecular orbitals is that they have strong directional character and there is a one-to-one correlation between the spatial orientation of the orbitals and the molecular geometry. Thus, for oriented molecules and linearly polarized X-rays the intensities of resonances associated with, for example, σ^* and π^* final states should exhibit a dramatic and different angular dependence.

The angular dependence of the cross section is contained in the dipole matrix element, that for linearly polarized X-rays in the direction of unit vector \mathbf{e} assumes a simpler form

$$\langle \psi_f | \mathbf{e} \cdot \mathbf{p} | \psi_i \rangle = \mathbf{e} \cdot \langle \psi_f | \mathbf{p} | \psi_i \rangle \equiv \mathbf{e} \cdot \mathbf{O}, \quad (2.45)$$

where O is the Transition Dipole Moment (TDM) and, if the initial state is the total-symmetric $1s$ orbital, it points in the direction of the final state orbital. The cross section (and therefore also the transition intensity) becomes:

$$I_{if} \propto |\langle \psi_f | \mathbf{e} \cdot \mathbf{p} | \psi_i \rangle|^2 = |\mathbf{e} \cdot \mathbf{O}|^2 = \cos^2 \delta \quad (2.46)$$

where δ is the angle between the vector field and the TDM.

During the experiments discussed in this work, X-ray absorption has been investigated with linearly polarized photons in perpendicular or parallel direction with respect to the plane of incidence (polarization s and p, respectively). Thus, in s polarization the electric field oscillates parallel to the Ir surface while in p polarization and for small incidence angles the predominant component of the electric field is perpendicular to the surface. Differences in the integral area of a resonance between p- and s-polarization is called dichroism. By analyzing dichroism of some MO resonances it is possible to deduce the orientation in space of the whole molecule with respect to the surface. The specific formula to be used in order to obtain angles from dichroism depends on the experimental apparatus and on the investigated system. In the present case, the substrate three fold symmetry cancels the azimuthal angle dependence in intensity [111]. The formula to find tilt angle Φ , with respect to the surface, from the dichroism of a π^* resonance, specifically for our experimental setup is

$$\Phi(A_p/A_s) = \arcsin\left(\sqrt{\frac{2\cos^2\theta}{A_p/A_s + 3\cos^2\theta - 1}}\right) \quad (2.47)$$

where A_p and A_s are respectively the p- and s-polarization NEXAFS intensities given by the integral area of the π^* resonance and $\theta = 6^\circ$ is photon incidence grazing angle with respect to the surface.

NEXAFS data analysis and fitting procedure

ENERGY CALIBRATION Photon energies are affected by a systematic error caused by the mechanical backlashes of the monochromator and by changes in the electron beam position in the ring. This yields rigid energy shifts of the obtained spectra, thus a preparatory energy calibration is necessary to correct it. Calibration is carried out by exploiting the drain current (I_0) of the last mirror which focuses the X-ray beam on the sample, measured simultaneously with the course of the experiment. Calibration is carried out by comparing the absorption current I_0 , collected during the experiment, with reference absorption current (I_0^R): the reference spectrum was previously collected while measuring the NEXAFS spectrum of molecules in the gas-phase (N_2 , CO), with transitions whose energy is well-known. Thus, by computing the energy difference between these resonances and the toroidal mirror absorption features, it is possible to derive the correct absolute energy positions of the latter within a 0.02 eV uncertainty. In conclusion, the effective calibration procedure consists in shifting the NEXAFS spectrum in order to match the corresponding I_0 to the I_0^R reference current.

NORMALIZATION The normalization of the N 1s and Fe 2p absorption edges consists in a division by the corresponding Gr/Ir(111) sample spectrum. This procedure allows eliminating also the modulation of the spectra caused by the energy-dependent transmission function of the beamline, mainly associated with the energy-dependent absorption of the last mirror.

X-ray absorption by the graphene carbon atoms makes quite complex the normalization process for the NEXAFS C 1s edge absorption. In particular, performing the simple division by the clean sample spectrum, i.e. Gr/Ir(111), would be incorrect. In fact, we expect the X-ray absorption by the graphene carbon atoms to change after the molecules deposition. According to this argument, the result of the simple division by the clean sample spectrum would be affected by unpredictable anomalous effects. We used an alternative normalization method, exploiting the absorption signal (I_0) of the last mirror: In particular, supposing the photon flux coming out from the monochromator to be nearly constant, at least in the energetic range of interest, the procedure consists in determining the energy-dependent reflectivity of the toroidal mirror from I_0 . Then, normalizing the sample absorption spectrum to the mirror reflectivity, we expect to eliminate the modulation induced by the energy-dependent transmission function of the toroidal mirror. With this normalization procedure, the C 1s edge spectra will contain both the contribution of the adsorbed molecular layer and the graphene support. The Kramers-Kronig relations were used to calculate the reflectivity from the measured absorption signal, a process that still has some degrees of freedom left, coming from the choice of the integration constants: the best parameters were chosen in order to reproduce the same modulation reported in literature for the Gr/Ir(111) C 1s edge signal intensity in the 283 – 287 eV energy range.

FITTING As mentioned above, the final states can be divided in bound states and a continuum of final states:

- The transitions to **bound states** are resonant processes, thus yielding absorption peaks in the spectra. Typical NEXAFS features are resonances to molecular orbitals or Rydberg states, which are electronically excited states whose energies converge to the VL. The Rydberg peaks are usually very sharp and intense in the absorption spectra of atoms or molecules in the gas phase, but in the case of adsorbed molecules, they weaken and merge into the ionization potential step, making it difficult to unambiguously resolve the two features. The unoccupied molecular orbitals are usually labeled by σ^* and π^* according to the spatial symmetry. Resonant transition processes are theoretically described by a Lorentzian function with the FWHM that is inversely proportional to the mean lifetime of the final electronic state. Besides, it is possible to find asymmetric peaks, usually associated with σ^* resonances located above the IP step, due to the relative vibrational fine structure or to the dependence

of the final state lifetime on the kinetic energy, related to the overcoming of the centrifugal potential barrier;

- In NEXAFS spectra, in addition to resonance peaks, one or more **step-like** features are always present, caused by electronic transitions to a continuum of states. The first and usually more evident type of step is located at the Ionization Potential (IP) and it is due to transitions to the continuum of free electron final states above the VL. The fit function for the IP is a square step function convoluted with a Lorentzian and a Gaussian function. In addition to the IP step, absorbed molecule spectra usually exhibit a step located at lower energies, corresponding to the transitions from states above the FL (Fermi fit function).

It is important to point out that the absorption spectra of the same system, collected with different polarizations, must be fitted letting varying only the amplitudes, according to the corresponding dichroic behavior, while all lineshapes are expected to be the same.

2.3.5 ARPES

Valence Band (VB) spectroscopy, also known as Ultraviolet Photoelectron Spectroscopy (UPS), is another valuable tool for the characterization of materials. As XPS, it is based on the photoelectric effect but, instead of probing the strongly bound core electrons, VB spectroscopy usually employs less energetic radiation to explore the valence band of the specimen. For molecules in the gas phase or adsorbed at the surface, this technique allows to access the frontier orbitals in the proximity of the vacuum level.

The resulting spectrum at the sample surface includes the following features: the onset of the photoemission signal at the Fermi edge, primary peaks associated with occupied frontier orbitals, a valence band from the metal substrate, and a sloping background caused by secondary electrons. Because of the improved energy and momentum resolution, reduced beam damage, and higher cross-section for excitation, the valence band is best investigated at low photon energies (typically < 100 eV for ultraviolet). The typical photoemission spectrum has a sharp cutoff at zero kinetic energy (E_{kin}) that can be used to determine the sample work function (see section 2.3.3). As XPS, photoemission data in this thesis are presented versus binding energy, setting to zero the Fermi level of the metal substrate.

If an angle-resolved setup is utilized, i.e. using Angle-Resolved Photoemission Spectroscopy (ARPES), the parallel and perpendicular momenta of the outgoing electron are determined by:

$$k_{||} = \sqrt{2m_e E_{kin}} \sin\theta \quad (2.48)$$

$$k_{\perp} = \sqrt{2m_e E_{kin}} \cos\theta \quad (2.49)$$

or further converting $k_{//}$ into two cartesian components k_x and k_y :

$$k_x = k_{//} \cos\phi \quad (2.50)$$

$$k_y = k_{//} \sin\phi \quad (2.51)$$

where θ and ϕ are the polar and azimuth angles at which the electrons leave the surface, respectively. As mentioned before, unlike the wave vector components parallel to the surface, the perpendicular k_z component is not conserved when the photoelectrons are transmitted from the sample into the vacuum above. The full angular distribution of the photocurrent ($I(k_x, k_y)$), also known as a momentum map, can be acquired in one single image.

One important consideration of using electron spectroscopy for surface analysis is the high surface sensitivity. In the kinetic energy range of interest, 10 to 100 eV, the mean free path λ for photoelectrons is only of a few Ångströms (see Fig. 2.15). Therefore, photoemission spectroscopy is suited to probe the near-surface region, where the main contribution of the total photoemission intensity originates from.

Data analysis

The non-conservation of k_z , which depends on the angle of emission, yields an uneven distribution of the electron energy in the (ideally) isoenergetic $I(k_x, k_y)$ maps. To fix this error, a quadratic interpolation is applied to all the $I(E_{kin}, k_x, k_y)$ stacks, in such a way to have a homogeneous intensity in the image with $E_{kin} = 0$ (Fermi level). Then, a rigid interpolation is applied to set the Fermi level at zero binding energy.

To limit the beam damage of the specimen, data has been acquired in raster scan mode in our case. Because of surface irregularities, sometimes the image is slightly misaligned; therefore, when summing the stacks to improve statistics, a rigid translation is applied to each (k_x, k_y) layer to match the addendum one.

NanoEsca Beamline

The ARPES data reported in this thesis were acquired at the NanoESCA beamline of the Elettra synchrotron in Trieste, Italy, run by Peter Grünberg Institute 6 of Forschungszentrum Jülich. The endstation consists of an UHV setup with a commercially available NanoESCA PEEM, which has been modified as described in [112] and a separated chamber for in-situ preparation. Generally, the microscope can be operated in a direct and a momentum imaging mode. Momentum maps were collected to analyze the photoemission intensity in a lateral reciprocal space range of $k_x, k_y \in [-2.1, +2.1] \text{ \AA}^{-1}$. In all the measurements performed here the sample was kept at a constant temperature of 90 K, achieving a total energy and momentum resolution better than 100 meV and $0.0.3 \text{ \AA}^{-1}$, respectively.

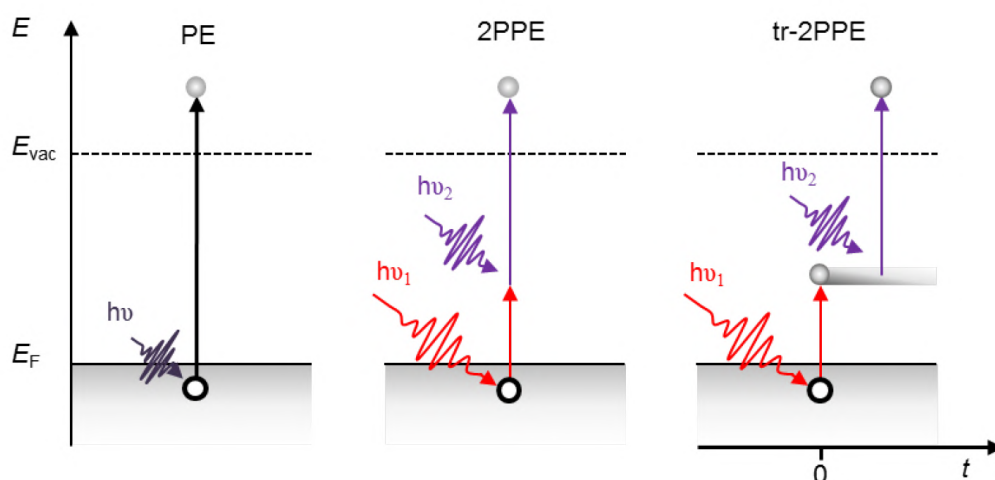


Figure 2.20: Single-photon (left), two-photon (center) and time-resolved two-photon photoemission mechanisms. One-photon photoemission requires energy $h\nu$ to be larger than the work function Φ ; for 2PPE $h\nu_1$ and $h\nu_2$ energies are smaller than Φ and two photons are needed to have photoemission; on the left, the electron can relax for a time t before photoemission (from [114]).

2.4 TWO-PHOTON PHOTOEMISSION SPECTROSCOPIES

Two-photon photoemission is a well-established surface science technique frequently used to characterize organic layers. In standard UPS, electrons are directly photoemitted by the absorption of a single photon with energy greater than the work function. In 2PPE the photon energy $h\nu$ is not high enough to have direct photoemission: in this case electrons are first excited to a virtual state by a pump photon of energy $h\nu_1$ ($h\nu_1 < \Phi$) and then photoemitted by a probe photon with $h\nu_2$ energy. Fig. 2.20 is a schematic representation of standard photoemission and 2PPE processes: from the left to the right there are one-photon photoemission, two-photon photoemission and time-resolved two-photon photoemission. By means of this double-photon process it is possible to have an insight into initially unoccupied states lying above the Fermi Level, measuring photoelectrons' kinetic energy as described in the previous section [113].

In the case of emission by absorption of two photons, the kinetic energy is given by the same equation (2.26) used for one-photon photoemission

$$E_k = h\nu_2 - E_B - \Phi \quad (2.52)$$

where the photon energy $h\nu_2$ is the probe pulse energy (see Fig. 2.20): in this case the binding energy E_B will be positive because electrons are photoemitted from excited states lying between E_F and E_{VAC} .

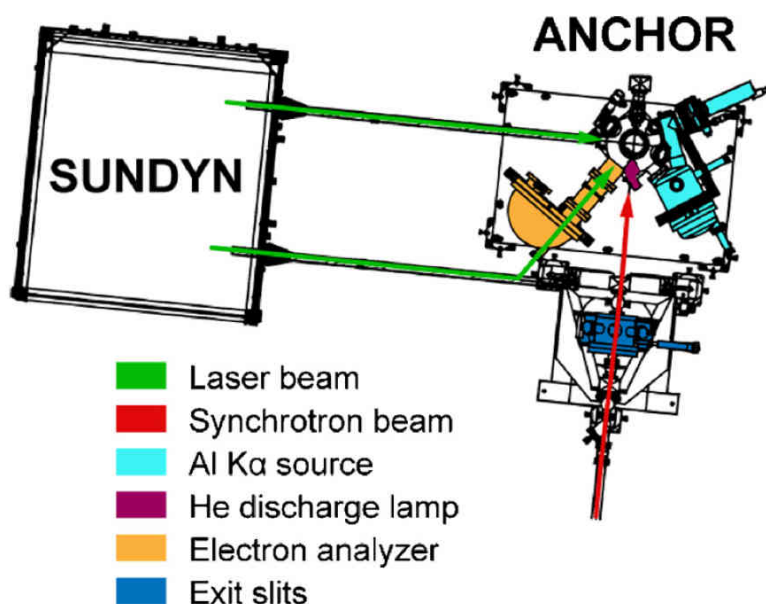


Figure 2.21: Drawing of the ANCHOR endstation and SUNDYN apparatus: the electron analyser and the laser light have been used for 2PPE experiments; UPS measurements have been performed using the helium discharge lamp [116].

2.4.1 Time-resolved 2PPE

We said that 2PPE spectroscopy is performed exploiting high power sources like pulsed lasers: if the pulses are short enough, it is possible to study the dynamical behaviour of excited electrons as a function of time. Indeed, ultrafast laser pulses have made possible to access electronic dynamical properties, down to a few femtoseconds [115]. Electrons are first excited above E_F by a pump pulse and then photoemitted by a probe pulse: by varying the delay Δt between pump and probe pulses it is possible to map the time evolution of electronic states near the Fermi level [116]. The acquired data are usually reported as 2D maps of intensity as a function of binding energy (from Eq. (2.52)) and pulses delay time. Time-resolved 2PPE mechanism is explained in Fig. 2.20 where on the right the excited electron state evolves for a time t before photoemission.

2.4.2 ANCHOR-SUNDYN setup

Tr-2PPE measurements have been performed at the ANCHOR branchline of the ALOISA beamline (CNR, at the Elettra synchrotron radiation facility, Trieste). The setup consists of a pulsed laser radiation source, coupled with the UHV chamber and the electron analyser. Samples were prepared in the UHV chamber and the molecules were evaporated by means of the same evaporator used for SFG experiments; laser radiation reaches the sample in the chamber and the photoemitted electrons enter the analyser.

The SUNDYN radiation source is a Yb:YAG fiber laser, with a fundamental wavelength of 1030 nm (1.2 eV). Nonlinear beta barium borate (BBO) crystals are used to generate the higher harmonics up to the 5th (515, 343, 257 and 206 nm). The laser can operate at repetition rates between 175 kHz and 2 MHz, controllable by software. In this range, it provides > 35 W of average power. Consequently, the energy/pulse ranges from 200 μ J down to \sim 18 μ J. The pulse duration can be varied from 310 fs up to 10 ps. An optical parametric amplifier (OPA) is installed in order to have full photon energy tunability in the 210 – 2600 nm wavelength range. It has been configured for operation at 385 kHz.

The SUNDYN optical table lies close to the ANCHOR endstation and the optical beam can be delivered into the UHV chamber at an angle of 90° or 35° with respect to the incoming synchrotron beam (see Fig. 2.21). The spot size of the laser at the sample when delivered through the hemispherical analyser is about $700 \times 300 \mu\text{m}^2$, while in the other configuration it is $200 \mu\text{m}^2$. A LabVIEW software package has been developed for data acquisition and for controlling the laser and beamline optics. More setup details can be found in [116].

In this setup the sample can be excited by a tunable pump pulse with energy $h\nu_1$ in the range 0.5–5.9 eV and probed by fourth ($h\nu_2 = 4.8$ eV) or fifth ($h\nu_2 = 6$ eV) harmonic pulses of the laser. The time delay between pump and probe pulses is varied via a motorized delay line with a travel length of 50 cm.

3 | UHV CHARACTERIZATION

3.1 Gr/Ir(111)

3.1.1 Sample Preparation

The Ir(111) surface was cleaned by standard cycles of Ar⁺ sputtering ($I_{\text{sputt}} \sim 10 \mu\text{A}$, 2 keV) and annealing @1300 – 1350 K, alternated with treatments in oxygen background in the 330 – 1070 K temperature range. Before growing graphene, the sample was finally annealed to 1300 – 1350 K in UHV. Graphene was grown by thermal cracking of ethylene dosed from the background *in vacuo*, following established recipes [117]. In detail, after saturation with ethylene at room temperature, the crystal was annealed to 1000 K. At 1100 K, an ethylene background was introduced, and the temperature was further increased up to 1300 K. A temperature cycle (1300 – 500 – 1300 K) followed, always in ethylene background. The complete Gr growth treatment lasted about 30 min.

3.1.2 SFG

The clean graphene IR-Vis SFG spectrum, reported in Fig. 3.1 for the 1450 – 1700 cm⁻¹ energy range, shows two resonances fitted with the same width $\Gamma = 14 \pm 2 \text{ cm}^{-1}$: the one at 1625 cm⁻¹ is attributed to the graphene optical G phonon [55, 118], while the one at 1640 cm⁻¹ is attributed to a replica of the principal graphene phonon induced by the Moiré pattern [119, 120]. A similar splitting of the graphene phonon was also observed in good quality graphene spectra previously measured in our setup [55].

3.1.3 LEED

The quality of graphene was checked by monitoring the corresponding LEED pattern (see Fig. 3.2A-D). As well known, graphene on Ir(111) shows a Moiré pattern due to the mismatch between the graphene cell and the iridium underneath. In particular, 10 graphene unit vectors repeat over 9 iridium cells, with a resulting Moiré periodicity of $\approx 2.5 \text{ nm}$ and a corrugation in *z* of less than 0.3 Å (see Fig. 3.2E) [117, 119, 121]. Locally, graphene forms three lattice structures above the iridium atoms, resulting in alternating hexagonal-closed-package (hcp) and face-centered-cubic (fcc) arrangements in the proximity of the Moiré valleys and atop-type regions in Moiré domes (where a Gr aromatic ring is centered on an Ir atom). In our LEED images, the diffraction spots related to the Ir,

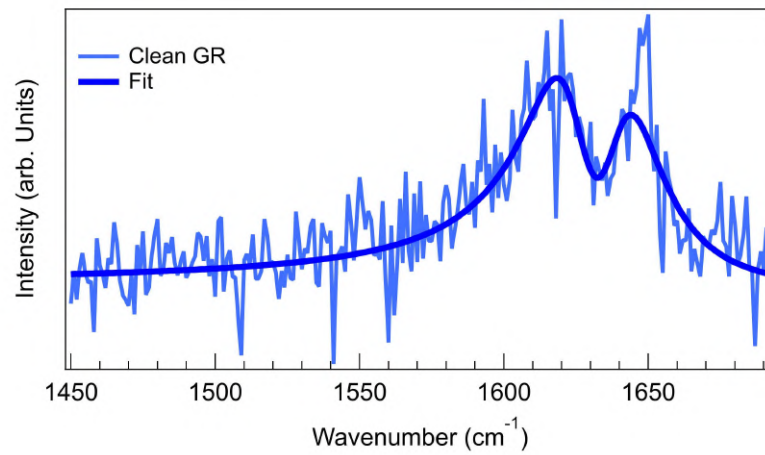


Figure 3.1: IR-Vis SFG spectrum of clean graphene and best fit. The fit function includes two resonances of same width Γ attributed to graphene phonon ($\approx 1625 \text{ cm}^{-1}$) and its Moiré-induced replica ($\approx 1640 \text{ cm}^{-1}$).

graphene, and Moiré unit cells can be clearly distinguished and, in the latter case, even the second diffraction order can be resolved (see Fig. 3.2B): this is representative of the high crystallographic quality of the graphene sheet, confirmed also by the absence of rotational domains.

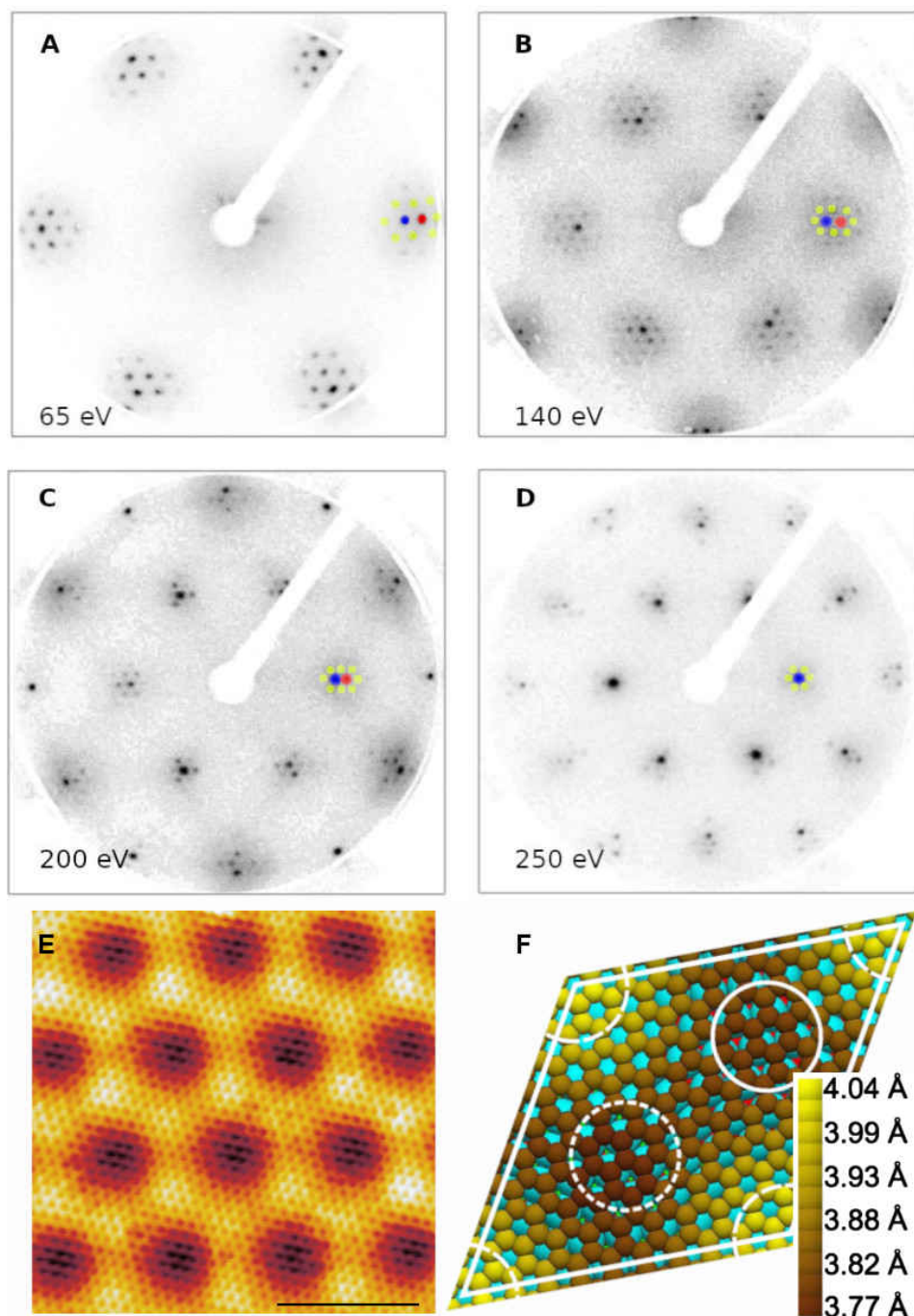


Figure 3.2: **A-D)** LEED patterns of the bare, as prepared graphene monolayer on Ir(111) collected at room temperature, as a function of the electron energy. Blue spots correspond to the iridium unit vector, red spots to graphene unit vector, and yellow spots to the moiré first order diffraction pattern; **E)** Atomic resolution STM image @77 K of the graphene single foil obtained on the Ir(111) following the recipe described in the text. Scale bar=3 nm, $I_{set} = 1$ nA, $U_{bias} = -100$ meV; **F)** Schematic illustration of the DFT optimized $C(10 \times 10) = Ir(9 \times 9)$ unit cell. Shading of the C atoms corresponds to their heights as calculated by DFT. 1st, 2nd, and 3rd layer Ir atoms are colored cyan, red, and green. Hcp-type region: full circle, fcc-type region: short-dashed circle, atop-type region: dashed circle segments [121].

3.2 MONO-METALLIC MOFS: CoTPyP AND FeTPyP

In this section the geometry, vibrational and electronic structure, and thermal stability in UHV of the mono-metallic CoTPyP/Gr/Ir(111) and FeTPyP/Gr/Ir(111) monolayers will be addressed. The results are functional for the following study of CoTPyP-based bi-metallic MOFs and near ambient pressure experiments.

3.2.1 MOF growth

The (Co-Fe)TPyP/Gr/Ir(111) monolayers have been grown *in vacuo* by physical vapor deposition of the molecules on the Gr substrate. Cobalt and iron tetra-pyridyl-porphyrins chlorides¹ (CoTPyP_{Cl} and FeTPyP_{Cl}) were purchased from Frontier Scientific. The molecular source was a heated boron nitride crucible. The deposition time for a monolayer, in the range of 15 – 40 min, was calibrated either by means of a quartz microbalance, N 1s and C 1s core levels intensity ratio analysis (in XPS), or direct STM inspection, depending on the currently available technique. In order to avoid long outgassing of the molecules in UHV, necessary to get rid of the residual organic contaminants, the molecules have been kept at 500 K for a night directly during the bake of the organic evaporator, with a pressure lower than 10^{-6} mbar. The (Co-Fe)TPyP deposition on graphene/Ir(111) was performed with the sample kept at 500 K (unless specified otherwise) in a residual background pressure of 5×10^{-10} mbar. The temperature of the crucible is about 600 K for both molecules. The chloride ligand, which guarantees the chemical stability of the porphyrin in air, detaches from the molecule in the evaporation process [32, 122].

3.2.2 STM - CoTPyP

When deposited on graphene, the CoTPyP molecules aggregate forming large islands hundreds of nanometers wide (Fig. 3.3A). As expected, this indicates the relatively weak coupling that these porphyrins have on this support, as already reported for a similar systems [55, 118, 123]. At closer inspection (Fig. 3.3 B-D), the molecular ordering is revealed, showing that they alternate in two rows, particularly evident at a negative bias (Fig. 3.3B). Inside of a single row, the CoTPyPs appear to be identical, while in the adjacent row they have a different azimuthal orientation. We can provide the unit cell by taking a $1.50 \times 2.80 \text{ nm}^2$ rectangular Bravais lattice with base, as shown in Fig. 3.3C. The different azimuthal rotation of the CoTPyPs inside the unit cell, whose mirror axes are not aligned with the principal unit vectors, yields a chiral domain (Fig. 3.3C, green lines). This packed structure is favored by the attractive interaction between the electronegative N-atom of the pyridyl endgroup and one H-atom from a neighboring pyrrole moiety [124–126].

¹ CoTPyP_{Cl} = 5, 10, 15, 20-tetra(4-pyridyl)21*H*, 23*H*-porphyrin Co(III) chloride; FeTPyP_{Cl} = 5, 10, 15, 20-tetra(4-pyridyl)21*H*, 23*H*-porphyrin Fe(III) chloride

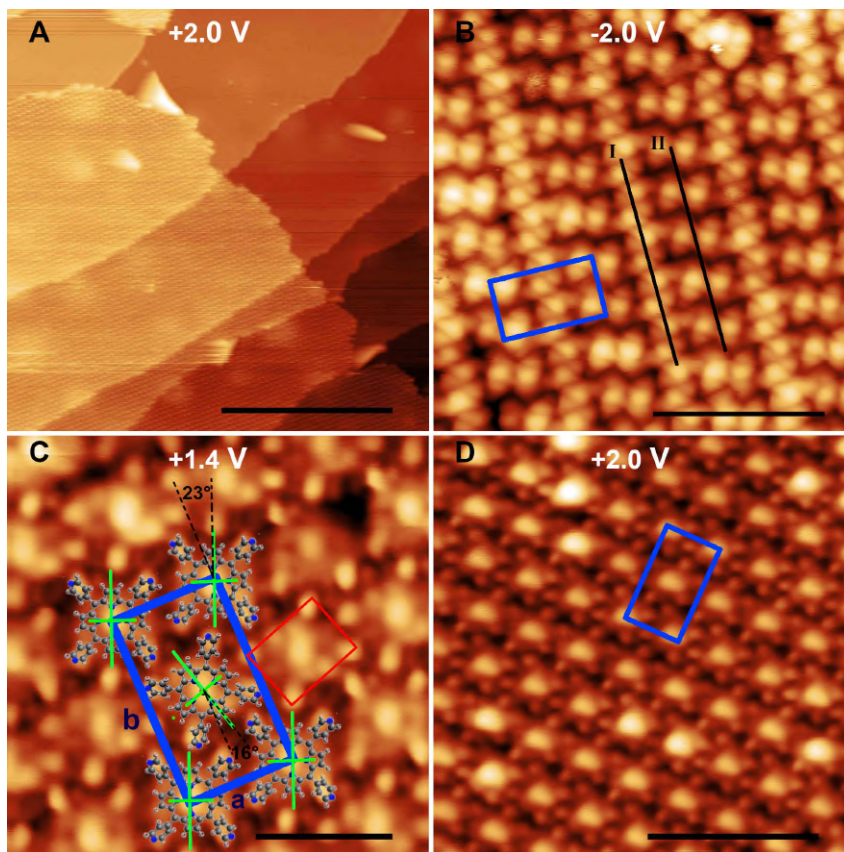


Figure 3.3: STM images @77 K of ~ 0.5 ML of CoTPyP/Gr/Ir(111) at different bias and scales. The unit cell is indicated with blue lines. **A)** On a large scale, large CoTPyP islands are visible, indicating the high porphyrin mobility on graphene during the MOF growth and the predominant lateral attraction, mediated by the pyridyl residues (scale bar = 50 nm, $I_{set} = 0.1$ nA, $U_{bias} = +2.0$ V); **B)** At negative bias, where the HOMO is visible with a four lobes "butterfly-like" shape, the CoTPyPs are packed into two rows (black lines). In each row, the molecules are simply translated, while, in the adjacent one, they show a different azimuthal rotation (scale bar = 5 nm, $I_{set} = 0.1$ nA, $U_{bias} = -2.0$ V); **C)** With a bias closer to the HOMO-LUMO gap, the topography of the layer is clearer, with the CoTPyPs' two-fold symmetry due to saddle-shape adsorption configuration, the alternatively rotated pyridyl groups yielding a rectangular appearance (red rectangle), and the chirality of the cell originating from misalignment between the molecule principal axis (green lines) and the unit cell. $a = 1.5$ nm, $b = 2.8$ nm (scale bar = 2 nm, $I_{set} = 0.3$ nA, $U_{bias} = +1.4$ V); **D)** At +2.0 V, the LUMO appears as a spherical protrusion centered on the cobalt atom (scale bar = 5 nm, $I_{set} = 0.2$ nA, $U_{bias} = +2.0$ V).

The STM appearance exhibits a strong dependence on the applied bias. No image could be acquired in the -1.0 - $+1.0$ V bias range, a sign of a large HOMO-LUMO energy gap, as confirmed by the STS investigation. At -2.0 V bias (Fig. 3.3B), the molecular HOMO

shows a butterfly shape, with the molecular orbital extending over the whole macrocycle. At +2.0 V bias, instead, the LUMO appears as a spherical protrusion highly localized on the cobalt atom (Fig. 3.3D), surrounded by four smaller features attributed to the pyridyl residues [39, 123]. At lower bias (+1.4 V), the geometry of the porphyrin becomes even clearer (Fig. 3.3C), with a more defined shape of the pyridinic and pyrrolic groups. Indeed, when the applied bias is within the gap, the tip-sample distance is reduced because of the absence of molecular states, with a subsequent increase of the topographic rather than electronic information [127–129]. A closer inspection in Fig. 3.3C reveals that the molecules show a rectangular rather than a square-like appearance (red rectangle): this is attributed to the alternatively rotated out of the porphyrin plane, as already reported in a similar case of 2HTpyP/Ag(111) [39, 123], lowering the symmetry from four-fold D_{4h} to two-fold D_{2d} . In the same image, also the macrocycle shows a two-fold symmetry, due to the typical saddle-shape adsorption configuration, where the pyrrolic groups forming the macrocycle are lifted/lowered in opposite pairs, to reduce the steric hindrance [48, 130, 131]. As we will see in the following paragraph, the whole geometric interpretation is fully supported by DFT and NEXAFS.

3.2.3 STS - CoTPyP

Scanning Tunneling Spectra and Maps have been acquired in the range between -2 and $+2$ V (probing occupied and unoccupied states, respectively) to characterize the electronic structure of the CoTPyP/Gr/Ir(111) heterostack, as reported in Fig. 3.4 and 3.5. In particular, the two figures refer to two different tip configurations and measurement parameters.

The two STS spectra of fig 3.4 and 3.5, both acquired on top of the cobalt atom, have been measured with an initial setpoint of 2.0 V/0.2 nA for Fig. 3.4 and -2.0 V/0.2 nA for Fig. 3.5. The two curves show similar results: a large gap of more than 2 eV can be observed in both graphs. Remarkably, looking at the two insets, the weak signal shows a linear dispersion that can be attributed to the underlying graphene which, despite the great spatial separation from the tip, can still be measured. In the range between -2.0 and -1.3 V, an intense signal, in both graphs 200 times stronger than graphene LDOS, is attributed to the molecular HOMO. A signal of comparable magnitude can be observed above the Fermi level, attributed to the molecular LUMO, in the range between $+1.3$ and $+2.0$ V.

The comparison between the two tips shows modulation of the local density of states, which is thus a function of the tip configuration and/or functionalization. In particular, tip-effects can also be attributed to the unphysical negative dI/dV signal reading, together with the barrier height for the tunneling electrons that is a function of the applied voltage [129]. The thermal drift, which should cause a negative offset in the dI/dV curve if the tip moves away from the sample, can be neglected by checking the good matching between two consecutive dI/dV curves, not reported in this thesis. Additional STS spectra taken on

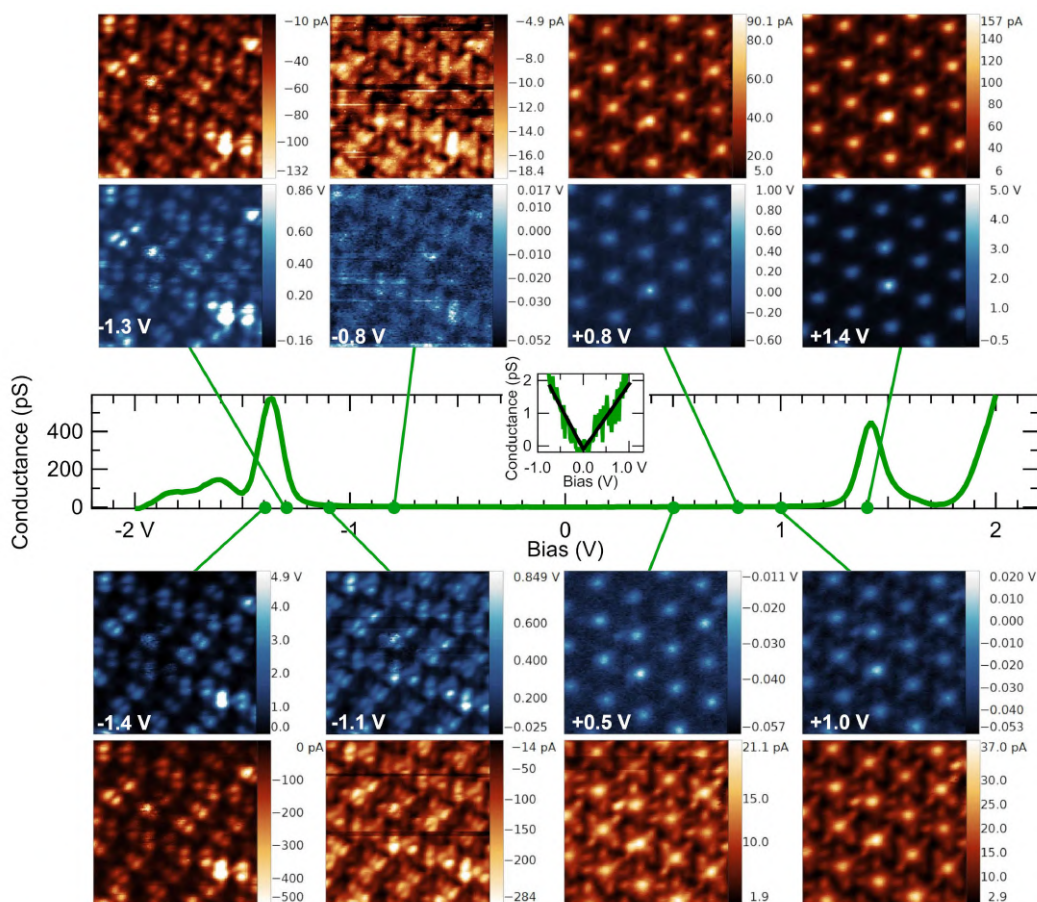


Figure 3.4: STS spectrum, dI/dV maps (blue palette), and simultaneously acquired current signal (red palette) of the CoTPyP/Gr/Ir(111) monolayer at 77 K. In the inset, a zoom of the STS curve is reported. The STS spectrum is acquired on the cobalt with an starting setpoint of 2.0 V/0.2 nA. The dI/dV maps are collected with an initial setpoint of +1.4 V/300 pA, with the tip on top of the cobalt atom ($6 \times 6 \text{ nm}^2$).

the CoTPyP macrocycle, also not reported in this manuscript, do not show any significant additional information but a decrease of the LUMO intensity, since it is highly localized on cobalt at the center of the molecule.

The spatial distribution of the discussed states is revealed by looking at the local density of states maps in Figs. 3.4 and 3.5, also in this case acquired with two different tip configurations. The STS maps (blue palette) are shown together with the simultaneously acquired current output (red palette).

- **In the HOMO energy range**, the strongest signal intensity (look at the side color scale numbers) is found at about -1.4 V , where the spatial electron charge distribution is spread throughout the macrocycle. The latter shows a two-fold configuration, due to the macrocycle adsorption configuration (saddle shape): indeed, the charge

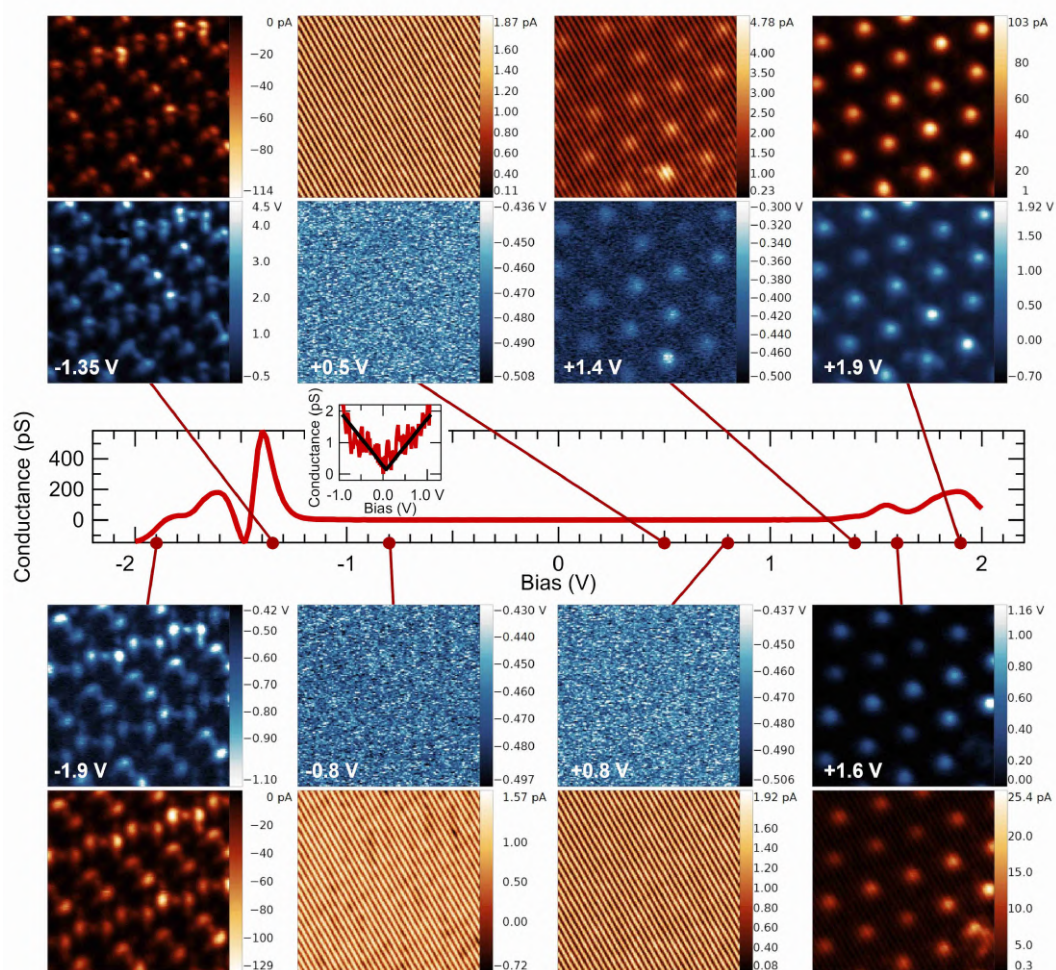


Figure 3.5: STS spectrum, dI/dV maps (blue palette), and simultaneously acquired current signal (red palette) of the CoTPyP/Gr/Ir(111) monolayer at 77 K. In the inset, the a zoom of the STS graph is reported. The STS spectrum is acquired on the cobalt with a starting setpoint of -2.0 V/ 0.2 nA. The dI/dV maps with a distance set by the initial -1.35 V/ 100 pA setpoint on the cobalt (6×6 nm²). Another tip configuration is used, with to respect the data shown in Fig. 3.4. The maps at -0.8 , $+0.5$, and $+0.8$ V have such a flat signal that only the lock-in carrier modulation can be detected)

is located mainly on the pyrrolic groups, with a vertical (w.r.t the surface) nodal plane passing in between the C_β and the closest iminic nitrogen atom, that gives the “butterfly” shape, together with dim spherical charge distribution at the center of the porphyrin. At an even lower bias (-1.9 V), the orbital on top of the cobalt atom is more pronounced, and the nodal plane at the center of the pyrroles disappears. At the same energy, some charge on the pyridinic residues, barely visible at -1.4 V, can be observed, which gives the molecule the “H” envelope, due to their alternating dihedral angle rotation (see paragraph 3.2.2).

- **In the LUMO energy range**, the most intense signal is detected between +1.4 and +1.9 V, depending on the tip functionalization, and corresponds to a bright spherical charge distribution on top of the cobalt atom, which we may attribute to the Co $3d_{z^2}$. Typically, in Co-metalated porphyrins, a large splitting of the $3d_{z^2}$ spin channels has been observed, yielding an unoccupied channel, which is often the LUMO (our case) or LUMO+1, while the occupied counterpart is located even below the HOMO [27]. If the substrate is sufficiently interacting, the unoccupied $3d_{z^2}$ spin channel can be lowered and partially occupied, with the formation of a covalent bond [27]. In our case, this is not observed, indicating the weak interaction of the CoTPyP with graphene.
- **In the gap**, instead, just noise is detected, as in Fig. 3.5, or a faint signal if the tip is sufficiently close, as in Fig. 3.4. However, in the latter case, it is important to keep in mind that the images at, for example, +0.5 and +1.4 V, have a current intensity (dI/dV signal) modulation ratio of the order of 10 (100), meaning that some electrons can still tunnel from the tip into the sample even in the HOMO-LUMO gap; as can be noticed in dI/dV maps at -0.8 and $+0.5$ V of Fig. 3.4), the resemblance of the HOMO and LUMO states, respectively, would suggest a second order electron tunneling that sees the HOMO/LUMO orbitals as intermediate virtual states [129, 132].

3.2.4 DFT - CoTPyP

STM and STS images have been simulated with *ab initio* DFT and reported in Fig. 3.6 [133]. In general, there is very good agreement with the experimental data (Figs 3.4 and 3.5). The iridium atoms have been omitted in the simulation since - in presence of Ir - we observed no geometry variation of the Gr carbon atoms, nor the presence of graphene pinning. A large gap of about 2 eV is present, with intense molecular state contributions both in the HOMO and LUMO range. In more detail:

- **In the HOMO energy range**, the "butterfly" shape is evident from -1 to -1.5 eV, corresponding to states localized, as observed in the experimental data, on the tilted macrocyclic pyrroles. Carefully looking at the -1.2 eV image, we can observe a mirror nodal plane (vertical w.r.t. the surface) cutting the two lobes (red line in the figure), which disappears at higher energy (-1.5 eV), as observed also experimentally. The projection on the cobalt 3d orbitals shows a contribution of the $3d_{zx}$ and $3d_{zy}$, and they can even be seen in the STS image at -1.5 eV, by the presence of four smaller lobes, with four-fold symmetry, with the principal rotation axis passing by the CoTPyP center. At -0.8 eV, both STS and STM simulation show the topography of the molecule, with the saddle-shaped macrocycle, the cobalt, and the pyridinic groups, once again in agreement with the corresponding experimental images (in Fig. 3.4)

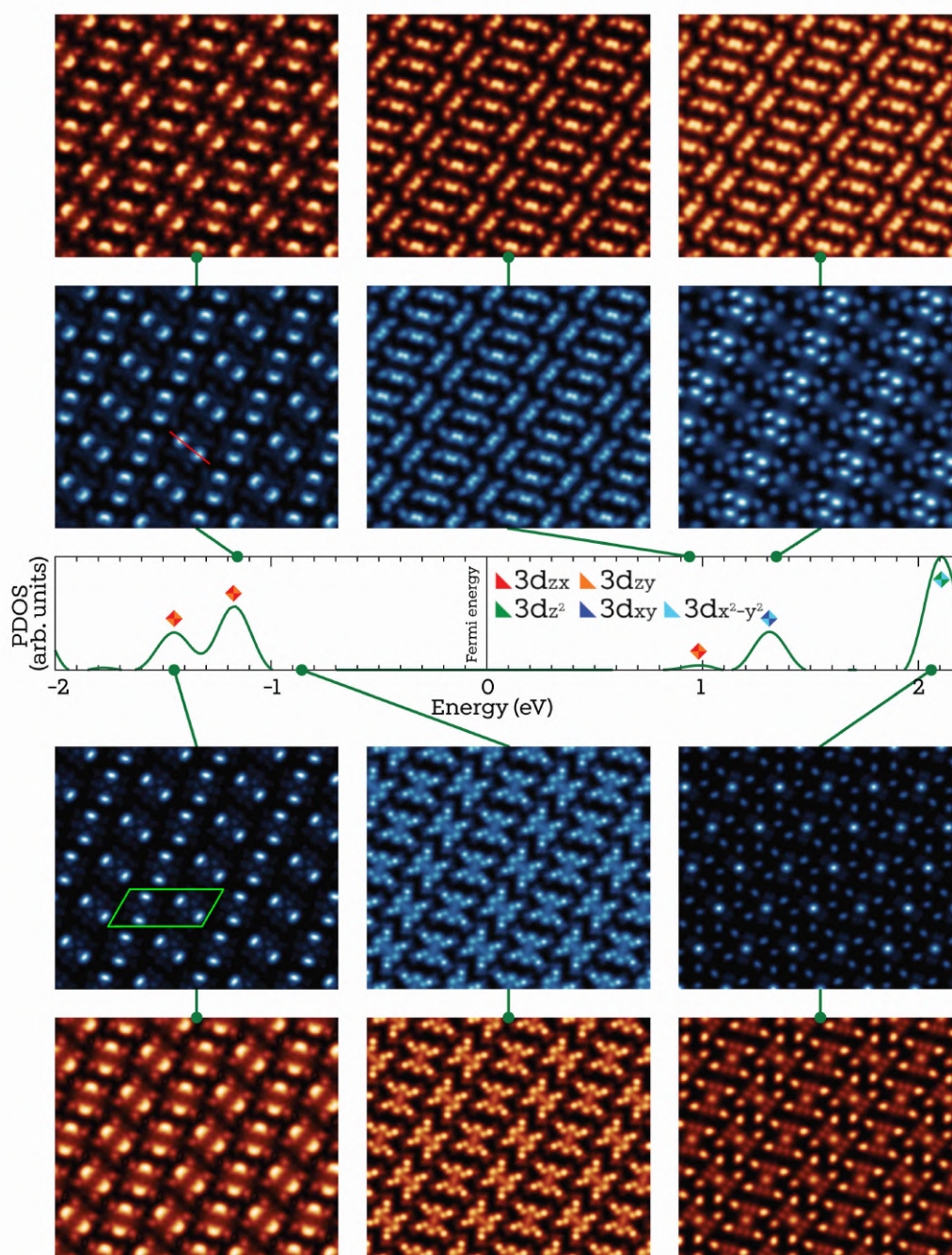


Figure 3.6: *Ab initio* DFT-simulated STS (blue palette) and STM images (red palette) of the CoTPyP/Gr layer, with the corresponding DOS curves, projected on the 3d and 4s cobalt states. The Fermi level is set in correspondence of the Dirac cone. The images has been obtained with the Tersoff Hamann approximation, at a constant height between 2.5 and 3.0 Å, with an integration interval of 0.1 eV for the STS maps.

- In the **LUMO energy range**, two main contributions are present: at +1.3 eV, the PDOS is mainly constituted by the planar $3d_{xy}$ and $3d_{x^2-y^2}$ cobalt orbitals and, thus, scarcely visible with STS; at +2.1 eV, instead, the sharp $3d_{z^2}$ empty orbital is highly localized at the porphyrin center, and couples with experimental data, where we see such orbital at a lower energy (in a broad range between 1.5 and 2.0 eV). By looking at the simulated STM image at 2.1 eV, the H-shape is recovered, arising from the joint contribution of the cobalt, tilted pyrroles, and alternatively rotated pyridinic groups.

3.2.5 XPS - CoTPyP and FeTPyP

The core level analysis is a valuable tool to probe the chemical environment of a selected element. In this section, the N 1s, Co $2p_{3/2}$, and Fe $2p_{3/2}$ core levels for pristine CoTPyP/Gr/Ir(111) and FeTPyP/Gr/Ir(111) are reported. These results will be used at a later stage to prove the formation of bi-metallic TPYP-based networks, to spectroscopically characterize them, and to use this information for later NAP experiments. As we will see, the use of different metal combinations (iron and cobalt) greatly simplifies the complex Co $2p_{3/2}$ and Fe $2p_{3/2}$ core level analysis, thanks to the building-block approach. The data presented here have been acquired at the ALOISA beamline (CNR-IOM) at the Elettra Synchrotron in Trieste.

N 1s

Figure 3.7A-B shows the N 1s core-level spectra of CoTPyP/Gr/Ir(111) and FeTPyP/Gr/Ir(111) with the corresponding deconvolution profiles. The line profiles of the two non-equivalent species of nitrogen atoms are modeled with two Voigt functions, centered at 399.1 eV (398.94) for the pyridinic and 398.82 eV (398.48) for the iminic species in the CoTPyP (FeTPyP) monolayer, in agreement with the literature [134, 135]. As a first approximation, all components share the same Lorentzian width of 0.27 eV, which is the value found in our other experiment with better energy resolution [135]. In addition, a shake-up feature has been fitted with a Gaussian function centered at higher binding energy, in the specific at 400.31 eV in CoTPyP and at 399.96 eV in FeTPyP. The best fitting parameters are reported in Appendix (Tab. A.1).

THERMAL ANNEALING In order to investigate the thermal stability of the layer, two annealing experiments have been made for CoTPyP/Gr/Ir(111) and FeTPyP/Gr/Ir(111) monolayers, in a range of temperatures between RT (MOF growth temperature) up to about 970 K. Hence, we report the evolution of the N 1s core level spectra, measured at RT after stepwise flashes to selected temperature values. For both series (Fig. 3.8), the pyridinic and iminic components have a fixed Lorentzian width of 0.27 eV, coherently with the previous analysis. The position and the Gaussian parameters, instead, were let

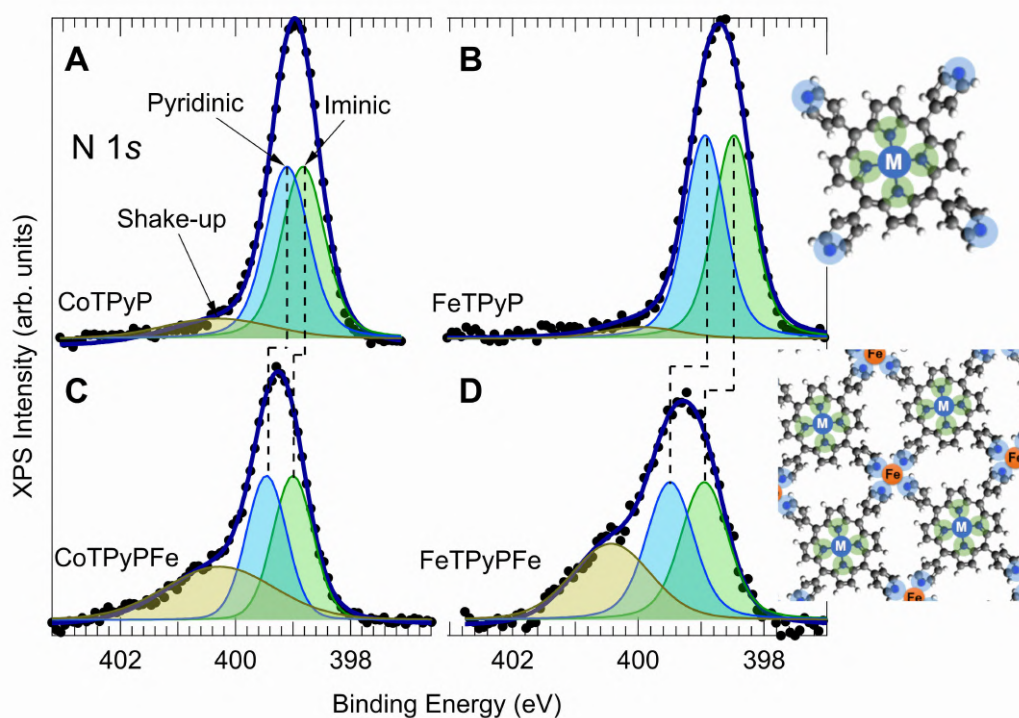


Figure 3.7: A-D) XPS experimental data for the N 1s core level (dotted curves), together with their fit function (blue solid lines) and deconvolution (filled profiles). The corresponding samples are labeled in the figure.

free to vary, in order to take into account possible structural rearrangements. The two nitrogen species share the same Gaussian width.

For CoTPyPs (Fig. 3.8A), annealing to 470 K induces a chemical shift of +130 meV for the iminic and +210 meV for the pyridinic nitrogen species, possibly indicating the coexistence, at lower temperature, of a metastable phase where the pyridinic nitrogen does not directly interact with pyrrolic hydrogen atoms [136]. The Gaussian width does not change within the error, indicating an irrelevant change in the sample heterogeneity. A further investigation, which should be carried out with parallel STM measurements, is behind the purpose of this thesis. Hence, only the most thermodynamically favored phase (hexagonal lattice, see section 3.2.2) has been taken into account in the rest of this manuscript. Annealing to 550 K does not induce any relevant change. Similarly, FeTPyPs annealed to 550 K (Fig. 3.8B) exhibit a negligible change of the Gaussian width (from 0.60 ± 0.02 eV to 0.61 ± 0.03), and a $\sim +110$ meV increase of the binding energy of both iminic and pyridinic components.

At higher temperature, the line shape and the relative BE of the three peaks were locked, while the absolute BE of the whole envelope was left free.

In the CoTPyP/Gr/Ir(111) system (Fig. 3.8A), from 550 K and above, we added to the fit-function a further (weak) Gaussian component at ~ 402 eV, associated with graphitic

N atoms (*i.e.* nitrogen atoms substituting carbon atoms in the graphene honeycomb-like lattice) [137, 138]. Although this component is adiabatic, we decided to fit it with a Gaussian profile in place of a Voigt function, due to the low signal-to-noise ratio of these spectra collected at high temperature. The occurrence of this peak at high binding energies can be explained in terms of the decomposition of the CoTPyP molecules. Moreover, at 970 K, we introduced another Voigt centered at low binding energy (398.27 eV), associated with a strongly substrate-interacting nitrogen species [139]. The same component can be observed also in the FeTPyP series, where it appears at 700 K and is the only one to survive at 970 K, with almost the same intensity (Fig. 3.8B).

The intensity of the spectral contributions remains almost constant up to 550 K for both systems, which is a clear sign of good stability within this temperature range. Finally, for higher temperature, there is a significant decrease in the signal intensity of the spectroscopic features, which is attributable to the partial desorption of porphyrins from graphene.

Co 2*p*_{3/2}

The Co 2*p*_{3/2} core level of the CoTPyP monolayer has a complex structure due to the coupling, in the photoemission process, between the ionized 2*p* core-level and the high-spin valence electrons (see Fig. 3.9A) [135, 139, 140]. The multiplet splitting (MS) structure has been empirically modeled, according to literature, with a Doniach Šunjić (DS) function centered at 780.6 eV ($\Gamma = 0.1$ eV) and a Gaussian component at 782.2 eV. An additional DS at 779.4 eV accounts for the Gunnarsson and Schönhammer (GS) transfer of the screening charge [140, 141]. Indeed, in the CoTPyP multilayer spectrum (Fig. 3.9A, top) the GS is quenched, since the transfer charge from the substrate is suppressed.

Fe 2*p*_{3/2}

For the description of the complex MS structure of the Fe 2*p*_{3/2} XPS core level in the FeTPyP/Gr/Ir(111) heterostack, a similar argument to the Co 2*p*_{3/2} analysis has to be taken into account [142] as reported in Fig. 3.9B. The partially unresolved MS structure is modeled by two DS centered at 708.9 and 710.1 eV ($\Gamma = 0.05$ eV), and by a broad Gaussian at 712.5 eV, which accounts also for the non-adiabatic photo-emitted electrons. Also in this case, the GS screening charge is present, as indicated by the DS at lower binding energy (707.9 eV).

3.2.6 NEXAFS - CoTPyP and FeTPyP

NEXAFS is a powerful tool sensitive to the chemical environment of a selected element, since it indirectly probes close-to-Fermi unoccupied states. In this paragraph we will describe the N 1*s* absorption edge, since nitrogen species are an optimal benchmark to prove the binding of a single metal species to the pyridinic groups.

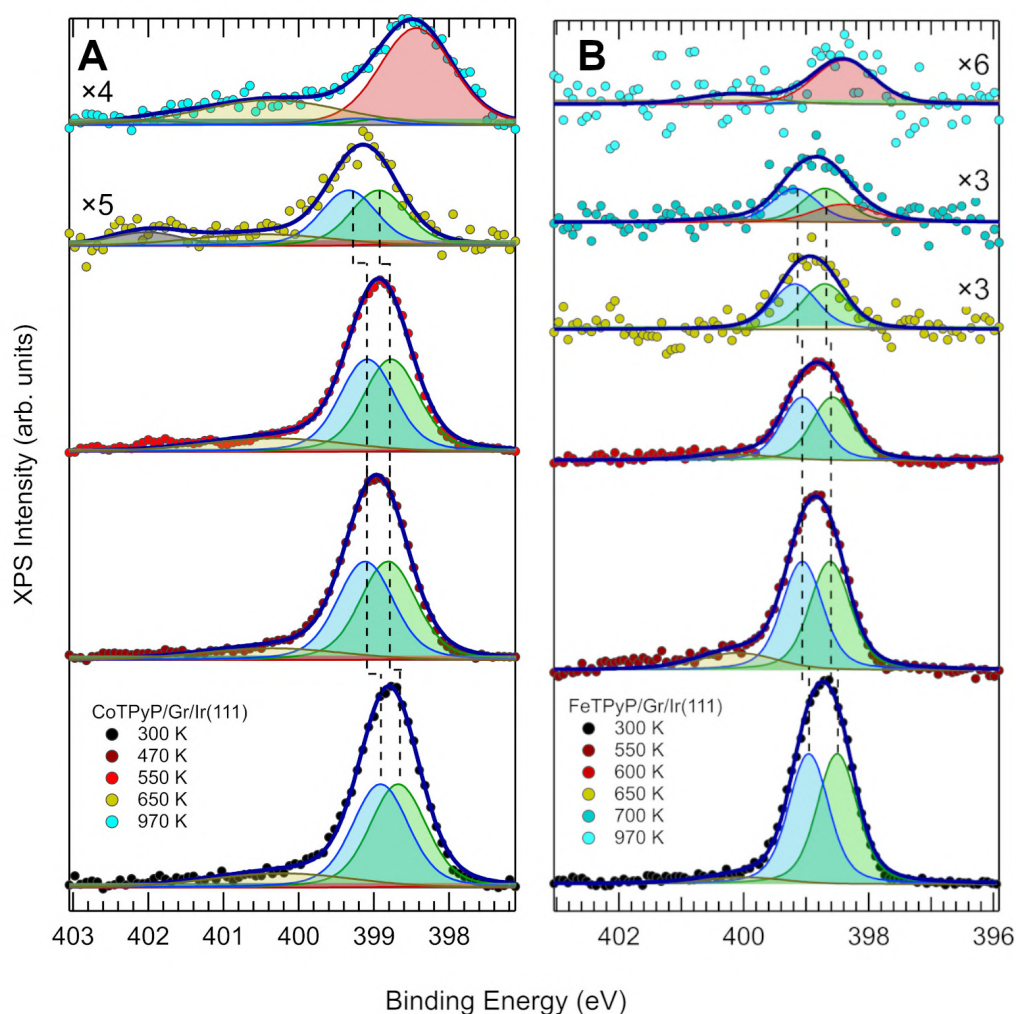


Figure 3.8: *N 1s* core level spectra of **A)** CoTPyP/Gr/Ir(111) and **B)** FeTPyP/Gr/Ir(111) collected at room temperature and subsequent heating to the indicated temperatures. The best fit envelope and the respective deconvolution are shown for each spectrum. Fill colors: green refers to iminic nitrogen and magenta to pyridinic nitrogen; grey refers to satellite features.

N 1s

Fig. 3.10A-D show the *N 1s* edge NEXAFS spectra collected for CoTPyP/Gr/Ir(111) and FeTPyP/Gr/Ir(111), respectively, with the best fit curve and the corresponding deconvolution profiles, together with the assignment of the spectral components based on literature, which are also shown for each spectrum. As said, these MOFs contain four iminic nitrogen in the macrocycle and four pyridinic N in the external residues; this means that, as a first approximation, we can use a “building block” method for the attribution of the NEXAFS resonances. Fig. 3.11 reports the literature *N 1s* edge NEXAFS spectra of FeTPP thin films (panel A) and gas-phase Pyridine (panel B) [143, 144]. The two molecules were chosen in such a way to present alternatively the iminic or the pyridinic contribution, respectively.

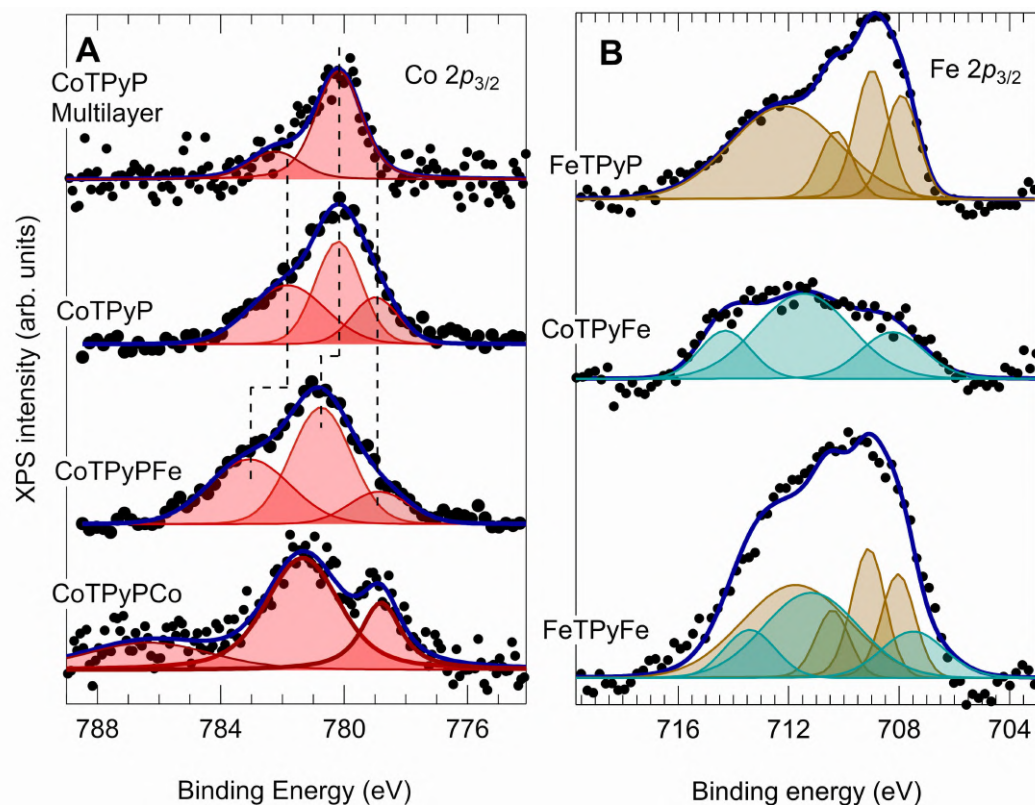


Figure 3.9: XPS experimental data for the A) $\text{Co } 2p_{3/2}$ and B) $\text{Fe } 2p_{3/2}$ core level (dotted curves), together with their fit function (blue solid lines) and deconvolutions (filled profiles). The corresponding samples are labeled in the figure.

By comparison with our monometallic MOF (Fig. 3.10A-D), we can make three observations: 1) the two resonances centered at about 401 and 402 eV in MTPyP in p-pol relate to those in FeTPP at the same energies; 2) the resonance at 402.5 eV in Pyridine clearly appears in MTPyP s-pol (Fig. 3.10B,D) and as a shoulder in p-pol (Fig. 3.10A,C); 3) lastly, the sharp component at 398.5 eV is present in all cases, and it is thus ascribed both to the iminic and the pyridinic species. Based on these observations, we fitted the MTPyP data identifying as π^* all the discussed transitions using Voigt functions. In particular, the two contributions (iminic and pyridinic) at 398.5 eV were constrained to share the same line shape, to limit the fit degrees of freedom: as a result, we find the iminic species to be centered at 398.64 eV (398.58) and the pyridinic one at 399.04 eV (398.98) for CoTPyP (FeTPyP). In addition to the already discussed transitions at 401.0 (iminic), 402.0 (iminic), and 402.5 eV (pyridinic), the introduction of an unassigned resonance centered at about 404.5 eV (fitted with a Gaussian function) is necessary in order to properly describe the experimental data.

Following the literature assignment [144], we set at 404.8 eV the initial value for the ionization potential step position before relaxing both its lineshape and its energy position for CoTPyP p-pol: the new set of parameters so found were kept constant for all spectra. In addition, the non-zero absorption in the 400 – 402 eV energy region (MTPyP s-pol)

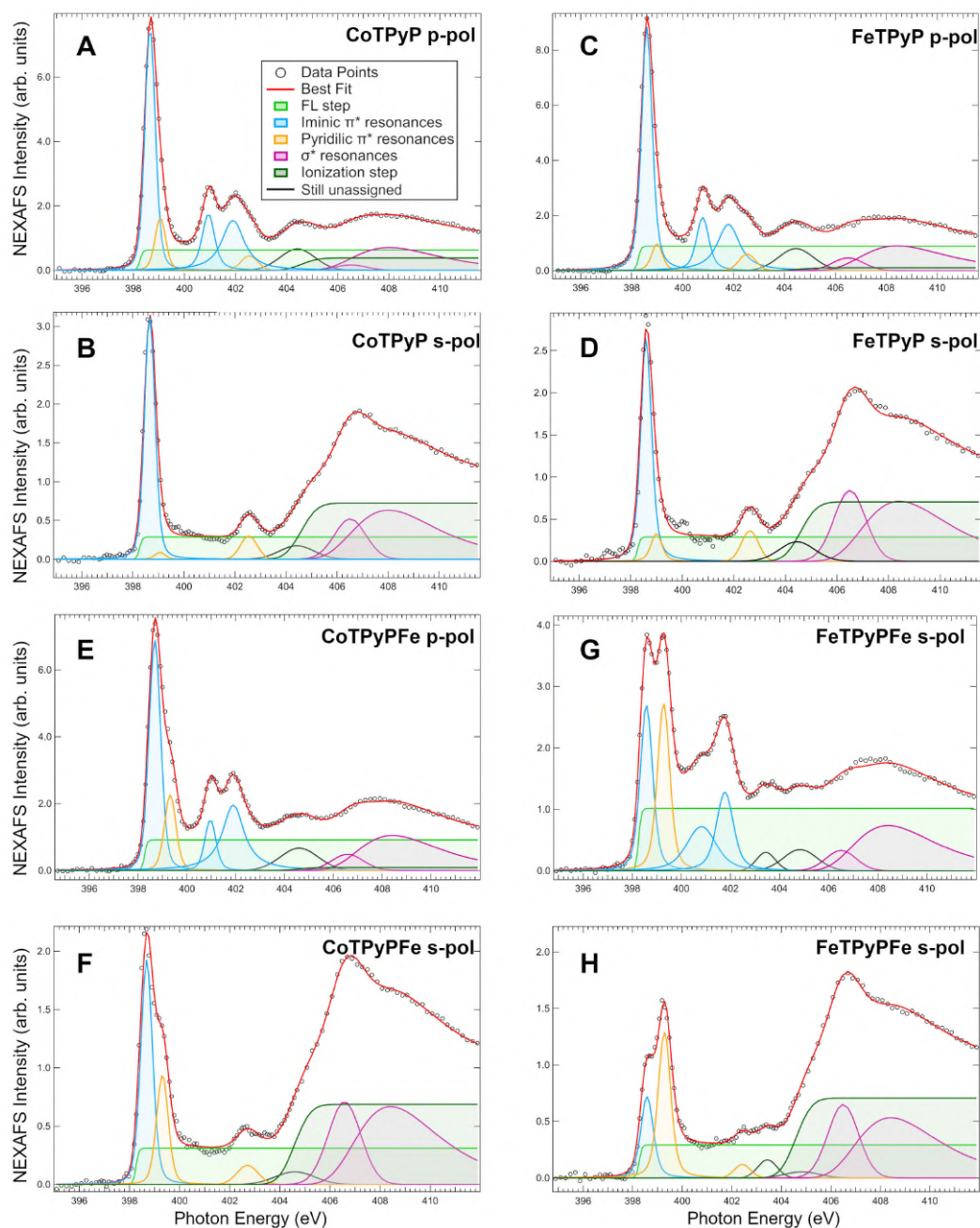


Figure 3.10: NEXAFS experimental data for the N 1s absorption edge (dotted curves), together with their fit function (red solid lines) and deconvolutions (filled profiles). **A)** CoTPyP p-pol; **B)** CoTPyP s-pol; **C)** FeTPyP p-pol; **D)** FeTPyP s-pol; **E)** CoTPyPFe p-pol; **F)** CoTPyPFe s-pol; **G)** FeTPyPFe p-pol; **H)** FeTPyPFe s-pol.

indicates the presence of another step, which is attributed to the transition to the continuum of the graphene's empty states, hence fitted with a Fermi function. Ultimately, two σ^* resonances have been identified at higher photon energies, especially examining the s-polarization spectra; they were both fitted with a Gaussian function, with an asymmetry

parameter for the higher energy one, associated with an unresolved vibrational structure. The data were fitted with the sum of the listed spectral components convoluted with a 0.2 eV Gaussian function, in order to take into account the known experimental resolution of the beamline configuration adopted for the measurements.

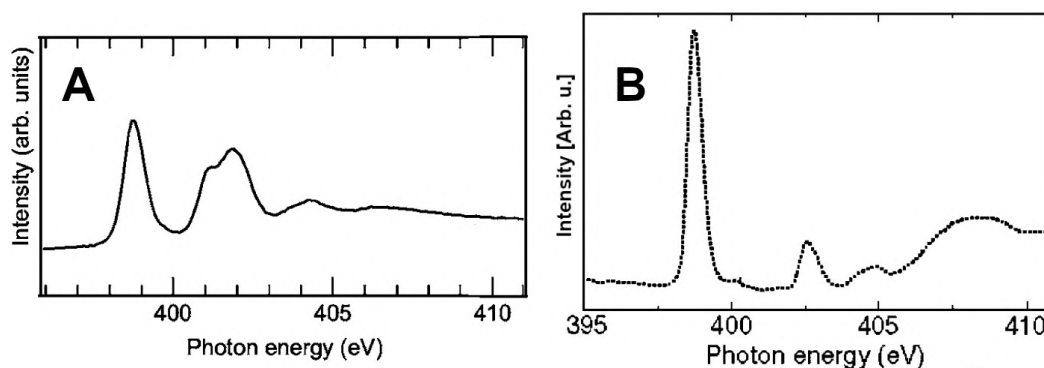


Figure 3.11: *N 1s* edge NEXAFS spectra of **A)** thin films of FeTPP/MoS₂, adapted from [143], and **B)** of Pyridine in the gas phase, adapted from [144].

The molecular adsorption geometry can be inferred by the dichroic behavior of the resonances. We can attribute a tilting angle (with respect to the graphene plane) of $36 \pm 4^\circ$ for the pyridinic residues and $38 \pm 4^\circ$ for the iminic group, analyzing the resonances in the 399 – 400 eV range. Nevertheless, the hypothesis of the adsorption geometry consisting in the whole macrocycle inclined with respect to the surface may be quite confidently ruled out. Indeed, the resonances centered at about 401 eV and 402 eV, ascribed likewise to the iminic component, show almost perfect dichroism in all the best-fit deconvolutions (see Fig.3.10A-D), thus strongly suggesting the horizontal plane adsorption geometry for the macrocycle. The non-zero inclination angles obtained for the iminic resonance is explained, in agreement with STM (see section 3.2.2), by a non-planar geometry of the macrocycle called saddle-shape, featuring the two pairs of opposite macrocyclic pyrrole rings tilted by the same angle but in the opposite vertical directions [145–147].

3.2.7 SFG - CoTPyP and FeTpyP

In this section, an SFG characterization in the $1100 - 3100 \text{ cm}^{-1}$ of the CoTPyP/Gr/Ir(111) and FeTpyP/Gr/Ir(111) layers has been carried out by means of coverage-dependent, temperature-growth dependent, and stepwise annealing experiments. The characterization includes the description of the vibrational modes of the layer, its stability in temperature, and the possible presence of metastable phases (whose thorough description is beyond the purpose of this thesis).

Coverage dependence @RT and @500K - CoTPyP

Two different coverage uptake experiments have been performed, on CoTPyP/Gr/Ir(111), by means of IR-Vis SFG: in the first case, the sample was kept at RT during the MOF growth, while in the second case it was heated at 500 K after each deposition.

DEPOSITION AT ROOM TEMPERATURE The first experiment is the stepwise deposition @RT of CoTPyPs on Gr/Ir(111) in 0.1 ML steps up to monolayer completion. In Fig. 3.12, the first spectrum at the bottom is clean graphene, needed as a reference for the identification of the molecular-related modes. At each CoTPyP deposition, we measured an IR-Vis SFG spectrum in the 1200 – 1760 cm^{-1} and 2950 – 3150 cm^{-1} ranges. We are interested in the system behavior up to 1 ML coverage: higher coverage spectra have not been fitted, but they are reported for completeness, to show the comparison with the monolayer.

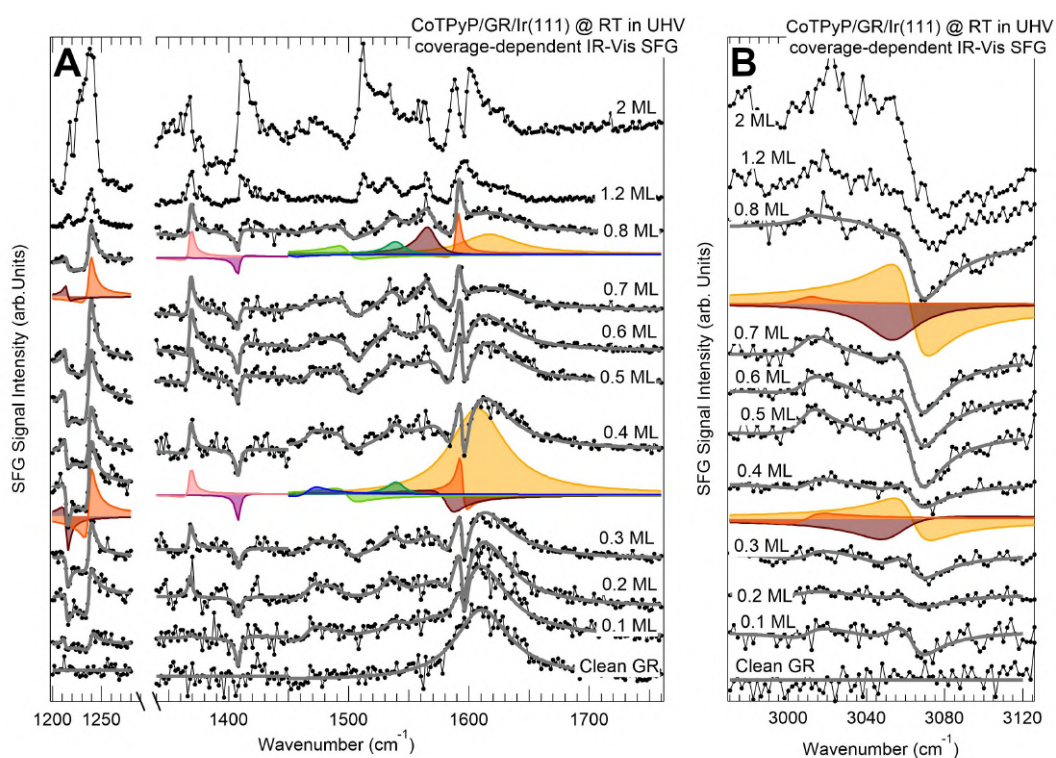


Figure 3.12: Room temperature CoTPyP coverage uptake: from the bottom to the top there are the clean graphene spectrum and the increasing CoTPyP coverage spectra. The last two at (1.2 ML and 2 ML) have not been deconvoluted due to the complexity of the observed modulations. In grey the fit functions, with deconvolutions at 0.4 ML and 0.8 ML : the first is well-representative of the spectrum at low coverages and the differences with the high coverage spectrum (discussed in this paragraph) can be observed.

In the 1200–1280 cm^{-1} range, two resonances are present, at 1214 cm^{-1} and 1238 cm^{-1} . Their phases evolve with surface coverage, their amplitudes increase but the position is nearly constant. Their Lorentzian width has been fitted in parallel for the all series, procedure that we refer to as "global-fitting". The attributed modes are the pyridinic group symmetric bending mode $\delta(\text{pyr})$ and $\nu(\text{C}_\alpha - \text{N})$ stretching of the macrocycle, respectively.

Two molecular features have been found in the 1340–1450 cm^{-1} range at 1368 cm^{-1} and 1408 cm^{-1} . Positions and width have been fitted globally, while amplitudes and phases were optimized for each spectrum. The resonances could be associated with the $\delta(\text{C}_m - \text{pyr})$ bending and $\nu(\text{C}_\alpha - \text{N})$ stretching.

Six additional resonances have been distinguished in the 1450–1760 cm^{-1} range, and their positions were left free to evolve with coverage. Their energy values (the average value over the 0.1–0.8 ML spectra) are 1465 cm^{-1} , 1498 cm^{-1} , 1538 cm^{-1} , 1577 cm^{-1} , 1593 cm^{-1} , 1610 cm^{-1} . The large feature centered at about 1610 cm^{-1} (199.6 meV) that is present also in the first spectrum of clean graphene, has been attributed to the graphene G phonon (section 3.1.2). The graphene G phonon shifts with the TPyPs coverage from 1609 to 1616 cm^{-1} . The most evident molecular feature is the one at 1593 cm^{-1} , related to the pyridinic group bending $\delta(\text{pyr})$, the others corresponding to stretching modes of the macrocycle. Pyridinic and graphene modes have been treated differently from the other macrocycle resonances. As it is possible to see in Fig. 3.12A, the graphene feature is wider than the others, and the pyridinic one is sharper: thus, graphene and $\delta(\text{pyr})$ modes widths have been global-fitted on the spectra series, and the other resonances widths have been global-fitted together. In this energy range, positions and phases evolve with coverage, as it is possible to see from the fit parameters in Appendix (Tab. A.1).

Between 0.4–0.5 ML some relative phases change abruptly, suggesting that at 0.4 ML (and lower coverages) the molecules undergo a different geometrical arrangement. This behavior will be more evident in the coverage uptake with annealing spectra, where the heating favors the molecules self-assembly and ordering. Positions and widths have been fitted globally in the range 2970–3150 cm^{-1} , yielding resonant energies of 3010 cm^{-1} , 3053 cm^{-1} and 3063 cm^{-1} . Amplitudes and phases have not been global-fitted, but in this case, phases are compatible with constants. The modes in this energy range are generally assigned to the $\nu(\text{C} - \text{H})$ [148–150].

DEPOSITION AT 500 K By increasing the sample temperature from RT to 500 K during CoTPyP deposition, changes in the SFG peaks' relative intensities have been observed (Fig. 3.13). The analysis has been carried out in analogy to the room temperature experiment.

The identified resonances relative to the macrocycle normal modes do not shift with coverage and show little amplitude changes. On the contrary, the intensity of the $\delta(\text{pyr})$ mode at 1614 cm^{-1} has a much greater amplitude increase, toward the monolayer saturation, much greater with respect to the room temperature experiment: the non-linear

growth of the peak with coverage suggests a rotation of the pyridinic rings out of the surface plane that enhances the out-of-plane dipole moment, detected with SFG.

The variations in amplitude and energy position of some features upon deposition at different temperatures and coverages are likely to relate to different geometrical phases of the porphyrins self-assembled on graphene. According to the previous experiment, there is a sudden variation in the phases from 0.5 ML to 0.67 ML (Fig. 3.13C-F) which could suggest a change in the structural organization of the layer. In both the coverage uptake experiments, the graphene phonon shifts towards higher energies as a function of the molecular coverage, as said for the room temperature uptake: this could be interpreted to be an effect of molecules-graphene interaction.

In conclusion, thermal annealing promotes the hexagonal closed-packed phase, as already seen in STM, which turns out to be the most stable. Hence, for all the experiments in this paper, unless explicitly specified, the MOF has been grown at 500 K.

Thermal stability - CoTPyP

Temperature stability of the CoTPyP/Gr/Ir(111) layer has been investigated in UHV at temperatures ranging from RT up to 600 K. The sample is prepared by CoTPyP physical vapor deposition at room temperature, and, then, SFG spectra were collected after each heating step. The normalized data and spectral deconvolutions are reported in Fig. 3.14.

The fitting parameters have been globally optimized in the full temperature range. The Lorentzian width has been kept the same for all resonances, and the energy locked for each vibrational mode. The best fitting parameters are reported in Appendix (Tab. A.9).

In conclusion, the data suggest that the layer remains almost unaltered below 550 K and then, at higher temperatures, the molecules progressively desorb and degrade, until resonances are no longer identified. This is in agreement with the corresponding XPS data, as discussed in section 3.2.5.

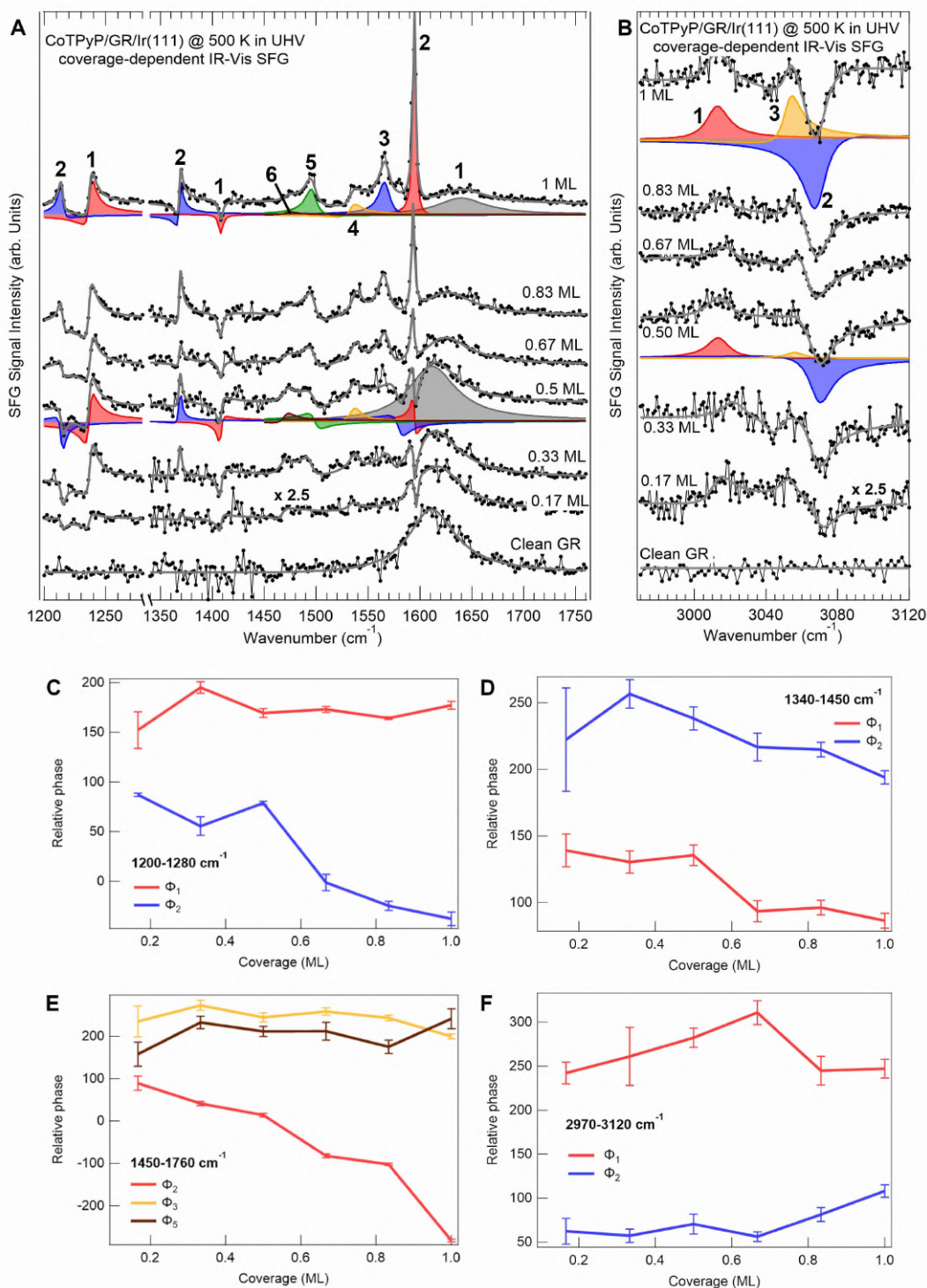


Figure 3.13: A-B) CoTPyP coverage uptake @500 K. Experimental data are plotted with black circles, the best fitting curve with solid grey lines, and the deconvolutions with filled profiles; C-F) Plot of some SFG resonance relative phases as a function of the CoTPyP coverage, corresponding to the spectra shown in the same figure. In particular, Φ_2 in C), Φ_1 in D), and Φ_2 in E) show a sudden variation at about 0.5 ML, probably a sign of a phase change at this coverage. The phases corresponding to the other resonances are constant or undetermined, so they have not been plotted.

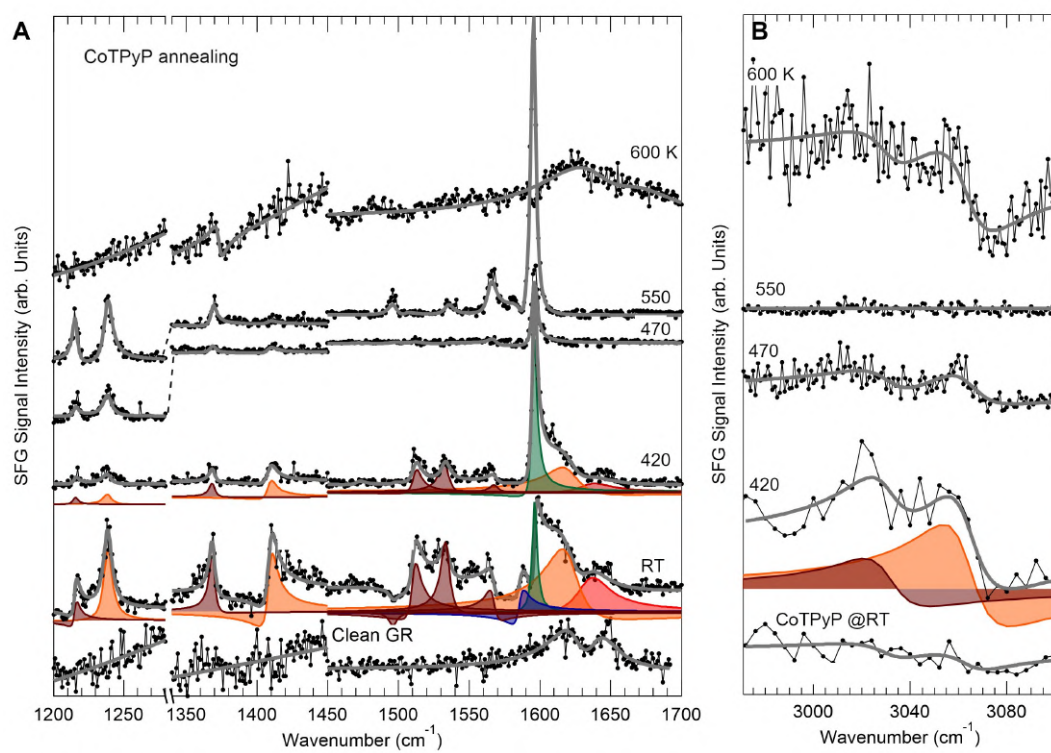


Figure 3.14: A-B) IR-Vis SFG spectra of the CoTPyP layer, heated at the indicated temperatures in the graph. At 600 K, the molecular features are no longer identifiable.

3.3 BI-METALLIC MOF: CoTPyPCo, CoTPyPFe, AND FeTPyPFe

In this section, we will discuss the formation and the characterization of the TPyP-based bi-metal-organic frameworks grown with combinations of iron and cobalt atoms. The metal atoms have been evaporated on the hot sample (500 K), with the molecular layer already prepared, by means of thermal sublimation. From now on, we will adapt the notation $\text{CoTPyP}_y\text{Co}_x$, where y is the absolute CoTPyP coverage, in the CoTPyP unit cell, and x is the absolute coverage of the evaporated cobalt, with the same unit. When not specified, x and/or y have the value of 1. It must be kept in mind that 1 CoTPyP ML corresponds to about 2% ML with respect to the Ir(111) unit cell. The typical metal atom deposition time is of the order of 10 minutes, with the sample-metal source distance of about 10 cm. In analogy with the previous section, the system will be tackled by means of STM, STS, space-averaging spectroscopic techniques, and comparison with *ab initio* DFT simulations carried out within the framework of a collaboration. Additional measurements are also addressed at the end of the section.

3.3.1 STM - CoTPyPCo

Unsaturated CoTPyPCo

The STM images of $\text{CoTPyP}_{0.5}\text{Co}_{0.3}$ are shown in Fig. 3.15, acquired at different bias and scales. The first striking difference after cobalt deposition is the radical change of the molecular arrangement, passing from a hexagonal to a near-square lattice. In particular, when a cobalt atom lands on a CoTPyP island it coordinatively binds, as expected, to four adjacent CoTPyP molecules through their pyridinic residues, with the formation of a square $(\text{CoTPyP})_4\text{Co}$ "block", and, thus, prevailing the lateral direct interactions of the tectons. Interestingly, on a more interacting substrate, such as Au(111), Co and Cr can coordinate to TPyPs in a similar four-fold manner only if the molecules were previously assembled in a near-square lattice (and not if the metal lands on a TPyP close-packed pattern) [136].

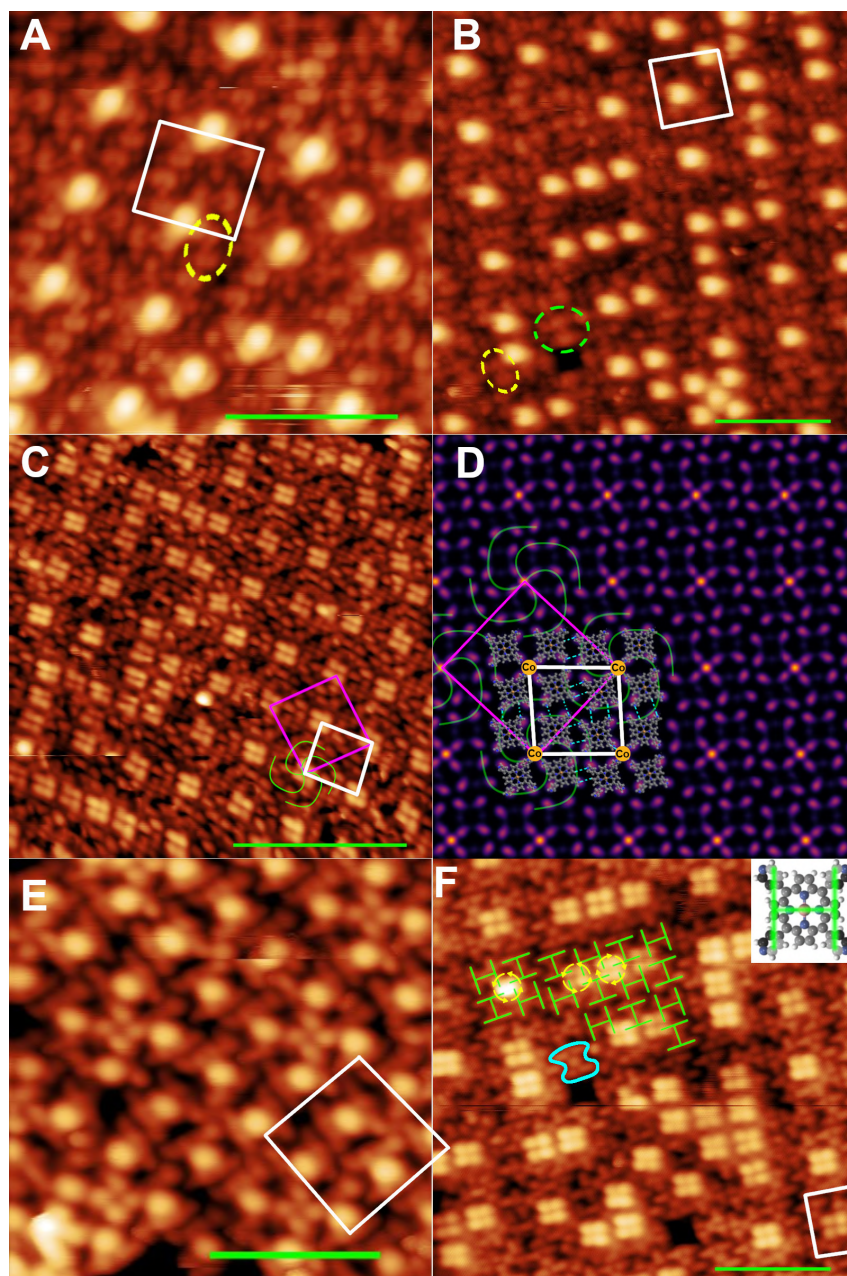


Figure 3.15: STM images @77 K on the unsaturated $\text{CoTPyP}_{0.5}\text{Co}_{0.3}$ layer, taken at different bias and scales. Co-coordinated (non-coordinated) CoTPyP HOMO is highlighted with yellow (cyano) dotted ovals. The (2×2) unit cell is indicated with white lines. **A)** (scale bar=5 nm, $I_{\text{set}} = 100$ pA, $U_{\text{bias}} = -2.5$ V); **B)** (scale bar=5 nm, $I_{\text{set}} = 50$ pA, $U_{\text{bias}} = -2.0$ V); **C)** The $(2\sqrt{2} \times 2\sqrt{2})R45^\circ$ supercell, taking into account the chiral structure indicated with the green "pinwheel", is indicated with purple lines (scale bar=10 nm, $I_{\text{set}} = 100$ pA, $U_{\text{bias}} = +1.4$ V); **D)** Non *ab initio* (see text for explanation) topographic simulation of the (2×2) structure; **E)** (scale bar=4 nm, $I_{\text{set}} = 100$ pA, $U_{\text{bias}} = +2.0$ V); **F)** The H-shape is highlighted with green lines. In the inset, lower pyridinic C atoms are darker. A non-coordinated CoTPyP is enveloped with cyano solid line. Refer to the text for detailed discussion (scale bar=5 nm, $I_{\text{set}} = 60$ pA, $U_{\text{bias}} = +2.5$ V).

The presence of the evaporated cobalt atoms can be spotted both at negative (panels A and B) and positive bias (panels C, E, and F). At -2.5 and -2.0 V, a bright spherical protrusion can be seen on top of the new cobalt. The butterfly-shaped HOMO molecular state, observed also in the CoTPyP pristine layer, is highlighted by dotted ovals in Fig. 3.15A-B). At positive bias, bright four-leaf clover-shaped states appear in correspondence with the new cobalt atoms, similarly to what was observed for Co-TCNPP/Au(111) after deposition of Fe atoms [151]. In panel F, with a bias of -2.5 V, both Co-coordinated and non-coordinated CoTPyPs have been highlighted with green and cyano lines, respectively: the H shape is preserved in both cases, coming from the alternating rotation of the pyridinic dihedral angles, as shown in the inset of panel F (where lower pyridinic carbon atoms are darker). In the same panel, it can be seen how four CoTPyPs coordinate to cobalt forming a cell that can have a chiral clockwise or anticlockwise orientation of the pyridinic groups surrounding the cobalt and, when two cells are adjacent, their orientation is reversed, as indicated by the yellow circular arrows in the same panel. A similar behavior has already been observed for other pyridyl-substituted porphyrins [152]. At the same bias, a spherical charge distribution can be observed at the center of the porphyrin. With a tip change, the latter can be much more pronounced, as in panel E.

Interestingly, looking at panel C of Fig. 3.15, it can be noticed that, at low coverage, the cobalt atoms initially arrange themselves to form a (2×2) structure², as indicated by the white unit cell in the figure. Carefully looking at the same image, it can be seen that the molecular ordering surrounding the new Co centers is such that the whole molecular domain has a specific chirality: to guide the eye, a green pinwheel is drawn, following the position and the orientation of the pyridinic terminations. If we consider this superstructure, which contains 16 CoTPyPs for each “pinwheel”, we can describe the lattice with a near-square $(2\sqrt{2} \times 2\sqrt{2})R45^\circ$ unit cell with basis.

Since *ab initio* DFT simulations of the (2×2) unsaturated structure is currently computationally unaffordable, non *ab initio* tomographic map has been simulated starting from the relaxed CoTPyP geometry of the fully saturated CoTPyPCo layer, and matching by hand positions and rotational angles according to the STM map. The resulting image (3.15D) shows that this supercell has a double nature: 1) the alternating rotation of the pyridyl dihedral angles, which gives also the H-shape to the porphyrin; 2) if we think of four CoTPyPs bonded to one Co as a single square block, then the four blocks are all rigidly rotated by about 7° anticlockwise: this favors lateral attraction mediated by N-H bonding, highlighted with cyano dotted lines in panel D. It is possible, indeed, that the formation of the (2×2) structure could be driven by this lateral bonding network; in this perspective, molecular dynamics simulations could shed light on the MOF growth mechanism. On the other hand, intuition would suggest that the (1×1) pattern at saturation ($x = 1$) would be the most favourable one, since it should involve the least amount of CoTPyP turns: in this view, the stability of the (2×2) structure must be explained by some other effect

² The (1×1) structure refers to CoTPyPCo saturation, where the stoichiometry between CoTPyP and Co atoms is 1:1.

rather than simple electrostatic attraction, such, for example, magnetic polarization of the macrocycle/pyridyl residues, overall electronic configuration and stability, or substrate mediated-interaction. By looking at the CoTPyP_{0.5}Co_{0.3} layer on a larger scale, such as in Fig. 3.16, it is clear that the $(2\sqrt{2} \times 2\sqrt{2})R45^\circ$ lattice is dominant, followed by a “crossword-like” pattern where the new cobalt atoms are embedded into the MOF in single rows and adjacent sites and, very rarely, the diagonal $(\sqrt{2} \times \sqrt{2})R45^\circ$ arrangement.

Increasing the cobalt coverage, the “crossword-like” pattern becomes the most abundant (Fig. 3.16), and saturation is soon achieved at the borders of the MOF islands. This could be partially due to the cobalt atoms coming from the graphene sheet, which are highly mobile at the growth temperature of 500 K [153], or also to the lower CoTPyP coordination number, implying lower barriers and lower kinetic hindrance for molecular rearrangements. The last reason is particularly evident due to the presence of many vacancy defects in the MOF lattice. Indeed, it is probable that, for an optimal MOF crystalline quality, the molecules and the cobalt atoms should be evaporated at the same time and the same (sufficiently low) rate. When fully saturated, some small islands (~ 20 nm wide) even detach completely from their main domain and migrate on graphene, a further indication of the weak coupling with the substrate and the structural integrity of the saturated MOF. In the inset of Fig. 3.16A, the contrast is enhanced in order to show the cobalt cluster (their height is about 0.2 nm) on graphene formed by the extra cobalt atoms that were not able to be loaded into the MOF. The histogram of the azimuthal angles of the CoTPyPCo network with respect to the graphene moiré shows a broad variety of values (see Fig. A.12 in Appendix); thus, the absence of a preferential orientation is a sign of the weak interaction between the MOF and the substrate.

It is worth mentioning that, in the literature, Ni, Fe, Co, and Cr atoms were found to coordinate TPyPs in a similar four-fold pyridyl junction, but often with the presence of a vertical metal dimer and/or different tilting of the pyridinic residues [136, 152, 154]: though, in all cases, the different types of junctions can be easily identified by STM visual inspection. In our case, we find a homogeneous appearance of the coordinative site, suggesting the presence of only a single cobalt atom in the four-fold TPyP-junction.

Saturated CoTPyPCo

The STM images of a CoTPyPCo saturated island are shown in Fig. 3.17. Taking into account the alternating orientation of the pyridinic group, highlighted by the yellow circular arrows, the lattice is described by lattice vectors with magnitude 2.84 and 2.02 nm and a 45 degree angle between them (white lines in the figure). The STM appearance follows what already said for the unsaturated layer: at positive biases (panel A, B, and D) the four-leaf clover-shaped orbital is visible on top of the evaporated cobalt atom. At 1.2 V, the alternating rotation of such orbital in a chessboard pattern is visible (green dotted lines in panel B). Besides, at this bias, the tip is sufficiently close to detect also the

spherical charge distributed on the Co in the macrocycle, which disappears at a higher bias (panel D). At -2.0 V, both cobalt species appear as spherical blobs.

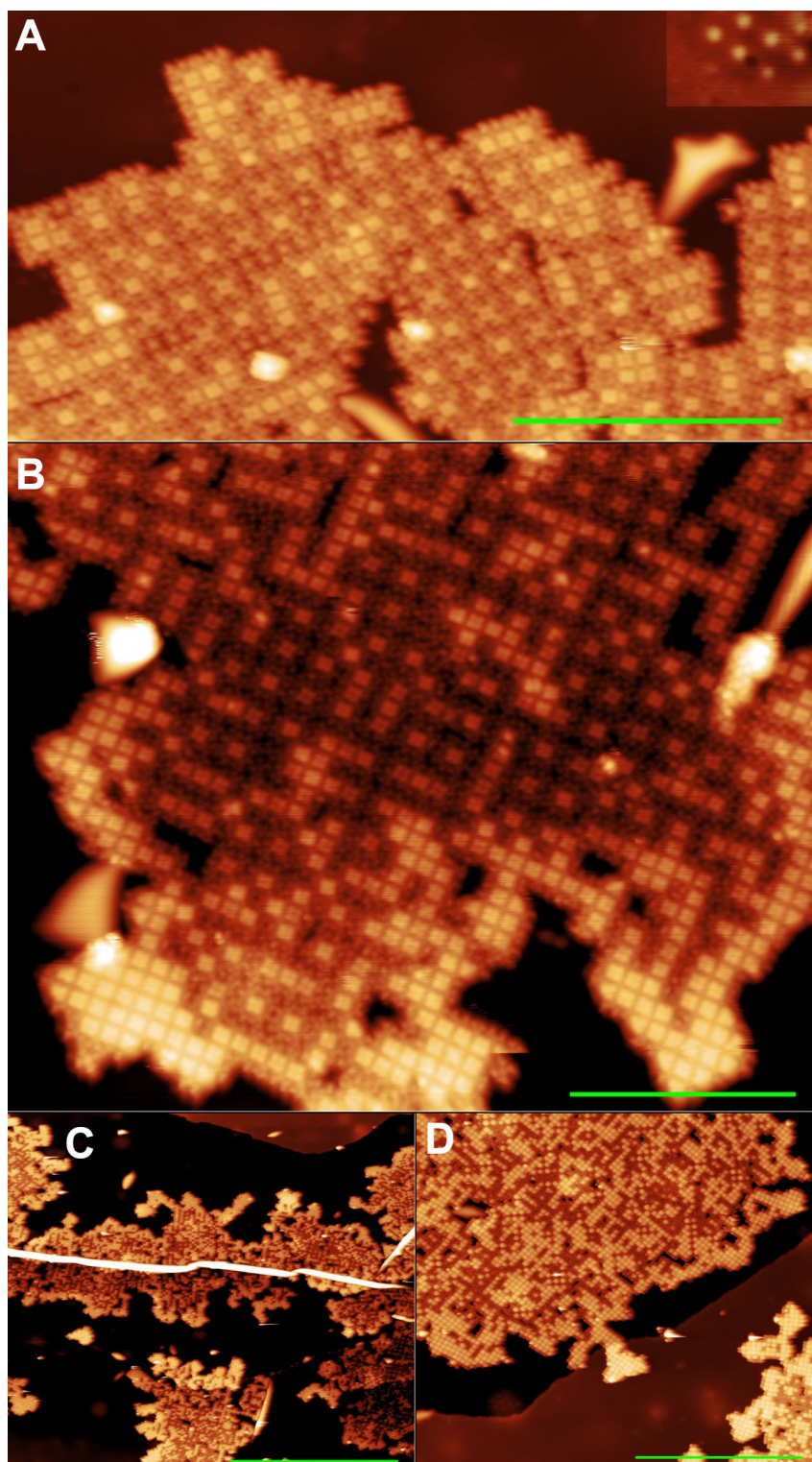


Figure 3.16: STM images @77 K on CoTPyP_{0.5}Co_x for: **A)** $x = 0.3$ (scale bar = 20 nm, $I_{set} = 0.1$ nA, $U_{bias} = +2.0$ V), **B)** $x = 0.8$ (scale bar = 5 nm, $I_{set} = 0.05$ nA, $U_{bias} = +2.2$ V), **C)** $x = 1.2$ (scale bar = 100 nm, $I_{set} = 0.05$ nA, $U_{bias} = +2.2$ V), and **D)** $x = 2.0$. At this coverage, we measure an average $45 \pm 7\%$ of y/x saturation ratio (Co_xTPyPCo_y) in the bulk of the island, i.e. away from the fully saturated borders (scale bar = 50 nm, $I_{set} = 0.05$ nA, $U_{bias} = +2.2$ V). In the inset of panel A, the contrast is enhanced to show cobalt clusters on graphene.

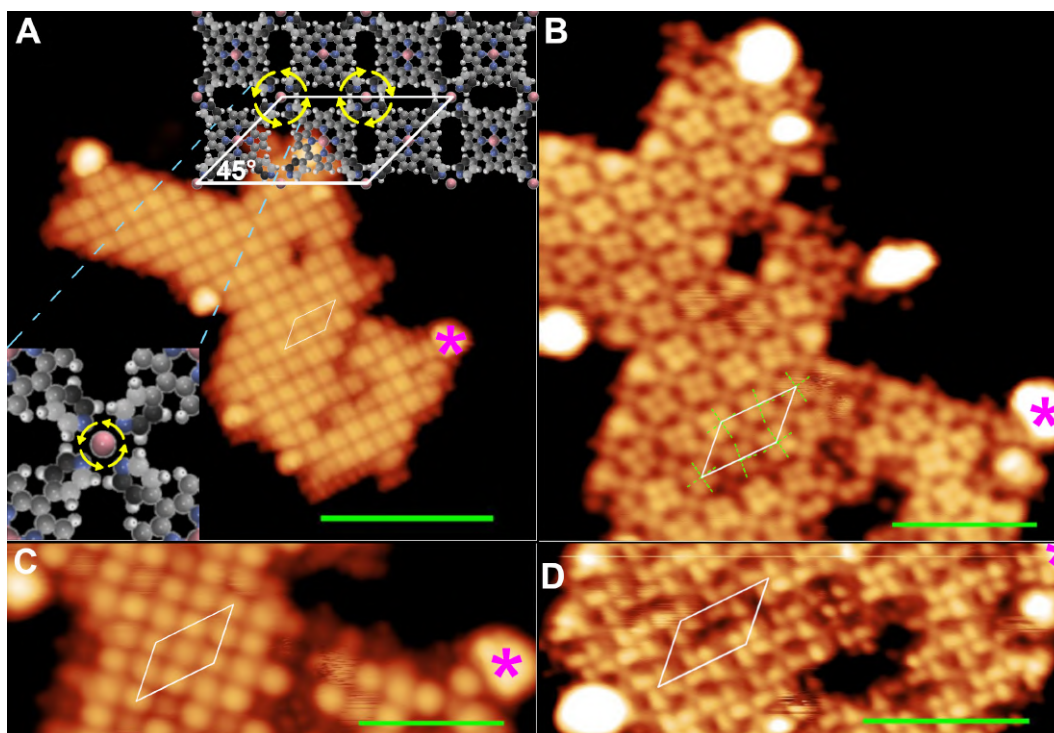


Figure 3.17: STM images @77 K on a saturated CoTPyPCo island at different scales and bias. The $2.84 \times 2.02 \text{ nm}^2$ unit cell is indicated (white line), and the purple asterisk indicates the position of the same physical spot on the sample. **A)** The alternating orientation of the pyridinic terminations are indicated with the yellow circular arrows (scale bar = 10 nm, $I_{set} = 50 \text{ pA}$, $U_{bias} = +2.2 \text{ V}$), **B)** (scale bar = 5 nm, $I_{set} = 50 \text{ pA}$, $U_{bias} = +1.2 \text{ V}$), **C)** (scale bar = 5 nm, $I_{set} = 50 \text{ nA}$, $U_{bias} = -2.0 \text{ V}$), and **D)** (scale bar = 5 nm, $I_{set} = 50 \text{ pA}$, $U_{bias} = +1.4 \text{ V}$).

3.3.2 STS - CoTPyPCo

Unsaturated CoTPyPCo

Fig. 3.18A shows STS spectra collected on a selection of the 25 possible $xLyD$ ($x, y \in [0, 4]$) unsaturated configurations (read the figure caption for the notation). In a first approximation, HOMO and LUMO states rigidly shift as a function of the particular structure. For example, in the 0L0D, 0L1D, and 0L2D the HOMO linearly shifts by about -0.4 , -0.3 , and -0.2 eV (with the 4L4D taken as a reference) while an abrupt change occurs in 0L4D, with a resulting energy shift of more than -0.6 eV. Additionally, the position in energy of the HOMO in the saturated layer (4L4D), which has its maximum intensity at about -1.0 V, is different from any other configuration. In general, we can state that there is a long-range influence between the different CoTPyPCo sites, which depends on the specific geometry. In a future outlook, systematic measurements with the use of Spin-Resolved Scanning Tunneling Microscopy could shed more light on the mechanism of such interactions.

Saturated CoTPyPCo

In analogy with the experiment carried out for the CoTPyP/Gr/Ir(111), Scanning Tunneling Spectra and Maps have been acquired in the range between -2 and $+2$ V (probing occupied and unoccupied states, respectively) to characterize the electronic structure of the fully saturated CoTPyPCo/Gr/Ir(111) heterostack, as reported in Fig. 3.19. In Figure 3.20, the simultaneously acquired current maps are also shown. In particular, the images have been acquired at the center of the Co-saturated island in Fig. 3.17. The STS spectra and STS maps have been acquired with two different tip conditions, due to tip instability at liquid nitrogen temperature. Despite some small discrepancies between STS spectra and STS maps, the main picture is coherent for both techniques.

STS curves have been acquired in the -2.0 - $+2.0$ V energy range on pyridinic cobalt (CoTPyPCo, blue curves in Fig. 3.19) and on the cobalt atom in the macrocycle (CoTPyPCo, red curves). It can be noticed that the two cobalt species show very different features, as already guessed by the STM images previously discussed.

- The CoTPyPCo curve is already different from the one previously observed for the CoTPyP layer, which is characterized by a large gap and distinct features at ~ -1.4 and $\sim +1.7$ V, whereas in the bimetallic network, the HOMO-LUMO gap is about 1 eV. Nevertheless, it must be kept in mind that the tip finite lateral resolution causes a signal leakage from the surrounding LDOS, especially if the signal is weak, or the tip-sample distance is large, such as in the case of CoTPyPCo, where the maximum intensity is 4 (20) times lower with respect to the maximum intensity in LUMO (HOMO) CoTPyP LDOS (Fig. 3.4 and 3.5). At any rate, the feature at $\sim +0.4$ V is definitively a new feature, absent in the CoTPyP case.

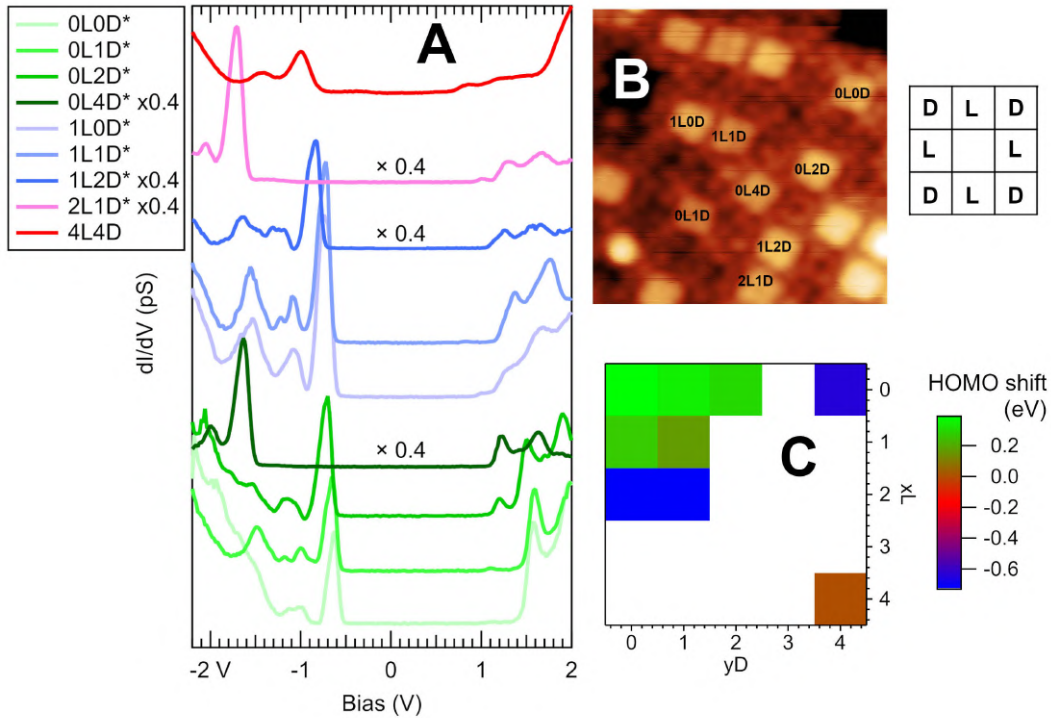


Figure 3.18: *A) STS spectra were collected on some different CoTPyPCo structures of the unsaturated layer, with the tip located on CoTPyPCo. As indicated in the lateral diagram, the notation $xLyD$ refers to the 25 possible configurations surrounding a single $(\text{CoTPyP})_4\text{Co}$ block, that in panel **B** appears as a single bright square (scale bar=9.6 nm, $I_{\text{set}} = 50$ pA, $U_{\text{bias}} = +2.0$ V); xL notation corresponds to the number of lateral "squares", sharing one edge, and with $0 \leq x \leq 4$, while yD corresponds to the number of diagonal "squares", sharing one vertex, and with $0 \leq y \leq 4$; **C)** False color 2D plot of the HOMO shift of the investigated structure, with respect to the 4L4D system, as a function of xL and yD . The spectra labeled with an asterisk (legend of panel **A**) have been acquired with the same tip state and on the same physical region of the sample.*

- The CoTPyPCo curve, instead, reveals a widespread LDOS with an onset at about 0.6 V, dramatically increasing in intensity at about +1.7 V. Below Fermi, an intense feature appears at -1.0 V, with some modulations at lower energies.

The analysis of our STS maps gives more information on the nature of the states just described:

- In the LUMO energy range, we notice the presence of two distinct shapes of charge distributions: a spherical distribution is observed on top of the CoTPyPCo up to 0.5 V; at higher energy, instead, the four-leaf clover shape, observed also in STM images (see the previous section), is centered on CoTPyPCo and extends up to +2.0 V. A

tenfold increase of the intensity, related to such state, is recorded by increasing the tip-sample voltage from 1.4 to 1.6 V. Indeed, at higher bias, the manual retraction of the tip was needed in order not to saturate the lock-in reading. The corresponding current maps in Figure 3.20 perfectly match the dI/dV data: close to Fermi, a spherical shape on CoTPyPCo is visible; from +0.6 to +1.6 V, four-leaf clover states also appear; at +1.8 and +2.0 V, only the states on CoTPyPFe remain, because of their much higher intensity, and because of tip retraction.

- In the HOMO energy range, instead, a weak signal is detected from Fermi down to -0.4 V, showing spherical electron distribution localized on top of both cobalt atoms. At -0.1 V, with the tip being sufficiently close to the MOF, also the pyridyl groups morphology can be revealed. In the range between -0.8 and -1.0 V, in agreement with STS curves, a bright protrusion is observed only on top of the CoTPyPFe, persisting down to -2.0 V. Sometimes, in this range, the lock-in reads negative values, as already noticed in the CoTPyP case, probably due to change of tunneling barrier as a function of the voltage applied, as discussed in section 3.2.3. Also in this case, the parallel current maps carry similar information, with a signal of the order of just few pA from Fermi down to -0.6 V, and then increasing from 20 to 300 pA from -0.8 down to -2.0 V, coherently with the dI/dV spectra.

Moreover, it must be kept in mind that, according to our DFT calculations, the CoTPyPFe is about 0.2 \AA higher than CoTPyPCo: this means that the intensity ratio of the two cobalt species states, observed in the STS map, must be always treated *cum grano salis* since electron tunneling spectroscopy is extremely sensitive to such tiny topographic variations. This means that, for example at -1.4 and -2.0 V, the dim signal at the CoTPyP center, about six times with respect to the one observed on the CoTPyPFe, must be in reality more intense. This would partially explain also some relative intensity differences among the same atomic species, for example much evident at -0.8 V of both Fig. 3.19 and 3.20. A final remark is the absence of the intense butterfly-shaped state, localized on the tilted macrocyclic pyrroles, previously associated with CoTPyP HOMO, and sometimes visible in the unsaturated CoTPyPCo (see Fig. 3.15A-B).

3.3.3 DFT - CoTPyPFe

Analogously to the monometallic case, *ab initio* DFT simulations have been carried out also for CoTPyPFe to have a deeper insight into the MOF electronic structure, and corroborate the data presented so far [133]. For what concerns the omission of the Ir atoms, the same considerations that we did for the previous case (see section 3.2.4) are still valid. In Fig. 3.21, STS and STM images have been simulated starting from the relaxed geometry, within the unit simulation cell indicated in the figure (green lines). Already at first glance, by looking at the PDOS for the two cobalt species, we can confirm the

different chemical identity, due to the different charge redistribution with the different surrounding chemical environments. In more detail:

- In the **HOMO energy range**, we observe a -0.2 eV shift of the **CoTPyPCo** states, and the presence of new features at -0.8 and -2.0 eV coming from the pyridinic cobalt. In particular, the intense peak at -0.8 eV gives origin to the spherical shape, localized on the **CoTPyPCo**, visible in Fig. 3.21: it comes from the hybridization of the vertical Co $3d_{zx}$ and $3d_{zy}$, the planar $3d_{xy}$ and $3d_{x^2-y^2}$, with the pyridinic states which are responsible of the chiral appearance, predicted also by DFT, which we previously discussed in the corresponding STM images. A closer inspection reveals a "hole" right at the center of the cobalt species, obviously coming from the nature of the aforementioned orbitals, and that could not be resolved experimentally.
- In the **LUMO energy range**, we observe the same -0.2 eV shift of the **CoTPyPCo**, together with the presence of a very broad band from $+1.0$ to $+2.0$ eV, attributable to **CoTPyPCo**, and with the four-clover leaf appearance experimentally observed. The latter, in particular, originates from the contribution of the $3d_{z^2}$

In general, we have a remarkable agreement between theory and experiment. The only discrepancy arises from the rigid shift of the **CoTPyPCo** states, upon Co atom evaporation, which in the experiment is larger (of the order of -0.7 eV), while the DFT predicts only -0.2 eV. The information is pretty robust since STS, UPS (section 3.4.1), and ARPES (section 3.4.2) all converge to the same conclusion. Thus, we consider this discrepancy a DFT limit.

Figure 3.22 reports the $4s$ and $3d$ orbitals electron occupancy in the two cobalt species. The macrocyclic Co shows almost no change, between **CoTPyP** and **CoTPyPCo**, as already suggested by the simulated PDOS, where only a rigid shift of -0.2 eV is observed. The **CoTPyPCo**, instead, shows a different occupancy of the $3d_{xy}$ orbital, with a larger spin polarization with respect to the **CoTPyPCo** counterpart:³ this reflects on different values for the oxidation state, considering only electrons not involved in chemical bonding (thus, with an occupancy larger than 50%). For the same reason, we get a magnetization of $\sim 1\mu_B$ for the macrocyclic Co, and $\sim 2\mu_B$ for the pyridinic one.

³ The $3d_{xy}$ computed for **CoTPyPCo** and the computed $3d_{x^2-y^2}$ for **CoTPyPCo** refer to the same physical orbital, because of the local 45° frame of reference between the two species.

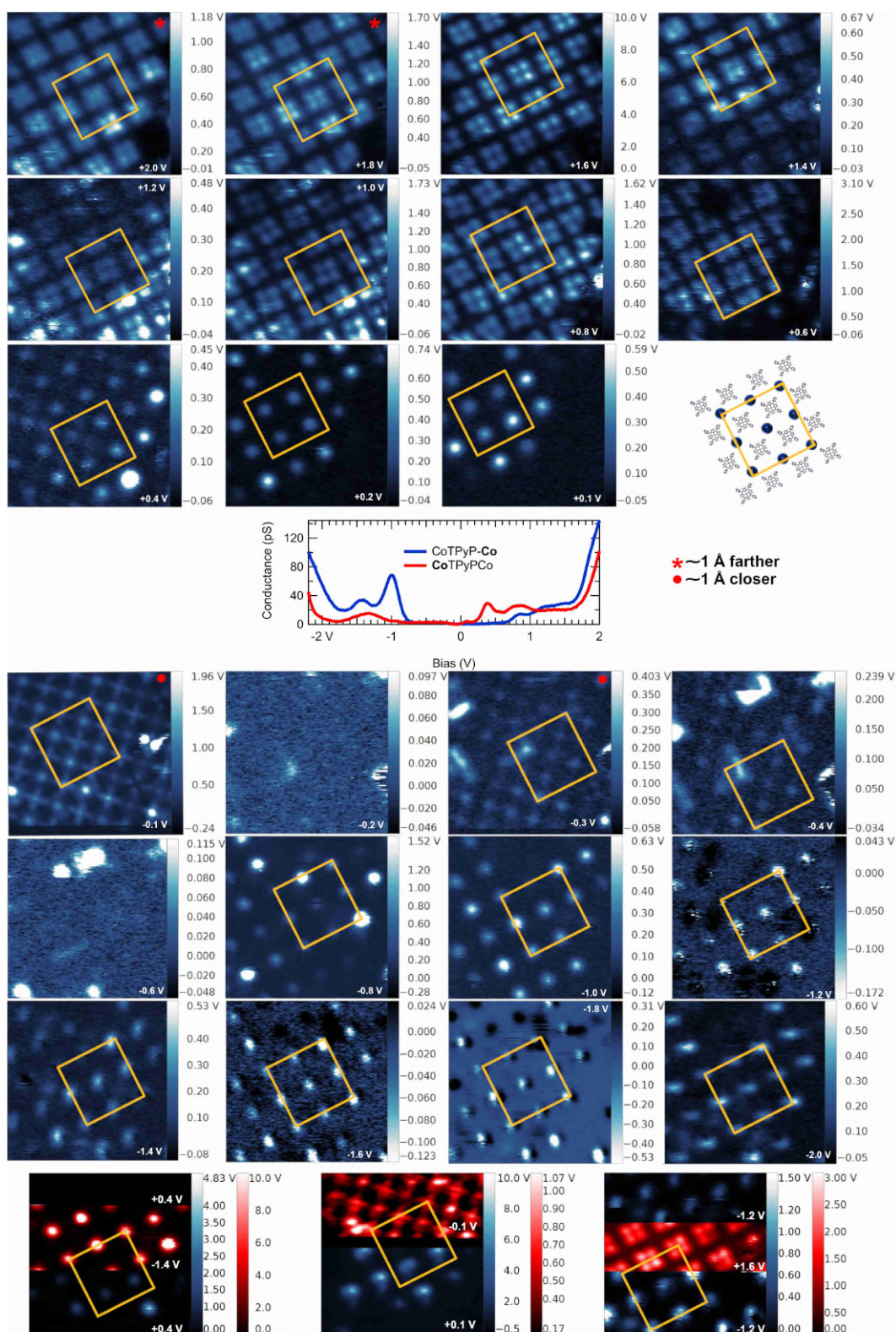


Figure 3.19: STS spectrum, dI/dV maps of the fully saturated CoTPyPCo/Gr/Ir(111) monolayer at 77 K. The STS maps are acquired with a starting setpoint of 2.0 V/50 pA on top of the pyridinic cobalt. Blue STS spectra are acquired on top of the external Co, while red STS spectra are acquired at the macrocycle center. Red asterisk and circle indicates images taken with the tip 1 Å farther or closer with respect to the initial setpoint. Conventional unit cell is shown with yellow lines. Map size: $6 \times 6 \text{ nm}^2$

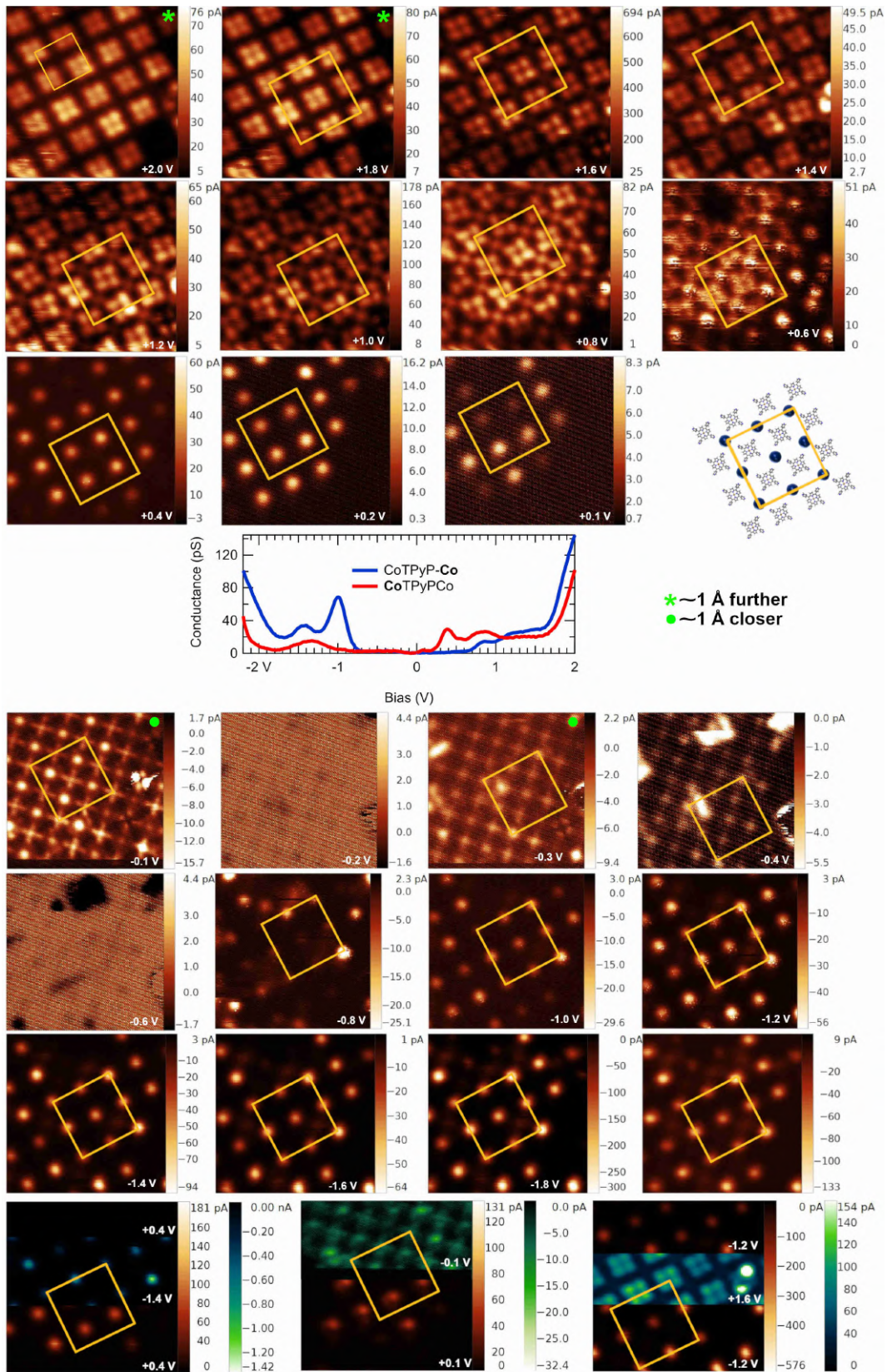


Figure 3.20: Current output simultaneously acquired with the corresponding dI/dV maps reported in Fig. 3.19. The STS curves are the same of Fig. 3.19.

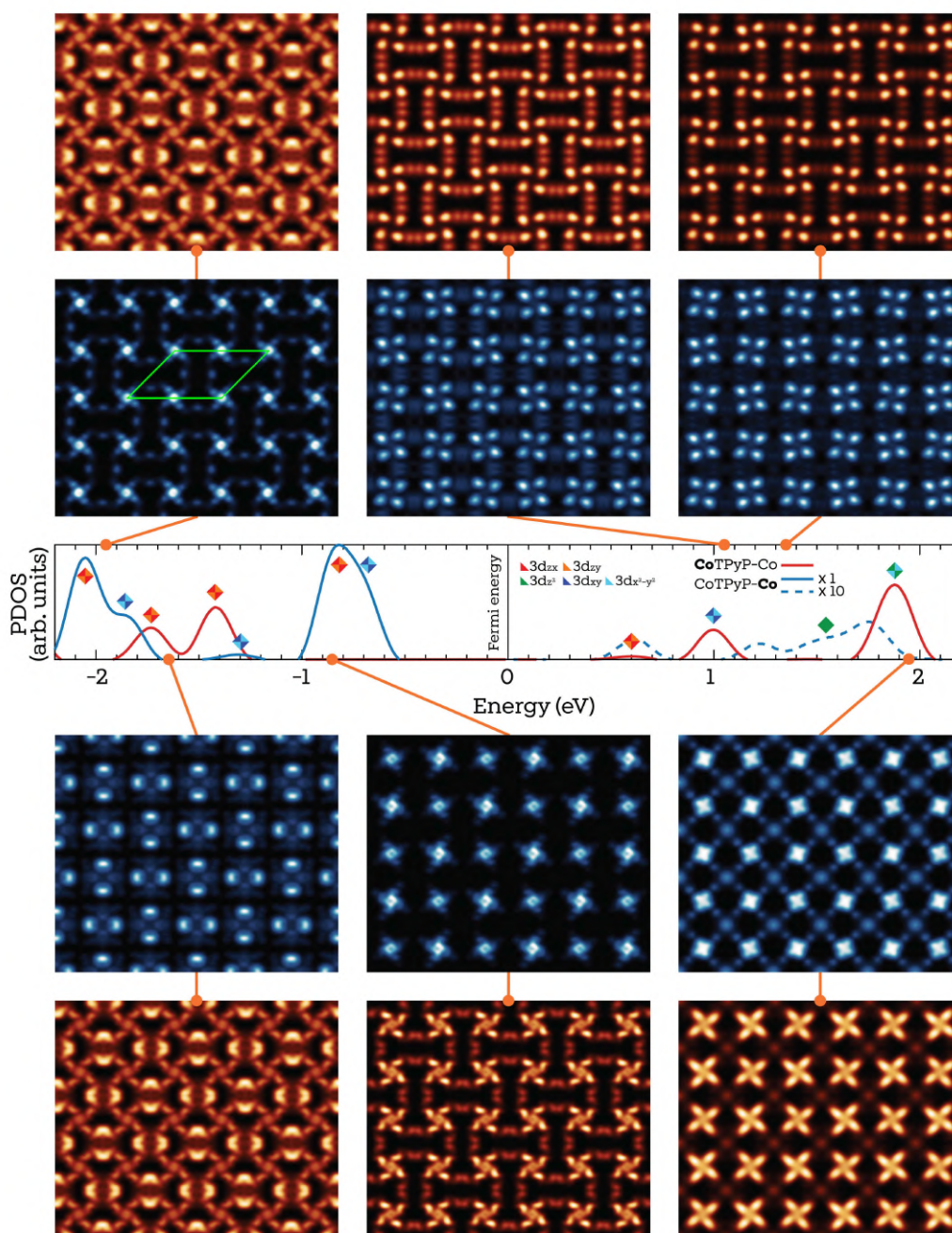


Figure 3.21: *Ab initio* DFT simulations of the STS (blue palette) and STM images (red palette) of the CoTPyPCo/Gr layer, with the corresponding DOS curves, projected on the 3d and 4s states of the two different species of Co atoms. The Fermi level is set in correspondence of the Dirac cone. The images has been obtained with the Tersoff Hamann approximation, at a constant height between 2.5 and 3.0 Å, with an integration interval of 0.1 eV for the STS maps.

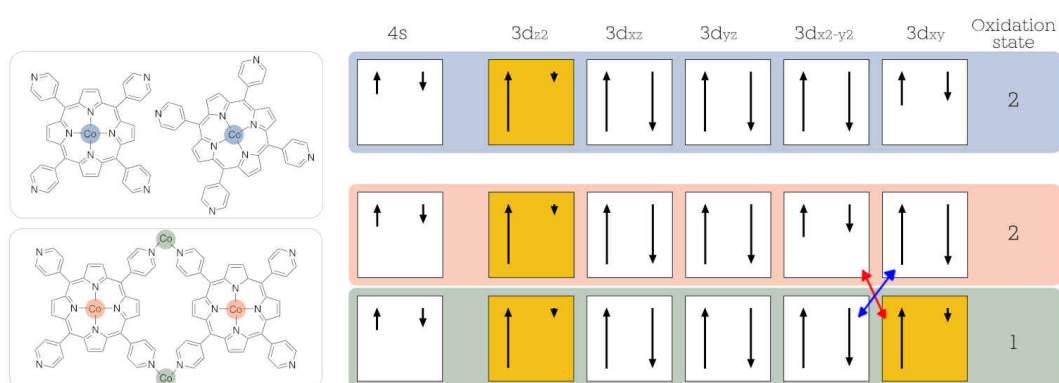


Figure 3.22: *Ab initio* DFT gives insight in the electronic occupancy of the cobalt species in the CoTPyP and CoTPyPCo MOFs. The length of the black arrows indicates the electron spin-resolved occupancy. For oxidation state calculation, an electron is counted if its occupancy is greater than 50%. The red and blue arrows indicate the physical equivalence of the $3d_{x^2-y^2}$ and $3d_{xy}$ orbital in CoTPyPCo and CoTPyP, respectively (and vice-versa), simply due to the local 45° rotation, around the out-of-plane axis, of the reference frame for the two cobalt species.

3.3.4 XPS - CoTPyPCo, CoTPyPFe, and FeTPyPFe

The formation of the TPyP-based bi-metallic frameworks grown on Gr/Ir(111) reflects important changes in the photoemission of nitrogen, iron, and cobalt core levels that will be described in this section. The N 1s core level shows shifts of the order of 0.5 eV, and a radical change of the shake-up spectral weight. The analysis of the Co and Fe 2p_{3/2} core levels indicates firstly that the influence of the external metal on the one inside the macrocycle can be detected in terms of BE shift and multiplet splitting structure remodulation and, secondly, that the two metals are chemically non-equivalent in the case of the homo-metallic layers.

N 1s

Coordination of pyridinic N with Fe atoms yields relevant changes in the N 1s core level, as shown in Fig. 3.7C-D.

The fitting strategy consists in starting from the parameters of the corresponding mono-metallic layer and releasing the amplitudes, the Gaussian widths, and the binding energies of the three peaks. The two DS, attributed to the iminic and the pyridinic N atoms, share the same amplitude and Gaussian width.

According to our interpretation, the DS attributed to pyridinic N undergoes a chemical shift of +330 (+550) meV in the case of CoTPyPFe (FeTPyPFe), due to direct binding to elemental iron. A minor chemical shift is observed for the DS corresponding to the iminic N atoms species, +210 meV for CoTPyPFe and +470 meV for FeTPyPFe, indicating that also the electronic configuration of the macrocycle is partially affected in the metal-organic framework. The other possible interpretation, in which the pyridinic component does not shift and the iminic component undergoes a shift of ~ 1 eV, is unlikely since we expect the pyridinic species to undergo the major shift. The Gaussian width slightly changes upon metalation, showing an inverse trend between CoTPyPFe (decreasing from 0.74 ± 0.01 to 0.62 ± 0.02 eV) and FeTPyPFe (increasing from 0.61 ± 0.02 to 0.74 ± 0.04 eV).

Further evidence of the Fe-N interaction resides in the remarkable growth of the non-adiabatic spectral weight, given by the broad shake-up resonance, whose amplitude almost triplicates in CoTPyPFe (from 0.21 ± 0.01 to 0.53 ± 0.02) and quintuplicates in FeTPyPFe (from 0.06 ± 0.01 to 0.30 ± 0.04): this probably relates to the formation of new states close to the pyridinic N atoms, which allow novel relaxation channels for the non-adiabatic shake-up process [155].

In addition, DFT calculations predict a relative core level shift of $\Delta(N\ 1s)_{CLS} = 0.28$ eV between the pyridinic and iminic N species in CoTPyP, which increases to 0.82 eV in the case of CoTPyPFe, in agreement with our experimental data and interpretation (the relative positions of the two species are also correct) [133].

Co 2p_{3/2}

The consequence of the iron deposition on the Co 2p_{3/2} core level is shown in Fig. 3.9A: the resonances associated with the MS shift towards higher binding energies, specifically +0.3 eV for the DS at 780.1 eV, and +0.6 eV for the Gaussian component at 782.2 eV; instead, due to its different origin, the Gunnarsson and Schönhammer resonance stays at the same BE of 779.4 eV, while its spectral weight diminishes by 30%, possibly indicating a partial decoupling from the substrate due to the suppression of the electron transfer [69]. The MS described by the Gaussian component at 783 eV undergoes a broadening from 1.7 to 2.2 eV, witnessing a remodulation of the MS amplitudes, possibly associated with a change of the electronic configuration in the cobalt valence states.

For the CoTPyPCo monolayer, the analysis is less straightforward because of the coexistence of both cobalt species, together with the absence of a reference spectrum where only the cobalt bonded to the pyridinic terminations is present. The experimental data, together with the best fitting curve and deconvolution, is shown in Fig. 3.9A (bottom): the experimental curve is well deconvoluted by using three DS at 781.3, 778.8, and 786.3 eV. We attribute the DS at lower BE to the evaporated cobalt, since a BE close to ~ 779 eV is usually attributed to Co(I) [47, 51, 156], in agreement with the oxidation number predicted by our DFT calculations. In this picture, the DS at 781.3 eV would be associated with the cobalt inside the macrocycle that, shifting by about ~ +1 eV, would move from a +2 towards a +3 oxidation state. At higher BE, the large component extending in the range from 784 to 788 eV, absent in all the other treated systems, is attributed to a shake-up resonance. As a first approximation, the three peaks have been fitted with the same Lorentzian width, yielding a value of 1.2 ± 0.7 eV: the large error is due to the poor signal-to-noise ratio for this spectrum, yielding crosstalk with Gaussian enveloping.

Fe 2p_{3/2}

Given the complexity of the iron 2p lineshape (Fig. 3.9B), we adopted a building-block model where the Fe 2p_{3/2} profile in FeTPyPFe is a linear combination of the one in FeTPyP, where only the iron in the macrocycle is present, and the one in CoTPyPFe, where only the iron bonded to the pyridinic terminations is present. This model assumes a complete decoupling between the metal atoms inside and outside the macrocycle, which we know to be incorrect in light of the above analysis on the Co 2p_{3/2} core level. Nevertheless, as we shall see, the large spectral difference between the Fe 2p_{3/2} profiles in FeTPyP and CoTPyPFe encouraged us to use in any case this model as a first approximation.

In CoTPyPFe (Fig. 3.9B), the Fe 2p_{3/2} profile is described by two DS centered at 711.4 and 714.3 eV, associated with the MS structure, and a third one at 708.2 eV, associated with the GS screening charge, as in the cobalt core level analysis. As said, the FeTPyPFe Fe 2p_{3/2} envelope is fitted by using a linear combination, with equal weight, of the fitting curves found for FeTPyP and CoTPyPFe, as highlighted in Fig. 3.9B (bottom) by means of different colors: the pretty satisfactory result is a confirmation of the different chemical

identities between the Fe embedded in the macrocycle and the one linked to the pyridinic terminations.

3.3.5 NEXAFS - CoTPyPFe, and FeTPyPFe

N 1s

Following the Fe evaporation, the N 1s edge NEXAFS spectra show the most dramatic difference in 398–400 eV energy region, as can be seen for the CoTPyPFe (Fig. 3.10E-F) and FeTPyPFe (Fig. 3.10E-F) monolayers: indeed, we can now resolve, in both polarizations and particularly well in FeTPyPFe, the presence of two $1s \rightarrow \pi^*$ resonances at 398.66 (398.56) eV and 399.29 (399.26) eV in CoTPyPFe (FeTPyPFe) absorption spectra. We shall ascribe the first to the iminic N π^* transition and the second to the pyridinic N π^* transitions, since the second undergoes the major shift of almost +0.3 eV, due to direct linking of pyridinic nitrogen atoms to the additional iron. On the contrary, the iminic species exhibits an irrelevant shift of only 0.02 eV in both systems. The discussed energy positions are summarized in Tab. 3.1. On the other hand, the other π^* and σ^* transitions, whose parameters were relaxed as well in the bimetallic systems, do not show relevant differences, both in energy and dichroism, meaning that the internal geometry of the porphyrins is not heavily affected by the iron metalation. The fitting parameters of the ionization potential and the Fermi level have been fixed to the pre-deposition values.

	CoTPyP	CoTPyPFe	FeTPyP	FeTPyPFe
Iminic	398.64	398.66	398.58	398.65
Pyridinic	399.04	399.29	398.98	399.26

Table 3.1: Energy position (in eV) of π^* resonances, deconvoluted from the NEXAFS N 1s absorption edge spectra, attributed to the iminic and the pyridinic nitrogen species.

3.3.6 SFG - CoTPyPCo

So far, we've seen that when Co atoms are evaporated on the CoTPyP/Gr/Ir(111) monolayer, they bind to the nitrogen atoms of the pyridinic groups, as confirmed by STM, XPS, and NEXAFS experiments, to form a covalent-bonded MOF associated with a deep change in electronic structures. This difference could be appreciated also by looking at the IR-Vis SFG spectra of the CoTPyP monolayer, with respect to CoTPyPCo, as reported in Fig. 3.23. The first, striking difference is the huge increase of the non-resonant background, by a factor of ~ 50 (at 1700 cm^{-1}): the easiest explanation is the reduction of the energy gap, from ~ 2.3 to ~ 1.5 eV: indeed, considering the ~ 1 eV intrinsic width of the HOMO and

CoTPyP	CoTPyPCo
1214 ± 1	1207 ± 3
1237 ± 1	1250 ± 9
1369 ± 1	1368 ± 1
1408 ± 1	1415 ± 1
1474 ± 8	
1496 ± 1	1512 ± 2
1535 ± 2	1557 ± 2
1567 ± 1	1568 ± 1
1595 ± 1	1601 ± 1
1639 ± 3	1645 ± 8
3012 ± 4	
3053 ± 4	2998 ± 2
3069 ± 2	3077 ± 1

Table 3.2: Energy of the CoTPyP and CoTPyPCo normal modes detected by IR-Vis SFG (in wavenumber - cm^{-1} - units).

LUMO molecular states observed in this chapter with multiple techniques, and considering that our Vis photon has an energy of ~ 2.3 eV, we expect a higher joint density of states (JDOS) with the reduction of the energy gap.

Secondly, with cobalt loading into the MOF, the many molecular resonances change positions and phases, indicating that Co ligation affects not only locally the pyridinic termination, but the entire macrocycle. The comparison between vibrational energies of CoTPyP and CoTPyP-Co is summarized in Tab. 3.2. In particular, it is worth to notice that the mode associated with the asymmetric bending of the pyridinic groups at 1595 cm^{-1} , directly involved in the ligation with Co, undergoes a blue-shift of about 6 cm^{-1} .

Thirdly, in literature, the typical assumption is that of a constant non-resonant background, very weakly depending on the the IR photon excitation energy. However, in our case, a linear term had to be introduced in order to reproduce the experimental data, according to the following equation:

$$I_{norm}(\omega_{IR}) = \left| A_{NR}^{(0)} + A_{NR}^{(1)}(\omega_{IR} - \omega_0) + \sum_n \frac{A_n e^{i\Delta\phi_n}}{\omega_{IR} - \omega_n + i\Gamma_n} \right|^2, \quad (3.1)$$

where ω_0 is arbitrarily chosen in order to roughly match the center of the different IR energy windows corresponding to each SFG spectrum sub-range, and its introduction is purely based on practical reasons (minimization of the crosstalk between $A_{NR}^{(0)}$ and $A_{NR}^{(1)}$).

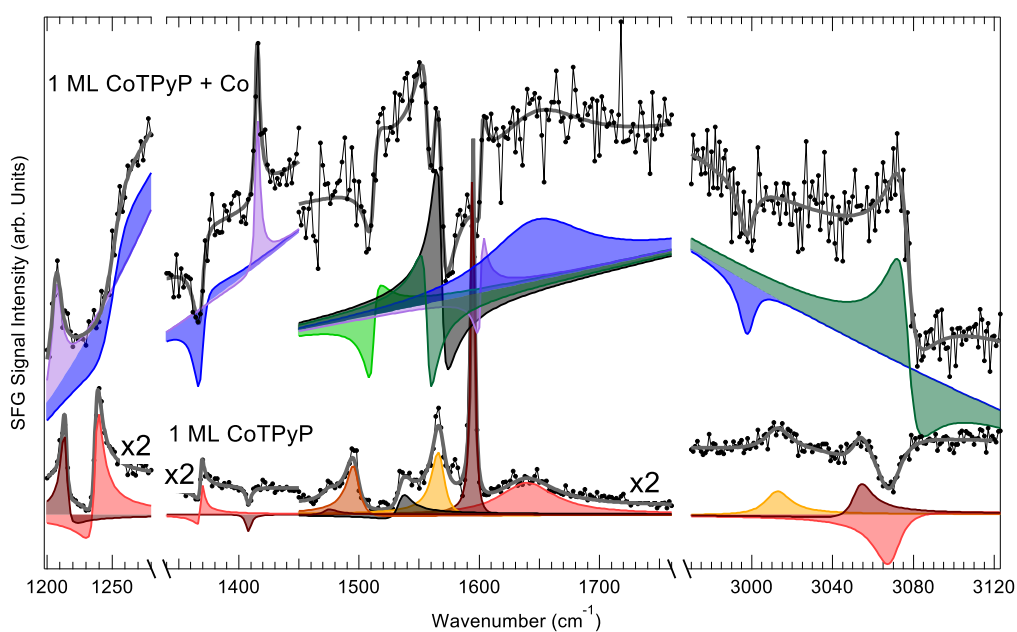


Figure 3.23: IR-Vis SFG spectra of a CoTPyP and a CoTPyPCo ML, with their best-fit (in grey) and peak deconvolution; the same vibrational features are present in both spectra, with energy shifts and phase rotations. The remarkable increase in non-resonant background amplitude is evident at all energies.

3.4 ADDITIONAL MEASUREMENTS

3.4.1 UPS and Work Function

The valence band of bare graphene, the CoTPyP monolayer, the CoTPyP multilayer, and the CoTPyPCo layer has been investigated by means of UPS (He II, 40.8 eV) up to 15 eV of BE (Fig. 3.24).

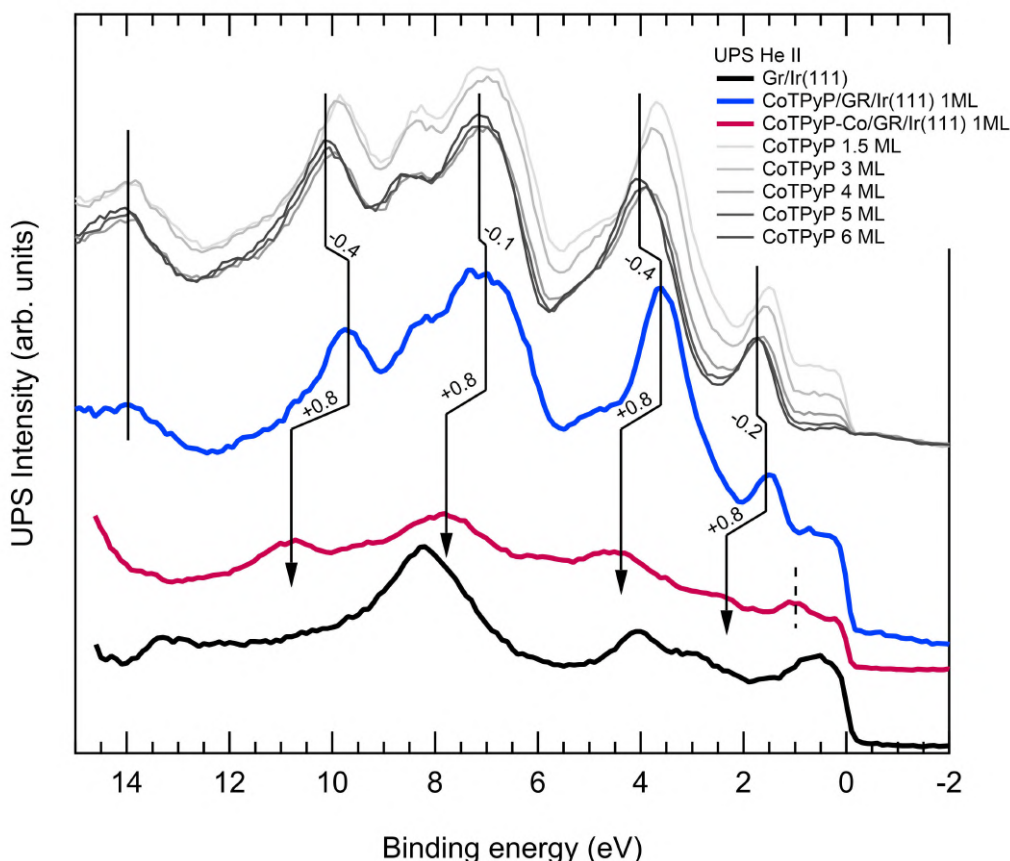


Figure 3.24: UPS (He II) spectra of bare Gr/Ir(111), CoTPyP monolayer, CoTPyP multilayer, and CoTPyPCo. The molecular states in the CoTPyP monolayer, identified by comparison with bare graphene and CoTPyP multilayer, undergo a rigid shift of about 0.8 eV upon cobalt atom deposition. HOMO of CoTPyP monolayer is visible at ~ 1.5 eV, only slightly shifted with respect to the one corresponding multilayer. The curves are vertically shifted for better clarity.

By comparison between bare graphene and CoTPyP multilayer, we can assign the peaks centered at 1.5, 3.5, 7.0, 9.8, and 14 eV to the CoTPyP occupied states. The position of the HOMO (1.5 eV), in particular, agrees with the one found in STS spectroscopy, corresponding to electron density localized on the pyrrole groups. The small shift of the valence states with respect to the multilayer, of the order of 0.2-0.4 eV, is a further sign of the weak interaction that the layer has with graphene. The addition of cobalt atoms

induces a further rigid shift of about +0.8 eV, and the formation of a new HOMO at about +1.0 eV, in good agreement with what observed in STS spectroscopy, which we know to be related with charge localized on the CoTPyPCo (see Fig. 3.19).

The work functions (WF) of the CoTPyP and CoTPyPCo monolayers, calculated by DFT and experimentally measured, are reported in figure 3.25. Both theory and experiment agree with a large WF decrease of about 1 eV ($\Delta\Phi_{EXP} = 0.8$ eV, $\Delta\Phi_{DFT} = 1.2$ eV) upon cobalt atom deposition. This value is remarkable, considering that a decrease of 1 eV of WF has been observed after the deposition of a full monolayer of FeTPyP on an Au(111) surface [126]. This implies that the tiny amount of evaporated cobalt contributes to a radical change in the surface electronic structure, in agreement with the results presented so far.

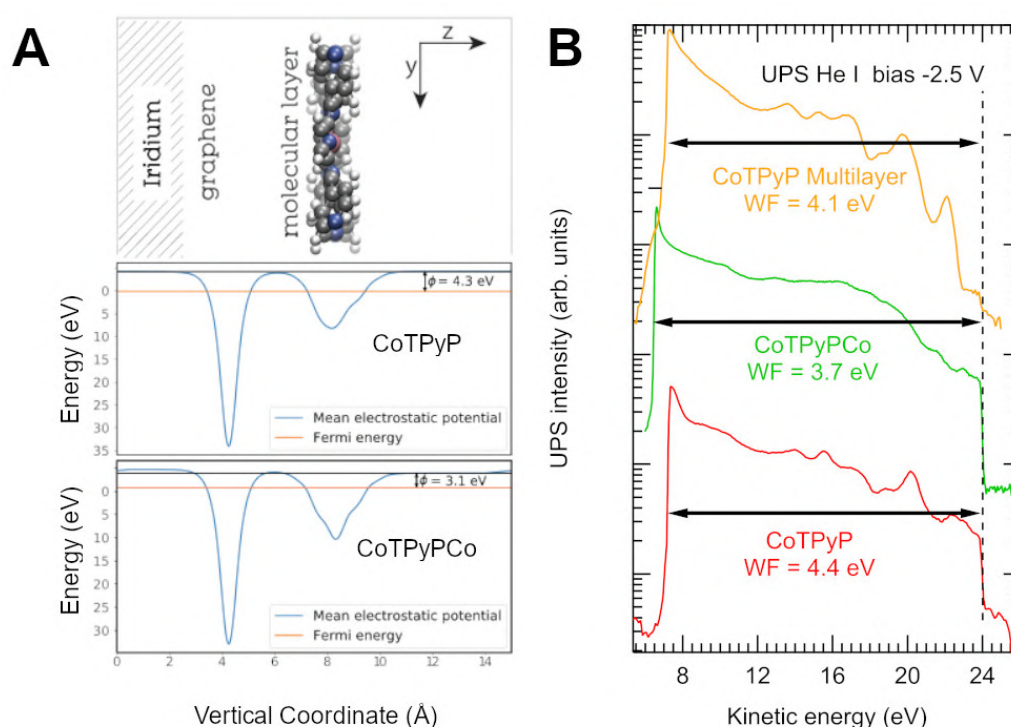


Figure 3.25: Work function of the CoTPyP and CoTPyPCo monolayers **A)** calculated by DFT and **B)** experimentally measured (UPS, He I, $h\nu = 21.2$ eV, -2.5 V sample bias). In panel B, the work function of the CoTPyP multilayer is also reported (about 6 ML), and the curves are vertically shifted for better clarity.

3.4.2 ARPES

Momentum-resolved photoelectron distribution of the valence states (0 – 2.5 eV) was measured to investigate the MOF band dispersion predicted by Mandal *et al.* [54]. An electrostatic photoelectron emission microscope operated in the momentum mode (k -

PEEM) was used, so that a (k_x, k_y) image, whose intensity indicates the photoelectron distribution as a function of the parallel momentum, could be collected in a single shot, at the selected kinetic energy. The molecular states appear to have a circular symmetry in the parallel momentum plane, hence, we only report the vertical cut of the three-dimensional data cube ($E_{binding}, k_x, k_y$) along the $M - \Gamma - M$ direction of the graphene Brillouin zone, to avoid the intense graphene features as much as possible: the result is reported in Fig. 3.26 for the CoTPyP, CoTPyPCo, and CoTPyPFe MOFs. In each case, the signal of the bare Gr/Ir(111) has been subtracted, after being scaled via affine transformation of all the cubic data-set, to match the substrate features⁴ partially attenuated by the metal-organic layer: this step was necessary in order for the MOF signal to stand out from the Gr/Ir(111) background, especially in the case of CoTPyPCo and CoTPyPFe. To validate this operation, we observed that, following the Co(Fe) atom deposition, the graphene is only slightly n-doped producing a downward shift of less than 30 meV of the Dirac cones.

In the CoTPyP/Gr/Ir(111) case (Fig. 3.26 top), the HOMO ring (orthogonal to the image plane) extends in energy from 1 to 1.8 eV has a radius of 1.3 \AA^{-1} , in perfect agreement with STS, UPS, and literature [157].

Following cobalt atom evaporation (Fig. 3.26 bottom left), we see a relevant change in the valence states: the HOMO, previously found centered at 1.5 eV, has completely disappeared. On the other hand, a new HOMO appears at 0.9 eV, once again in agreement with STS and UPS, and a less intense HOMO-1 can be barely seen at 2.0 eV. With the knowledge of UPS, which suggests a rigid shift of 0.7 eV of all the valence states in CoTPyPCo upon Co deposition, we can assign the HOMO-1 to the former CoTPyP HOMO shifted by about +0.5 eV. The new HOMO, instead, is attributed to the new CoTPyPCo state, and its intensity is the same all across the momentum space, as typically observed for non dispersive $3d$ bands in cobalt substrates [158, 159]. For the CoTPyPFe case, a very similar situation is found, with only some small shifts in energy. In general, as can be seen, no band dispersion has been noticed. Nevertheless, it must be taken into account that:

- The sum of many rotational configurations could have a "flattening" effect over the momentum space;
- The predicted dispersion has a modulation of only 100 meV [54], corresponding to only 4 pixels in the images and, so, at the very edge of our experimental resolution;
- The strong background signal makes the analysis very challenging, and small modulations difficult to distinguish.

So, we cannot exclude the presence of dispersing features and, in a future outlook, a similar experiment could be carried out on a weakly interacting substrate, as Au(111), with less complex valence features, and on which the MOF has a preferential orientation.

⁴ In particular, the "vertex" of the Dirac cone was used, at about 100 meV below Fermi.

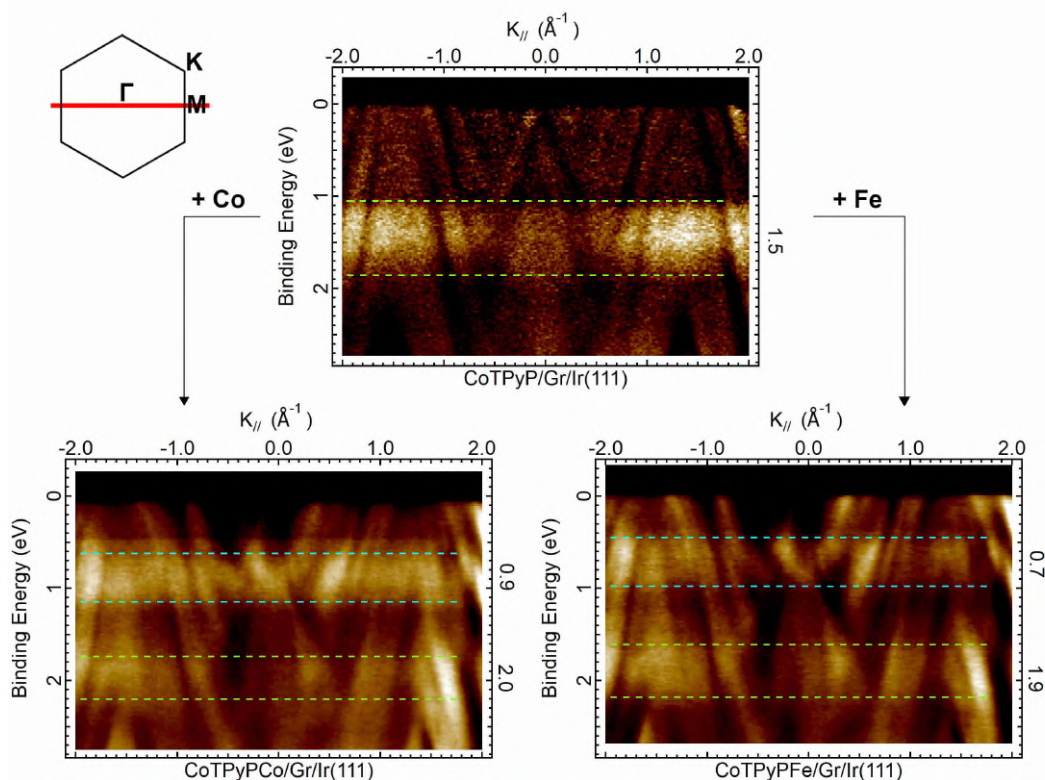


Figure 3.26: Overview of the momentum-resolved photoelectron distribution along the substrate $M - \Gamma - M$ direction (graphene Brillouin zone indicated at the top left) of CoTPyP monolayer (top), CoTPyPCo (bottom left), and CoTPyPFe (bottom right) collected at a photon energy of 35 eV using p -polarized light. The dotted lines are drawn to guide the eye at the edges of the molecular HOMO and HOMO-1. The center of the band is indicated on the right side. The sharp vertical features are attributed to the Gr/Ir(111) substrate.

3.4.3 Tr-2PPE

In this section, the unoccupied states of the CoTPyP, CoTPyPCo, and CoTPyP multilayer are probed by means of tr-2PPE experiment. The three systems were excited with a pump of 531 nm (2.33 eV) and probed with a 257 nm photon (4.82 eV), both in p -polarization. The photoemitted electron intensity is reported in 2D plots as a function of the delay and BE in Fig. 3.27. Only in this experiment, positive values of BE correspond to unoccupied states above the Fermi level. Since the probe energy is larger than the sample work function (measured in section 3.4.1), directly photoemitted electrons generate the noisy bands below the Fermi level that can be seen in panels A, C, and D of figure 3.27.

In the CoTPyP multilayer (Fig. 3.27, panel A), a bright feature centered at +0.2 ps extends from 0 up to 0.5 eV above the Fermi level, and rapidly decays in about 0.3 ps, value at the edge of the experimental resolution. By plotting the intensity profile (Fig. 3.27B) as a function of the delay, with an energy averaging from 0.05 to 0.25 eV (yellow rectangle

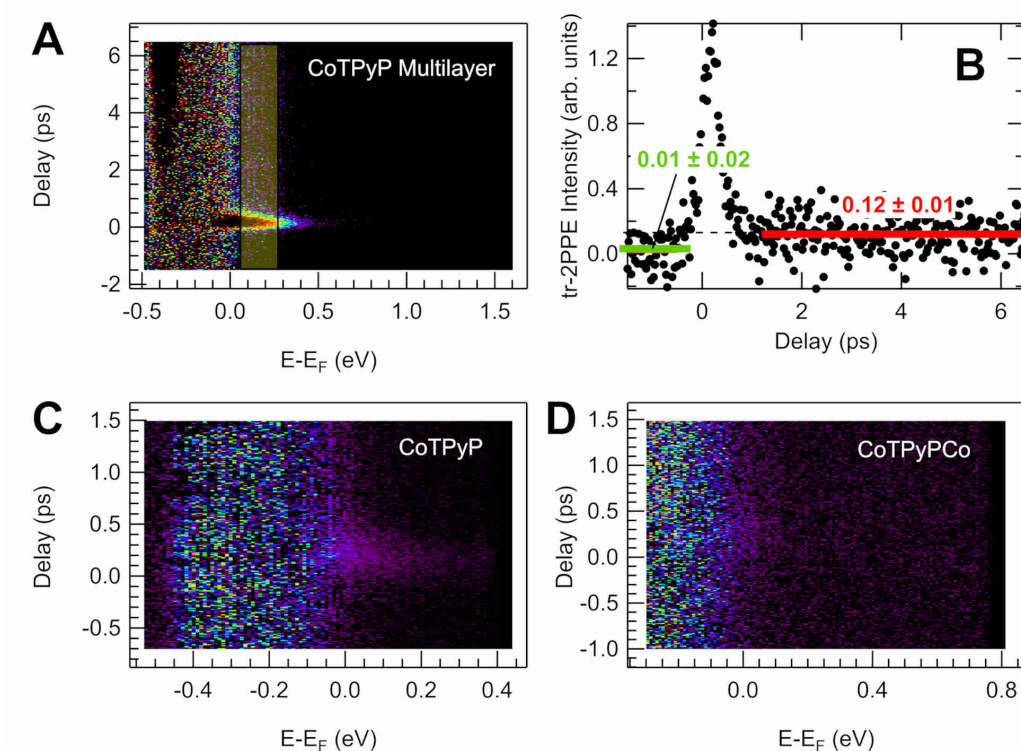


Figure 3.27: *Tr-2PPE photoemission intensity maps are plotted as a function of energy and delay time, for A) the CoTPyP multilayer, C) the CoTPyP/Gr/Ir(111), and D) the CoTPyPCo/Gr/Ir(111). B) Intensity plot as a function of delay time averaged on the energy region evidenced by the vertical rectangular band in A. In A and C, a bright short-lived state at 0 ps is visible up to 0.5 eV; at higher delay times a long-lived state is observable (panel B). See text for further details.*

in Fig. 3.27A), we observe that, together with the aforementioned short-lived state, a long-lived state is revealed looking at the higher mean value of the background. In this case, the lifetime would be higher than 6 ps, which was the maximum delay available for this setup. The origin of both states is currently unknown, considering that the large band gap found with STS suggests the absence of any molecular-related state at 0.2 eV above Fermi.

A similar picture is found for the CoTPyP case (Fig. 3.27C), where the short-lived state is clearly visible; on the contrary, the long-lived one is likely to be hidden by the noise. Interestingly, in CoTPyPCo (Fig. 3.27D), no excited state can be observed, a further indication of the different electronic configurations of the two MOFs.

3.5 MAIN RESULTS

In this chapter we have witnessed the transition from a molecular array (M_1 TPyP) to a 2D MOF (M_1 TPyPM₂). STM and NEXAFS clearly show the bonding, in particular for the CoTPyPCo case, of the additional metal atom to four CoTPyPs, via in-plane tetra-coordination to the nitrogen atoms of adjacent TPyP-pyridinic terminations. Remarkably, this strong covalent bond completely rearranges the geometry of the layer, passing from a triangular to a square lattice, by overcoming the weaker lateral inter-tectons interactions. Regarding the electronic configuration, STS, DFT, XPS, and UPS agree on the non-equivalent chemical identity of the macrocyclic and pyridinic cobalt atoms in CoTPyPCo, even though both present a local N tetra-coordination environment. In particular, macrocyclic Co undergoes oxidation, from +2 (gas phase) towards a +3 configuration upon Co deposition, while the other one shows a +1 oxidation state. Local STS on unsaturated CoTPyPCo suggests the presence of long-range (> 1.5 nm) electronic interaction within the MOF, reflecting shifts in the CoTPyPCo HOMO of the order of fraction of eV. Further UHV characterization concerns the vibrational characterization of the layer (SFG), the thermal stability (XPS and SFG), with degradation and desorption processes occurring only above 500 K, and the probable presence of multiple phases below 500 K (SFG). In conclusion, no crystalline band dispersions was observed with ARPES within the available moment and energy resolution.

As discussed in the Introduction, the both Oxygen Reduction Reaction (ORR) and the Oxygen Evolution Reaction (OER) (Fig. 4.1) play essential roles in many technological applications, such as electrolyzers (OER), fuel cells (ORR), or secondary metal-air batteries (both ORR and OER). Now, let's focus on the ORR, since every consideration will still be valid for the opposite reaction [160].

Molecular O₂ can be reduced in two ways [160], yielding the formation of water (4-electron pathway) as shown in the chemical equation below, with the corresponding Nernst equation:¹



$$E_{O_2/H_2O} = E_{O_2/H_2O}^\circ - \frac{RT}{4F} \ln \frac{a_{H_2O}^2}{a_{O_2} a_{H^+}^4}, \quad (4.2)$$

or hydrogen peroxide (2-electron pathway):



$$E_{O_2/H_2O_2} = E_{O_2/H_2O_2}^\circ - \frac{RT}{4F} \ln \frac{a_{H_2O_2}^2}{a_{O_2} a_{H^+}^2}. \quad (4.4)$$

In general, the formation of water is favored, considering the Nernst standard potentials versus the standard hydrogen electrode (SHE) of $E_{O_2/H_2O}^\circ = +1.229$ V (in equation 4.2) and $E_{O_2/H_2O_2}^\circ = +0.695$ V (in equation 4.4) [160]. Nevertheless, hydrogen peroxide, even being one of the 100 most significant compounds for its many applications such as bleaching, water treatment, and the production of organic compounds [162], is often an unwanted and even detrimental side-product, such as in the case of metal-air batteries [16]. Thus, it is important to understand the fundamentals of the reaction pathway and, in particular, which mechanism steers the 2- vs 4- electron routes.

In the following paragraph, we will take advance of the current knowledge of the ORR/OER reaction pathway occurring at the solid-aqueous interface in heterogeneous catalysis, to then transfer this understanding to our experiment, dealing with the CoTPyP/Gr/Ir(111) solid-gas heterogeneous model catalyst.

The equilibrium equations 4.1 and 4.3 are overall expressions for the complete ORR (and OER) processes. However, both reactions involve several elementary steps, and, in particular, electron transfer, proton transfer (coupled or decoupled with the electron transfer), bond-breaking (ORR) or bond-forming (OER) are involved [160, 163]. Focusing

¹ a_i is the activity of species i in water.

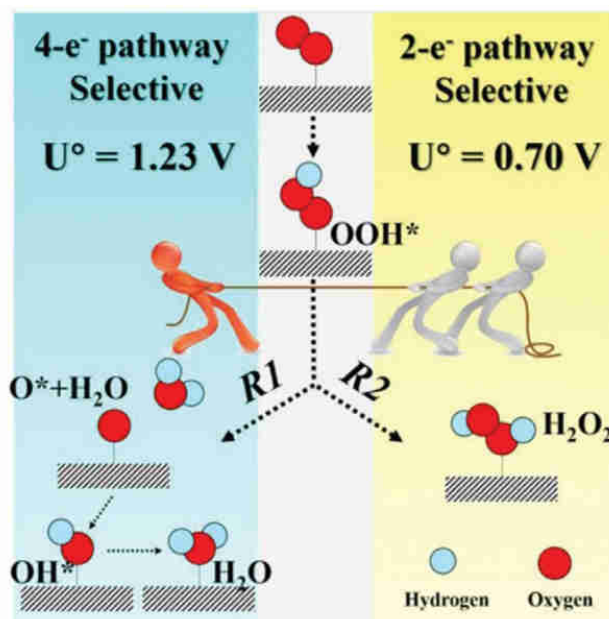


Figure 4.1: Schematic illustration of the reactions and the equilibrium potentials during the oxygen electrochemical reduction. Image taken from [161]

on the thermodynamically favored ORR reaction (H_2O formation), an overview of the fundamental intermediate steps is provided in Fig. 4.2A [160]. In particular, three alternative steps are proposed for the formation of OH^{ads} , the precursor of H_2O :

- **Dissociation:** O_2 immediately breaks into O^{ads} species, the latter subsequently interacting with H^+ in solution to form OH^{ads} ;
- **Associative:** O_2^{ads} combines with H^+ to form OOH , namely the *hydroperoxyl radical*; then, the $O-O$ bond will be cleaved and OH^{ads} species is formed;
- **Peroxo mechanism:** upon O_2^{ads} adsorption and OOH formation (as in the associative first step), the $HOOH^{ads}$ peroxide group is formed (peroxide group = $R-O-O-R$, R = any element). Then, the $O-O$ bond is cleaved and OH^{ads} is formed.

The first pathway (**dissociation**) involves very high O_2 adsorption energies (1 – 10 eV, Fig. 4.2B), with a considerable amount of charge transfer into the dioxygen molecule that is needed to cleave the $O-O$ bond [162]. From a geometrical point of view, this process usually goes along with a horizontal O_2 adsorption geometry (Fig. 4.2C), such as Griffiths-type (side-on coordination on one metal atom) or Yeager-type (side-on bridge coordination on two adjacent metal atoms) [162]. It is demonstrated that Pt catalysts coated with amorphous carbon layers can eliminate accessible Pt ensemble sites and promote selective end-on adsorption (Pauling-type, Fig. 4.2C) of O_2 on the Pt surface, which significantly enhances H_2O_2 selectivity in ORR [164]. This example is suggestive of

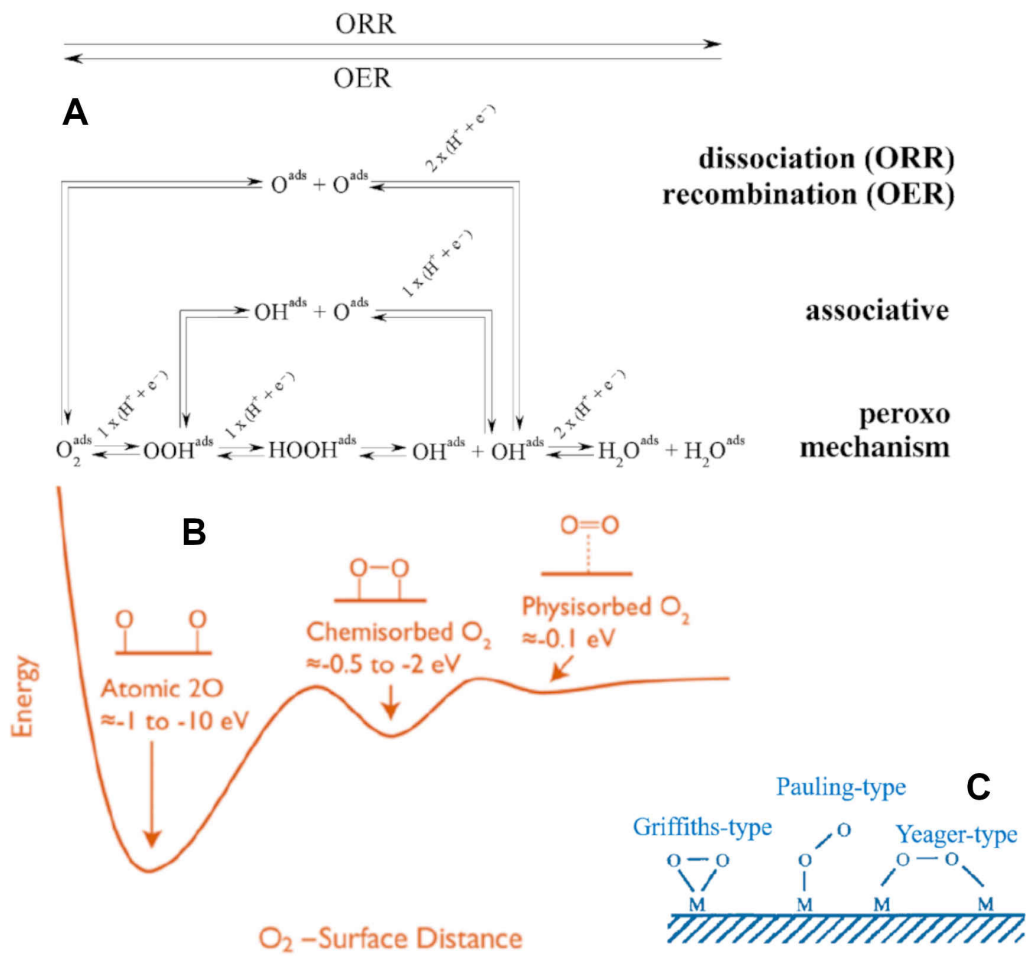
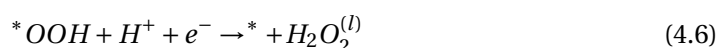


Figure 4.2: A) Fundamental steps of ORR/OER [160]; B) One-dimensional potential energy diagram of an oxygen molecule approaching a metal surface [162]; C) Schematic three types structure of O_2 adsorption on metal surface [162].

the strong correlation between the geometry of the active site, the O₂ adsorption geometry, and the catalyst selectivity, suggesting in this way that in principle, by properly tuning the charge transfer amount, single-atom catalysts could switch between Griffiths- and Pauling- adsorption type [70, 162], thus determining the reaction selectivity.

In both the associative and peroxo mechanisms, the formation of the hydroperoxyl species occurs, as well as in the 2-electron ORR pathway, as shown in the equation below (the asterisk indicating the catalyst active site) [162]:



Since its first observation [165], the hydroperoxyl molecule has gained the widely accepted role of the fundamental reaction intermediate [17, 162, 166]. Many theoretical/computational papers describe the stability of this molecule, its bonding geometry to catalytically active metal sites, and the energetics of the fundamental ORR reaction steps [162, 167, 168]. The influence of solvation is tackled in detail at the fundamental level but only in the gas-phase, shedding light on the stability and properties of H₂O – O₂H clusters [169–172] and the reactivity of singlet dioxygen species [173]. Despite all these efforts, the O₂H intermediate has shown an elusive behavior up to now, and thus, both its stability and its effective, actual role in steering the ORR reaction pathway are liable to be questioned. Pioneering *in situ* spectroscopic evidence of the formation of O₂H and its role in the ORR was obtained very recently on model single-crystal Pt terminations, leaving however an open point about the possible role of “solution species” [174, 175]. Indeed, while the adsorbed reaction intermediates were successfully characterized, the second interaction sphere with the solvent could not be experimentally addressed.

In this chapter, we report the spectroscopic evidence obtained at room temperature of a stable O₂H – H₂O/Co complex at the solid-gas interface, at the limit of water condensation conditions. We show that its formation is associated with its stabilization by a surprising combination of charge transfer, dipole, and chemical H-bonding with physisorbed water. Indeed, we work at room temperature and exploit the CoTPyP/Gr/Ir(111) single-atom catalyst (SAC) at near-ambient pressure (NAP) conditions within the framework of a biomimetic approach, at the limit of water condensation conditions. As explained in the introduction, recent fundamental advances have allowed the investigation of biomimetic tetrapyrrole-based 2D materials beyond UHV surface science conditions, up to the solid-gas and solid-liquid interfaces [10, 27, 30, 55, 70, 118].

The system is characterized *in situ* at NAP by combining IR-Vis SFG, time-resolved IR-Vis SFG, and high-resolution NAP-XPS with synchrotron X-Ray radiation. Complementary information is obtained in UHV using STM, IR-Vis SFG, and XPS, while fundamental insight is obtained by means of *ab initio* calculations performed within the framework of DFT.

4.1 RESULTS AND DISCUSSION

O₂ and H₂O are dosed at room temperature on an ordered monolayer of cobalt tetrapyrrolylporphyrins (CoTPyP) deposited and self-assembled on an almost free-standing graphene (Gr) single sheet of excellent crystalline quality (grown *in situ* on the Ir(111) single crystal termination [176] and checked with LEED).

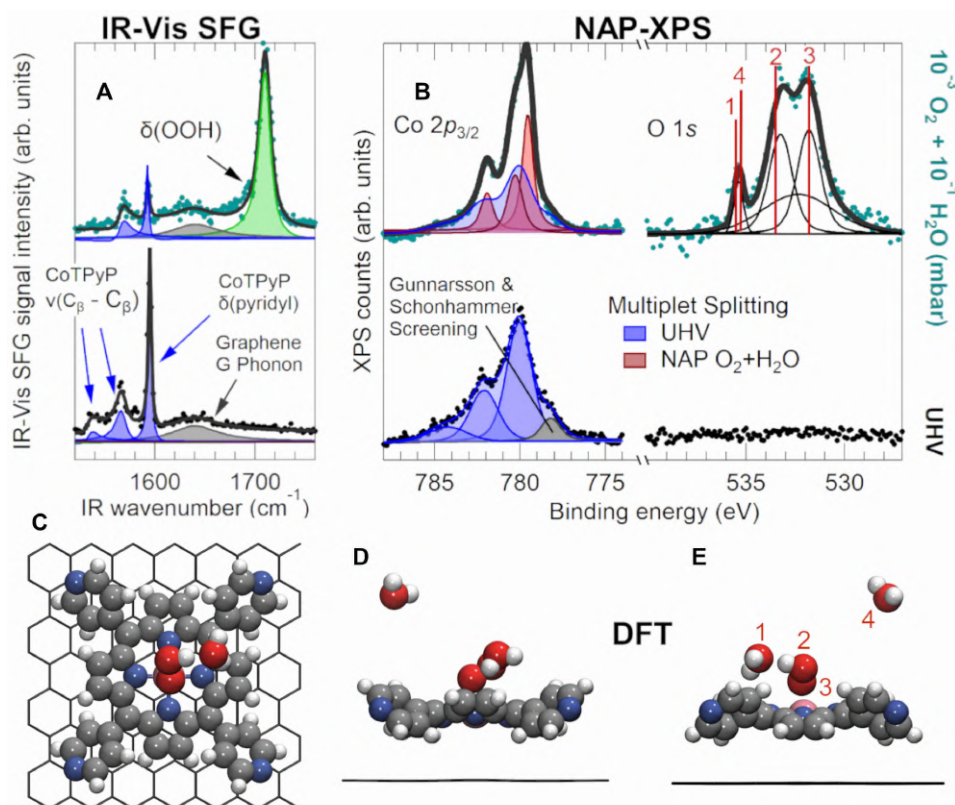


Figure 4.3: Spectroscopic and geometric characterization of the hydroperoxyl-water complex. **A)** IR-Vis SFG spectra of the pristine CoTPyP/GR layer in UHV (bottom) and in 10^{-3} mbar O₂ + 10^{-1} mbar H₂O at room temperature (top); experimental data (markers) are reported together with the best fit (continuous lines) and deconvolution envelopes (filled profiles) [177]. **B)** NAP-XPS spectra of the Co 2p_{3/2} (left, $h\nu = 910$ eV) and O 1s (right, $h\nu = 660$ eV) core levels corresponding to the same conditions as in (A); red vertical lines indicate the binding energies obtained for the optimized O₂H-H₂O complex on CoTPyP/Gr from *ab initio* DFT calculations for different O 1s core levels, as labelled in (e): 1 – physisorbed/wetting water, 2 – OOH, 3 – OOH, 4 – gas phase water. **C)** Top view of the DFT optimized model of the O₂H-H₂O/Co/TPyP/Gr system. **D-E)** Side views of the same system with an additional water molecule in the gas phase from two different points of view, to show the order-2 rotational symmetry of the CoTPyP, with a saddle shape macrocycle and peripheral pyridyl groups alternatively rotated by $+39 \pm 5^\circ$ and $-39 \pm 5^\circ$ with respect to GR.

As discussed in the previous chapter, the CoTPyP monolayer can be described by an hexagonal lattice where the porphyrins alternate their azimuthal angle within two alternating rows. This corresponds to a $1.5 \times 2.8 \text{ nm}^2$ rectangular unit cell with two base vectors (see section 3.2.2). The local geometry of the self-assembled layer is more distorted with respect to the almost square cell previously observed for similar porphyrins and phthalocyanines on Gr/Ir(111) [118, 178] and on Au(111) [126, 134, 179].

The corresponding IR-Vis SFG spectrum is characterized in the $1500 - 1750 \text{ cm}^{-1}$ range by the presence of four main vibronic resonances (Fig. 4.3a, bottom panel; Table Appendix A.8), ascribed to the $\nu C - C$ modes at 1535 and 1567 cm^{-1} and to the δ_{pyr} mode at 1595 cm^{-1} of the porphyrins [180–182], together with the Gr/Ir(111) G phonon that shifts from 1608 to 1639 cm^{-1} after the CoTPyP deposition [55, 118].

4.2 EXPOSURE TO O₂ AND H₂O

Exposure of the 2D system at room temperature to $P_{O_2} = 10^{-3}$ mbar or to $P_{H_2O} = 10^{-1}$ mbar yields neither substantial vibrational (IR-Vis SFG), nor electronic (AP-XPS) spectroscopic modifications with respect to the pristine layer (Figs. S1-Fig. 4.4A-B). Instead, exposure of the surface to the mixture of the two gases (Fig. 4.3a, top panel) yields dramatic changes, with rates depending on the order in which the reactants are introduced (Fig. 4.4).

While only slight energy shifts and phase changes of the resonances associated with the CoTPyP/Gr layer are detected, the growth of a new, very intense resonance at 1712 cm^{-1} is observed both in ppp and ssp polarization combinations (Fig. 4.4C). The feature can be attributed to the δ_{OOH} mode of O₂H in a metastable O₂H-H₂O complex, in remarkable agreement with previous predictive calculations about the dynamical behavior of hydroperoxyl radical water clusters, including the enhanced spectroscopic cross section [170, 171]. We find that the complex reacts/dissolves already after mild heating (Fig. 4.4D) above room temperature, coherently with an enhancement of the surface reaction rate towards a mass-transport-limited condition.

Exposure of the CoTPyP monolayer to the oxygen/water mixture is also associated with the growth of O 1s core level components (Fig. 4.3b, right) in the AP-XPS spectra. We can distinguish the contribution from water at 535.4 eV [183] plus two features at 533.4 and 531.8 eV , respectively. *Ab initio* DFT calculations of the O₂H-H₂O/CoTPyP/Gr system (Fig. 4.3c) yield an optimized structure in which a water molecule participates in the formation of a stable complex with the hydroperoxyl radical. The computed O 1s core level binding energies for the different O species (from 1 to 4) are in remarkable agreement with the spectroscopic line positions (vertical, red lines in Fig. 4.3b, right), thus allowing their straightforward interpretation and confirming the vibrational assignment. Specifically, we attribute the peak at 535.4 eV to both gas phase (4) and physisorbed/wetting (1) water. The peaks at 533.4 (531.8) eV are assigned to the OOH (OOH) ligand at the Co site (numbers 2

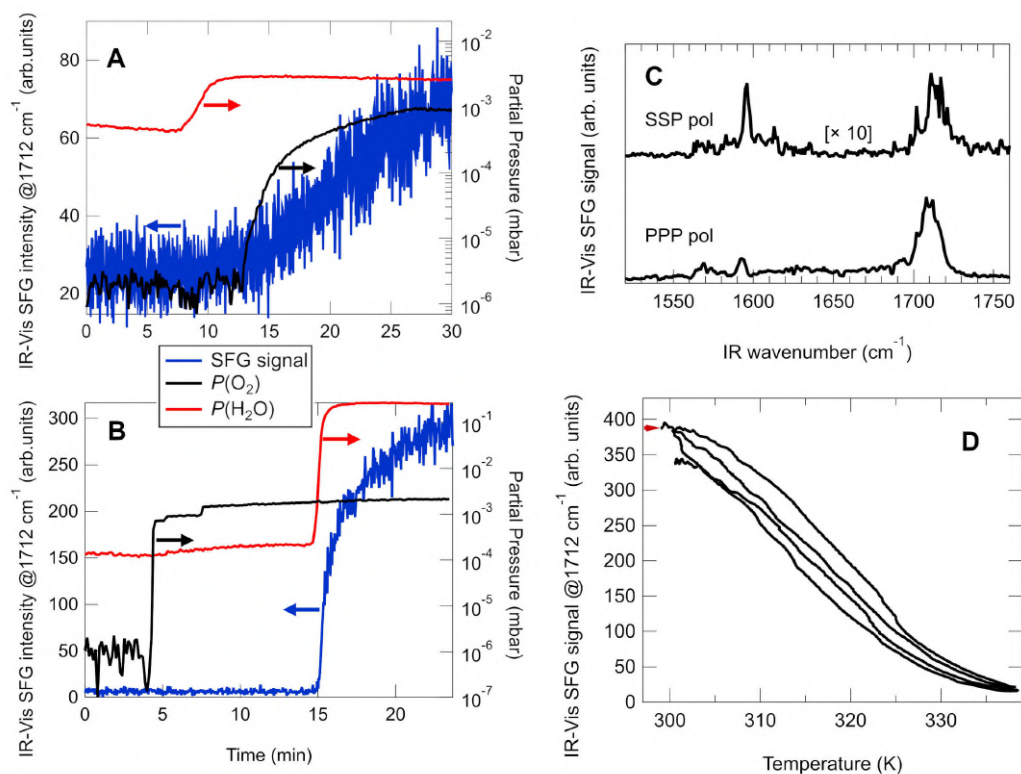


Figure 4.4: **A-B)** Evolution of the IR-Vis SFG resonant intensity @ 1712 cm^{-1} as a function of the reactants' partial pressure. Time-dependent evolution of the intensity (cyan, left axis) of the IR-Vis SFG resonance associated with the δ_{OOH} mode observed at 1712 cm^{-1} measured in situ at room temperature as a function of the reactants' partial pressure (O_2 – black, H_2O – red, right axis); In A), oxygen is introduced after water and a slow uptake is observed; In B), oxygen is introduced before water, and a sudden uptake is observed; **C)** Comparison between normalized ppp (bottom) and ssp (top) IR-Vis SFG spectra measured in situ in 10^{-3} mbar O_2 + 10^{-1} mbar H_2O . **D)** IR-Vis SFG intensity at 1712 cm^{-1} as a function of the cycling of surface temperature measured in situ in 10^{-3} mbar O_2 + 10^{-1} mbar H_2O .

and 3, respectively, in Fig. 4.3e). Accordingly, the two latter peaks are observed to grow in parallel and with almost equal intensity as a function of the background gases pressure. A broad, almost Gaussian contribution progressively develops at 532.4 eV upon aging (hours of exposure) of the sample, associated with OH, OH-OH, O-H₂O, C-O poisoning at defective sites, and Gr oxidation [183–185], indicating its slow degradation.

The Co $2p_{3/2}$ core level lineshape is strongly influenced by the reaction (Fig. 4.3b, left), displaying a strong remodulation of the multiplet splitting structure with respect to the pristine sample, showing an intensity decrease of the components at 784.3, 782.1, and 780.1 eV and the growth of new peaks at 781.9, 780.3, and 779.6 eV. In a very recent report on Co-based metalorganic frameworks [186], the latter component was associated with CoOOH species. The lowest binding energy feature that is evident at 778.2 eV on the “as grown” sample is due to the Gunnarsson and Schonhammer transfer of the screening charge from the substrate [141, 187]. The observed quenching of the latter peak upon exposure to the water/oxygen mixture witnesses binding of the ligands to the Co metal site [142], possibly associated with a change of the metal oxidation state [185, 188].

4.3 THE TIME-RESOLVED IR-VIS SFG EXPERIMENT

To investigate the role of the O₂H-H₂O interaction, we exploited the IR-Vis tunable delay and the intrinsic width of the two pulses to perform time-resolved SFG, as explained in detail the method chapter, by measuring the SFG response as a function of the IR-to-Vis pulse delay (Fig. 4.5a). When the system is pre-excited with the IR pulse, we observe that the vibronic energy of the δ_{OOH} resonance is transferred to the water roto-vibrational modes [189] on a 10 ps time-scale (Fig. 4.5A-B, Fig. in Appendix A.13). This indicates strong coupling between the hydroperoxyl species and co-adsorbed water. The latter phenomenon is known to participate in the stabilization of the complex, in analogy to what theoretically predicted [169–173, 190] and observed by 2D-IR spectroscopy, regarding hydration shell reorganization and H-bonding exchange [191]. Similarly, the hydrogen bond strengthening, followed by relaxation and thermalization, mediating the energy transfer process, was observed in liquid water [192]. While it was found that the former process occurs on a 0.1-1 ps timescale, vibrational energy is then efficiently funneled through the H-bonding network into all degrees of freedom in water on a several-ps time scale, in agreement with our observations. This leads to an increased local temperature, as water vibrations are known to have strongly mixed intra- and inter-molecular character [192, 193].

Similar mechanisms take place also in heme enzymatic reaction centers. In Hb/Mb, an imidazole group of the protein histidine residue provides a stabilizing H-bonded network for the Fe-peroxo intermediate [194] so that, by artificially engineering the H-bonding structure of Mb, the protein can be modified to promote O₂ reduction to water via the 4e⁻ mechanism [195]. In synthesized Fe porphyrin complexes, the H bonding network is

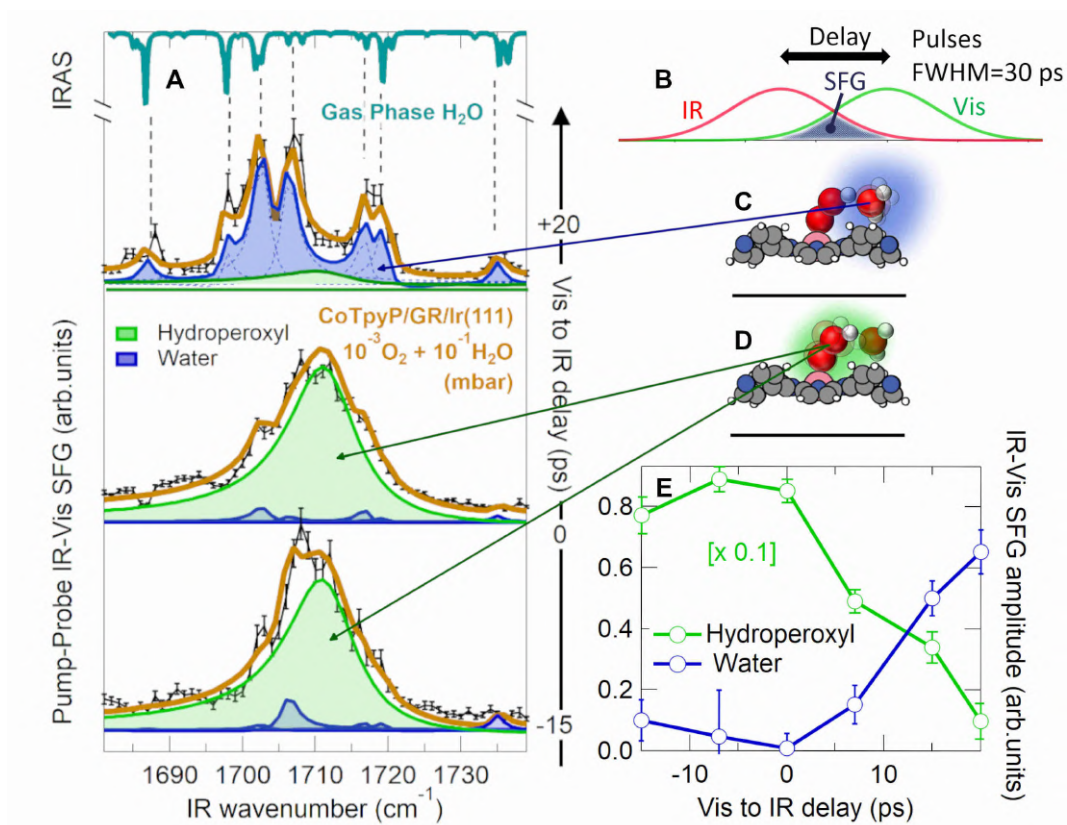


Figure 4.5: Energy coupling and stabilization of the ligated hydroperoxyl-water cluster. **A)** IR-Vis SFG spectra of the evolution of the δ_{OOH} mode lineshape at 1712 cm^{-1} as a function of the Vis-to-IR delay; the spectra were normalized by the overlap integral of the IR and Vis pulses and are reported together with the best fit (continuous lines) and deconvolution envelopes (filled profiles) [177]; in the top part, IR roto-vibrational spectrum of gas phase water [189]. **B)** Sketch of the delayed IR and Vis pulsed used to generate the time-resolved SF signal. **C-D)** Best structural model of the O₂H-H₂O/CoTPyP/Gr system as obtained from DFT calculations (as in Fig. 4.3c-e), evidencing the contribution of the different moieties to the spectral evolution reported in (a) and (b); Gr is only sketched for better clarity. **E)** Normalized IR-Vis SFG amplitude of the OOH and water modes obtained from the fit as a function of the IR-to-Vis delay.

exploited to promote protonation to specifically form the hydroperoxide intermediate complex [196, 197].

4.4 AB INITIO CALCULATIONS

In the case of the system discussed here, we find that water directly participates in the stable O_2H-H_2O complex with concurrent bonding and energy transfer mechanisms, while O_2H binds directly to the Co center. The picture is consolidated by *ab initio* simulations obtained within the framework of a collaboration, yielding a high complex-CoTPyP binding energy of 6.12 eV for the most stable configuration with the terminal $O^{(3)}$ atom of hydroperoxyl bound to the metal center (Co-OOH, Fig. 4.6A, bottom panel), in line with calculations on a similar model system [168]. Most interestingly, upon bonding, three phenomena take place in parallel, contributing to the stabilization of the whole system: i) $0.15 e^-$ are transferred from the CoTPyP inner macrocycle to both O atoms of O_2H (Fig. 4.7) through the Co $3d_{z^2}$ atomic orbital hybridization with the ligand's orbitals (Fig. 4.6D-E); ii) O_2H and H_2O form a strong hydrogen-mediated bond within the complex, with charge accumulation in the bond (Fig. 4.6D-F); iii) long range van der Waals forces, associated with charge redistribution and dipole formation, develop extensively among the water molecule, hydroperoxyl, and adjacent pyrrolic and pyridinic moieties of the CoTPyP (Fig. 4.6F). Interestingly, also hydroperoxyl alone would be strongly bonded to the Co metal center (by 5.40 eV) (Fig. 4.6A-B, central panels).

However, water addition induces a charge redistribution also in the Co-OOH bond (Fig. 4.6B, bottom left panel). The simultaneous adsorption of O_2H and H_2O on the Co atom, with the water molecule interacting also with adjacent moieties of the tetrapyrrole, stabilizes the complex itself, whose binding energy increases by 0.22 eV with respect to the gas-phase configuration (Fig. 4.6C). A second adsorption geometry for hydroperoxyl, in which binding to Co occurs via the hydroperoxyl central $O^{(2)}$ atom (Co-OHO), is less favorable by only 160 meV, implying that both configurations (Co-OOH and Co-OHO) could be populated in principle, depending on the temperature and on the local surrounding environment.

4.5 MAIN RESULTS

By means of a combination of *in situ* measurements and theoretical methods, we have shown that a cobalt single-atom biomimetic model catalyst, based on a self-assembled monolayer of Co-porphyrins grown on an almost free-standing graphene sheet, stabilizes a hydroperoxyl-water cluster at room temperature in O_2+H_2O atmosphere. The interplay between charge transfer, dipole and H-bonding, and water solvation is found to determine ultimately the stability and bonding geometries, unveiling the core step of the ORR. This

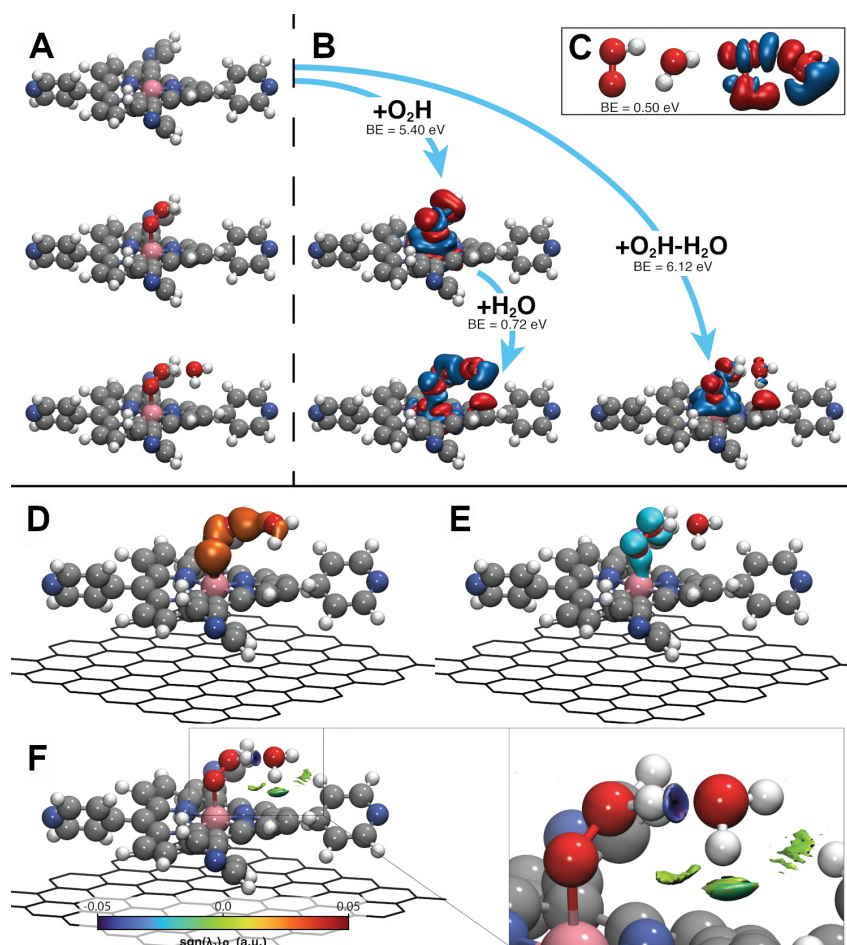


Figure 4.6: *Ab initio* insight on the bonding nature of the $\text{O}_2\text{H}-\text{H}_2\text{O}/\text{CoTPyP}$ system. **A)** From top to bottom, optimized models for CoTPyP/Gr , $\text{O}_2\text{H}/\text{CoTPyP}/\text{Gr}$, $\text{O}_2\text{H}-\text{H}_2\text{O}/\text{CoTPyP}/\text{Gr}$, showing that CoTPyP is globally unaffected by the adsorption of O_2H and H_2O , apart from a small lifting of the Co atom by 0.16 \AA . **B)** Bonding-induced rearrangement of the electron density distribution in the $\text{O}_2\text{H}-\text{H}_2\text{O}/\text{CoTPyP}/\text{Gr}$ system, with respect to the individual constituents. Iso-surfaces upon adsorption of: (left) firstly O_2H and then H_2O ; (right) the whole $\text{O}_2\text{H}-\text{H}_2\text{O}$ complex (red/blue for electron gain/loss, isovalues: $\pm 0.001 \text{ a.u.}$). **C)** Optimized configuration of the complex in gas phase, and electron charge redistribution upon complex formation – isosurfaces as in (B). **D-E)** Spatially-resolved Local Density of States integrated in two relevant energy ranges (Fig. 4.8A-E) (surfaces isovalue: 0.005 a.u.). In (D) the charge accumulation in the $\text{O}_2\text{H}-\text{H}_2\text{O}$ bonding region is visible, and in both (D) and (E) the hybridization of the $\text{Co } 3d_{z^2}$ and $2p$ orbitals of the terminal O atom of O_2H ($\text{O}^{(3)}$ in Fig. 4.3E). **F)** Visualization of noncovalent interactions by means of an isosurface of the Reduced Energy Gradient (RDG): the blue color of the isosurface between O_2H and H_2O indicates a region with rather strong noncovalent bonding, and the green color of the isosurface between H_2O and the pyrrolic and pyridinic moieties of the CoTPyP indicates a region with moderate noncovalent bonding (RDG value: 0.6 a.u. , with color depending of the local value of the electron density).

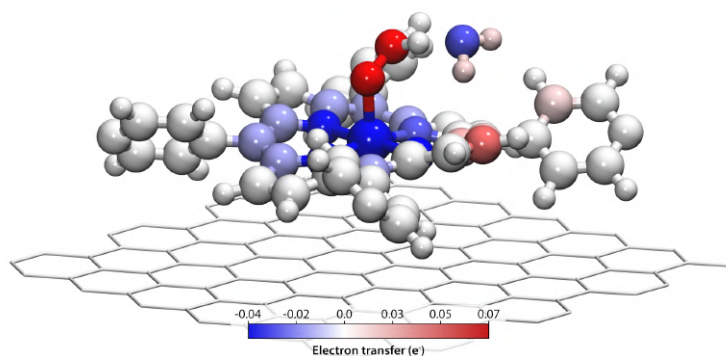


Figure 4.7: Charge redistribution in the $O_2H-H_2O/CoTPyP/Gr$ system upon bonding of the O_2H-H_2O complex to the $CoTPyP/Gr$. The charge rearrangement is obtained from the difference of the Löwdin atomic charges [198] between the entire system ($O_2H-H_2O/CoTPyP/Gr$) and the two constituents separately (O_2H-H_2O and $CoTPyP/Gr$). The color of each atom indicates the amount of electron variation: red/blue correspond to electron gain/loss.

teases the mind towards a picture in which selectivity for 2 vs 4 e^- ORR could be driven by the configuration of the hydroperoxyl ligand at the catalysts' active site, ultimately defined by the unraveled interplay between charge transfer, chemical, dipole and H-bonding (solvation) phenomena [172], thus paving the way towards novel approaches to the reaction control.

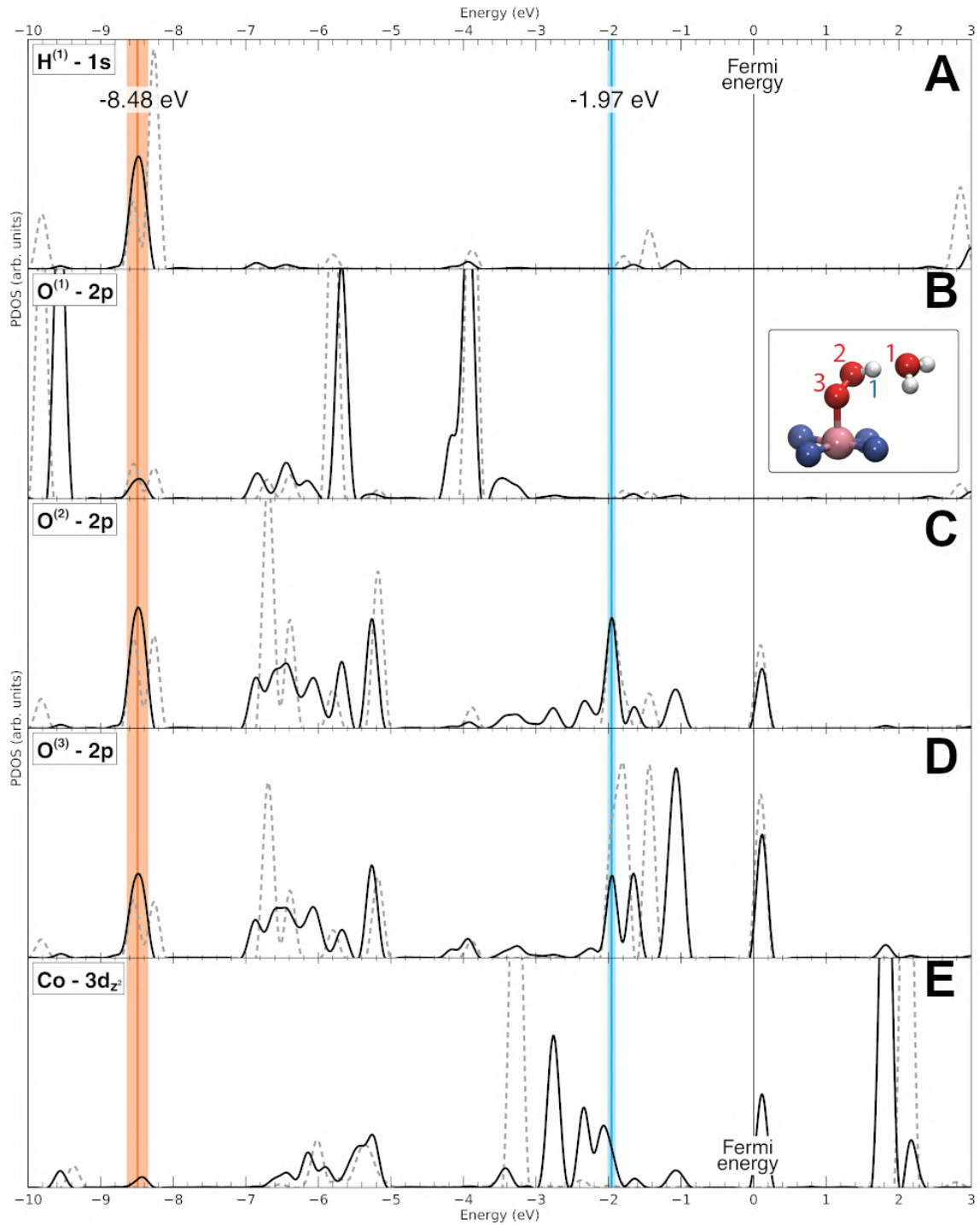


Figure 4.8 (preceding page): PDOS for some relevant atomic orbitals: **A)** H 1s ($\times 3$), **B-D)** O 1s of the three different O atoms of the complex ($\times 0.35$), **E)** $3d_{z^2}$ of Co atom of the porphyrin. Solid black lines refer to the full $O_2H - H_2O/CoTPyP/GR$ system with the complex bonded to the porphyrin; dashed grey lines refer to the separated configurations of the constituents (pristine CoTPyP/GR layer and isolated $O_2H - H_2O$ complex). Blue and orange vertical stripes identify selected energy ranges (orange: from -8.65 eV to -8.31 eV; blue: from -1.97 to -1.93 eV) characterized by the superposition of Co $3d_{z^2}$ and O $2p$ contributions in the bound configuration and not in the separated configuration, in order to highlight the orbital overlapping associated with chemical bonding. The Local Density of States integrated in the two energy windows and summed over all the relevant atoms is shown in Fig. 4.6D – E. The simulation for $O_2H - H_2O$ in gas phase was made by leaving the molecular layer in the unit cell and moving away the complex, to guarantee the same reference energy for all the configurations.

5 | CO AT NAP ON CoTPyPCo

Carbon monoxide, thanks to its strong dipole and adsorption energy, is an ideal probe to tackle the local adsorption environment of a MOF active site. In this chapter, by combining NAP IR-Vis SFG experiments and *ab initio* DFT, we demonstrate the different chemical nature of the two cobalt sites in CoTPyPCo/Gr/Ir(111) by exploiting CO as an extremely sensitive probe able to detect the finest changes of the CO adsorption potential related to long-range interactions (≥ 1.5 nm) driven by the MOF itself. In this experiment, the cobalt evaporation rate is calibrated with Auger spectroscopy, by taking the graphene sheet as the monolayer reference. Apart from the last section, where explicitly specified, the IR-Vis SFG spectra are collected in ppp polarization.

The SFG spectra, that will be shortly presented, have been fitted with a simultaneous optimization of the fitting parameters, a handy procedure already implemented in the toolkit of Igor Pro 9 used for the analysis, which is called "Global Fit". In this way, parameter constraints can be set across different spectra, making the analysis faster and more reliable. From now on, when a fitting parameter will be simultaneously optimized over different spectra in a data set, we shall refer to it as being "global-fitted". Lastly, all the error bars reported in this analysis correspond to one standard deviation.

5.1 CO ADSORPTION IN CoTPyPCo

Panel A of Fig. 5.1 shows IR-Vis SFG spectra, acquired in the CO stretching range ($1800 - 2100 \text{ cm}^{-1}$), as a function of the amount of cobalt atoms evaporated on a 0.5 ML CoTPyP/Gr/Ir(111) submonolayer, and measured at a constant CO pressure of 1×10^{-3} mbar at RT. Starting from the bottom, the spectrum corresponding to the CoTPyP layer before cobalt exposure is completely flat, indicating that no CO adsorption occurs on the CoTPyP molecules.

Going upward in the series, the second spectrum is collected after deposition of 0.12 ML of Co, corresponding to a CoTPyP:Co stoichiometry of about 8 : 1 (that is because, as STM shows, the CoTPyPs do not uniformly spread on graphene but, rather, condense in large islands). Two intense resonances arise at 1943 and 1965 cm^{-1} , related to $\nu(\text{CO})$. Already from this simple experiment, we can already conclude the very different chemical identities of the two cobalt species and, as we'll demonstrate in this chapter, the CoTPyPCo is the only active site for CO adsorption. We can exclude that the observed resonances belong to CO adsorbed on the cobalt nanoclusters on bare graphene since, as we will see in the following paragraph, their associated stretching mode is located above 2000 cm^{-1} . The non-resonant amplitude also changes upon metalation, growing by a factor of

5 (panel B of Fig. 5.1, dotted lines), probably due to the decrease of the HOMO-LUMO gap (see section 3.3). We recall that in this experiment, carried at room temperature, CO spontaneously desorbs because of thermal excitations. Thus, what we measure is a dynamical equilibrium condition, where the actual CO average coverage results from the balanced contribution of adsorption and desorption processes.

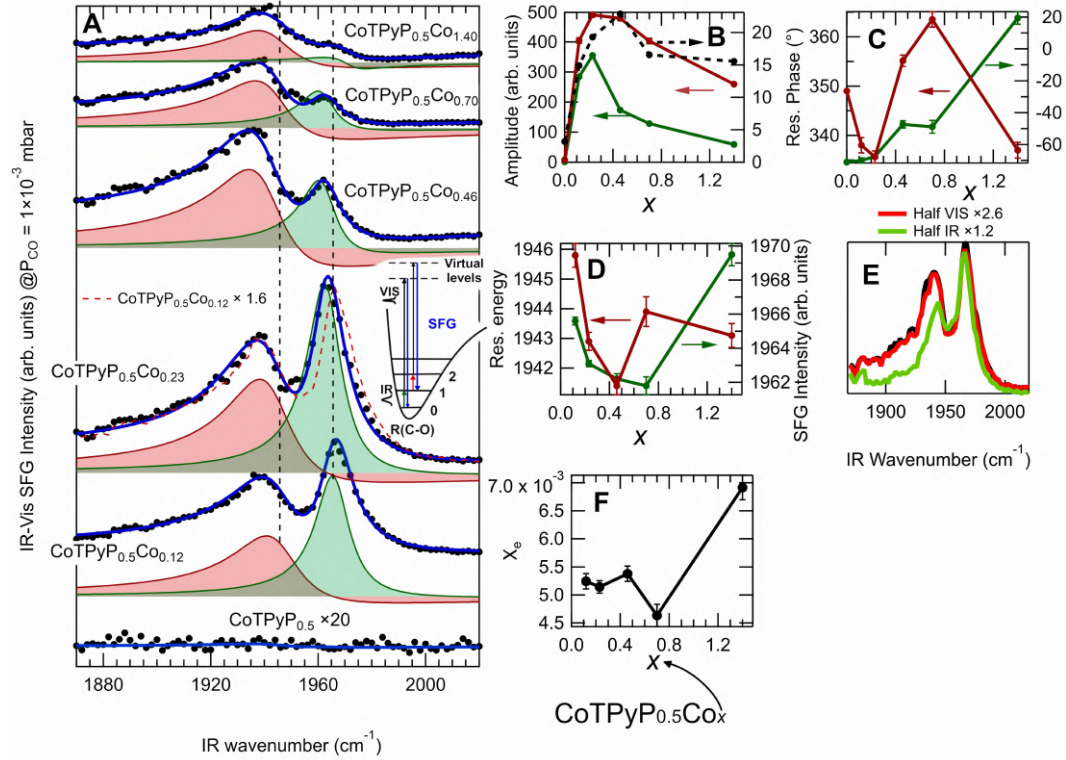


Figure 5.1: A) Normalized IR-Vis SFG spectra of CoTPyP_{0.5}Co_x/Gr/Ir(111) measured *in situ* with a CO pressure of 1×10^{-3} mbar, as a function of evaporated cobalt atom coverage (x); experimental data (black dots), best fitting curve (blue lines), deconvolutions (filled profiles). In the inset, a schematic of the fundamental transition ($0 \rightarrow 1$, $\omega_{01} \sim 1965 \text{ cm}^{-1}$) and the so-called hot-band ($1 \rightarrow 2$, $\omega_{12} \sim 1945 \text{ cm}^{-1}$); B, C, D) show the fitted evolution of amplitudes, phases, and resonant energies, respectively, as a function of x ; E) Comparison between SFG spectra collected with full IR/Vis impulse energy (black line), half IR (green), and half Vis (red) (see text for more details); F) evolution of the anharmonic constant as a function of x .

By increasing the cobalt coverage to 0.23 ML (third spectrum from bottom), the profiles remain identical, apart from a multiplication factor of about $\times 1.6$. This is due, of course, to the increase of concentration of the active sites. On a closer inspection, both resonances slightly shift by about $-2.7 \pm 0.1 \text{ cm}^{-1}$, indicating the slight change of the electronic environment: indeed, in sections 3.2 and 3.3, we have observed (with STM) an ensemble of many CoTPyP_{*n*}Co_{*m*} structures that coexist below Co-saturation.

At higher cobalt dosages (last three spectra in upper Fig. 5.1A), we observe a general decrease of the intensities, probably correlated to a change of the electronic SFG matrix element, also by looking at the parallel decrease of the non-resonant background (panel B, dotted lines). It cannot be caused by the diminution of the squared dynamical dipole moment $(\partial\mu/\partial z)^2$, since our spectra show an intensity decrease at least of a factor of 2, while, for example for CO-Ni(111), only a 15% decrease of $(\partial\mu/\partial z)^2$ has been predicted (and, so, SFG intensity) passing from a 0.08 to 0.14 ML of CO coverage (w.r.t the Ni(111) unit cell), where the minimum distance of the p(2 × 2) CO adsorption pattern (the only one present at $\theta_{CO} < 0.25$ ML) is of about 7 Å, much lower than our case (~ 1.5 nm) [199].

With increasing cobalt coverage, we also observe a spectral weight increase of the lower energy resonance, and changes in the resonant energies and phases of both transitions (panels C and D). The Lorentzian width has been global-fitted with a value of 14.5 ± 0.4 cm⁻¹ for the low- and 7.7 ± 0.2 cm⁻¹ for the high-energy resonance, respectively.

We now discuss the nature of the two peaks. Panel E in Fig. 5.1 shows three spectra, acquired in a condition where both resonances are clearly visible (CoTPy_{0.5}PCo_{0.12}, $P_{CO} = 5 \times 10^{-4}$ mbar): in the red spectrum, the visible impulse energy has been halved, while in the green spectrum the same has been done for the IR pulse, and the black one is collected at IR-Vis full power (~ 250 μJ). Interestingly, while the red curve shows an identical profile compared to the black one, in the green curve the spectral weight of the low-energy resonance is quenched. This behavior, together with the separation in energy between the two resonances, of the order of 20 cm⁻¹, is in great agreement with what has been already observed multiple times in literature [200–203], regarding CO probed by means of SFG with sufficiently high-intensity pulses. The right peak corresponds to the CO fundamental transition, from the ground state to the first excited vibrational state, while the low-energy one corresponds to the transition from the first to the second excited state (see inset in Fig. 5.1A). The latter, often called "hot-band", was observed for the first time by Hess *et al.* in 2000, while studying CO chemisorbed on Ru(001) with SFG, where the hot-band was visible together with the fundamental and even the 2 → 3 transition, already at $\theta_{CO} = 0.006$ ML [201]. Indeed, the IR intensity pulse is strong enough ($\sim 10^7$ W) to cause a population inversion, with the consequent partial population of the first excited state, from where SFG can also occur. The energy difference between consecutive levels in the CO vibrational spectrum that in the harmonic approximation are equispaced, shows in reality a monotonic (decreasing) trend, due to the anharmonicity of the adsorption potential. As a matter of fact, by assuming the Morse oscillator model and calculating the energy correction with first-order perturbation theory, we get the expression for the transition between vibrational level ν and $\nu + 1$:

$$\omega(\nu \rightarrow \nu + 1) = \omega_e(1 - 2\chi_e(1 + \nu)), \quad (5.1)$$

where ω_e is the harmonic frequency and χ_e is the anharmonicity constant [200]. So, considering the transition energies for $0 \rightarrow 1$ and $1 \rightarrow 2$, which we will indicate with ω_{01} and ω_{12} , respectively, and solving for χ_e , we get:

$$\chi_e = \frac{\omega_{01} - \omega_{12}}{2\omega_{01}}. \quad (5.2)$$

By using this equation, we calculated the anharmonic coefficient χ_e as a function of the cobalt coverage, as shown in panel F of Fig. 5.1. As it can be seen, χ_e shows an increasing trend, from 5×10^{-3} to 7×10^{-3} , indicating a tuning of the shape of the CO adsorption potential curve as a function of the Co coverage. For catalytic applications, this is particularly important, since the anharmonic constant is strongly correlated with the C-O dissociation energy. In addition, the Lorentzian widths of the fundamental and hot-band transitions are in remarkable agreement with the values found, for example, for CO/Ru(001), where Hess *et al.* measure (@390 K) $\Gamma_{01} = 8.4 \pm 0.2 \text{ cm}^{-1}$ (fundamental) and $\Gamma_{12} = 14.5 \pm 0.6 \text{ cm}^{-1}$ (hot-band) [201], in spite of the very different coordination environment (a bare metal surface vs. an almost free standing MOF). In particular, they claim that the "excited CO-stretch vibration is generally assumed to decay through electron-hole pair excitation in the metal": since in our case the metal is far from CO and graphene, which is also decoupled, giving only a small contribution to the close-to-Fermi density of states, we could suppose that the main broadening mechanism is temperature-driven, or caused by laser-stimulated deexcitation [201].

Before going on with the analysis, one aspect must be clarified. The hot-band transition can be detected by two mechanisms: via population of $\nu = 1$, or overtone polarization [203]. The first process is dominant, accounting for about 99% of the $1 \rightarrow 2$ transition probability: this means that, in order to see the hot-band, one should tune the IR energy to the fundamental transition. In our case, the IR photon has an energy resolution better than 0.3 cm^{-1} , meaning that, while measuring the hot-band, we just match the Lorentzian tail of the fundamental transition. By contrast, in the literature dealing with CO hot-band, typically broadband IR pulses are used, centered at the fundamental transition energy. The consequence is that the shape and the amplitude of the hot-band transition are distorted with our measurement setup, since they both depend on the intensity of the fundamental transition, the $0 \rightarrow 1$ transition probability, the lifetime in 1, and the energy position where we are measuring (which in turn changes the intensity of the fundamental...). Because of this complex convolution of factors, we decided not to perform any data treatment on the hot-band. Ideally, in a controlled experiment one should use an IR pump, always tuned with the fundamental transition, with fixed intensity, and another IR pulse, involved in the SFG detection of the hot-band, sufficiently weak not to affect the population distribution and sufficiently strong to generate SFG signal with enough statistics. Thus, for the quantitative analysis that will shortly be presented, only the parameters of the fundamental transition reflect a direct physical interpretation.

5.2 CO UPTAKES AT NAP

In the previous section, we have seen how the anharmonicity constant χ_e changes as a function of the MOF electronic structure, i.e. the amount of cobalt loaded into the MOF. We now show how long-range interactions, mediated by the MOF and triggered by CO adsorption, induce measurable variations of χ_e as well, together with a CO non-cooperative adsorption mechanism. For the last point, the Hill and Temkin models have been successfully tested, giving coherent results. We will show how this information can be extracted from the analysis of the CO uptake in pressure, at a fixed Co coverage. Thus, for this experiment, two samples have been prepared *ex novo* to match the same experimental conditions for the second and last spectrum of Fig. 5.1, corresponding to the (CoTPyP_{0.5}Co_{0.12}) and the (CoTPyP_{0.5}Co_{1.40}) MOF layers. In particular, we will demonstrate that, when the Co loading is sufficiently low (and, thus, the CO-CO average distance is sufficiently high) the uptake is compatible with the classical Langmuir (non-cooperative) uptake, and χ_e mildly varies within the error; on the contrary, with more cobalt embedded into the porphyrinic network, the CO adsorption is better described by non-cooperative models, and χ_e shows a monotonic increase (CO-CO distance ~ 1.4 nm).

The CO pressure in the high-pressure SFG cell, during the uptake, has been monitored by a full-range gauge (FRG), composed by a penning cold cathode and a Pirani filament, which can measure from 5×10^{-9} to 1 bar. At the same time, the pressure was also monitored in the main chamber via an adjustable pressure leak in the range between 1×10^{-8} and 1×10^{-7} : in this way, the steadiness of the CO pressure could be doubly checked, with variations less than 5%, and the purity of the SFG cell atmosphere could be constantly checked with a residual gas analyzer. In order to correct for the low reliability of the Pirani reading in its low-pressure range ($\sim 1 \times 10^{-4}$ mbar), a separate calibration has been specifically done, in this range, by simultaneously measuring the SFG cell pressure both *in situ* with the FRG and in the main chamber, by means of a hot gauge, by leaving a small opening between the two chambers. The calibration has been done by assuming as true the reading of the cold-cathode in its high-pressure range (6×10^{-4} mbar), the Pirani reading above 1×10^{-2} mbar (which, according to the constructor, should be correct within 10%), and assuming a linear behavior in between (Fig. A.14 in Appendix).

5.2.1 CO uptake with CoTPyP_{0.5}Co_{0.12}

As shown in Fig. 5.2, IR-Vis SFG spectra have been collected *in situ* on the CoTPyP_{0.5}Co_{0.12} layer exposed to increasing CO pressure, from low 10^{-8} up to 10^{-3} mbar, where the CO coverage is saturated. The SFG spectra cover the CO spectral range (~ 1960 cm⁻¹) and the antisymmetric pyridinic stretching (~ 1610 cm⁻¹), which were the only two ranges showing significant changes during the uptake.

CO Uptake fitting strategy - CO range

In agreement with what already seen at the beginning of this chapter, two resonances monotonically increase, as a function of the CO pressure, at about 1965 and 1950 cm^{-1} , corresponding to the $0 \rightarrow 1$ and $1 \rightarrow 2$ transitions of the CO vibrational levels (Fig. 5.2A). For the first (the fundamental transition) the following fitting strategy has been adopted:

- **Amplitude** A_{01} : free for each spectrum;
- **Phase** ϕ_{01} : free for each spectrum; global-fitted up to 1×10^{-6} mbar;
- **Resonant energy** ω_{01} : free for each spectrum; global-fitted up to 1×10^{-6} mbar;
- **Lorentzian width** Γ_{01} : global-fitted. $\Gamma_{01} = 7.7 \pm 0.05 \text{ cm}^{-1}$.

Regarding the low-energy transition (hot-band) we have:

- **Amplitude** A_{12} : free for each spectrum;
- **Phase** ϕ_{12} : free for each spectrum; global-fitted up to 5×10^{-7} mbar;
- **Resonant energy** ω_{12} : free for each spectrum; global-fitted up to 5×10^{-7} mbar;
- **Lorentzian width** Γ_{12} : global-fitted. $\Gamma_{12} = 13.8 \pm 0.1 \text{ cm}^{-1}$.

Furthermore, as it can be seen, the pumpout spectrum is perfectly flat, sign of the complete reversibility of the adsorption process. In Fig. 5.3, the evolution of the non-constant parameters is shown. In panels **A**) and **B**), the evolution of the fundamental (green) and hot-band (red) resonant amplitudes are fitted with two different adsorption models [204]. The first is the Hill curve that describes cooperative adsorption processes, typically used in the biochemistry, such as the sigmoidal di-oxygen binding curve of hemoglobin. It has the same profile of the Langmuir uptake, but with an n exponent to the pressure (or "ligand concentration", in biochem.):

$$\frac{\theta(P_{CO})}{\theta_{SAT}} = \frac{\frac{s_0 P_{CO}^n}{\rho \sqrt{2\pi m_{CO} m_{at} k_B T}}}{\frac{s_0 P_{CO}^n}{\rho \sqrt{2\pi m_{CO} m_{at} k_B T}} - \nu_0 e^{E_d/k_B T}}, \quad (5.3)$$

where θ_{SAT} is the saturation coverage, n is the Hill coefficient, $m_{CO} = 28 \text{ u}$, $m_{at} = 1.66 \times 10^{-27} \text{ Kg}$, $\rho = 4.4 \times 10^{17} \text{ (porphyrins/m}^2\text{)}$, $k_B = 1.3806 \times 10^{-23} \text{ m}^2 \text{ kg s}^{-2} \text{ K}^{-1}$, $T = 300 \text{ K}$, $\nu_0 = 1 \times 10^{13} \text{ s}^{-1}$ (fixed in order to avoid crosstalk with E_d), $s_0 = 1$ (sticking coefficient), E_d is the desorption energy, and pressure is expressed in Pa. The Hill coefficient is equal to one for non-cooperative adsorption (Langmuir case), $n > 1$ for cooperative adsorption, and $n < 1$ for anti-cooperative adsorption. In panel **A**, both fundamental and hot-band curves are well fitted with the Hill model: the fundamental has $n = 1.03 \pm 0.02$ and, thus, it is compatible with a Langmuir uptake. This is reasonable, since we expect at such low

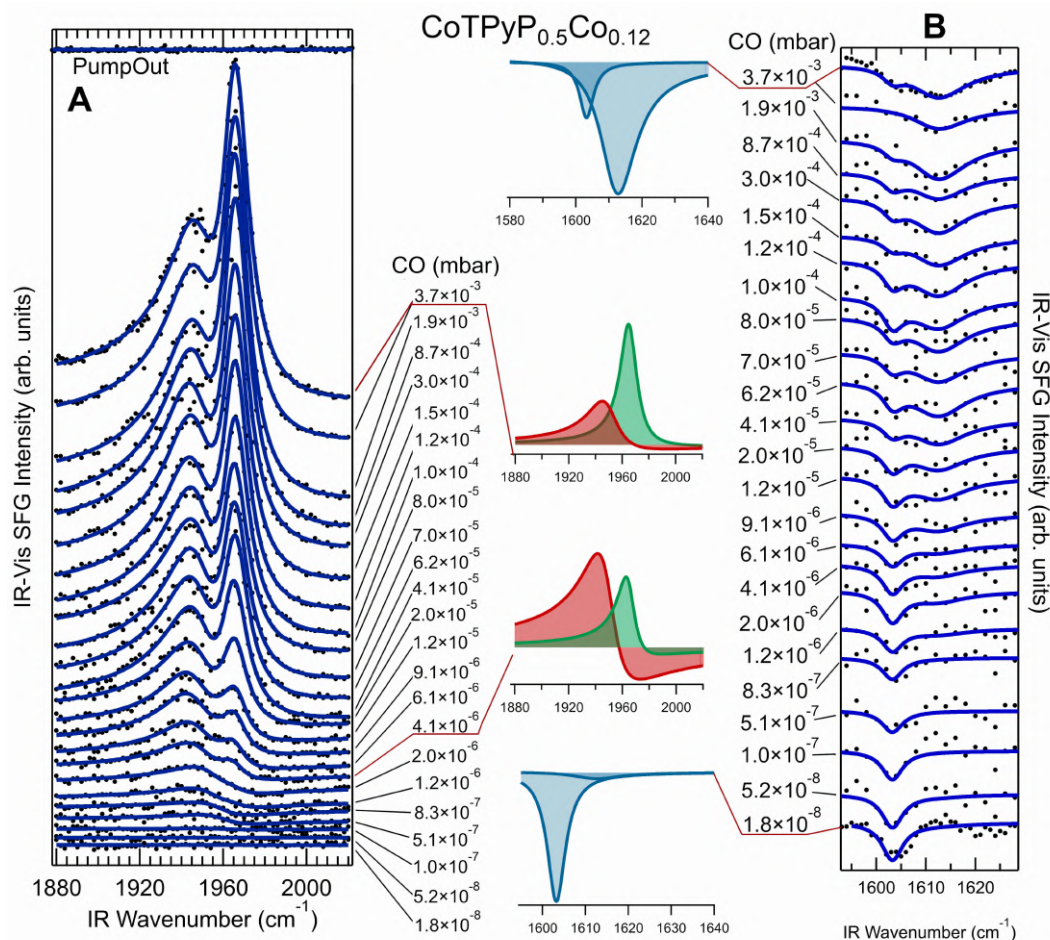


Figure 5.2: Normalized IR-Vis SFG spectra collected *in situ* on the CoTPyP_{0.5}Co_{0.12} submonolayer, in **A**) the CO range and in **B**) the pyridyl antisymmetric bending range at the selected CO pressures ($\omega_1 = 1603 \text{ cm}^{-1}$, $\phi_1 = 88^\circ$, $\Gamma_1 = 2.6 \text{ cm}^{-1}$; $\omega_2 = 1612 \text{ cm}^{-1}$, $\phi_2 = 79^\circ$, $\Gamma_2 = 6.5 \text{ cm}^{-1}$). The raw data (black dots) are shown together with best fitting curve (blue lines), and deconvolutions for the indicated pressure values (filled profiles).

cobalt loading not to have relevant coupling between the distant Co adsorption sites; the desorption energy is $E_d = 0.698 \pm 0.003 \text{ eV}$ (indeed, CO desorbs from the MOF at room temperature) and an additional 0.02 eV error must be taken into account if we consider a systematic error of 10% on the pressure reading. The hot-band curve is well fitted with a Hill coefficient less than one but, as mentioned at the beginning of the chapter, the amplitude analysis of this fourth-order transition is tricky and won't be considered as reliable. Besides, it is clear that, from a physical point of view, the two transitions must have the same evolution since they belong to the same CO molecule and, as a consequence, the same Hill coefficient.

We used a second cooperative model - the Temkin model - in order to check the coherence with the Hill model and extract additional quantitative information, such as the

change in adsorption energy [204]. The Temkin model is a Langmuir model where the desorption energy (or adsorption energy, if the activation barrier is absent) changes with coverage according to the following expression:

$$E_d(\theta) = E_d^0(1 + \alpha_T \theta / \theta_{SAT}), \quad (5.4)$$

where α_T is the Temkin coefficient and E_d^0 is the adsorption energy in the low-coverage limit. Positive values of α_T yield cooperative adsorption, while negative values imply anti-cooperativity. So, the CO coverage at equilibrium reads:

$$\frac{\theta(P_{CO})}{\theta_{SAT}} = \frac{\frac{s_0 P_{CO}}{\rho \sqrt{2\pi m_{CO} m_{at} k_B T}}}{\frac{s_0 P_{CO}}{\rho \sqrt{2\pi m_{CO} m_{at} k_B T}} - \nu_0 e^{E_d^0(1 + \alpha_T \theta / \theta_{SAT}) / k_B T}}, \quad (5.5)$$

which cannot be solved analytically. We used an iterative approach where we construct a θ_k sequence with the following property: $\lim_{k \rightarrow \infty} \theta_k(P_{CO}) = \theta(P_{CO})$: once a certain P_{CO} value is fixed, the $k = 0$ term is calculated by using the Langmuir expression, and the k -th value is calculated by recalling the $k - 1$ term in this way:

$$\frac{\theta_k(P_{CO}, \theta_{k-1})}{\theta_{SAT}} = \frac{\frac{s_0 P_{CO}}{\rho \sqrt{2\pi m_{CO} m_{at} k_B T}}}{\frac{s_0 P_{CO}}{\rho \sqrt{2\pi m_{CO} m_{at} k_B T}} - \nu_0 e^{E_d^0(1 + \alpha_T \theta_{k-1} / \theta_{SAT}) / k_B T}}. \quad (5.6)$$

The iteration is stopped when the relative difference between θ_{k-1} and θ_k is less than 0.1%. The fit results, reported in panel B, are compatible with the Hill model: indeed, for the fundamental transition, the α_T coefficient is compatible with zero ($\alpha_T = 0.002 \pm 0.002$), indicating and confirming a non-cooperative uptake, and E_d is compatible within 6 meV with the previous model. The evolution of the hot-band amplitude is also compatible with the Hill model, with a negative Temkin parameter. It must be pointed out that the compatibility with a Langmuir curve, for both models, is also a test to verify the goodness of the pressure calibration procedure and data analysis, which is needed to justify and corroborate the results reported in the following section, where the high-cobalt coverage case is treated.

The resonance phases and energies are plotted in panel C of Fig. 5.3. While the fundamental transition does not exhibit, within the error, any shift in energy nor phase, the hot-band shows slight drift of phase ($\sim 30^\circ$) and energy ($\sim 5 \text{ cm}^{-1}$), which, in turn, yield a very mild evolution of the anharmonic constant, plotted in panel E (same figure). It must be considered that the potential energy for the CO dipole-dipole interaction, with expression

$$U(r) = \frac{p_{CO}^2}{4\pi\epsilon_0 r^3}, \quad (5.7)$$

has a value of the order of 3×10^{-6} eV, which corresponds to about 0.02 cm^{-1} and, thus, completely negligible (by setting $r = 1.4 \text{ nm}$ and $p_{CO} = 0.112 \text{ D}$) [118]. In addition, dipole-dipole interactions generate a blue-shift, while we observe a mild red-shift of the hot-band [205].

CO Uptake fitting strategy - $\delta_{asym}(Pyr)$ range

In the pyridyl antisymmetric bending region, at about $1580 - 1640 \text{ cm}^{-1}$, the SFG spectra are well fitted by two resonances at 1603 and 1612 cm^{-1} (Fig. 5.2B). The low energy one, with $\Gamma = 2.6 \text{ cm}^{-1}$, is visible in UHV conditions (bottom spectrum), and is compatible with the pyridyl groups non-coordinated with cobalt atom: Both its frequency (1603 cm^{-1}) and width are compatible with the ones observed in the previous UHV analysis. At this cobalt coverage (CoTPyP_{0.5}Co_{0.12}), a larger SFG contribution from this pyridyl species is expected, because of its relative abundance (about 1 : 7) in comparison with the Co-coordinated one. The amplitude of this resonance linearly decreases during the uptake (with CO pressure), as can be seen in Fig. A.15A. The other pyridyl-related feature grows with the CO pressure, and does not show changes in energy, nor phase, and has a wider Lorentzian width ($\Gamma = 6.5 \text{ cm}^{-1}$). The amplitude of the resonance at 1612 cm^{-1} is plotted, as a function of the CO pressure, together with those of the CO vibrational transitions (white-filled dots in Fig. 5.3A-B): interestingly, they overlap, a further indication of the ligation of CO to CoTPyPCo. Finally, the Non-Resonant background of both CO- and pyridyl-ranges are compared in panel D of Fig. 5.3, showing an identical trend. A separate fit of the pyridyl-range uptake has been done by using only one resonance, as reported in Fig. A.15B: the fit is still good, but the nonphysical increase of the Lorentzian width from 2.5 to 10 cm^{-1} allowed us to exclude this latter model (Fig. A.15C).

5.2.2 CO uptake with CoTPyP_{0.5}Co_{1.4}

The same experiment has been repeated with a cobalt coverage of 1.4 ML . On this layer (CoTPyP_{0.5}Co_{1.40}) STM showed a high percentage of Co-saturation (see section 3.3.1), with a consequent decrease of the mean distance between non-equivalent CO adsorption sites. As we shall see, this reflects in important changes in the evolution of the hot-band and, correspondingly, of χ_e . Again, the analysis of the pyridinic modes shows a trend correlated with the CO amplitude evolution, similarly to what already observed in the CoTPyP_{0.5}Co_{0.12}, a further confirmation of CoTPyPCo as the active site.

CO Uptake fitting strategy - CO range

Similarly to the previous case, when the CoTPyP_{0.5}Co_{1.4} layer is exposed to CO, both the CO fundamental and hot-band resonances grow, as a function of pressure, starting from 10^{-7} mbar and reaching saturation in the low 10^{-2} mbar , almost one order of magnitude above the previous case (Fig. 5.4A). This time, because of the considerable amount of cobalt clusters on bare graphene, the SFG signal coming from CO/Co/Gr/Ir(111) must be taken into account: for this purpose, SFG spectra have been collected in an extended pressure range from 1800 up to 2200 cm^{-1} (see Fig. A.16): the high-energy resonance (blue filled profiles in Fig. 5.4A), which blue-shifts from 2015 cm^{-1} (at 10^{-8} mbar) up to

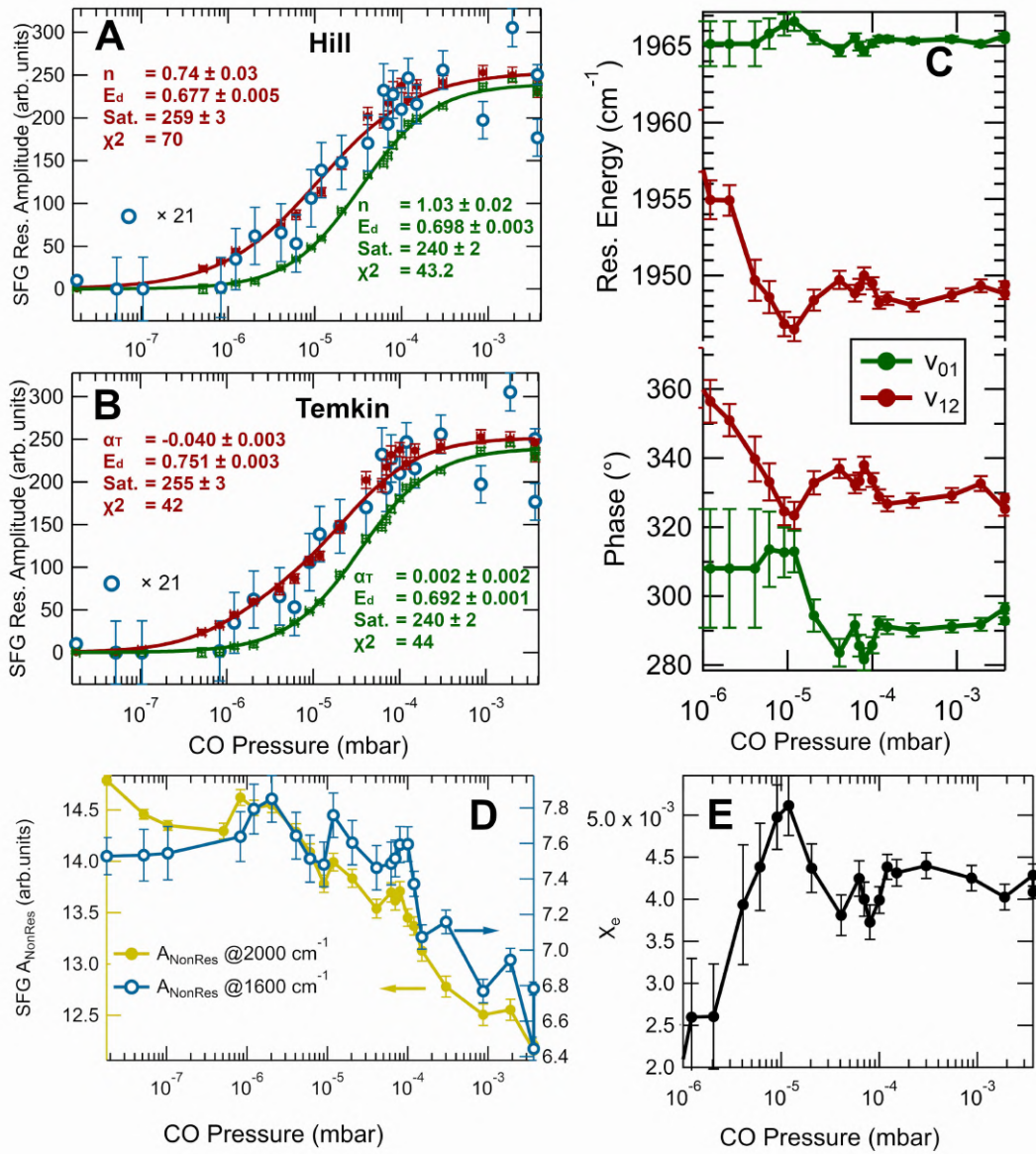


Figure 5.3: Evolution of the SFG fitting parameters of Fig. 5.2. **A-B)** Resonant amplitudes of the fundamental (green) and hot-band (red) CO transition, whose evolutions are fitted in the two panels with two different uptake models (solid lines), together with the evolution of the pyridinic resonance at 1612 cm^{-1} (blue filled dots), **C)** Phase and Resonant energy, and **D)** Non-Resonant amplitude evolution. In panel **E)**, the measured anharmonic constant χ_e is plotted as a function of the CO uptake pressure. [E_d]=[eV].

2052 cm^{-1} (at 10^{-2} mbar) because dipole-dipole interactions is attributed to CO adsorbed on Co clusters [206]. We can exclude the presence of CO intercalated under graphene essentially for two reasons: firstly, we have observed in our setup CO intercalation (at about 2040 cm^{-1}) under graphene only above 1 mbar after several tens of minutes of

exposure, and even without the porphyrin layer which could act as cap; secondly, two subsequently acquired spectra, taken at the saturation pressure of 2×10^{-2} mbar, show no progressive evolution of the signal, meaning that there is no CO accumulation and, thus, excluding intercalation. The spectra including CO/Co have been fitted separately, and the fitting parameters corresponding to such resonance ($\phi_{CO/Co}$, $\omega_{CO/Co}$, $\Gamma_{CO/Co}$) have been linearly interpolated for the selected pressures in Fig. 5.4A, with the release of amplitude only. It must be noticed that there is a slight fit discrepancy in the $1960 - 1970 \text{ cm}^{-1}$ range for the spectra up to 4×10^{-6} mbar. This is maybe due to the presence of additional CO adsorbed on the cluster's edges [206] and it has not been fitted to avoid overfitting. In fact, the discrepancy is very small, and it only affects the amplitude of the hot-band, which is non-zero already in low 10^{-8} mbar and, thus, the corresponding amplitude evolution presents a non-zero background. For this reason, the hot-band phase (ϕ_{12}) and the energy position (ω_{12}) have been locked together for the spectra collected up to 4×10^{-6} mbar. It is also important to notice that this fitting discrepancy has no influence regarding the most important results of this section (i.e. χ_e evolution and anti-cooperative adsorption), since the evolution of χ_e is studied for $P_{CO} > 1 \times 10^{-5}$ mbar, as well as the growth of the fundamental resonance, as we shall see in a moment.

Thus, given these latter considerations, the following fit strategy has been adopted: for the fundamental CO transition we have

- **Amplitude** A_{01} : free for each spectrum, zero up to 4×10^{-6} mbar;
- **Phase** ϕ_{01} : global-fitted, $\phi_{10} = 349 \pm 1^\circ$;
- **Resonant energy** ω_{01} : global-fitted, $\omega_{10} = 1967.8 \pm 0.1 \text{ cm}^{-1}$;
- **Lorentzian width** Γ_{01} : fixed to the value found in the previous experiment, $\Gamma_{10} = 7.7 \text{ cm}^{-1}$,

while for the hot-band:

- **Amplitude** A_{12} : free for each spectrum;
- **Phase** ϕ_{12} : free for each spectrum; global-fitted up to 1×10^{-6} mbar;
- **Resonant energy** ω_{12} : free for each spectrum; global-fitted up to 4×10^{-6} mbar;
- **Lorentzian width** Γ_{12} : fixed to the value found in the previous experiment, $\Gamma_{12} = 13.8 \text{ cm}^{-1}$.

In Fig.5.5, the evolution of the non-constant parameters is shown: in panel **A**, **B**, and **C** the amplitudes of the fundamental (green) and hot-band (red) resonant amplitudes are fitted with the Langmuir (Hill with fixed to $n = 1$), the Hill, and the Temkin model, respectively. At a first glance, all three models seem to well reproduce the experimental data. But if we focus on the green curve (fundamental transition), we notice that four

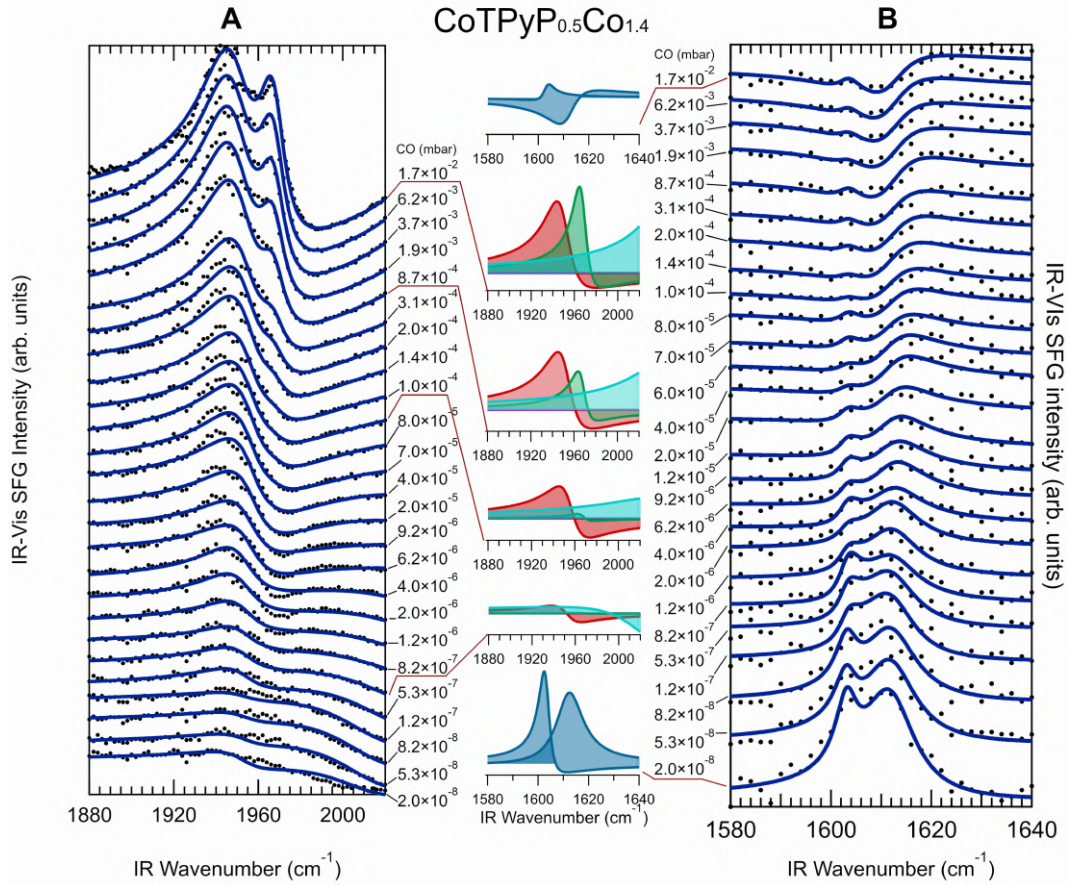


Figure 5.4: Normalized IR-Vis SFG spectra collected in situ on the $\text{CoTPyP}_{0.5}\text{Co}_{1.4}$ submonolayer; in **A**) the CO range and in **B**) the pyridyl antisymmetric bending range at the selected CO pressures ($\omega_1 = 1603 \text{ cm}^{-1}$, $\Gamma_1 = 2.6 \text{ cm}^{-1}$; $\omega_2 = 1612 \text{ cm}^{-1}$, $\Gamma_2 = 6.5 \text{ cm}^{-1}$). $\phi_1 = 235 \pm 4^\circ$ except for $P_{\text{CO}} = 2.0 \times 10^{-8} \rightarrow \phi_1 = 273 \pm 9^\circ$; $P_{\text{CO}} = 5.3 \times 10^{-8} \rightarrow \phi_1 = 280 \pm 8^\circ$; $P_{\text{CO}} = 8.2 \times 10^{-8} \rightarrow \phi_1 = 272 \pm 10^\circ$. The raw data (black dots) are shown together with best fitting curve (blue lines), and deconvolutions for the indicated pressure values (filled profiles).

experimental data-points are above the fitting curve, between 1×10^{-4} and 5×10^{-4} mbar, and the following three experimental data-points lie below the fitting curve. In the other two models, instead, only one/two data-points are further than 1σ . Looking at the χ^2 value, also reported in the same panels, the Temkin model results as the best one ($\chi_{\text{Temkin}}^2 = 118$), with a slightly lower value with respect to the Hill ($\chi_{\text{Hill}}^2 = 133$) and a much lower one with respect to the Langmuir ($\chi_{\text{Langmuir}}^2 = 181$). In particular, the Hill coefficient, equal to $n = 0.84 \pm 0.02$, reveals an anti-cooperative adsorption as well as the Temkin coefficient, which is equal to -0.019 ± 0.002 . The maximum difference in adsorption energy ΔE_d , according to equation 5.4, is about $\Delta E_d = 15 \text{ meV}$, which corresponds to about 2% of its zero-coverage limit. This value is typically below the DFT computational error, and experimentally very challenging to measure. Also for this reason, this is the first time, to

our knowledge, that such small value has been measured on a comparable system. Indeed, this is possible thanks to our SFG setup, which can easily measure such systems at the NAP dynamical adsorption/desorption equilibrium, at room temperature, and with the high confidence sample preparation level typical of UHV chambers. The amplitude evolution of the hot-band also shows an anti-cooperative behavior but, as already discussed (see section 5.2.1), it won't be considered meaningful. Another interesting aspect concerns the CO adsorption energy which, on the high-Co-coverage MOF, increases by about 0.015 ± 0.003 eV (Hill model: $E_d = 0.713 \pm 0.005$ eV) and 0.007 ± 0.003 eV (Temkin model: $E_d = 0.760 \pm 0.002$ eV) (considering only the fundamental transitions), a further indication of the MOF electronic structure change upon CoTPyPCo saturation.

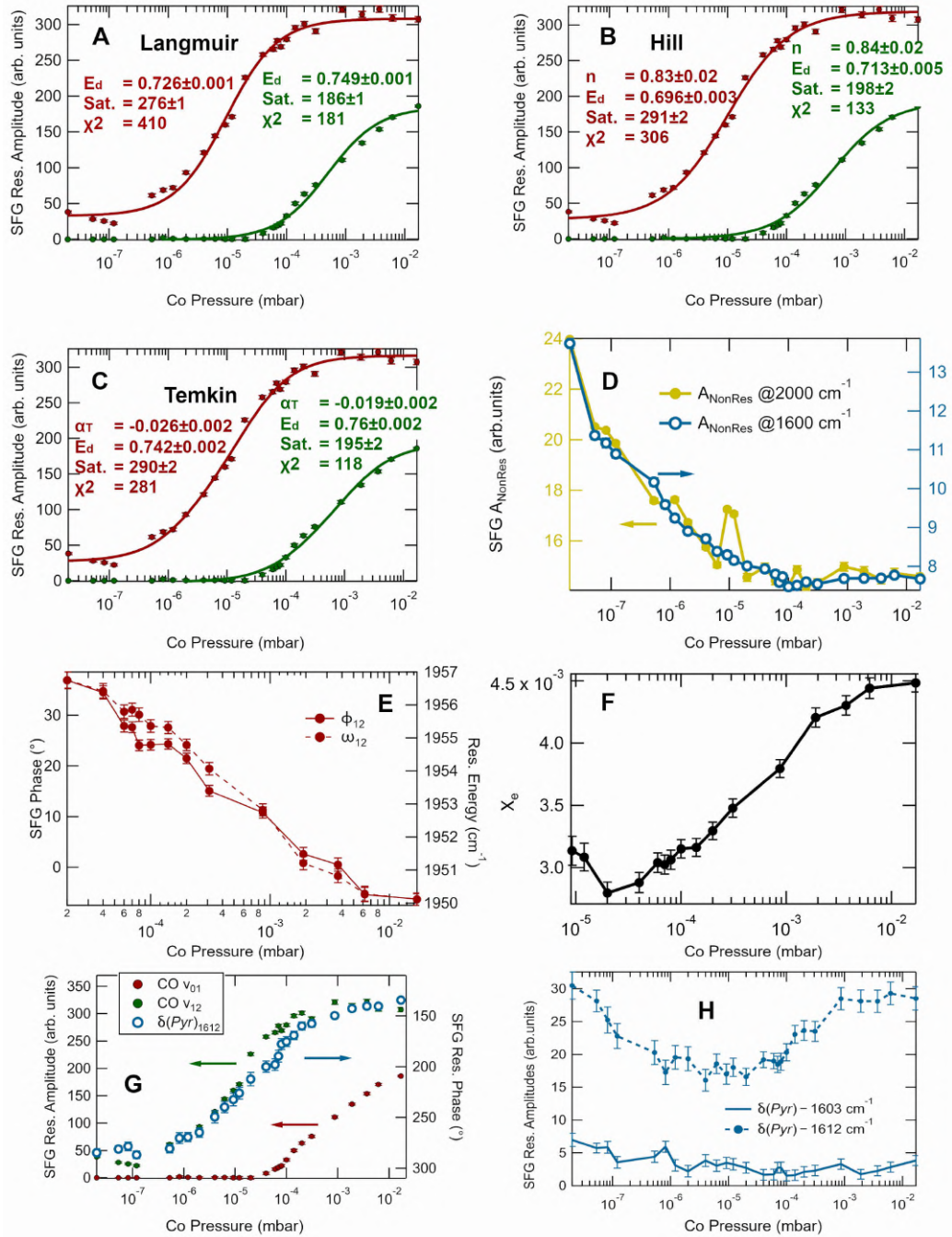


Figure 5.5: Evolution of the SFG fitting parameters of Fig. 5.4. **A-C)** Resonant amplitudes of the fundamental (green) and hot-band (red) CO transition, whose evolutions are fitted in the three panels with the three labeled uptake models (solid lines); **D)** Evolution of the non-resonant background in the 1600 and 2000 cm^{-1} energy range; **E)** evolution of the CO hot-band resonance phase and energy; **F)** evolution of the measured χ_e ; **G)** comparison between the CO-related resonance amplitudes and the pyridinic asymmetric bending phase (at 1612 cm^{-1}); **H)** evolution of the pyridyl-related SFG resonant amplitudes. $[E_d]=[\text{eV}]$.

In panel E, of Fig. 5.5, the evolution of the hot-band phase and resonant energy is shown. They have a similar trend, both substantially changing within the considered pressure range ($\Delta\phi_{12} = 35^\circ$, $\Delta\omega_{12} = 7 \text{ cm}^{-1}$). In particular, the blue-shift of the vibrational energy corresponds to a remarkable evolution of χ_e , shown in panel F, which increases by about 50% from 3.0×10^{-5} to 4.5×10^{-2} mbar. This is coherent with our picture, since in the Co saturated layer we expect a greater interaction, with respect to the unsaturated layer, between the active sites. Also in this case, the uptake series is well fitted with constant energy and phase for the fundamental transition, confirming once again the absence of dipole-dipole interactions as already discussed. The resonant stretching frequency ($1967.8 \pm 0.1 \text{ cm}^{-1}$) is only 3 cm^{-1} larger than the CoTPyP_{0.5}Co_{0.12} case, indicating the lower sensitivity of the fundamental transition, with respect to the hot-band, to the MOF electronic structure changing.

An additional CO uptake curve has been extrapolated by summing the integrals of the two SFG (fundamental and hot-band) resonances (see in Appendix, Fig. A.19). The data have been fitted with the Hill model, which gives $n_{Hill} = 1.25$ for the CoTPyP_{0.5}Co_{0.12} and $n_{Hill} = 0.80$ for the CoTPyP_{0.5}Co_{1.4} monolayers, respectively. As it can be seen, the same anti-cooperative trend is preserved, in agreement with the rest of the analysis. However, the cooperative uptake ($n_{Hill} = 1.25$) observed for the CoTPyP_{0.5}Co_{0.12} is unphysical, since we expect a non-cooperative adsorption for this layer with such diluted active sites. Also for this reason, we proposed the other method as the empirically more appropriate for this part of the analysis.

CO Uptake fitting strategy - $\delta_{asym}(Pyr)$ range

As in section 5.2.1, SFG spectra have been collected in the pyridyl asymmetric bending region ($\sim 1610 \text{ cm}^{-1}$) during the CO uptake. Also in this case, a reversible-with-pump-out evolution of the SFG intensity is clearly visible and related to the parallel CO evolution. The series have been fitted with the same two resonances found in the CoTPy_{0.5}PCo_{0.12} case, at $\omega_1 = 1603$ and $\omega_2 = 1612 \text{ cm}^{-1}$, with the following strategy:

- **Amplitude** A_1 : free for each spectrum;
- **Phase** ϕ_1 : global fitted (see caption of Fig. 5.4);
- **Res. energy** ω_1 : Fixed (1603 cm^{-1})
- **Lorentzian width** Γ_1 : Fixed (2.6 cm^{-1}),

for the low-energy resonance, attributed to non-Co-coordinated pyridyl residues, while for the other (Co-coordinated) pyridyl species:

- **Amplitude** A_2 : free for each spectrum;
- **Phase** ϕ_2 : plotted in Fig. 5.5G;

- **Res. energy** ω_2 : Fixed (1612 cm^{-1})
- **Lorentzian width** Γ_2 : Fixed (6.5 cm^{-1}).

In agreement with our picture, the phase evolution of the 1612 cm^{-1} resonance perfectly matches the evolution of the amplitudes of the CO transitions, as it can be seen in Fig. 5.5G, indicating that one can use this MOF mode as a vibrational benchmark for the CoTPyPCo active site. Furthermore, the intensity ratio of the two resonances is reversed (Fig. 5.5H) with respect to the CoTPy_{0.5}PCo_{0.12}, since in the CoTPy_{0.5}PCo_{1.4} layer we expect a higher number of Co-coordinated pyridyl groups (with respect to non-Co-coordinated ones). Also in this series, the Non-Resonant backgrounds of both CO- and pyridyl-range uptake are compared in panel D of Fig. 5.5, where they, once again, show an identical trend.

5.3 FINAL REMARKS

Before concluding, some additional aspects need to be discussed and clarified.

5.3.1 Comparison with DFT

Ab initio DFT calculations have been performed, in the framework of a collaboration, and we obtained the overall energy gain of the CoTPyP/Gr and the CoTPyP₁Co₁/Gr systems in presence of one or more chemisorbed CO ligands [133]. The iridium underneath has been omitted from the simulation, because of the large computational effort, and since its absence does not affect the outcomes, as discussed in section 3.2.4. The computed adsorption energy values, summarized in Table 5.1, are consistent with the experimental data. In fact, the CO adsorption energy is much larger on the pyridinic cobalt, rather than on the Co embedded in the macrocycle, with an energy difference of almost 1 eV. This is a further confirmation of our experimental results, which show that the CO uptake is correlated with the parallel evolution of the $\delta_{asym}(pyr)$ mode. Regarding the anti-cooperativity, instead, the presence of CO, bonded to adjacent CoTPyPCo adsorption sites does not affect¹ the adsorption energy, with respect to the case where only a single CO is bonded to one of the two sites.

5.3.2 Absence of Förster transfer

It is known that, as well as excitons, also vibrational excitations can be transferred via the non-radiative Förster process, mediated by dipole-dipole interactions. In this model, two oscillators, an acceptor and a donor, can transfer the vibrational energy if their spectral overlap integral $J(\tilde{\nu})$ is different from zero, their relative distance R is sufficiently small,

¹ Within the DFT error considered greater than 0.01 eV

	En. (eV)	#CO	En./CO (eV)
CoTPyP + CoTPyP	0.40	1	0.40
CoTPyP + CoTPyP	0.78	2	0.39
CoTPyPCo + CoTPyPCo		1	0.45
CoTPyPCo + CoTPyPCo	0.90	2	0.45
CoTPyP Co + CoTPyPCo	1.30	1	1.30
CoTPyP Co + CoTPyP Co	2.61	2	1.31
CoTPyPCo + CoTPyPCo	3.44	4	0.86

Table 5.1: *Ab initio* DFT calculations show the energy gain upon adsorption of one or more CO molecules in the $2 \times \text{CoTPyP}(\text{Co})$ unit cell. The unit cell contains two CoTPyP molecules and two additional Co-atom in the saturated CoTPyPCo case. In the first column, the adsorption site, where only one CO is bonded, is indicated with bold font. In the second column, the total energy of the system is reported. In the third column, the total number of CO in the simulation cell is reported. In the last column, the average energy per CO molecule is reported.

the dipoles of the acceptor (μ_A) and of the donor (μ_B) are non-zero, and if the dipole geometrical factor k is also non-zero (for parallel dipoles, $K = 1$) [200]. Indeed, the transfer Förster rate w can be calculated with the following expression:

$$w = \frac{1}{-\hbar^2 c} \cdot \left(\frac{1}{4\pi\epsilon_0} \cdot \frac{k\mu_D\mu_A}{R^3} \right)^2 \int_0^\infty d\tilde{\nu} J(\tilde{\nu}). \quad (5.8)$$

For two normalised Lorentzians at center frequencies ν_1 and ν_2 and respective line widths Γ_1 and Γ_2 , the $J(\tilde{\nu})$ integral term evaluates as [207]:

$$\int_0^\infty d\tilde{\nu} J(\tilde{\nu}) = \frac{1}{\pi} \frac{\Gamma_1 + \Gamma_2}{(\Gamma_1 + \Gamma_2)^2 + (\nu_1 - \nu_2)^2}. \quad (5.9)$$

In our case, even if we supposed the most favorable conditions for the transfer, by setting $\Gamma = 7.7 \text{ cm}^{-1}$ (the lowest value found), a perfect frequency matching ($\nu_1 - \nu_2 = 0$), a perfect dipole alignment $k = 1$, a minimum distance of $R = 14 \text{ \AA}$, and a dipole intensity of $\mu_a = \mu_B = 0.4 \text{ D}$ (one of the strongest found for CO in literature [200]), we find a value for the Förster transfer rate of about $w = (500 \text{ ps})^{-1}$, which is way above our laser pulse duration (FWHM about 20 ps). Another proof of the absence of Förster transfer is that, in presence of such energetic coupling, localized oscillators can be thought as delocalized phonons, with a consequent breaking down of the classical harmonic oscillator levels, in favor of a band structure. This phenomenon, which leads to the merging of the fundamental and $1 \rightarrow 2$ states into a unique band, has already been observed multiple times for CO adsorbed on metal surfaces [200–203]. In our case, we never observe such merging, thus excluding such possibility. Additionally, we neither observe a change in the FWHM of the CO transitions, also correlated to the excitation transfer and consequent reduction of the lifetime. With these last considerations, we demonstrate how the changes in χ_e and the anti-cooperative CO adsorption that cannot be induced by Förster transfer or other

dipole-dipole interactions, are probably driven by the MOF itself. A possible mechanism, for instance, could be the long-range magnetic coupling between metal centers caused by partial magnetization of the organic macrocycle/pyridinic groups, as proposed by Mandal *et al.* [54]. Substrate-induced effects are unlikely to occur, considering the weak coupling that the MOF has with the supporting graphene sheet.

5.3.3 Polarization dependence

IR-Vis SFG spectra have been acquired at selected pressures, close to CO saturation, with different polarization combinations (ppp and ssp) and reported in Appendix (Fig. A.17). The CO ppp/ssp intensity ratio is about 10:1 in the CoTPyP_{0.5}Co_{0.12}, and about 5:1 in the CoTPyP_{0.5}Co_{1.4} layer. This could tentatively be associated with the CO molecule standing more upright in the first case [208], meaning that the change of the MOF's electronic structure would induce also a geometrical adsorption distortion.

5.3.4 χ_e dependence on IR-Vis impulses delay

After the acquisition of the data collected in Fig. 5.1 we observed that there is a dependence of the χ_e as a function of the delay (and, so, effective IR power) between Vis and IR (see Fig. A.18 in Appendix). In particular, for the CoTPyP_{0.5}Co_{0.12} layer, χ_e is constant from -30 up to -15 ps,² and shows a 25% increase when the IR-Vis delay is zero. In order to get rid of this dependence, we decided to measure at -15 ps of delay. To sum up, the data reported in section 5.1 have been collected with zero delay, while all the other dataset with -15 ps of delay. Nevertheless, it is important to remark that all the important outcomes reported in this chapter are trends extracted from spectra collected in identical conditions, where only one parameter (Co coverage or CO pressure) was changing.

5.4 MAIN RESULTS

In this chapter, we studied the CoTPyPCo chemical affinity to CO by means of near ambient pressure *in situ* IR-Vis SFG spectroscopy. Coherently with the UHV chapter, the different chemical identity of the two (CoTPyPCo and CoTPyPCo) cobalt species reflects in a different binding strength for CO, which is almost 1 eV stronger in the case of the pyridinic cobalt. In this way, a sizable CO population is observed by measuring at room temperature and $P_{CO} < 0.01$ mbar. Pressure uptake experiments allowed us to inspect the presence of an anti-cooperative adsorption mechanism, provided that the cobalt saturation is large enough, possibly stemming from long-range electronic interactions: indeed, after careful discussion, CO dipole-dipole interactions and Förster transfer can

² negative delay values mean that the IR impulse hits the sample after the Vis one

be both excluded. Though, the energy associated with the observed anti-cooperative interaction is pretty tiny, of the order of 0.2% (15 meV) of the bonding energy.

6

CONCLUSIONS AND FUTURE PERSPECTIVES

This thesis focuses on the UHV growth and characterization, and on the reactivity to small gases from UHV to near ambient pressure of TPyP-based mono- and bi-metallic 2D MOFs self-assembled on almost free-standing graphene on Ir(111). Indeed, tetra-pyridylporphyrins are already known to be promising single-atom catalysts for the Oxygen Reduction Reaction (ORR), an electrocatalytic process where molecular oxygen is converted into water, of fundamental importance for energy storage and production applications (i.e. fuel cells and metal-air batteries). For this purpose, we exploited a combination of experimental surface science techniques *in vacuo* (STM, NEXAFS, ARPES, XPS, tr-2PPE, and UPS) together with state-of-the-art approaches beyond UHV conditions (IR-Vis SFG, NAP-XPS), corroborated by *ab initio* DFT techniques within the framework of an external collaboration, yielding atomic-level insight into the geometrical, electronic, chemical, and magnetic properties of the layer.

In the first part of the thesis (third chapter), we have characterized the geometry, the electronic states, and some spectroscopic features of the already-metalated porphyrins evaporated on the weakly interacting graphene support in UHV conditions. In particular, we found that such square molecules self-assemble in large islands with an almost hexagonal lattice driven by lateral pyridinic-pyrrolic interactions. We checked that the layers are generally stable up to 250 °C, while at higher temperatures desorption and degradation processes occur. We have also hints of the presence of multiple phases if the layer is grown at lower temperatures, but a systematic study is beyond the purpose of this thesis and will be addressed in future works. Then, we have successfully demonstrated the formation of bimetallic $M_1\text{TPy}M_2$ ($M_{1,2}=\text{Fe, Co}$) monolayers, grown *in vacuo* by physical evaporation of the transition metal atoms on the metalloporphyrin layer. We have found complementary spectroscopic fingerprints of the metal bonding by all exploited techniques. For the CoTPyPCo case, the fine details of the electronic structure have been successfully examined by direct comparison of STS maps with DFT simulations. Thanks to the weakly interacting support, we observe a complete change in the molecular arrangement, passing from a hexagonal closed package to a square lattice. Furthermore, we observed a remarkable chemical inequivalence between the two different metal species in the homo-bi-metallic compounds that, as we have shown in the last chapter, is intimately connected to the chemical affinity of the MOF. Real-space imaging showed the coexistence of multiple chiral structures, in the cobalt unsaturated regions, driven by long-range (> 1.5 nm) interactions, which, together with the MOF growth dynamics, could be an interesting topic for future work (to be tackled, for example, with molecular dynamics and fast-scanning STM studies). In addition, all experimental techniques converge in an

important influence of the pyridyl-coordinated on the macrocyclic metal, resulting in a rigid shift (~ 0.7 eV) of all electronic states of the porphyrin. This is important because it could be at the basis of the long-range interactions observed multiple times in this thesis. We found that this effect can be only partially reproduced by DFT, which predicts a shift of only 0.2 eV.

In the fourth chapter of this thesis, we exposed a CoTPyP/Gr/Ir(111) monolayer to a mixture of water and oxygen gases (fractions of mbar), and an intense bending mode associated with the hydroperoxyl molecule appeared @1712 cm^{-1} in sum frequency generation spectra collected *in situ*. NAP-XPS measurements performed at the HIPPIE beamline of Max IV confirmed our thesis: the interpretation of the O 1s core level corroborated by DFT calculations is straightforward and one-to-one attribution is provided to the four oxygen species, while the complex Co 2p core level lineshape indicates bonding of the ligand at the cobalt site. Pump-probe SFG then allowed us to directly inspect the stabilizing coupling between the hydroperoxyl and the surrounding water molecules. The detection of this elusive intermediate, directly detected only a few times in literature, is at the core of the Oxygen Reduction Reaction, strategic for many energy production and storage applications. Indeed, the OOH is at the crossroad for the two ORR (two- or four-electron) pathways, yielding either water or hydrogen peroxide.

In the last chapter, we used carbon monoxide as an optimal probe of the fine details of the CoTPyPCo/Gr/Ir(111) local active sites, by investigating the system from UHV to CO near ambient pressure. In more detail, the strong IR pulses, needed for SFG detection, caused a population inversion in the CO vibrational levels, such that also the 1 \rightarrow 2 transition was visible together with the fundamental one. This observation directly leads to the direct measurement of the anharmonicity constant (χ_e), which, as we observed, is affected (up to 50% increase) by long-range MOF-driven interactions, provided that active sites are sufficiently close to each other. In the finely detailed analysis of the SFG amplitude, the CO amplitude uptake curves are - coherently to the observation of anti-cooperativity in the adsorption processes - better fitted by the Hill and the Temkin anticooperative model, with respect to the non-cooperative Langmuir curve. Dipole-dipole effects, including the possibility of Förster vibrational energy transfer, have been excluded after discussion. The parallel uptake of the MOF pyridinic resonance modes, as well as being a vibrational fingerprint for the active site, shows perfect correlation with the CO-related feature and, thus, we can attribute CoTPyPCo as the only active site, in agreement also with the DFT predictions. This experiment reveals to be an effective approach to investigate subtle effects in the MOF chemical affinity, which could be responsible for the remarkable non-linear increase of the electrocatalytic activity for ORR and OER of the bimetallic M_1 TPyPM₂ compounds, which is one of the scientific interests at the basis of this thesis. Recent experiments, performed by our group, have shown how the anharmonicity constant can also be tuned by changing the chemical identity of the metal embedded in the macrocycle, enlarging the parameter space needed for a deeper comprehension of such long-range effects.

A | APPENDIX

A.1 UHV

A.1.1 XPS

	CoTPyP		CoTPyPFe		FeTpyP		FeTPyPFe	
	Value	σ	Value	σ	Value	σ	Value	σ
Γ_1	0.27		0.27		0.27		0.27	
G_1	0.74	0.01	0.67	0.03	0.61	0.02	0.74	0.04
A_1	0.79	0.01	0.53	0.01	0.53	0.003	0.34	0.02
BE_1	398.82	0.002	399.03	0.01	398.48	0.01	398.95	0.02
Γ_2	0.27		0.27		0.27		0.27	
G_2	0.74	0.01	0.67	0.03	0.61	0.02	0.74	0.04
A_2	0.79	0.01	0.53	0.01	0.53	0.003	0.34	0.02
BE_2	399.10	0.01	399.43	0.02	398.94	0.01	399.49	0.02
Γ_3	0.27		0.27		0.27		0.27	
G_3	2.10		2.10		1.34		1.34	0.14
A_3	0.21	0.01	0.53	0.02	0.06	0.01	0.30	0.04
BE_3	400.31	0.08	400.28	0.04	399.96		400.43	0.07

Table A.1: Best fit parameters of the N1s core level. Γ : Lorentzian width (eV), G : Gaussian width (eV), A : Amplitude (arb. units), BE : Binding Energy (eV). Asymmetry is always set to zero. When the σ is missing, it means that the parameter has been locked to a specific value. Subscripts 1 and 2 refer to iminic and pyridinic N species, respectively, and 3 to non-adiabatic shakeup.

A.1.2 XPS stepwise annealing

	CoTPyP	CoTPyPFe	CoTPyPCo
Γ_1	0.3	0.3	1.2 ± 0.7
G_1	1.7	2.2	2.1 ± 0.6
A_1	0.33	0.48	0.11 ± 0.07
BE_1	780.1	780.7	781.3 ± 0.1
Γ_2	0.3	0.3	1.2 ± 0.07
G_2	2.8	2.2	4.1 ± 1.6
A_2	0.3	0.36	0.044 ± 0.06
BE_2	782.2	782.8	786.3 ± 0.4
Γ_3			1.2 ± 0.07
G_3			0.7 ± 0.6
A_3			0.043 ± 0.01
BE_3			778.8 ± 0.1
Γ_{GS}	0.3	0.3	
G_{GS}	1.7	2.2	
A_{GS}	0.15	0.13	
BE_{GS}	778.9	778.9	

Table A.2: Best fit parameters of the Co $2p_{3/2}$ core level for CoTPyP, CoTPyPFe, and CoTPyPCo. Γ : Lorentzian width (eV), G : Gaussian width (eV), A : Amplitude (arb. units), BE : Binding Energy (eV). Asymmetry is always set to zero. Numerical subscripts account for the multiplet splitting and shake up, and GS refers to the Gunnarsson and Schönhammer resonance. When not explicitly written, the error on binding energy is about 30 meV, and on Gaussian widths and amplitudes is about 10% of the value.

	FeTPyP	CoTPyPFe
Γ_1	0.3	0.3
G_1	1.1	4.0
A_1	0.3	0.39
BE_1	709.0	711.4
Γ_2	0.3	0.3
G_2	1.1	2.2
A_2	0.16	0.85
BE_2	710.1	714.3
Γ_3	0.3	
G_3	2.6	
A_3	0.012	
BE_3	712.4	
Γ_{GS}	0.3	0.3
G_{GS}	1.1	2.57
A_{GS}	0.19	0.073
BE_{GS}	707.9	708.2

Table A.3: Best fit parameters of the Fe $2p_{3/2}$ core level for FeTPyP and CoTPyPFe. Γ : Lorentzian width (eV), G : Gaussian width (eV), A : Amplitude (arb. units), BE : Binding Energy (eV). Asymmetry is always set to zero. Numerical subscripts account for the multiplet splitting and shake up, and GS refers to the Gunnarsson and Schönhammer resonance. Error on binding energy is about 30 meV, on Gaussian widths and amplitudes is about 10% of the value.

	300 K		470 K		550 K		650 K		970 K	
	Value	σ								
Γ_1	0.27		0.27		0.27		0.27		0.27	
G_1	0.73	0.07	0.73	0.06	0.72	0.05	0.71	0.30	0.71	0.30
A_1	0.83	0.02	0.79	0.02	0.73	0.02	0.08	0.01	0.01	0.02
BE_1	398.67	0.06	398.80	0.03	398.76	0.03	398.93	0.11	398.82	
Γ_2	0.27		0.27		0.27		0.27		0.27	
G_2	0.73	0.07	0.73	0.06	0.72	0.05	0.71	0.30	0.71	0.30
A_2	0.83	0.02	0.79	0.02	0.73	0.02	0.08	0.01	0.01	0.02
BE_2	398.90	0.12	399.11	0.07	399.13	0.05	399.31	0.23	399.20	0.23
Γ_3	0.27		0.27		0.27		0.27		0.27	
G_3	2.10		2.10		2.10		2.10		2.10	
A_3	0.36	0.02	0.30	0.02	0.34	0.02	0.05	0.02	0.13	0.02
BE_3	399.82	0.09	399.95	0.09	399.95	0.09	400.07	0.09	399.97	0.09
Γ_4	0.27		0.27		0.27		0.27		0.27	
G_4	1.00		1.00		1.00		1.00		1.00	
A_4	0.00		0.00		0.00		0.03	0.01	0.01	0.01
BE_4	402.02	0.06	402.15	0.06	402.15	0.06	402.28	0.06	402.17	0.06
Γ_5	0.27		0.27		0.27		0.27		0.27	
G_5	1.03	0.14	1.03	0.14	1.03	0.14	1.03	0.14	1.03	0.14
A_5	0.00	0.03	0.00	0.03	0.00	0.03	0.00	0.02	0.25	0.05
BE_5	398.27	0.07	398.40	0.07	398.36	0.07	398.53	0.07	398.40	0.07

Table A.4: Best fit parameters of N 1s core level spectra of the CoTPyP/Gr/Ir(111) stepwise annealing experiment. Γ : Lorentzian width (eV), G : Gaussian width (eV), A : Amplitude (arb. units), BE : Binding Energy (eV). Asymmetry is always set to zero. When the σ is missing, the parameter has been locked to a specific value. Subscripts 1 and 2 refer to iminic and pyridinic N species, respectively, 3 to non-adiabatic shakeup, 4 to graphitic N, and 5 to N atoms strongly interacting with substrate.

	300 K		550 K		600 K		650 K		700 K		970 K	
	Value	σ										
Γ_1	0.27		0.27		0.27		0.27		0.27		0.27	
G_1	0.60	0.02	0.61	0.03	0.64	0.05	0.71	0.16	0.71	0.16	0.71	0.16
A_1	0.53	0.01	0.45	0.01	0.27	0.01	0.07	0.01	0.05	0.01	0.00	0.01
BE_1	398.50	0.01	398.62	0.01	398.58	0.02	398.70	0.06	398.70	0.06	398.70	0.06
Γ_2	0.27		0.27		0.27		0.27		0.27		0.27	
G_2	0.60	0.02	0.61	0.03	0.64	0.05	0.71	0.16	0.71	0.16	0.71	0.16
A_2	0.53	0.01	0.45	0.01	0.27	0.01	0.07	0.01	0.05	0.01	0.00	0.01
BE_2	398.96	0.01	399.06	0.01	399.06	0.02	399.18	0.02	399.18	0.02	399.18	0.02
Γ_3	0.27		0.27		0.27		0.27		0.27		0.27	
G_3	1.34		1.34		1.34		1.34		1.34		1.34	
A_3	0.05	0.01	0.13	0.01	0.04	0.01	0.00	0.01	0.01	0.01	0.01	0.01
BE_3	399.98		400.10		400.06		400.18		400.18		400.18	
Γ_4	0.27		0.27		0.27		0.27		0.27		0.27	
G_4	1.00	0.39	1.00	0.39	1.00	0.39	1.00	0.39	1.00	0.39	1.00	0.39
A_4	0.00	0.02	0.00	0.02	0.00	0.02	0.00	0.02	0.04	0.03	0.04	0.03
BE_4	398.20	0.26	398.32	0.26	398.28	0.26	398.40	0.26	398.40	0.26	398.40	0.26

Table A.5: Best fit parameters of N 1s core level spectra of the FeTPyP/Gr/Ir(111) stepwise annealing experiment. Γ : Lorentzian width (eV), G : Gaussian width (eV), A : Amplitude (arb. units), BE : Binding Energy (eV). Asymmetry is always set to zero. When the σ is missing, the parameter has been locked to a specific value. Subscripts 1 and 2 refer to iminic and pyridinic N species, respectively, 3 to non-adiabatic shakeup, and 4 to N atoms strongly interacting with substrate.

A.1.3 SFG coverage dependent experiment

CoTPyP/Gr/Ir(111) growth at RT

1200 – 1280 cm^{-1}					
	Graphene	0.1 ML	0.2 ML	0.3 ML	0.4 ML
A_{NR}	0.73 ± 0.01	0.65 ± 0.02	0.81 ± 0.02	0.65 ± 0.02	0.69 ± 0.02
A_1	–	0.4 ± 0.2	0.8 ± 0.2	1.0 ± 0.2	1.4 ± 0.2
$\Delta\Phi_1$	–	201 ± 45	186 ± 22	202 ± 18	187 ± 14
ω_1	–	1240 ± 3	1237 ± 2	1238 ± 1	1238 ± 1
Γ_1	–	3.4 ± 0.3	3.4 ± 0.3	3.4 ± 0.3	3.4 ± 0.3
A_2	–	0.1 ± 0.1	0.3 ± 0.2	0.5 ± 0.2	0.7 ± 0.2
$\Delta\Phi_2$	–	329 ± 106	35 ± 38	45 ± 25	47 ± 16
ω_2	–	1212 ± 5	1215 ± 2	1215 ± 1	1215 ± 1
Γ_2	–	2.2 ± 0.5	2.2 ± 0.5	2.2 ± 0.5	2.2 ± 0.5

	0.5 ML	0.6 ML	0.7 ML	0.8 ML
A_{NR}	0.49 ± 0.02	0.52 ± 0.02	0.41 ± 0.02	0.31 ± 0.02
A_1	1.5 ± 0.2	1.9 ± 0.2	2.1 ± 0.2	1.6 ± 0.2
$\Delta\Phi_1$	194 ± 12	180 ± 11	190 ± 11	197 ± 14
ω_1	1238 ± 1	1237 ± 1	1238 ± 1	1238 ± 1
Γ_1	3.4 ± 0.3	3.4 ± 0.3	3.4 ± 0.3	3.4 ± 0.3
A_2	0.6 ± 0.2	0.7 ± 0.2	0.5 ± 0.2	0.4 ± 0.2
$\Delta\Phi_2$	1 ± 22	16 ± 18	334 ± 32	353 ± 42
ω_2	1214 ± 1	1214 ± 1	1213 ± 1	1215 ± 2
Γ_2	2.2 ± 0.5	2.2 ± 0.5	2.2 ± 0.5	2.2 ± 0.5

Figure A.1: IR-Vis SFG fit parameters of CoTPyP/GR/Ir(111) coverage uptake at room temperature, in the range 1200 – 1280 cm^{-1} . A_{NR} : Non-Resonant Amplitude (arb. units); A_i : i -resonance Amplitude (arb. units); $\Delta\Phi_i$: i -resonance phase ($^\circ$); ω_i : i -resonance frequency (cm^{-1}); Γ_i : i -resonance Lorentzian width (cm^{-1}).

1340 – 1450 cm^{-1}					
	Graphene	0.1 ML	0.2 ML	0.3 ML	0.4 ML
A_{NR}	12.1 ± 0.2	11.7 ± 0.2	12.1 ± 0.2	10.3 ± 0.2	9.9 ± 0.2
A_1	–	4 ± 2	3 ± 2	3 ± 2	5 ± 2
$\Delta\Phi_1$	–	106 ± 25	98 ± 35	90 ± 31	104 ± 22
ω_1	–	1408 ± 1	1408 ± 1	1408 ± 1	1408 ± 1
Γ_1	–	2.4 ± 0.5	2.4 ± 0.5	2.4 ± 0.5	2.4 ± 0.5
A_2	–	0 ± 2	2 ± 2	3 ± 2	4 ± 2
$\Delta\Phi_2$	–	267 ± 223	278 ± 46	245 ± 35	236 ± 26
ω_2	–	1368 ± 1	1368 ± 1	1368 ± 1	1368 ± 1
Γ_2	–	2.1 ± 0.6	2.1 ± 0.6	2.1 ± 0.6	2.1 ± 0.6

	0.5 ML	0.6 ML	0.7 ML	0.8 ML
A_{NR}	8.3 ± 0.2	7.7 ± 0.2	6.3 ± 0.2	5.4 ± 0.1
A_1	6 ± 2	7 ± 2	6 ± 2	7 ± 2
$\Delta\Phi_1$	117 ± 19	116 ± 15	124 ± 16	116 ± 14
ω_1	1408 ± 1	1408 ± 1	1408 ± 1	1408 ± 1
Γ_1	2.4 ± 0.5	2.4 ± 0.5	2.4 ± 0.5	2.4 ± 0.5
A_2	5 ± 2	7 ± 2	7 ± 2	7 ± 2
$\Delta\Phi_2$	226 ± 21	217 ± 16	234 ± 17	226 ± 17
ω_2	1368 ± 1	1368 ± 1	1368 ± 1	1368 ± 1
Γ_2	2.1 ± 0.6	2.1 ± 0.6	2.1 ± 0.6	2.1 ± 0.6

Figure A.2: IR-Vis SFG fit parameters of CoTPyP/GR/Ir(111) coverage uptake at room temperature, in the range 1340 – 1450 cm^{-1} . A_{NR} : Non-Resonant Amplitude (arb. units); A_i : i -resonance Amplitude (arb. units); $\Delta\Phi_i$: i -resonance phase ($^\circ$); ω_i : i -resonance frequency (cm^{-1}); Γ_i : i -resonance Lorentzian width (cm^{-1}).

		1450 – 1760 cm^{-1}								
	Graphene	0.1 ML	0.2 ML	0.3 ML	0.4 ML	0.5 ML	0.6 ML	0.7 ML	0.8 ML	
A_{NR}	11.2 ± 0.3	10.3 ± 0.2	8.7 ± 0.5	7.4 ± 0.2	6.8 ± 0.2	6.6 ± 0.2	5.8 ± 0.2	4.5 ± 0.3	4.1 ± 0.3	
A_1	175 ± 29	205 ± 19	240 ± 32	227 ± 21	272 ± 26	226 ± 21	239 ± 27	128 ± 17	117 ± 17	
$\Delta\Phi_1$	261 ± 8	264 ± 8	264 ± 8	264 ± 8	264 ± 8	264 ± 8	264 ± 8	264 ± 8	264 ± 8	
ω_1	1609 ± 4	1607 ± 3	1607 ± 4	1607 ± 3	1606 ± 3	1610 ± 3	1607 ± 3	1616 ± 3	1616 ± 4	
Γ_1	28 ± 5	28 ± 5	28 ± 5	28 ± 5	28 ± 5	28 ± 5	28 ± 5	28 ± 5	28 ± 5	
A_2	–	7 ± 3	16 ± 6	17 ± 4	23 ± 5	19 ± 4	19 ± 4	15 ± 2	20 ± 3	
$\Delta\Phi_2$	–	65 ± 44	20 ± 34	316 ± 16	312 ± 13	343 ± 14	329 ± 17	233 ± 16	213 ± 14	
ω_2	–	1596 ± 2	1594 ± 1	1591 ± 1	1591 ± 1					
Γ_2	–	2.4 ± 0.3	2.4 ± 0.3	2.4 ± 0.3	2.4 ± 0.3	2.4 ± 0.3	2.4 ± 0.3	2.4 ± 0.3	2.4 ± 0.3	
A_3	–	15 ± 11	30 ± 18	41 ± 11	60 ± 16	61 ± 12	71 ± 14	53 ± 10	50 ± 10	
$\Delta\Phi_3$	–	76 ± 52	58 ± 59	39 ± 22	60 ± 17	45 ± 14	30 ± 15	296 ± 21	295 ± 24	
ω_3	–	1583 ± 8	1582 ± 9	1579 ± 3	1583 ± 2	1581 ± 2	1579 ± 2	1566 ± 3	1567 ± 3	
Γ_3	–	9.2 ± 0.8	9.2 ± 0.8	9.2 ± 0.8	9.2 ± 0.8	9.2 ± 0.8	9.2 ± 0.8	9.2 ± 0.8	9.2 ± 0.8	
A_4	–	8 ± 6	19 ± 8	18 ± 5	19 ± 6	19 ± 6	23 ± 7	31 ± 9	27 ± 8	
$\Delta\Phi_4$	–	244 ± 42	273 ± 85	289 ± 60	283 ± 52	267 ± 49	321 ± 45	296 ± 37	283 ± 43	
ω_4	–	1536 ± 8	1537 ± 11	1538 ± 8	1540 ± 7	1539 ± 7	1541 ± 6	1538 ± 5	1540 ± 6	
Γ_4	–	9.2 ± 0.8	9.2 ± 0.8	9.2 ± 0.8	9.2 ± 0.8	9.2 ± 0.8	9.2 ± 0.8	9.2 ± 0.8	9.2 ± 0.8	
A_5	–	3 ± 6	16 ± 14	18 ± 8	24 ± 8	41 ± 9	53 ± 9	48 ± 8	39 ± 7	
$\Delta\Phi_5$	–	32 ± 98	228 ± 281	3 ± 48	13 ± 34	45 ± 19	61 ± 15	26 ± 17	14 ± 16	
ω_5	–	1499 ± 7	1483 ± 29	1498 ± 6	1499 ± 5	1502 ± 3	1506 ± 2	1501 ± 2	1499 ± 2	
Γ_5	–	9.2 ± 0.8	9.2 ± 0.8	9.2 ± 0.8	9.2 ± 0.8	9.2 ± 0.8	9.2 ± 0.8	9.2 ± 0.8	9.2 ± 0.8	
A_6	–	14 ± 6	22 ± 17	13 ± 7	15 ± 7	15 ± 6	16 ± 6	10 ± 5	10 ± 15	
$\Delta\Phi_6$	–	193 ± 21	278 ± 128	219 ± 52	214 ± 43	171 ± 55	157 ± 49	140 ± 93	46 ± 158	
ω_6	–	1467 ± 7	1473 ± 14	1469 ± 8	1469 ± 7	1466 ± 8	1464 ± 7	1464 ± 12	1453 ± 21	
Γ_6	–	9.2 ± 0.8	9.2 ± 0.8	9.2 ± 0.8	9.2 ± 0.8	9.2 ± 0.8	9.2 ± 0.8	9.2 ± 0.8	9.2 ± 0.8	

Figure A.3: IR-Vis SFG fit parameters of CoTPyP/GR/Ir(111) coverage uptake at room temperature, in the range 1450 – 1760 cm^{-1} . A_{NR} : Non-Resonant Amplitude (arb. units); A_i : i -resonance Amplitude (arb. units); $\Delta\Phi_i$: i -resonance phase ($^\circ$); ω_i : i -resonance frequency (cm^{-1}); Γ_i : i -resonance Lorentzian width (cm^{-1}).

2970 – 3120 cm^{-1}					
	Graphene	0.1 ML	0.2 ML	0.3 ML	0.4 ML
A_{NR}	0.77 ± 0.01	0.69 ± 0.01	0.38 ± 0.01	0.40 ± 0.01	0.36 ± 0.01
A_1	–	0.2 ± 0.2	0.1 ± 0.2	0.3 ± 0.3	0.4 ± 0.3
$\Delta\Phi_1$	–	178 ± 74	213 ± 110	178 ± 60	185 ± 49
ω_1	–	3010 ± 5	3010 ± 5	3010 ± 5	3010 ± 5
Γ_1	–	9 ± 5	9 ± 5	9 ± 5	9 ± 5
A_2	–	1 ± 1	1 ± 1	1 ± 1	2 ± 1
$\Delta\Phi_2$	–	15 ± 56	15 ± 61	10 ± 58	15 ± 53
ω_2	–	3064 ± 3	3064 ± 3	3064 ± 3	3064 ± 3
Γ_2	–	9 ± 3	9 ± 3	9 ± 3	9 ± 3
A_3	–	1 ± 1	1 ± 1	2 ± 2	2 ± 2
$\Delta\Phi_3$	–	139 ± 69	117 ± 73	117 ± 56	125 ± 60
ω_3	–	3053 ± 10	3053 ± 10	3053 ± 10	3053 ± 10
Γ_3	–	16 ± 10	16 ± 10	16 ± 10	16 ± 10

	0.5 ML	0.6 ML	0.7 ML	0.8 ML
A_{NR}	0.56 ± 0.01	0.49 ± 0.02	0.50 ± 0.02	0.52 ± 0.02
A_1	0.6 ± 0.4	0.5 ± 0.3	0.5 ± 0.4	0.2 ± 0.3
$\Delta\Phi_1$	232 ± 39	220 ± 47	235 ± 44	252 ± 88
ω_1	3010 ± 5	3010 ± 5	3010 ± 5	3010 ± 5
Γ_1	9 ± 5	9 ± 5	9 ± 5	9 ± 5
A_2	3 ± 2	3 ± 2	3 ± 2	3 ± 2
$\Delta\Phi_2$	27 ± 43	22 ± 48	28 ± 45	24 ± 44
ω_2	3064 ± 3	3064 ± 3	3064 ± 3	3064 ± 3
Γ_2	9 ± 3	9 ± 3	9 ± 3	9 ± 3
A_3	2 ± 2	2 ± 3	2 ± 3	2 ± 3
$\Delta\Phi_3$	147 ± 69	121 ± 62	129 ± 68	91 ± 72
ω_3	3053 ± 10	3053 ± 10	3053 ± 10	3053 ± 10
Γ_3	16 ± 10	16 ± 10	16 ± 10	16 ± 10

Figure A.4: IR-Vis SFG fit parameters of CoTPyP/GR/Ir(111) coverage uptake at room temperature, in the range 2970 – 3120 cm^{-1} . A_{NR} : Non-Resonant Amplitude (arb. units); A_i : i -resonance Amplitude (arb. units); $\Delta\Phi_i$: i -resonance phase ($^\circ$); ω_i : i -resonance frequency (cm^{-1}); Γ_i : i -resonance Lorentzian width (cm^{-1}).

CoTPyP/Gr/Ir(111) growth at 500 K

1200 – 1280 cm⁻¹				
	Graphene	0.17 ML	0.33 ML	0.5 ML
A_{NR}	0.73 ± 0.01	0.58 ± 0.02	0.68 ± 0.02	0.58 ± 0.02
A_1	–	0.4 ± 0.2	0.9 ± 0.2	1.2 ± 0.2
$\Delta\Phi_1$	–	152 ± 55	195 ± 17	169 ± 14
ω_1	–	1237 ± 3	1238 ± 1	1237 ± 1
Γ_1	–	3.2 ± 0.2	3.2 ± 0.2	3.2 ± 0.2
A_2	–	2.5 ± 0.5	0.4 ± 0.1	2.1 ± 0.4
$\Delta\Phi_2$	–	87 ± 5	55 ± 28	79 ± 5
ω_2	–	1214 ± 3	1215 ± 1	1214 ± 1
Γ_2	–	2.3 ± 0.4	2.3 ± 0.4	2.3 ± 0.4

	0.67 ML	0.8 ML	1 ML
A_{NR}	0.40 ± 0.01	0.41 ± 0.01	0.34 ± 0.02
A_1	1.4 ± 0.2	1.8 ± 0.1	1.5 ± 0.2
$\Delta\Phi_1$	173 ± 9	164 ± 4	177 ± 12
ω_1	1238 ± 1	1237 ± 0	1237 ± 1
Γ_1	3.2 ± 0.2	3.2 ± 0.2	3.2 ± 0.2
A_2	0.4 ± 0.1	0.6 ± 0.1	0.7 ± 0.2
$\Delta\Phi_2$	359 ± 25	335 ± 14	322 ± 21
ω_2	1214 ± 1	1214 ± 1	1214 ± 1
Γ_2	2.3 ± 0.4	2.3 ± 0.4	2.3 ± 0.4

Figure A.5: IR-Vis SFG fit parameters of CoTPyP/GR/Ir(111) coverage uptake at 500 K, in the range 1200 – 1280 cm⁻¹. A_{NR} : Non-Resonant Amplitude (arb. units); A_i : i -resonance Amplitude (arb. units); $\Delta\Phi_i$: i -resonance phase (°); ω_i : i -resonance frequency (cm⁻¹); Γ_i : i -resonance Lorentzian width (cm⁻¹).

1340 – 1450 cm^{-1}				
	Graphene	0.17 ML	0.33 ML	0.5 ML
A_{NR}	0.05 ± 0.01	9.9 ± 0.2	10.7 ± 0.2	9.6 ± 0.2
A_1	–	2.9 ± 1.9	4.3 ± 1.9	4.9 ± 2.0
$\Delta\Phi_1$	–	139 ± 37	131 ± 25	136 ± 23
ω_1	–	1408 ± 1	1408 ± 1	1408 ± 1
Γ_1	–	2.6 ± 0.7	2.6 ± 0.7	2.6 ± 0.7
A_2	–	0.7 ± 1.7	3.0 ± 1.7	3.6 ± 1.7
$\Delta\Phi_2$	–	222 ± 116	257 ± 32	238 ± 26
ω_2	–	1369 ± 1	1369 ± 1	1369 ± 1
Γ_2	–	1.7 ± 0.6	1.7 ± 0.6	1.7 ± 0.6

	0.67 ML	0.8 ML	1 ML
A_{NR}	7.3 ± 0.1	7.2 ± 0.2	6.3 ± 0.1
A_1	4.4 ± 1.9	6.9 ± 2.2	6.5 ± 2.1
$\Delta\Phi_1$	94 ± 24	96 ± 17	87 ± 17
ω_1	1408 ± 1	1408 ± 1	1408 ± 1
Γ_1	2.6 ± 0.7	2.6 ± 0.7	2.6 ± 0.7
A_2	2.9 ± 1.7	6.9 ± 1.9	7.1 ± 1.9
$\Delta\Phi_2$	217 ± 31	215 ± 17	194 ± 15
ω_2	1369 ± 1	1369 ± 1	1369 ± 1
Γ_2	1.7 ± 0.6	1.7 ± 0.6	1.7 ± 0.6

Figure A.6: IR-Vis SFG fit parameters of CoTPyP/GR/Ir(111) coverage uptake at 500 K, in the range 1340 – 1450 cm^{-1} . A_{NR} : Non-Resonant Amplitude (arb. units); A_i : i -resonance Amplitude (arb. units); $\Delta\Phi_i$: i -resonance phase ($^\circ$); ω_i : i -resonance frequency (cm^{-1}); Γ_i : i -resonance Lorentzian width (cm^{-1}).

		1450 – 1760 cm^{-1}					
	Graphene	0.17 ML	0.33 ML	0.5 ML	0.67 ML	0.8 ML	1 ML
A_{NR}	0.05 ± 0.01	9.5 ± 0.3	7.6 ± 0.2	7.3 ± 0.2	4.9 ± 0.2	4.6 ± 0.2	3.6 ± 0.2
A_1	–	141 ± 23	200 ± 13	204 ± 13	156 ± 12	129 ± 12	117 ± 12
$\Delta\Phi_1$	–	264 ± 25	264 ± 25	264 ± 25	264 ± 25	264 ± 25	264 ± 25
ω_1	–	1616 ± 5	1612 ± 2	1610 ± 2	1621 ± 2	1624 ± 2	1639 ± 3
Γ_1	–	28 ± 5	28 ± 5	28 ± 5	28 ± 5	28 ± 5	28 ± 5
A_2	–	7 ± 4	10 ± 2	13 ± 2	12 ± 2	20 ± 2	48 ± 3
$\Delta\Phi_2$	–	89 ± 51	41 ± 15	14 ± 13	278 ± 13	258 ± 8	78 ± 9
ω_2	–	1597 ± 1	1595 ± 1	1594 ± 1	1593 ± 1	1593 ± 1	1595 ± 1
Γ_2	–	1.7 ± 0.2	1.7 ± 0.2	1.7 ± 0.2	1.7 ± 0.2	1.7 ± 0.2	1.7 ± 0.2
A_3	–	12 ± 10	18 ± 5	32 ± 6	35 ± 4	42 ± 5	45 ± 5
$\Delta\Phi_3$	–	210 ± 85	345 ± 28	45 ± 13	306 ± 16	274 ± 14	298 ± 16
ω_3	–	1589 ± 8	1572 ± 3	1580 ± 2	1568 ± 2	1566 ± 2	1567 ± 1
Γ_3	–	6.4 ± 0.4	6.4 ± 0.4	6.4 ± 0.4	6.4 ± 0.4	6.4 ± 0.4	6.4 ± 0.4
A_4	–	6 ± 6	15 ± 4	-15 ± 4	21 ± 4	28 ± 5	25 ± 5
$\Delta\Phi_4$	–	235 ± 109	273 ± 35	244 ± 31	258 ± 26	243 ± 20	200 ± 17
ω_4	–	1535 ± 13	1538 ± 4	1536 ± 4	1539 ± 3	1539 ± 2	1535 ± 2
Γ_4	–	6.4 ± 0.4	6.4 ± 0.4	6.4 ± 0.4	6.4 ± 0.4	6.4 ± 0.4	6.4 ± 0.4
A_5	–	0 ± 8	17 ± 4	19 ± 5	27 ± 4	38 ± 4	39 ± 4
$\Delta\Phi_5$	–	317 ± 1731	314 ± 33	12 ± 22	332 ± 18	330 ± 12	309 ± 15
ω_5	–	1491 ± 202	1493 ± 3	1499 ± 3	1497 ± 2	1498 ± 1	1496 ± 1
Γ_5	–	6.4 ± 0.4	6.4 ± 0.4	6.4 ± 0.4	6.4 ± 0.4	6.4 ± 0.4	6.4 ± 0.4
A_6	–	10 ± 8	12 ± 4	11 ± 5	6 ± 4	8 ± 4	6 ± 4
$\Delta\Phi_6$	–	158 ± 86	233 ± 40	211 ± 33	212 ± 61	175 ± 46	241 ± 69
ω_6	–	1467 ± 10	1469 ± 5	1470 ± 4	1471 ± 8	1468 ± 6	1474 ± 8
Γ_6	–	6.4 ± 0.4	6.4 ± 0.4	6.4 ± 0.4	6.4 ± 0.4	6.4 ± 0.4	6.4 ± 0.4

Figure A.7: IR-Vis SFG fit parameters of CoTPyP/GR/Ir(111) coverage uptake at 500 K, in the range 1450 – 1760 cm^{-1} . A_{NR} : Non-Resonant Amplitude (arb. units); A_i : i -resonance Amplitude (arb. units); $\Delta\Phi_i$: i -resonance phase ($^\circ$); ω_i : i -resonance frequency (cm^{-1}); Γ_i : i -resonance Lorentzian width (cm^{-1}).

2970 – 3120 cm^{-1}				
	Graphene	0.17 ML	0.33 ML	0.5 ML
A_{NR}	0.77 ± 0.01	0.79 ± 0.01	0.71 ± 0.01	0.61 ± 0.01
A_1	–	0.5 ± 0.2	0.4 ± 0.4	0.5 ± 0.2
$\Delta\Phi_1$	–	231 ± 37	274 ± 99	278 ± 33
ω_1	–	3013 ± 5	3022 ± 13	3014 ± 5
Γ_1	–	8 ± 2	8 ± 2	8 ± 2
A_2	–	0.3 ± 0.3	0.4 ± 0.4	0.1 ± 0.4
$\Delta\Phi_2$	–	277 ± 96	116 ± 100	276 ± 435
ω_2	–	3053 ± 9	3045 ± 9	3056 ± 31
Γ_2	–	6 ± 3	6 ± 3	6 ± 3
A_3	–	0.7 ± 0.4	1.4 ± 0.4	1.5 ± 0.7
$\Delta\Phi_3$	–	62 ± 44	57 ± 22	70 ± 34
ω_3	–	3070 ± 6	3068 ± 3	3069 ± 4
Γ_3	–	8 ± 1	8 ± 1	8 ± 1

	0.67 ML	0.8 ML	1 ML
A_{NR}	0.47 ± 0.01	0.53 ± 0.01	0.65 ± 0.02
A_1	0.4 ± 0.2	0.4 ± 0.2	0.8 ± 0.3
$\Delta\Phi_1$	306 ± 41	244 ± 49	258 ± 32
ω_1	3019 ± 6	3011 ± 7	3012 ± 4
Γ_1	8 ± 2	8 ± 2	8 ± 2
A_2	0.5 ± 0.6	0.6 ± 0.4	0.8 ± 0.5
$\Delta\Phi_2$	187 ± 64	235 ± 82	234 ± 53
ω_2	3054 ± 5	3054 ± 6	3053 ± 4
Γ_2	6 ± 3	6 ± 3	6 ± 3
A_3	2.2 ± 0.7	2.1 ± 0.5	2.4 ± 0.6
$\Delta\Phi_3$	56 ± 17	81 ± 24	108 ± 22
ω_3	3065 ± 2	3067 ± 2	3069 ± 2
Γ_3	8 ± 1	8 ± 1	8 ± 1

Figure A.8: IR-Vis SFG fit parameters of CoTPyP/GR/Ir(111) coverage uptake at 500 K, in the range 2970 – 3120 cm^{-1} . A_{NR} : Non-Resonant Amplitude (arb. units); A_i : i -resonance Amplitude (arb. units); $\Delta\Phi_i$: i -resonance phase ($^\circ$); ω_i : i -resonance frequency (cm^{-1}); Γ_i : i -resonance Lorentzian width (cm^{-1}).

A.1.4 SFG CoTPyP/Gr/Ir(111) Thermal Annealing

1200 – 1280 cm^{-1}					
	Graphene	300 K	420 K	470 K	550 K
A_{NR}	0.34 ± 0.01	0.14 ± 0.02	0.01 ± 0.09	0.01 ± 0.15	0.05 ± 0.06
A_1	–	1.3 ± 0.3	0.7 ± 1.3	0.9 ± 1.7	1.7 ± 0.3
$\Delta\Phi_1$	–	256 ± 50	349 ± 968	248 ± 1376	113 ± 47
ω_1	–	1239 ± 1	1239 ± 3	1239 ± 2	1239 ± 1
Γ_1	–	3.7 ± 0.7	3.7 ± 0.7	3.7 ± 0.7	3.7 ± 0.7
A_2	–	0.8 ± 1.3	0.3 ± 1.4	0.4 ± 1.4	0.8 ± 0.3
$\Delta\Phi_2$	–	132 ± 193	159 ± 1155	96 ± 2398	100 ± 100
ω_2	–	1215 ± 1	1215 ± 4	1215 ± 3	1216 ± 1
Γ_2	–	2.2 ± 0.7	2.2 ± 0.7	2.2 ± 0.7	2.2 ± 0.7
1340 – 1450 cm^{-1}					
	Graphene	300 K	420 K	470 K	550 K
A_{NR}	6.47 ± 0.08	4.04 ± 0.10	2.75 ± 0.06	2.44 ± 0.02	2.70 ± 0.05
A_1	–	9.7 ± 1.6	3.7 ± 1.0	1.4 ± 0.6	0.7 ± 0.8
$\Delta\Phi_1$	–	202 ± 12	223 ± 14	226 ± 18	232 ± 61
ω_1	–	1409 ± 1	1409 ± 1	1409 ± 1	1409 ± 1
Γ_1	–	3.8 ± 0.8	3.8 ± 0.8	3.8 ± 0.8	3.8 ± 0.8
A_2	–	4.8 ± 1.3	1.8 ± 0.8	1.1 ± 0.5	2.6 ± 0.8
$\Delta\Phi_2$	–	294 ± 16	288 ± 21	263 ± 21	236 ± 16
ω_2	–	1369 ± 1	1369 ± 1	1369 ± 1	1369 ± 1
Γ_2	–	2.5 ± 0.7	2.5 ± 0.7	2.5 ± 0.7	2.5 ± 0.7

Figure A.9: IR-Vis SFG fit parameters of the CoTPyP/GR/Ir(111) monolayer stepwise annealing experiment, in the range of 1200 – 1280 and 1340 – 1450 cm^{-1} . A_{NR} : Non-Resonant Amplitude (arb. units); A_i : i -resonance Amplitude (arb. units); $\Delta\Phi_i$: i -resonance phase ($^\circ$); ω_i : i -resonance frequency (cm^{-1}); Γ_i : i -resonance Lorentzian width (cm^{-1}).

A.1.5 SFG CoTPyPCo/Gr/Ir(111)

1450 – 1760 cm^{-1}					
	Graphene	300 K	420 K	470 K	550 K
A_{NR}	5.92 ± 0.13	3.96 ± 0.04	2.32 ± 0.03	2.68 ± 0.02	2.54 ± 0.03
A_1	49.1 ± 50.7	46.3 ± 2.0	21.4 ± 1.4	0.1 ± 0.9	0.4 ± 1.2
$\Delta\Phi_1$	237 ± 48				
ω_1	1640 ± 8	1635 ± 1	1635 ± 1	1635 ± 1	1635 ± 1
Γ_1	14 ± 2				
A_2	52.7 ± 51.3	82.6 ± 2.5	52.8 ± 1.6	0.1 ± 0.9	0.3 ± 1.6
$\Delta\Phi_2$	333 ± 45				
ω_2	1625 ± 8	1620 ± 1	1620 ± 1	1620 ± 1	1620 ± 1
Γ_2	14 ± 2				
A_3	–	31.5 ± 0.5	23.6 ± 0.4	12.6 ± 0.3	34.1 ± 0.4
$\Delta\Phi_3$	–	93 ± 1	200 ± 1	229 ± 1	242 ± 3
ω_3	–	1596 ± 1	1596 ± 1	1596 ± 1	1595 ± 1
Γ_3	–	2.1 ± 0.1	2.1 ± 0.1	2.1 ± 0.1	2.1 ± 0.1
A_4	–	15.6 ± 0.7	–	–	11.3 ± 0.7
$\Delta\Phi_4$	–	169 ± 5	–	–	6 ± 9
ω_4	–	1586 ± 1	–	–	1588 ± 1
Γ_4	–	3.8 ± 0.1	–	–	3.8 ± 0.1
A_5	–	12.6 ± 0.5	4.8 ± 0.8	4.0 ± 0.5	36.5 ± 0.4
$\Delta\Phi_5$	–	353 ± 5	286 ± 2	306 ± 1	62 ± 3
ω_5	–	1567 ± 1	1568 ± 1	1568 ± 1	1565 ± 1
Γ_5	–	3.8 ± 0.1	3.8 ± 0.1	3.8 ± 0.1	3.8 ± 0.1
A_6	–	49.7 ± 0.5	32.0 ± 0.7	20.3 ± 0.4	27.6 ± 0.4
$\Delta\Phi_6$	–	79 ± 2	76 ± 5	89 ± 15	92 ± 2
ω_6	–	1534 ± 1	1533 ± 1	1533 ± 1	1535 ± 1
Γ_6	–	3.8 ± 0.1	3.8 ± 0.1	3.8 ± 0.1	3.8 ± 0.1

Figure A.10: IR-Vis SFG fit parameters of the CoTPyP/IGR/Ir(111) monolayer stepwise annealing experiment, in the range of $1450 - 1760 \text{ cm}^{-1}$. A_{NR} : Non-Resonant Amplitude (arb. units); A_i : i -resonance Amplitude (arb. units); $\Delta\Phi_i$: i -resonance phase ($^\circ$); ω_i : i -resonance frequency (cm^{-1}); Γ_i : i -resonance Lorentzian width (cm^{-1}).

	2970 – 3120 cm^{-1}		
	300 K	420 K	470 K
A_{NR}	0.09 ± 0.02	0.16 ± 0.02	0.08 ± 0.02
A_1	1.2 ± 5.2	1.6 ± 0.7	1.1 ± 0.6
$\Delta\Phi_1$	55 ± 142	5 ± 39	7 ± 38
ω_1	3064 ± 7	3064 ± 7	3064 ± 7
Γ_1	13 ± 4	13 ± 4	13 ± 4
A_2	0.5 ± 0.9	0.8 ± 0.6	0.7 ± 0.5
$\Delta\Phi_2$	59 ± 133	353 ± 70	32 ± 61
ω_2	3031 ± 11	3031 ± 11	3031 ± 11
Γ_2	13 ± 4	13 ± 4	13 ± 4

Figure A.11: IR-Vis SFG fit parameters of the CoTPyP/IGR/Ir(111) monolayer stepwise annealing experiment, in the range of 2970 – 3120 cm^{-1} . A_{NR} : Non-Resonant Amplitude (arb. units); A_i : i -resonance Amplitude (arb. units); $\Delta\Phi_i$: i -resonance phase ($^\circ$); ω_i : i -resonance frequency (cm^{-1}); Γ_i : i -resonance Lorentzian width (cm^{-1}).

CoTPyP-Co				
	(a)	(b)	(c)	(d)
$A_{NR}^{(0)}$	1.20 ± 0.04	29.9 ± 0.1	32.2 ± 0.1	1.23 ± 0.01
$A_{NR}^{(1)}$	0.006 ± 0.002	0.045 ± 0.003	0.012 ± 0.001	0.0025 ± 0.0001
ω_0	1240	1395	1605	3060
A_1	1.3 ± 0.5	24 ± 2	20 ± 2	0.5 ± 0.1
$\Delta\Phi_1$	260 ± 15	126 ± 5	153 ± 6	97 ± 8
ω_1	1207 ± 1	1368 ± 1	1512 ± 1	2998 ± 1
Γ_1	5 ± 1	4.7 ± 0.5	4.5 ± 0.6	4.5 ± 0.9
A_2	3 ± 2	16 ± 1	42 ± 5	2.4 ± 0.1
$\Delta\Phi_2$	173 ± 17	252 ± 5	350 ± 7	356 ± 2
ω_2	1250 ± 3	1415 ± 1	1568 ± 1	3077 ± 1
Γ_2	15 ± 4	2.3 ± 0.3	4.5 ± 0.4	6.0 ± 0.3
A_3	–	–	10 ± 1	–
$\Delta\Phi_3$	–	–	184 ± 6	–
ω_3	–	–	1601 ± 1	–
Γ_3	–	–	2.2 ± 0.3	–
A_4	–	–	137 ± 8	–
$\Delta\Phi_4$	–	–	$264 \pm *$	–
ω_4	–	–	1644.9 ± 2.5	–
Γ_4	–	–	$50 \pm *$	–
A_5	–	–	29 ± 5	–
$\Delta\Phi_5$	–	–	20 ± 9	–
ω_5	–	–	1557 ± 1	–
Γ_5	–	–	4.5 ± 0.7	–

Table A.6: Fit parameters of CoTPyP-Co in the four energy ranges: (a) 1200 – 1280 cm^{-1} , (b) 1340 – 1450 cm^{-1} , (c) 1450 – 1760 cm^{-1} , (d) 2970 – 3120 cm^{-1} . The non-resonant background has two components, the constant $A_{NR}^{(0)}$ and the linear term $A_{NR}^{(1)}$ (see Eq. 3.1). The energy center of the linear term, ω_0 , was arbitrarily imposed by hand to coincide with the center of the considered energy interval. Due to the complexity of the spectrum, some parameters were extracted during a preliminary fit and then hold during the final fit: thus there is no errorbar associate to them, and they are marked by a *.

A.1.6 STM CoTPyPCo/Gr/Ir(111)

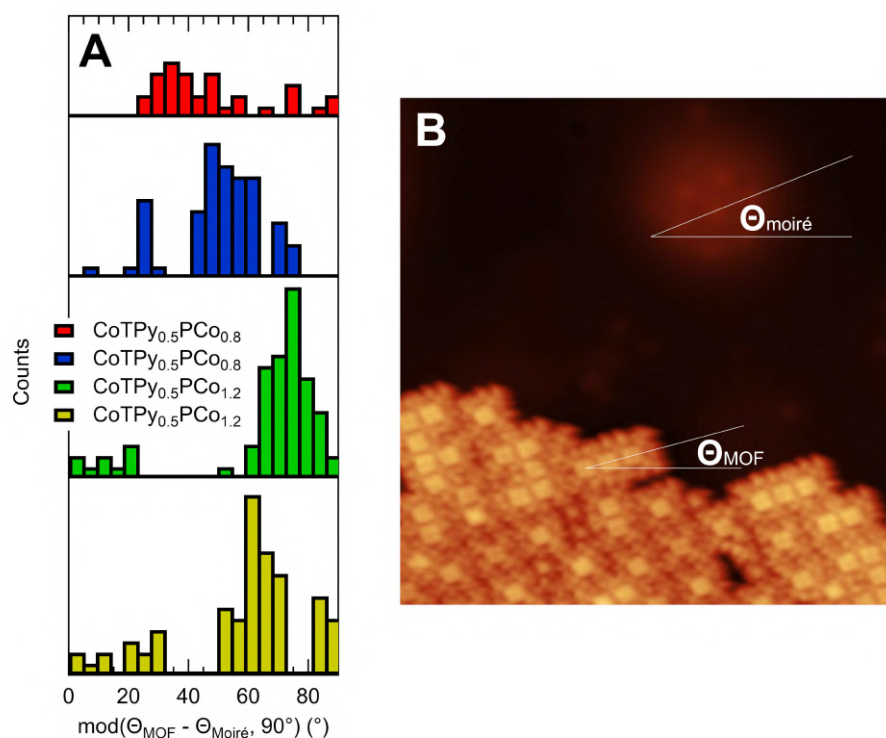


Figure A.12: A) Histograms of the azimuthal orientation of the CoTPyPCo layer with respect to the graphene moiré underneath, according to the angles measured as in panel B). The $\text{mod}(x,y)$ is the modulo operation which returns the remainder of the x/y division (used to take into account the four-fold symmetry of the CoTPyPCo MOF). The four histograms refer to four different analyzed STM images corresponding to $\text{CoTPyP}_{0.5}\text{Co}_{0.8}$ and $\text{CoTPyP}_{0.5}\text{Co}_{1.2}$ layers. The Co clusters on Gr moiré were used to trace the graphene orientation.

A.2 O₂+H₂O ON CoTPyP/Gr/Ir(111)

Mode	Literature [118, 180, 181, 209–213]	CoTPyP/Gr/Ir(111)
$\delta(\text{pyr})$	1214-1219	1212-1216
$\nu(C_\alpha - N) + \delta(C_\beta - H)$	1224-1238	1236-1240
$\delta(C_m - \text{pyr})$	1252-1255	
$\nu(C_\alpha - N)$	1270-1280	
$\nu(C - C) + \nu(C - N)$	1273-1276	
$\nu(C_\alpha - C_\beta)$	1293-1314	
$\nu(C_\alpha - C_\beta) + \delta(C_\beta - H)$	1333-340	
$\nu(C_\alpha - N) + \delta(C_\beta - H)$	1359-1370	1368-9
$\nu(C_\alpha - N)$	1352-1372	1408-9
$\nu(C_\alpha - C_\beta) + \delta(C_\beta - H); \nu(C_\alpha - C_\beta)$	1450-1472	1453-1474
$\nu(C_\beta - C_\beta)$	1492-1510	1490-1505
$\nu(C_\alpha - C_m)$	1510-1540	1533-1539
$\nu(C_\beta - C_\beta) + \delta(C_\beta - H); \nu(C_\beta - C_\beta)$	1542-1576	1564-1589
$\nu(C_\alpha - C_m); \nu(C_m - C_m)$	1561-1582	1564-1589
$\delta(\text{pyr})$	1594-1613	1585-1596
Graphene G mode	1608	1609-1659

Table A.7: Assignment of the observed (Ir-Vis SFG) vibrational modes on the basis of available literature, for the CoTPyP/Gr/Ir(111) system. C_m , C_α , and C_β stand for carbon atoms in meso-, alpha-, and beta-positions in the CoTPyP molecule, respectively.

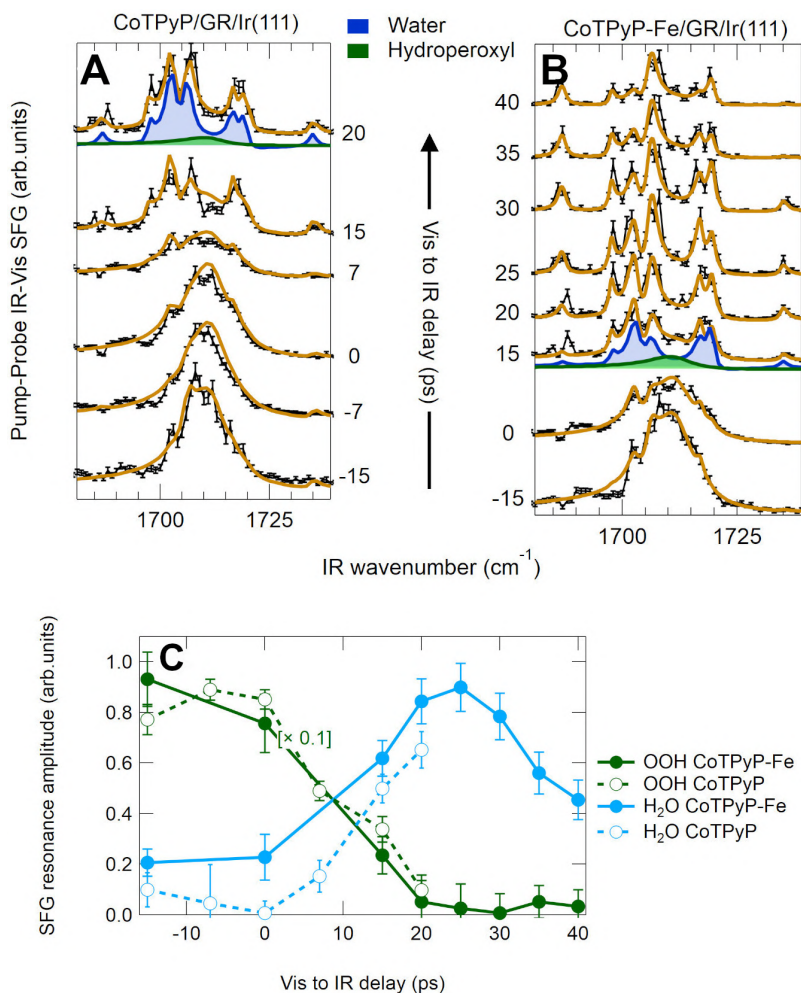


Figure A.13: Time-Resolved SFG. (a-b) IR-Vis SFG spectra collected at room temperature in situ upon exposure of the CoTPyP/Gr/Ir(111) system to both oxygen and water as a function of the Vis-to-IR pulses delay; a second system in which Fe atoms are coordinated to the vacant 4N sites among adjacent molecules, according to the literature [32, 59], is also reported, showing no changes in reactivity and a similar behavior; (c) evolution of the resonant amplitude with delay for the hydroperoxyl (green) and water (cyan) modes. As reported in the figure, both OOH-related curves (green) have been multiplied by 0.1 to fit in the graph.

A)			
ω_k (cm ⁻¹)	$\Delta\varphi_k$ (°)	A_{NonRes}	A_k (arb. units)
UHV		0.33	
1532	200		2.2
1567	298		4.1
1595	78		4.3
1639	264		10.7
NAP		0.41	
1532	200		0
1567	214		2.3
1592	78		2.7
1639	264		6.8
1710	291		9.6
B)			
BE (eV)	Lorentzian (eV)	Gaussian (eV)	Intensity (arb. Units)
O 1s NAP			
531.82	0.5	1.12	0.088
532.37	0.5	4	0.092
533.25	0.5	1.12	0.084
535.37	0.06	0.54	0.136
Co 2p_{3/2} UHV			
778.22	0.57	1.02	0.082
780.06	0.57	1.43	0.544
782.12	0.57	1.66	0.261
784.25	0.57	2.4	0.103
778.22	0.57	1.02	0.082

Table A.8: SFG and XPS fit Parameters relative to Fig. 4.3 **A)** IR-Vis SFG best fitting parameters, according to the lineshape described in the methods section above. **B)** XPS best fitting parameters (Voigt lineshapes) of the spectra plotted in Fig. 4.3

Delay (ps):	-15	-7	0	7	15	20
A_{NonRes} (arb. units)	0.63	0.39	0.46	0.51	0.61	0.8
A_1 (arb. units)	0.02	0.07	0	0	0.14	0.24
$\Delta\varphi$ (°)	267	267	267	267	267	267
ω_1 (cm ⁻¹)	1687	1687	1687	1687	1687	1687
Γ_1 (cm ⁻¹)	1	1	1	1	1	1
A_2 (arb. units)	0	0	0	0.03	0.19	0.29
$\Delta_2\varphi$ (°)	225	225	225	225	225	225
ω_2 (cm ⁻¹)	1698	1698	1698	1698	1698	1698
Γ_2 (cm ⁻¹)	0.7	0.7	0.7	0.7	0.7	0.7
A_3 (arb. units)	0.12	0.13	0.39	0.61	1.31	1.43
$\Delta_3\varphi$ (°)	293	293	293	293	293	293
ω_3 (cm ⁻¹)	1703	1703	1703	1703	1703	1703
Γ_3 (cm ⁻¹)	1.4	1.4	1.4	1.4	1.4	1.4
A_4 (arb. units)	0.61	0.24	0.16	0.2	0.68	1.28
$\Delta_4\varphi$ (°)	248	248	248	248	248	248
ω_4 (cm ⁻¹)	1706	1706	1706	1706	1706	1706
Γ_4 (cm ⁻¹)	1.4	1.4	1.4	1.4	1.4	1.4
A_5 (arb. units)	0.12	0.05	0.24	0.27	0.64	0.49
$\Delta_5\varphi$ (°)	299	299	299	299	299	299
ω_5 (cm ⁻¹)	1717	1717	1717	1717	1717	1717
Γ_5 (cm ⁻¹)	1	1	1	1	1	1
A_6 (arb. units)	0.12	0.04	0.09	0.11	0.42	0.58
$\Delta_6\varphi$ (°)	309	309	309	309	309	309
ω_6 (cm ⁻¹)	1720	1720	1720	1720	1720	1720
Γ_6 (cm ⁻¹)	1	1	1	1	1	1
A_7 (arb. units)	0.22	0.28	0.13	0.12	0.4	0.25
$\Delta_7\varphi$ (°)	268	268	268	268	268	268
ω_7 (cm ⁻¹)	1735	1735	1735	1735	1735	1735
Γ_7 (cm ⁻¹)	1	1	1	1	1	1

Delay (ps):	-15	-7	0	7	15	20
A_{OOH}	7.72	8.9	8.51	4.91	3.39	0.98
$\Delta\varphi_{OOH}$	302	302	302	302	302	302
ω_{OOH}	1712	1712	1712	1712	1712	1712
Γ_{OOH}	5.8	5.8	5.8	5.8	5.8	5.8

Table A.9: Time resolved IR-Vis SFG best fitting parameters of the CoTPyP/Gr, according to the lineshape described in the text.

Delay (ps):	-15	0	15	20	25	30	35	40
A_{OOH}	9.31	7.56	2.36	0.52	-0.26	-0.08	-0.52	0.34
$\Delta\varphi_{OOH}$	302	302	302	302	302	302	302	302
ω_{OOH}	1712	1712	1712	1712	1712	1712	1712	1712
Γ_{OOH}	5.8	5.8	5.8	5.8	5.8	5.8	5.8	5.8

Table A.10: Time resolved IR-Vis SFG best fitting parameters of the CoTPyP-Fe/Gr related spectra plotted in Fig. A.13b, according to the lineshape described in the text.

A.3 CO ON COTPYPCO

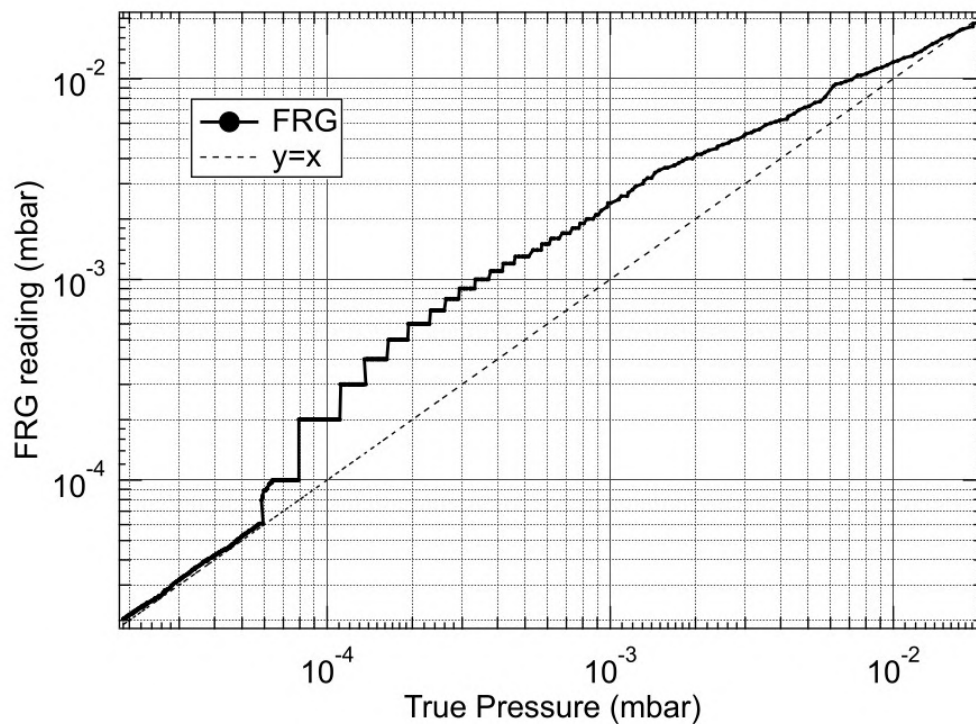


Figure A.14: FRG pressure calibration in the low pressure range of the Pirani vacuum gauge. The FRG reading (y data points) are plotted vs the hot gauge reading (x data points) in the main chamber, connected through a small hole to the NAP cell. The x values have been multiplied by a factor in such a way to match the FRG reading at $P < 6 \times 10^{-4}$ mbar.

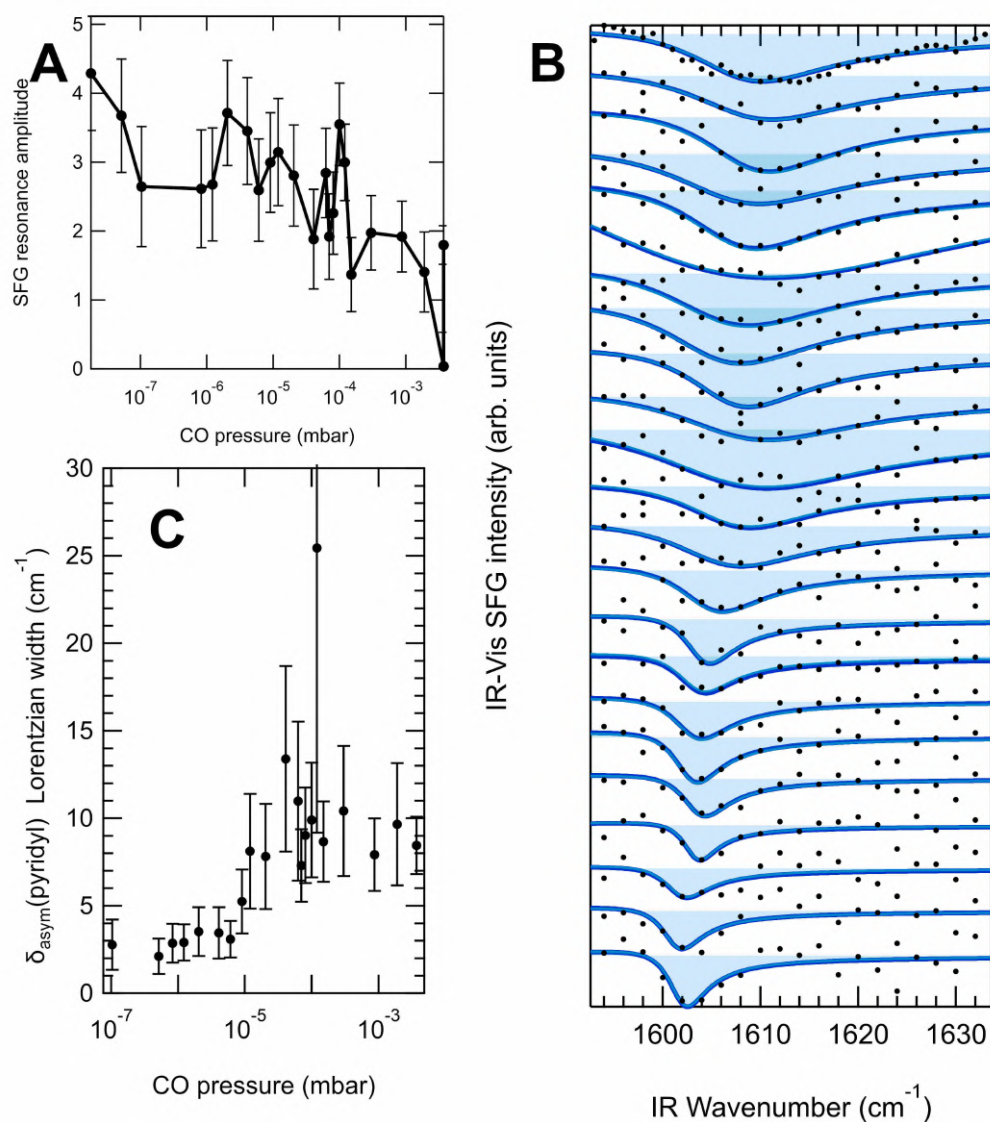


Figure A.15: **A)** Evolution of the resonant amplitude of the pyridyl asymmetric bending mode at 1603 cm^{-1} in Fig 5.2; **B)** Fit of the CO pressure uptake (CoTPy_{0.5}PCo_{0.12} layer) by using only one SFG resonance, and **C)** evolution of its Lorentzian width.

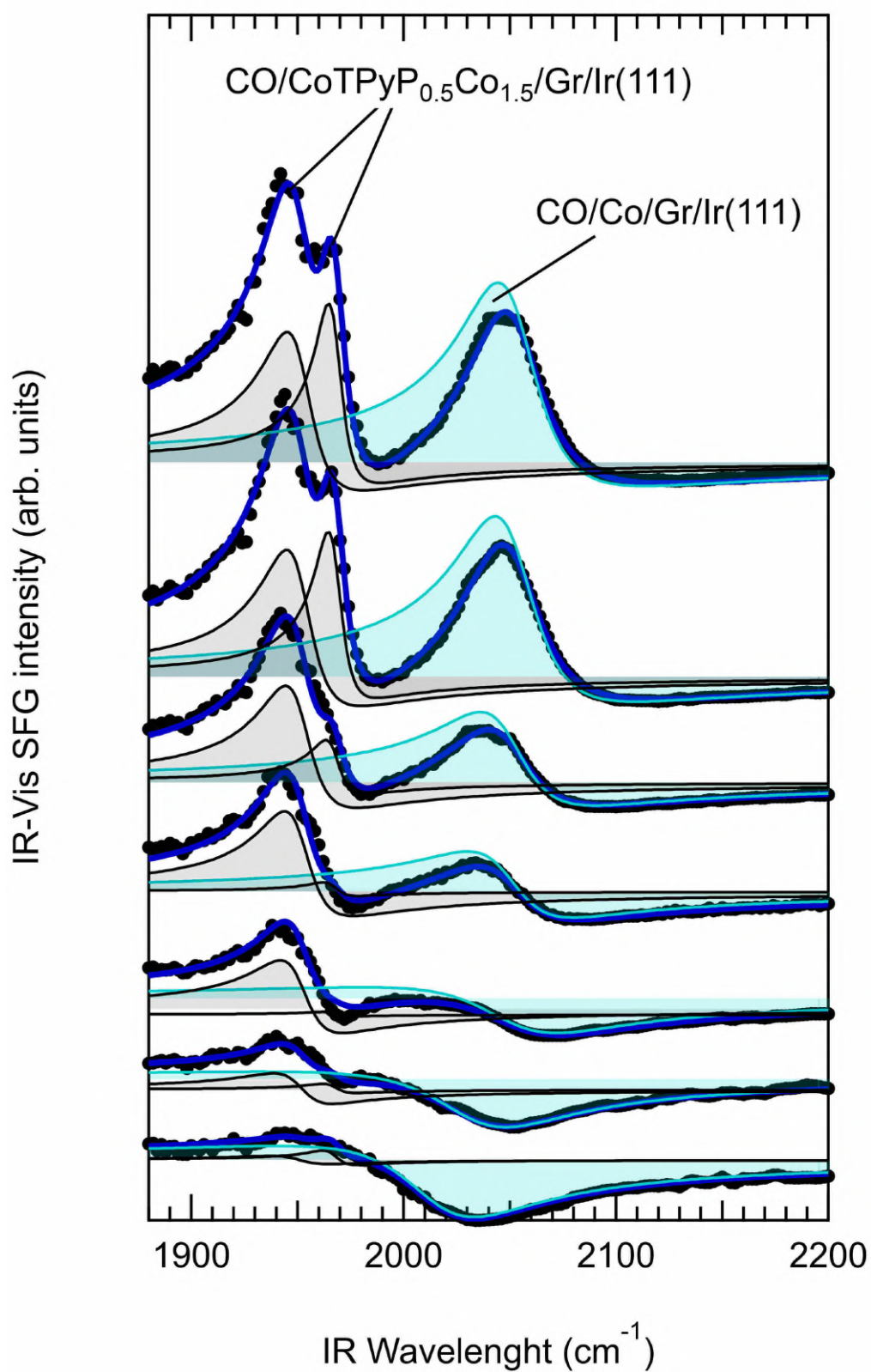


Figure A.16: IR-Vis SFG spectra of the CoTPyP_{0.5}Co_{1.4} layer exposed to increasing CO pressure, from 1×10^{-8} to 1×10^{-2} mbar, collected at each order of magnitude pressure increase. The light-blue resonance, at around 2050 cm^{-1} , is attributed to CO on Co/Gr/Ir(111).

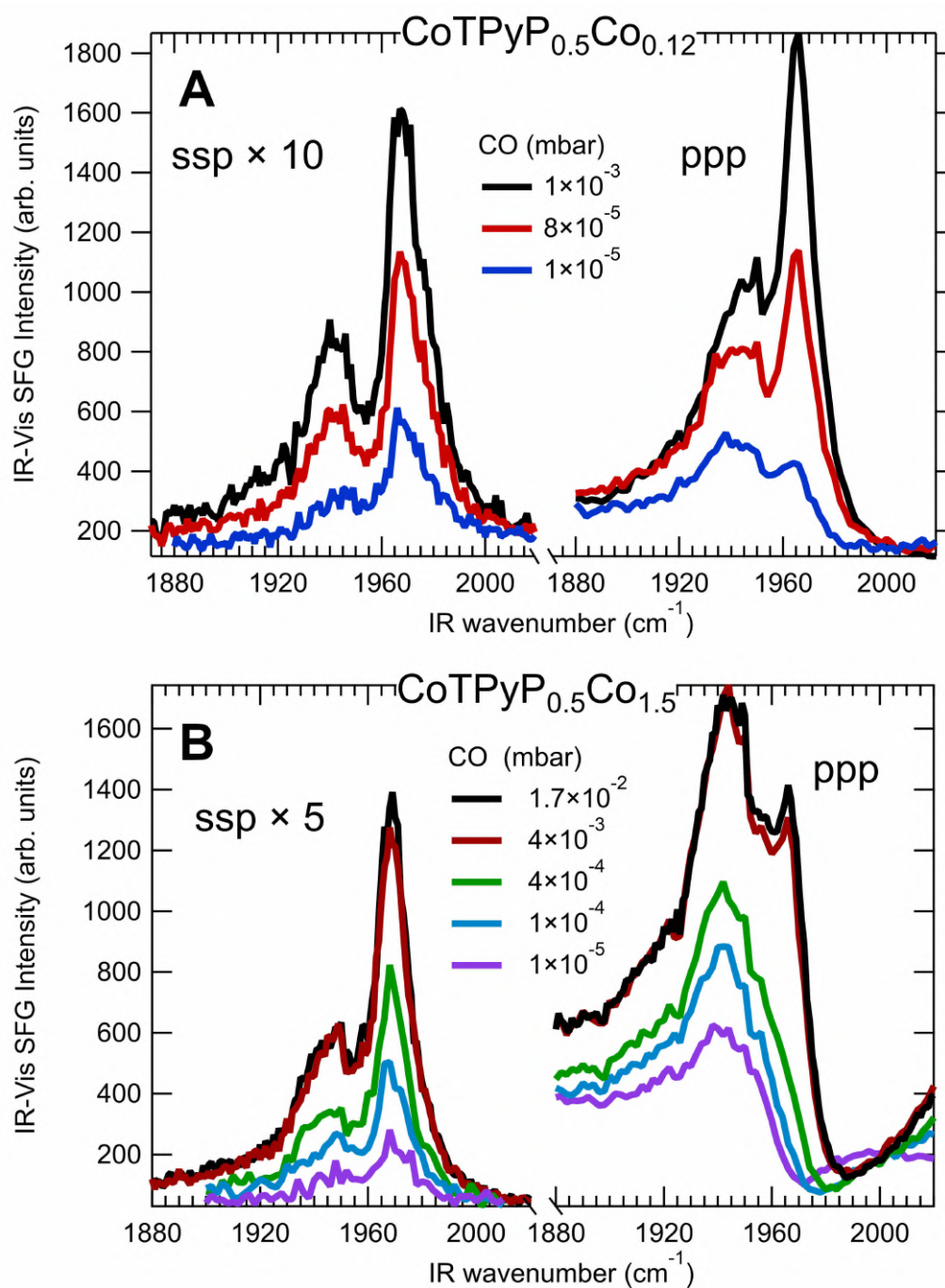


Figure A.17: Comparison between ppp and ssp polarization of the normalized IR-Vis SFG spectra of **A)** the CoTPyP_{0.5}Co_{0.12} and **B)** the CoTPyP_{0.5}Co_{1.4} layer collected at the indicated CO pressure.

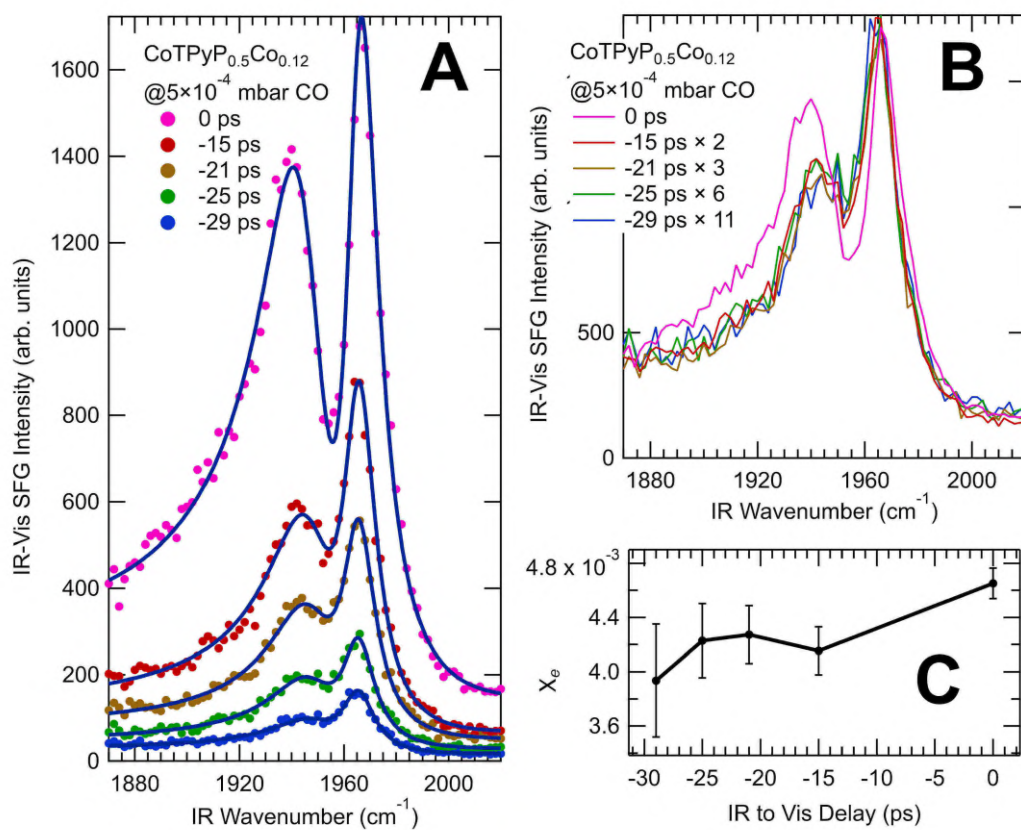


Figure A.18: A) Normalized IR-Vis SFG spectra of $\text{CoTPyP}_{0.5}\text{Co}_{0.12}$ layer exposed to 5×10^{-4} mbar of carbon monoxide, as a function of the IR-Vis indicated delay. Negative values mean Vis hitting the sample before the IR impulse; B) Same graph as A, but the spectra are shown with a multiplicative factor; C) The measurement of the anharmonicity constant shows a dependence on the delay.

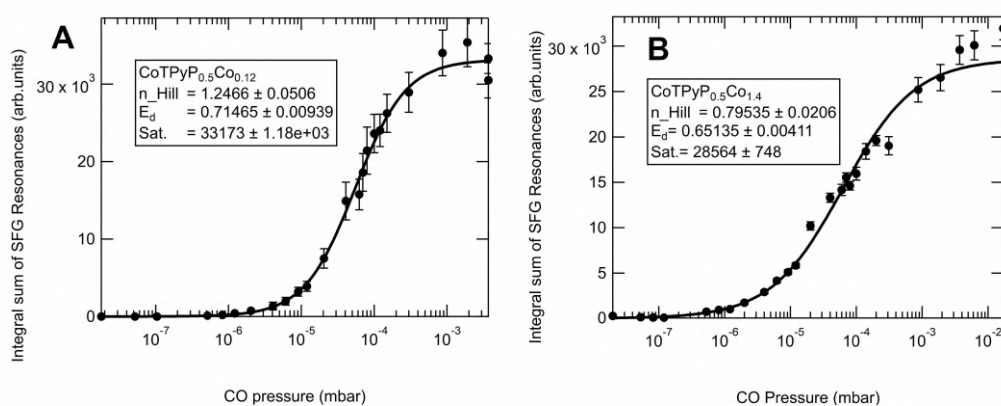


Figure A.19: CO coverage uptake relative to the **A)** CoTPyP_{0.5}Co_{0.12} (Fig. 5.2) and **B)** CoTPyP_{0.5}Co_{1.4} (Fig. 5.4), measured as the sum of the integrals of the two (fundamental and hot-band) SFG resonances. The experimental data (dotted circles) are plotted together with the best fit (Hill model).

ACRONYMS

List of Acronyms used in this thesis:

- **AP** Ambient Pressure
- **BE** Binding Energy
- **DOS** Density of States
- **DS** Doniach Sunjic
- **IR** Infrared
- **IR-Vis SFG** Infrared Visible Sum Frequency Generation
- **IP** Ionization Potential
- **FRG** Full Range Gauge
- **JDOS** Joint Density of States
- **LDOS** Local Density of States
- **GS** Gunnarsson and Schönhammer
- **MOF** Metallorganic Framework
- **MON** Metallorganic Network
- **MS** Multiplet Splitting
- **NAP** Near Ambient Pressure
- **NEXAFS** Near Edge X-Ray Absorption Fine Structure
- **OER** Oxygen Evolution Reaction
- **ORR** Oxygen Reduction Reaction
- **PEY** Partial Electron Yield
- **PDOS** Projected Density of States
- **RT** Room Temperature
- **SAC** Single Atom Catalyst/catalysis standard hydrogen electrode (SHE)

- **SFG** Sum Frequency Generation
- **SF** Sum Frequency
- **SHE** Standard Hydrogen Electrode
- **STM** Scanning Tunneling Microscopy
- **STS** Scanning Tunneling Spectroscopy
- **TDM** Transition Dipole Moment
- **TEY** Total Electron Yield
- **tr-2PPE** Time Resolved Two Photons Photoemission Spectroscopy
- **Vis** Visible
- **UHV** Ultra High Vacuum
- **UPS** Ultraviolet Photoemission Spectroscopy
- **VL** Valence Level
- **WF** Work Function
- **XPS** X-Ray Photoemission Spectroscopy

LIST OF PUBLICATIONS

- **Armillotta, F.**; Bidoggia, D.; Baronio, S.; Biasin, P.; Annese, A.; Scardamaglia, M.; Zhu, S.; Bozzini, B.; Modesti, S.; Peressi, M.; Vesselli, E. "Single Metal Atom Catalysts and ORR: H-Bonding, Solvation, and the Elusive Hydroperoxyl Intermediate" *ACS Catal.* 2022, 12 (13), 7950–7959. <https://doi.org/10.1021/acscatal.2c02029>
- **Armillotta, F.**; Pividori, A.; Stredansky, M.; Seriani, N.; Vesselli, E. "Dioxygen at Biomimetic Single Metal-Atom Sites: Stabilization or Activation? The Case of CoT-PyP/Au(111)" *Top. Catal.* 2020, No. 111. <https://doi.org/10.1007/s11244-020-01333-9>
- **Armillotta, F.**; D’Incecco, E.; Corva, M.; Stredansky, M.; Gallet, J.; Bournel, F.; Goldoni, A.; Morgante, A.; Vesselli, E.; Verdini, A. "Self-Metalation of Porphyrins at the Solid–Gas Interface" *Angew. Chemie* 2021, 133 (49), 26192–26197. <https://doi.org/10.1002/ange.202111932>.
- Sala, A.; Caporali, M.; Serrano-Ruiz, M.; **Armillotta, F.**; Vesselli, E.; Genuzio, F.; Menteş, T. O.; Locatelli, A.; Comelli, G.; Africh, C.; Verdini, A. "Black or Red Phosphorus Yields the Same Blue Phosphorus Film" *Nanoscale* 2022, 14 (43), 16256–16261. <https://doi.org/10.1039/D2NR02657K>.
- **Armillotta, F.**; Bidoggia, D.; Baronio, S.; Biasin, P.; Annese, A.; Cossaro, A.; Verdini, A.; Floreano, L.; Peressi, M.; Vesselli, E. "Geometric and electronic characterization of bimetallic TPyP-based metallorganic frameworks grown on weakly interacting Gr/Ir(111)" *in preparation*
- **Armillotta, F.**; Bidoggia, D.; Baronio, S.; Biasin, P.; Peressi, M.; Vesselli, E. "Long-range electronic effects in a Co-based metalorganic framework probed by near ambient pressure ligand adsorption" *in preparation*

RINGRAZIAMENTI

Credo che la parte più importante di questa tesi sia scritta al di fuori di queste pagine. La sua conclusione rappresenta per me il compimento di un lungo percorso, una parte significativa della mia vita, 8 anni passati a Trieste di cui 4 nel gruppo di Erik. Mi sento quindi in dovere di ringraziare tutte quelle persone che hanno scelto di circondarmi in questi anni, loro fortuna o loro malgrado, e che hanno dato vita e sapore a questa esperienza unica.

In primo luogo, ad Erik. Non so se esiste un relatore perfetto. Se esiste, ci si avvicina molto. Con Erik sono cresciuto come scienziato e come persona, ispirandomi al suo essere sempre presente, sempre attento, sempre entusiasta, dandomi sempre più fiducia di quanta non riponessi in me stesso. Mi rendo conto che non avrei potuto fare scelta più felice, come mentore e come amico.

Rimanendo nel gruppo Visp-Lab, che oramai si è allargato in maniera sesquipedale, un ringraziamento particolare va alle persone con cui più ho lavorato fianco a fianco. Pietro, mio diretto successore, compagno di vittorie ma soprattutto tante sconfitte in campo, con i restanti prodi della squadra Uni Fermi-Salisburgo, di cui le origini del nome si perdono nell'alba dei tempi. Uomo dalla singolare tenacia di carburo di boro, del quale ammiro enormemente l'atteggiamento Zen e il coraggio gastronomico. Poi Stefania, per la quale ho cercato - spero con successo - di essere un esempio così come Erik lo è stato per me. Lavorare con lei è stato semplicemente stupendo, stabilendo uno di quei legami che difficilmente vengono intaccati dall'usura del tempo. Per tutti i bei momenti passati assieme, per tutte le risate, dal grasso di balena, agli gnocchi, alla tua aura di fortuna, fino all'ultimo giorno passato insieme in lab, grazie. Un saluto affettuoso a tutti i viandanti passati per il lab e che hanno incrociato la mia strada, e un in bocca al lupo speciale ad Alessandro che quest'anno comincia lo stesso percorso che ho appena concluso. Un grazie doveroso va a Maria e al "nostro" teorico Davide, per i bellissimi risultati computazionali ottenuti, per la sua pazienza infinita, e per i giri in bici illegali a Stonehenge.

Un saluto al gruppo STM del CNR-IOM, formidabili collaboratori, pazientissimi prestatori di strumentazione ed insostituibili compagni di mensa: in particolare ad Alessandro, Mirco, Teresa, Sumati, Cristina e Giovanni. Un grazie a Silvio, inesauribile pozzo di conoscenza e fonte di innumerevoli espedienti. Un abbraccio a Valeria, la cui spontaneità risplende in ogni momento e luogo, e a Daniel, pizzaiolo verace e maestro di sci senza pari. Ringrazio tutta la popolazione di Elettra Sincrotrone che ho conosciuto, a partire da Hendrick (Endrico), il tedesco più italiano che abbia mai conosciuto, instancabile giramondo, dalle mete discutibili e dal fiuto incredibile per posti sconsigliabili. Un abbraccio affettuoso a Iulia, Matteo J., e Matus per le belle serate passate assieme, ad Ahmed

con le sue lezioni di italiano in bus, i ragazzi del nanolab, e gli "Aloisici". Un grazie a Philipp, per le nostre sessioni di chitarra e sax e per tutte le partite di spikeball mai giocate con Tanja ed Astra. Un saluto a tutti i colleghi dottorandi del mio ciclo di cui ho avuto l'onore di essere rappresentante per un anno. Lo stesso anno segnato dal Covid-19 e che, nonostante tutti i danni, mi ha tuttavia battezzato Genitore 2 di Daniele, con il quale ho condiviso larga parte del tempo trascorso negli ultimi anni, tra arrampicate (un saluto ad Angela e le conoscenze fortuite di Gravità Zero), cene, trekking, pedalate con Miguel, e sciate con Berto e Franz. Il suo essere estroverso e il suo entusiasmo sono di gran lunga il virus più contagioso. Un pensiero affettuoso va a tutti i compagni di avventura che hanno condiviso con me l'università dal primo giorno e, solo per citarne alcuni, a Riccardo, coinquilino insostituibile di casa Polh, ad Alice e Vittorio per le bellissime gite nel goriziano, ad Ilaria e Sam per i giri in bici in regione, a Matteo, Marta & Co per aver più volte immolato la loro casa, a Stefano per avermi attaccato il pallino del trekking, e a tutti gli altri che non nomino singolarmente solo perché la lista sarebbe troppo lunga, e con i quali spero di continuare a mantenere un legame speciale. Fuori dall'accademia, tra i tanti, un grazie agli amici del CUS Trieste, in particolare Rocco, Stefano, Federica e Nino per gli scarsi risultati in palestra ottenuti a favore dei bei momenti passati assieme.

Al di fuori di Trieste, ringrazio i miei amici abruzzesi, un punto di riferimento fisso con cui sentirmi sempre a casa, in particolare Federico guida alpina doc e organizzatore instancabile, gli Andrea, Federica, Sara, Matteo, Jacopo, e Alessio, esempi viventi del fatto che l'amicizia sopravvive al di là di qualsiasi confine spazio-temporale. Un ringraziamento particolare ad Enrico, mio professore di fisica al liceo, che per primo ha acceso in me la scintilla di questa materia affascinante, e senza il quale non trovo scontate le scelte che ho fatto.

Infine, non certo per ordine di importanza, un grazie va alla mia famiglia (gatti inclusi), per avermi insegnato i valori grazie ai quali ho potuto affrontare questo percorso; loro che, assieme agli zii, cugini e nonni, mi hanno sempre dato tanto affetto e hanno sempre saputo sopportare la nostra lontananza. L'ultimo grazie va a Giulia, insostituibile compagna, sempre al mio fianco in questo lungo viaggio, con la quale ho avuto la fortuna di poter condividere questi bei momenti.

BIBLIOGRAPHY

- [1] George M. Whitesides and George W. Crabtree. “Don’t Forget Long-Term Fundamental Research in Energy”. In: *Science* (80-.). 315.5813 (Feb. 2007), pp. 796–798. DOI: [10.1126/science.1140362](https://doi.org/10.1126/science.1140362).
- [2] European Commission. *Critical raw materials*. URL: https://single-market-economy.ec.europa.eu/sectors/raw-materials/areas-specific-interest/critical-raw-materials_en. Last visited on 06-Jan-2023.
- [3] K Hund et al. “Minerals for Climate Action: The Mineral Intensity of the Clean Energy Transition”. In: *World Bank Publ.* (2020), p. 110.
- [4] Vessela Petrova. “Metals in the circular economy”. In: *SHS Web Conf.* 120 (2021), p. 02014. DOI: [10.1051/shsconf/202112002014](https://doi.org/10.1051/shsconf/202112002014).
- [5] Frederic Simon Davide Patteri. *Metals in the circular economy*. URL: <https://www.euractiv.com/section/circular-economy/special-report/metals-in-the-circular-economy/>. Last visited on 06-Jan-2023.
- [6] Naoki Nitta et al. “Li-ion battery materials: Present and future”. In: *Mater. Today* 18.5 (2015), pp. 252–264. DOI: [10.1016/j.mattod.2014.10.040](https://doi.org/10.1016/j.mattod.2014.10.040).
- [7] Andoni Maiza-Larrarte and Gloria Claudio-Quiroga. “The impact of Sicominex on development in the Democratic Republic of Congo”. In: *Int. Aff.* 95.2 (2019), pp. 423–446. DOI: [10.1093/ia/iiz001](https://doi.org/10.1093/ia/iiz001).
- [8] Günther Rupprechter and Christian Weilach. “Mind the gap! Spectroscopy of catalytically active phases”. In: *Nano Today* 2.4 (Aug. 2007), pp. 20–29. DOI: [10.1016/S1748-0132\(07\)70114-7](https://doi.org/10.1016/S1748-0132(07)70114-7).
- [9] Rico Gutzler et al. “Mimicking Enzymatic Active Sites on Surfaces for Energy Conversion Chemistry”. In: *Acc. Chem. Res.* 48.7 (2015), pp. 2132–2139. DOI: [10.1021/acs.accounts.5b00172](https://doi.org/10.1021/acs.accounts.5b00172).
- [10] Erik Vesselli. “Stabilization and activation of molecular oxygen at biomimetic tetrapyrroles on surfaces: from UHV to near-ambient pressure”. In: *Nanoscale Adv.* 3.5 (2021), pp. 1319–1330. DOI: [10.1039/D0NA00827C](https://doi.org/10.1039/D0NA00827C).
- [11] Selina K. Kaiser et al. “Single-Atom Catalysts across the Periodic Table”. In: *Chem. Rev.* 120.21 (2020), pp. 11703–11809. DOI: [10.1021/acs.chemrev.0c00576](https://doi.org/10.1021/acs.chemrev.0c00576).
- [12] Xiao-feng Feng Yang et al. “Single-Atom Catalysts: A New Frontier in Heterogeneous Catalysis”. In: *Acc. Chem. Res.* 46.8 (Aug. 2013), pp. 1740–1748. DOI: [10.1021/ar300361m](https://doi.org/10.1021/ar300361m).

- [13] Masatake Haruta et al. “Novel Gold Catalysts for the Oxidation of Carbon Monoxide at a Temperature far Below 0 °C”. In: *Chem. Lett.* 16.2 (1987), pp. 405–408. DOI: [10.1246/cl.1987.405](https://doi.org/10.1246/cl.1987.405).
- [14] Andrew A. Herzing et al. “Identification of active gold nanoclusters on iron oxide supports for CO oxidation”. In: *Science (80-.)*. 321.5894 (2008), pp. 1331–1335. DOI: [10.1126/science.1159639](https://doi.org/10.1126/science.1159639).
- [15] Alexander Langner et al. “Self-recognition and self-selection in multicomponent supramolecular coordination networks on surfaces”. In: *Proc. Natl. Acad. Sci. U. S. A.* 104.46 (2007), pp. 17927–17930. DOI: [10.1073/pnas.0704882104](https://doi.org/10.1073/pnas.0704882104).
- [16] Jing Fu et al. “Electrically Rechargeable Zinc–Air Batteries: Progress, Challenges, and Perspectives”. In: *Adv. Mater.* 29.7 (2017). DOI: [10.1002/adma.201604685](https://doi.org/10.1002/adma.201604685).
- [17] Di Zhao et al. “Atomic site electrocatalysts for water splitting, oxygen reduction and selective oxidation”. In: *Chem. Soc. Rev.* 49.7 (2020), pp. 2215–2264. DOI: [10.1039/C9CS00869A](https://doi.org/10.1039/C9CS00869A).
- [18] Xunca Chen et al. “Recent Advances in Materials and Design of Electrochemically Rechargeable Zinc–Air Batteries”. In: *Small* 14.44 (2018), pp. 1–29. DOI: [10.1002/sml.201801929](https://doi.org/10.1002/sml.201801929).
- [19] John Muldoon, Claudiu B. Bucur, and Thomas Gregory. “Quest for nonaqueous multivalent secondary batteries: Magnesium and beyond”. In: *Chem. Rev.* 114.23 (2014), pp. 11683–11720. DOI: [10.1021/cr500049y](https://doi.org/10.1021/cr500049y).
- [20] Jang Soo Lee et al. “Metal-air batteries with high energy density: Li-air versus Zn-air”. In: *Adv. Energy Mater.* 1.1 (2011), pp. 34–50. DOI: [10.1002/aenm.201000010](https://doi.org/10.1002/aenm.201000010).
- [21] B. Bozzini et al. “In Situ and Ex Situ X-Ray Microspectroelectrochemical Methods for the Study of Zinc–Air Batteries”. In: *Encycl. Interfacial Chem.* Elsevier, 2018, pp. 174–194. DOI: [10.1016/B978-0-12-409547-2.11452-0](https://doi.org/10.1016/B978-0-12-409547-2.11452-0).
- [22] Md. Arafat Rahman, Xiaojian Wang, and Cuie Wen. “High Energy Density Metal-Air Batteries: A Review”. In: *J. Electrochem. Soc.* 160.10 (2013), A1759–A1771. DOI: [10.1149/2.062310jes](https://doi.org/10.1149/2.062310jes).
- [23] Bingjun Zhu et al. “Metal-organic frameworks and their derivatives for metal-air batteries”. In: *Energy Storage Mater.* 23 (2019), pp. 757–771. DOI: [10.1016/j.enstm.2019.05.022](https://doi.org/10.1016/j.enstm.2019.05.022).
- [24] Emanuele Marini, Ludwig Jörissen, and Sylvain Brimaud. “Rational design of a low-cost, durable and efficient bifunctional oxygen electrode for rechargeable metal-air batteries”. In: *J. Power Sources* 482. September 2020 (2021). DOI: [10.1016/j.jpowsour.2020.228900](https://doi.org/10.1016/j.jpowsour.2020.228900).
- [25] Jiabin Wu et al. “Densely Populated Isolated Single Co-N Site for Efficient Oxygen Electrocatalysis”. In: *Adv. Energy Mater.* 9.22 (2019), pp. 2–9. DOI: [10.1002/aenm.201900149](https://doi.org/10.1002/aenm.201900149).

- [26] Long Jiao and Hai Long Jiang. “Metal-Organic-Framework-Based Single-Atom Catalysts for Energy Applications”. In: *Chem* 5.4 (2019), pp. 786–804. DOI: [10.1016/j.chempr.2018.12.011](https://doi.org/10.1016/j.chempr.2018.12.011).
- [27] J. Michael Gottfried. “Surface chemistry of porphyrins and phthalocyanines”. In: *Surf. Sci. Rep.* 70.3 (2015), pp. 259–379. DOI: [10.1016/j.surfrep.2015.04.001](https://doi.org/10.1016/j.surfrep.2015.04.001).
- [28] *MgO₂*.
- [29] Carme Rovira. “The structure and dynamics of the Fe-CO bond in myoglobin”. In: *J. Phys. Condens. Matter* 15.18 (2003). DOI: [10.1088/0953-8984/15/18/314](https://doi.org/10.1088/0953-8984/15/18/314).
- [30] Willi Auwärter et al. “Porphyrins at interfaces”. In: *Nat. Chem.* 7.2 (Feb. 2015), pp. 105–120. DOI: [10.1038/nchem.2159](https://doi.org/10.1038/nchem.2159).
- [31] Mathias O. Senge et al. “Chlorophylls, Symmetry, Chirality, and Photosynthesis”. In: *Symmetry (Basel)*. 6.3 (Sept. 2014), pp. 781–843. DOI: [10.3390/sym6030781](https://doi.org/10.3390/sym6030781).
- [32] Benjamin Wurster et al. “Driving the Oxygen Evolution Reaction by Nonlinear Cooperativity in Bimetallic Coordination Catalysts”. In: *J. Am. Chem. Soc.* 138.11 (Mar. 2016), pp. 3623–3626. DOI: [10.1021/jacs.5b10484](https://doi.org/10.1021/jacs.5b10484).
- [33] Silvia Carlotto et al. “The Magnetic Behaviour of CoTPP Supported on Coinage Metal Surfaces in the Presence of Small Molecules: A Molecular Cluster Study of the Surface trans-Effect”. In: *Nanomaterials* 12.2 (2022). DOI: [10.3390/nano12020218](https://doi.org/10.3390/nano12020218).
- [34] Geoffrey Rojas et al. “Surface state engineering of molecule–molecule interactions”. In: *Phys. Chem. Chem. Phys.* 14.14 (2012), p. 4971. DOI: [10.1039/c2cp40254h](https://doi.org/10.1039/c2cp40254h).
- [35] Geoffrey Rojas et al. “Self-Assembly and Properties of Nonmetalated Tetraphenyl-Porphyrin on Metal Substrates”. In: *J. Phys. Chem. C* 114.20 (May 2010), pp. 9408–9415. DOI: [10.1021/jp1012957](https://doi.org/10.1021/jp1012957).
- [36] Jens Brede et al. “Dynamics of molecular self-ordering in tetraphenyl porphyrin monolayers on metallic substrates”. In: *Nanotechnology* 20.27 (July 2009), p. 275602. DOI: [10.1088/0957-4484/20/27/275602](https://doi.org/10.1088/0957-4484/20/27/275602).
- [37] Thomas A. Jung, R. R. Schlittler, and J. K. Gimzewski. “Conformational identification of individual adsorbed molecules with the STM”. In: *Nature* 386.6626 (Apr. 1997), pp. 696–698. DOI: [10.1038/386696a0](https://doi.org/10.1038/386696a0).
- [38] Francesca Moresco et al. “Conformational Changes of Single Molecules Induced by Scanning Tunneling Microscopy Manipulation: A Route to Molecular Switching”. In: *Phys. Rev. Lett.* 86.4 (Jan. 2001), pp. 672–675. DOI: [10.1103/PhysRevLett.86.672](https://doi.org/10.1103/PhysRevLett.86.672).
- [39] Willi Auwärter et al. “Self-assembly and conformation of tetrapyrrolyl-porphyrin molecules on Ag(111)”. In: *J. Chem. Phys.* 124.19 (May 2006), p. 194708. DOI: [10.1063/1.2194541](https://doi.org/10.1063/1.2194541).

- [40] Giovanni Di Santo et al. “Conformational Adaptation and Electronic Structure of 2H-Tetraphenylporphyrin on Ag(111) during Fe Metalation”. In: *J. Phys. Chem. C* 115.10 (Mar. 2011), pp. 4155–4162. DOI: [10.1021/jp111151n](https://doi.org/10.1021/jp111151n).
- [41] Daniel E. Hurtado Salinas et al. “Reactivity of Bioinspired Magnesium–Organic Networks under CO₂ and O₂ Exposure”. In: *ACS Omega* 4.6 (2019), pp. 9850–9859. DOI: [10.1021/acsomega.9b00762](https://doi.org/10.1021/acsomega.9b00762).
- [42] Stephen W. Ragsdale. “Metals and their scaffolds to promote difficult enzymatic reactions”. In: *Chem. Rev.* 106.8 (2006), pp. 3317–3337. DOI: [10.1021/cr0503153](https://doi.org/10.1021/cr0503153).
- [43] Sk Amanullah, Asmita Singha, and Abhishek Dey. “Tailor made iron porphyrins for investigating axial ligand and distal environment contributions to electronic structure and reactivity”. In: *Coord. Chem. Rev.* 386 (2019), pp. 183–208. DOI: [10.1016/j.ccr.2019.01.021](https://doi.org/10.1016/j.ccr.2019.01.021).
- [44] Erik Vesselli. “Tetrapyrroles at near-ambient pressure: porphyrins and phthalocyanines beyond the pressure gap”. In: *J. Phys. Mater.* 3.2 (Apr. 2020), p. 022002. DOI: [10.1088/2515-7639/ab7ab2](https://doi.org/10.1088/2515-7639/ab7ab2).
- [45] Ronald Breslow. “Biomimetic Chemistry and Artificial Enzymes: Catalysis by Design”. In: *Acc. Chem. Res.* 28.3 (1995), pp. 146–153. DOI: [10.1021/ar00051a008](https://doi.org/10.1021/ar00051a008).
- [46] Sam P. De Visser and Sason Shaik. “A proton-shuttle mechanism mediated by the porphyrin in benzene hydroxylation by cytochrome P450 enzymes”. In: *J. Am. Chem. Soc.* 125.24 (2003), pp. 7413–7424. DOI: [10.1021/ja034142f](https://doi.org/10.1021/ja034142f).
- [47] Wolfgang Hieringer et al. “The Surface Trans Effect: Influence of Axial Ligands on the Surface Chemical Bonds of Adsorbed Metalloporphyrins”. In: *J. Am. Chem. Soc.* 133.16 (Apr. 2011), pp. 6206–6222. DOI: [10.1021/ja1093502](https://doi.org/10.1021/ja1093502).
- [48] Takashi Yokoyama et al. “Nonplanar adsorption and orientational ordering of porphyrin molecules on Au(111)”. In: *J. Chem. Phys.* 115.8 (Aug. 2001), pp. 3814–3818. DOI: [10.1063/1.1389276](https://doi.org/10.1063/1.1389276).
- [49] Takashi Yokoyama et al. “Selective assembly on a surface of supramolecular aggregates with controlled size and shape”. In: *Nature* 413.6856 (Oct. 2001), pp. 619–621. DOI: [10.1038/35098059](https://doi.org/10.1038/35098059).
- [50] Rémy Pawlak et al. “Directed rotations of single porphyrin molecules controlled by localized force spectroscopy”. In: *ACS Nano* 6.7 (2012), pp. 6318–6324. DOI: [10.1021/nn301774d](https://doi.org/10.1021/nn301774d).
- [51] Iulia Cojocariu et al. “Reversible redox reactions in metal-supported porphyrin: The role of spin and oxidation state”. In: *J. Mater. Chem. C* 9.37 (2021), pp. 12559–12565. DOI: [10.1039/d1tc02222a](https://doi.org/10.1039/d1tc02222a).
- [52] Qiushi Zhang et al. “Switching Molecular Kondo Effect via Supramolecular Interaction”. In: *ACS Nano* 9.12 (Dec. 2015), pp. 12521–12528. DOI: [10.1021/acsnano.5b06120](https://doi.org/10.1021/acsnano.5b06120).

- [53] Shadi Fatayer et al. “Reorganization energy upon charging a single molecule on an insulator measured by atomic force microscopy”. In: *Nat. Nanotechnol.* 13.5 (2018), pp. 376–380. DOI: [10.1038/s41565-018-0087-1](https://doi.org/10.1038/s41565-018-0087-1).
- [54] Bikash Mandal, Jin Suk Chung, and Sung Gu Kang. “Theoretical Insight into M1TPyP-M2 (M1, M2 = Fe, Co) MOFs: Correlation between Electronic Structure and Catalytic Activity Extending to Potentiality in Capturing Flue Gases”. In: *J. Phys. Chem. C* 122.18 (2018), pp. 9899–9908. DOI: [10.1021/acs.jpcc.8b00080](https://doi.org/10.1021/acs.jpcc.8b00080).
- [55] Manuel Corva et al. “Learning from Nature: Charge Transfer and Carbon Dioxide Activation at Single, Biomimetic Fe Sites in Tetrapyrroles on Graphene”. In: *J. Phys. Chem. C* 123.6 (Feb. 2019), pp. 3916–3922. DOI: [10.1021/acs.jpcc.8b11871](https://doi.org/10.1021/acs.jpcc.8b11871).
- [56] Sumith Yesudasan, Xianqiao Wang, and Rodney D. Averett. “Molecular dynamics simulations indicate that deoxyhemoglobin, oxyhemoglobin, carboxyhemoglobin, and glycated hemoglobin under compression and shear exhibit an anisotropic mechanical behavior”. In: *J. Biomol. Struct. Dyn.* 36.6 (2018), pp. 1417–1429. DOI: [10.1080/07391102.2017.1323674](https://doi.org/10.1080/07391102.2017.1323674).
- [57] Rie Makiura and Oleg Konovalov. “Bottom-up assembly of ultrathin sub-micron size metal-organic framework sheets”. In: *Dalt. Trans.* 42.45 (2013), pp. 15931–15936. DOI: [10.1039/c3dt51703a](https://doi.org/10.1039/c3dt51703a).
- [58] Meiting Zhao et al. “Two-dimensional metal-organic framework nanosheets: Synthesis and applications”. In: *Chem. Soc. Rev.* 47.16 (2018), pp. 6267–6295. DOI: [10.1039/c8cs00268a](https://doi.org/10.1039/c8cs00268a).
- [59] Diana Hötger et al. “Stability of metallo-porphyrin networks under oxygen reduction and evolution conditions in alkaline media”. In: *Phys. Chem. Chem. Phys.* 21.5 (2019), pp. 2587–2594. DOI: [10.1039/C8CP07463A](https://doi.org/10.1039/C8CP07463A).
- [60] Esther K. van den Beuken and Ben L. Feringa. “Bimetallic catalysis by late transition metal complexes”. In: *Tetrahedron* 54.43 (Oct. 1998), pp. 12985–13011. DOI: [10.1016/S0040-4020\(98\)00319-6](https://doi.org/10.1016/S0040-4020(98)00319-6).
- [61] Daniel Baranowski et al. “Conservation of Nickel Ion Single-Active Site Character in a Bottom-Up Constructed π -Conjugated Molecular Network”. In: *Angew. Chemie* (Sept. 2022). DOI: [10.1002/ange.202210326](https://doi.org/10.1002/ange.202210326).
- [62] K. F. Peters et al. “Adsorption of carbon monoxide on Ni(110) above atmospheric pressure investigated with surface X-ray diffraction”. In: *Phys. Rev. Lett.* 86.23 (2001), pp. 5325–5328. DOI: [10.1103/PhysRevLett.86.5325](https://doi.org/10.1103/PhysRevLett.86.5325).
- [63] Bas Hulsken et al. “Real-time single-molecule imaging of oxidation catalysis at a liquid-solid interface”. In: *Nat. Nanotechnol.* 2.5 (2007), pp. 285–289. DOI: [10.1038/nnano.2007.106](https://doi.org/10.1038/nnano.2007.106).

- [64] Benjamin A. Friesen et al. “Single Molecule Imaging of Oxygenation of Cobalt Octaethylporphyrin at the Solution/Solid Interface: Thermodynamics from Microscopy”. In: *J. Am. Chem. Soc.* 134.36 (Sept. 2012), pp. 14897–14904. DOI: [10.1021/ja304431b](https://doi.org/10.1021/ja304431b).
- [65] Duncan Den Boer et al. “Detection of different oxidation states of individual manganese porphyrins during their reaction with oxygen at a solid/liquid interface”. In: *Nat. Chem.* 5.7 (2013), pp. 621–627. DOI: [10.1038/nchem.1667](https://doi.org/10.1038/nchem.1667).
- [66] Suyun Zhu et al. “HIPPIE: A new platform for ambient-pressure X-ray photoelectron spectroscopy at the MAX IV Laboratory”. In: *J. Synchrotron Radiat.* 28.2 (Mar. 2021), pp. 624–636. DOI: [10.1107/S160057752100103X](https://doi.org/10.1107/S160057752100103X).
- [67] Günther Rupprechter. “Sum Frequency Generation and Polarization-Modulation Infrared Reflection Absorption Spectroscopy of Functioning Model Catalysts from Ultrahigh Vacuum to Ambient Pressure”. In: *Adv. Catal.* 51 (2007), pp. 133–263. DOI: [10.1016/S0360-0564\(06\)51004-1](https://doi.org/10.1016/S0360-0564(06)51004-1).
- [68] Rosanna Larciprete et al. “Oxygen switching of the epitaxial graphene-metal interaction”. In: *ACS Nano* 6.11 (2012), pp. 9551–9558. DOI: [10.1021/nn302729j](https://doi.org/10.1021/nn302729j).
- [69] Ken Flechtner et al. “NO-induced reversible switching of the electronic interaction between a porphyrin-coordinated cobalt ion and a silver surface”. In: *J. Am. Chem. Soc.* 129.40 (2007), pp. 12110–12111. DOI: [10.1021/ja0756725](https://doi.org/10.1021/ja0756725).
- [70] F. Armillotta et al. “Dioxygen at Biomimetic Single Metal-Atom Sites: Stabilization or Activation? The Case of CoTPyP/Au(111)”. In: *Top. Catal.* 111 (2020). DOI: [10.1007/s11244-020-01333-9](https://doi.org/10.1007/s11244-020-01333-9).
- [71] Paolo Giannozzi et al. “QUANTUM ESPRESSO: a modular and open-source software project for quantum simulations of materials”. In: *J. Phys. Condens. Matter* 21.39 (Sept. 2009), p. 395502. DOI: [10.1088/0953-8984/21/39/395502](https://doi.org/10.1088/0953-8984/21/39/395502).
- [72] P. Giannozzi et al. “Advanced capabilities for materials modelling with Quantum ESPRESSO”. In: *J. Phys. Condens. Matter* 29.46 (Nov. 2017), p. 465901. DOI: [10.1088/1361-648X/aa8f79](https://doi.org/10.1088/1361-648X/aa8f79).
- [73] Paolo Giannozzi et al. “Quantum ESPRESSO toward the exascale”. In: *J. Chem. Phys.* 152.15 (Apr. 2020), p. 154105. DOI: [10.1063/5.0005082](https://doi.org/10.1063/5.0005082).
- [74] Andrew M. Rappe et al. “Optimized pseudopotentials”. In: *Phys. Rev. B* 41.2 (Jan. 1990), pp. 1227–1230. DOI: [10.1103/PhysRevB.41.1227](https://doi.org/10.1103/PhysRevB.41.1227).
- [75] Matteo Cococcioni and Stefano de Gironcoli. “Linear response approach to the calculation of the effective interaction parameters in the LDA+U method”. In: *Phys. Rev. B* 71.3 (Jan. 2005), p. 035105. DOI: [10.1103/PhysRevB.71.035105](https://doi.org/10.1103/PhysRevB.71.035105).
- [76] Luis G. G. V. Dias da Silva et al. “Many-body electronic structure and Kondo properties of cobalt-porphyrin molecules”. In: *Phys. Rev. B* 80.15 (Oct. 2009), p. 155443. DOI: [10.1103/PhysRevB.80.155443](https://doi.org/10.1103/PhysRevB.80.155443).

- [77] Stefan Grimme et al. “A consistent and accurate ab initio parametrization of density functional dispersion correction (DFT-D) for the 94 elements H-Pu”. In: *J. Chem. Phys.* 132.15 (Apr. 2010), p. 154104. DOI: [10.1063/1.3382344](https://doi.org/10.1063/1.3382344).
- [78] Julia Contreras-García et al. “NCIPLOT: A Program for Plotting Noncovalent Interaction Regions”. In: *J. Chem. Theory Comput.* 7.3 (Mar. 2011), pp. 625–632. DOI: [10.1021/ct100641a](https://doi.org/10.1021/ct100641a).
- [79] E. Pehlke and M. Scheffler. “Evidence for site-sensitive screening of core holes at the Si and Ge (001) surface”. In: *Phys. Rev. Lett.* 71.14 (Oct. 1993), pp. 2338–2341. DOI: [10.1103/PhysRevLett.71.2338](https://doi.org/10.1103/PhysRevLett.71.2338).
- [80] M. Methfessel and A. T. Paxton. “High-precision sampling for Brillouin-zone integration in metals”. In: *Phys. Rev. B* 40.6 (Aug. 1989), pp. 3616–3621. DOI: [10.1103/PhysRevB.40.3616](https://doi.org/10.1103/PhysRevB.40.3616).
- [81] Patrick H.L. Sit et al. “Simple, unambiguous theoretical approach to oxidation state determination via first-principles calculations”. In: *Inorg. Chem.* 50.20 (2011), pp. 10259–10267. DOI: [10.1021/ic2013107](https://doi.org/10.1021/ic2013107).
- [82] Bertrand Busson and Abderrahmane Tadjeddine. “Non-uniqueness of parameters extracted from resonant second-order nonlinear optical spectroscopies”. In: *J. Phys. Chem. C* 113.52 (2009), pp. 21895–21902. DOI: [10.1021/jp908240d](https://doi.org/10.1021/jp908240d).
- [83] Alexander Geoffrey Lambert, Paul B. Davies, and David J. Neivandt. “Implementing the Theory of Sum Frequency Generation Vibrational Spectroscopy: A Tutorial Review”. In: *Appl. Spectrosc. Rev.* 40.2 (May 2005), pp. 103–145. DOI: [10.1081/ASR-200038326](https://doi.org/10.1081/ASR-200038326).
- [84] Hong Fei Wang et al. “Quantitative sum-frequency generation vibrational spectroscopy of molecular surfaces and interfaces: Lineshape, polarization, and orientati”. In: *Annu. Rev. Phys. Chem.* 66.November 2014 (2015), pp. 189–216. DOI: [10.1146/annurev-physchem-040214-121322](https://doi.org/10.1146/annurev-physchem-040214-121322).
- [85] Bogdan Dryzhakov. *Sum frequency generation (SFG): Future plans observing SEI on gold in situ Investigation of the Electrolyte*.
- [86] Andrew J. Stentz and Robert W. Boyd. “Nonlinear optics”. In: *Handb. Photonics, Second Ed.* 2006.
- [87] Alexander Geoffrey Lambert. “Resonantly enhanced sum frequency spectroscopy of adsorption on hydrophilic mica substrates”. Ph.D. Thesis. University of Cambridge, 2001. DOI: <https://doi.org/10.17863/CAM.16301>.
- [88] J.H. Hunt, Philippe Guyot-Sionnest, and Yuen Ron Shen. “Observation of C-H stretch vibrations of monolayers of molecules optical sum-frequency generation”. In: *Chem. Phys. Lett.* 133.3 (Jan. 1987), pp. 189–192. DOI: [10.1016/0009-2614\(87\)87049-5](https://doi.org/10.1016/0009-2614(87)87049-5).

- [89] Shenghsien H. Lin and Albert A. Villaeys. “Theoretical description of steady-state sum-frequency generation in molecular adsorbates”. In: *Phys. Rev. A* 50.6 (Dec. 1994), pp. 5134–5144. DOI: [10.1103/PhysRevA.50.5134](https://doi.org/10.1103/PhysRevA.50.5134).
- [90] Ekspla. *SFG Spectrometer: Technical Description and User’s Manual*. 2013.
- [91] Ittipol Jangchud et al. “Scanning probe microscopes”. In: *Adv. Mater. Process.* 148.1 (1995), pp. 33–34. DOI: [10.5650/jos1996.49.1181](https://doi.org/10.5650/jos1996.49.1181).
- [92] G. Binnig et al. “Surface Studies by Scanning Tunneling Microscopy”. In: *Phys. Rev. Lett.* 49.1 (July 1982), pp. 57–61. DOI: [10.1103/PhysRevLett.49.57](https://doi.org/10.1103/PhysRevLett.49.57).
- [93] Flemming Besenbacher. “Scanning tunnelling microscopy studies of metal surfaces”. In: *Reports Prog. Phys.* 59.12 (1996), pp. 1737–1802. DOI: [10.1088/0034-4885/59/12/004](https://doi.org/10.1088/0034-4885/59/12/004).
- [94] J E Griffith and G P Kochanski. “Scanning Tunneling Microscopy”. In: *Annu. Rev. Mater. Sci.* 20.1 (Aug. 1990), pp. 219–244. DOI: [10.1146/annurev.ms.20.080190.001251](https://doi.org/10.1146/annurev.ms.20.080190.001251).
- [95] *The Advanced Photon Source - Synchrotron X-ray STM - Physical Concept*. URL: <https://www.aps.anl.gov/SXSPM/Research/Physical-Concept>. Last access on 06-Jan-2023.
- [96] Kurt W. Kolasinski. *Surface Science*. Chichester, UK: John Wiley & Sons, Ltd, Apr. 2012. DOI: [10.1002/9781119941798](https://doi.org/10.1002/9781119941798).
- [97] Steven De Feyter and Frans C. De Schryver. “Two-dimensional supramolecular self-assembly probed by scanning tunneling microscopy”. In: *Chem. Soc. Rev.* 32.3 (2003), pp. 139–150. DOI: [10.1039/b206566p](https://doi.org/10.1039/b206566p).
- [98] Zeljkovic Lab. *Scanning tunneling microscopy (STM)*.
- [99] Andrea Damascelli, Zahid Hussain, and Zhi Xun Shen. “Angle-resolved photoemission studies of the cuprate superconductors”. In: *Rev. Mod. Phys.* 75.2 (2003), pp. 473–541. DOI: [10.1103/RevModPhys.75.473](https://doi.org/10.1103/RevModPhys.75.473).
- [100] Pardis Simon, Víctor G. Baldovino-Medrano, and Robert Wojcieszak. “X-Ray Photoelectron Spectroscopy (XPS): Principles and Application for the Analysis of Photoactive Materials”. In: 2022, pp. 249–271. DOI: [10.1007/978-3-030-63713-2_10](https://doi.org/10.1007/978-3-030-63713-2_10).
- [101] Phil Woodruff. *Modern Techniques of Surface Science*. Vol. 41. 3. Cambridge: Cambridge University Press, Mar. 2016, pp. 90–92. DOI: [10.1017/CB09781139149716](https://doi.org/10.1017/CB09781139149716).
- [102] Stefan Hüfner. “Introduction and Basic Principles”. In: 2003, pp. 1–60. DOI: [10.1007/978-3-662-09280-4_1](https://doi.org/10.1007/978-3-662-09280-4_1).
- [103] M. P. Seah and W. A. Dench. “Quantitative electron spectroscopy of surfaces: A standard data base for electron inelastic mean free paths in solids”. In: *Surf. Interface Anal.* 1.1 (Feb. 1979), pp. 2–11. DOI: [10.1002/sia.740010103](https://doi.org/10.1002/sia.740010103).

- [104] Siegfried Hofmann. *Auger- and X-Ray Photoelectron Spectroscopy in Materials Science*. Vol. 49. Springer Series in Surface Sciences. Berlin, Heidelberg: Springer Berlin Heidelberg, 2013. DOI: [10.1007/978-3-642-27381-0](https://doi.org/10.1007/978-3-642-27381-0).
- [105] Fred A. Stevie and Carrie L. Donley. “Introduction to x-ray photoelectron spectroscopy”. In: *J. Vac. Sci. Technol. A* 38.6 (2020), p. 063204. DOI: [10.1116/6.0000412](https://doi.org/10.1116/6.0000412).
- [106] Sebastian Doniach and Marijan Sunjic. “Many-electron singularity in X-ray photoemission and X-ray line spectra from metals”. In: *J. Phys. C Solid State Phys.* 3.2 (Feb. 1970), pp. 285–291. DOI: [10.1088/0022-3719/3/2/010](https://doi.org/10.1088/0022-3719/3/2/010).
- [107] Miquel B. Salmeron, Robert. Schlog, and R Schlögl. “Ambient pressure photoelectron spectroscopy: A new tool for surface science and nanotechnology”. In: *Surf. Sci. Rep.* 63.4 (Apr. 2008), pp. 169–199. DOI: [10.1016/j.surfrep.2008.01.001](https://doi.org/10.1016/j.surfrep.2008.01.001).
- [108] K. R. Hoffman et al. “Total-cross-section measurements for positrons and electrons colliding with H₂, N₂, and CO₂”. In: *Phys. Rev. A* 25.3 (1982), pp. 1393–1403. DOI: [10.1103/PhysRevA.25.1393](https://doi.org/10.1103/PhysRevA.25.1393).
- [109] Grzegorz P. Karwasz et al. “Total cross sections for electron scattering on chloromethanes: Formulation of the additivity rule”. In: *Phys. Rev. A - At. Mol. Opt. Phys.* 59.2 (1999), pp. 1341–1347. DOI: [10.1103/PhysRevA.59.1341](https://doi.org/10.1103/PhysRevA.59.1341).
- [110] Stöhr Joachim. *NEXAFS Spectroscopy*. Springer-Verlag Berlin Heidelberg, 1992.
- [111] Alexei Nefedov and Christof Wöll. “Advanced Applications of NEXAFS Spectroscopy for Functionalized Surfaces”. In: *Springer Ser. Surf. Sci.* Vol. 51. 1. 2013, pp. 277–303. DOI: [10.1007/978-3-642-34243-1_10](https://doi.org/10.1007/978-3-642-34243-1_10).
- [112] C.M. Schneider et al. “Expanding the view into complex material systems: From micro-ARPES to nanoscale HAXPES”. In: *J. Electron Spectros. Relat. Phenomena* 185.10 (Oct. 2012), pp. 330–339. DOI: [10.1016/j.elspec.2012.08.003](https://doi.org/10.1016/j.elspec.2012.08.003).
- [113] P. Szymanski, S. Garrett-Roe, and C. B. Harris. “Time- and angle-resolved two-photon photoemission studies of electron localization and solvation at interfaces”. In: *Prog. Surf. Sci.* 78.1 (2005), pp. 1–39. DOI: [10.1016/j.progsurf.2004.08.001](https://doi.org/10.1016/j.progsurf.2004.08.001).
- [114] Wibke Bronsch. “Molecular Exciton Related Phenomena Studied by TwoPhoton Photoemission”. Ph.D. Thesis. Freir Universität Berlin, 2019. DOI: [10.17169/refubium-2709](https://doi.org/10.17169/refubium-2709).
- [115] H. Ueba and B. Gumhalter. “Theory of two-photon photoemission spectroscopy of surfaces”. In: *Prog. Surf. Sci.* 82.4-6 (2007), pp. 193–223. DOI: [10.1016/j.progsurf.2007.03.002](https://doi.org/10.1016/j.progsurf.2007.03.002).
- [116] R. Costantini et al. “ANCHOR-SUNDYN: A novel endstation for time resolved spectroscopy at the ALOISA beamline”. In: *J. Electron Spectros. Relat. Phenomena* 229. September (2018), pp. 7–12. DOI: [10.1016/j.elspec.2018.09.005](https://doi.org/10.1016/j.elspec.2018.09.005).

- [117] H. Hattab et al. "Growth temperature dependent graphene alignment on Ir(111)". In: *Appl. Phys. Lett.* 98.14 (Apr. 2011), p. 141903. DOI: [10.1063/1.3548546](https://doi.org/10.1063/1.3548546).
- [118] Manuel Corva et al. "Vibrational fingerprint of localized excitons in a two-dimensional metal-organic crystal". In: *Nat. Commun.* 9.1 (Dec. 2018), p. 4703. DOI: [10.1038/s41467-018-07190-1](https://doi.org/10.1038/s41467-018-07190-1).
- [119] Michael Endlich et al. "Moiré-induced replica of graphene phonons on Ir(111)". In: *Ann. Phys.* 526.9-10 (Oct. 2014), pp. 372–380. DOI: [10.1002/andp.201400091](https://doi.org/10.1002/andp.201400091).
- [120] Amjad Al Taleb et al. "Resolving localized phonon modes on graphene/Ir(111) by inelastic atom scattering". In: *Carbon N. Y.* 133 (2018), pp. 31–38. DOI: [10.1016/j.carbon.2018.03.008](https://doi.org/10.1016/j.carbon.2018.03.008).
- [121] Alpha T. N'Diaye et al. "Two-dimensional Ir cluster lattice on a graphene moiré on Ir(111)". In: *Phys. Rev. Lett.* 97.21 (2006), pp. 1–4. DOI: [10.1103/PhysRevLett.97.215501](https://doi.org/10.1103/PhysRevLett.97.215501).
- [122] Barry E. Murphy et al. "Homolytic Cleavage of Molecular Oxygen by Manganese Porphyrins Supported on Ag(111)". In: *ACS Nano* 8.5 (May 2014), pp. 5190–5198. DOI: [10.1021/nn501240j](https://doi.org/10.1021/nn501240j).
- [123] Willi Auwärter et al. "Controlled metalation of self-assembled porphyrin nanoarrays in two dimensions". In: *ChemPhysChem* 8.2 (2007), pp. 250–254. DOI: [10.1002/cphc.200600675](https://doi.org/10.1002/cphc.200600675).
- [124] Brian D. Baker Cortés et al. "Structural Transformation of Surface-Confined Porphyrin Networks by Addition of Co Atoms". In: *Chem. - A Eur. J.* 27.48 (2021), pp. 12430–12436. DOI: [10.1002/chem.202101217](https://doi.org/10.1002/chem.202101217).
- [125] Florian Buchner et al. "Ordering aspects and intramolecular conformation of tetraphenylporphyrins on Ag (111)". In: *111* (2010), pp. 13082–13090. DOI: [10.1039/c004551a](https://doi.org/10.1039/c004551a).
- [126] Arnulf Stein et al. "Electronic structure of an iron porphyrin derivative on Au(111)". In: *J. Phys. Condens. Matter* 31.4 (Jan. 2019), p. 044002. DOI: [10.1088/1361-648X/aaf296](https://doi.org/10.1088/1361-648X/aaf296).
- [127] Stefan Müllegger et al. "Spectroscopic STM studies of single gold(III) porphyrin molecules". In: *J. Am. Chem. Soc.* 131.49 (2009), pp. 17740–17741. DOI: [10.1021/ja908157j](https://doi.org/10.1021/ja908157j).
- [128] Fabian Mohn et al. "Imaging the charge distribution within a single molecule". In: *Nat. Nanotechnol.* 7.4 (2012), pp. 227–231. DOI: [10.1038/nnano.2012.20](https://doi.org/10.1038/nnano.2012.20).
- [129] Jascha Repp et al. "Molecules on Insulating Films : Scanning-Tunneling Microscopy Imaging of Individual Molecular Orbitals". In: *026803*. January (2005), pp. 1–4. DOI: [10.1103/PhysRevLett.94.026803](https://doi.org/10.1103/PhysRevLett.94.026803).

- [130] Knud Seufert et al. “Cis-dicarbonyl binding at cobalt and iron porphyrins with saddle-shape conformation”. In: *Nat. Chem.* 3.2 (2011), pp. 114–119. DOI: [10.1038/nchem.956](https://doi.org/10.1038/nchem.956).
- [131] Willi Auwärter et al. “Site-specific electronic and geometric interface structure of Co-tetraphenyl-porphyrin layers on Ag(111)”. In: *Phys. Rev. B* 81.24 (June 2010), p. 245403. DOI: [10.1103/PhysRevB.81.245403](https://doi.org/10.1103/PhysRevB.81.245403).
- [132] Kai Braun et al. “Active optical antennas driven by inelastic electron tunneling”. In: *Nanophotonics* 7.9 (2018), pp. 1503–1516. DOI: [10.1515/nanoph-2018-0080](https://doi.org/10.1515/nanoph-2018-0080).
- [133] “Courtesy of my colleague Davide Bidoggia who did DFT simulations in collaboration with the group of prof. Maria Peressi (Uni. Trieste - ICTP)”.
- [134] Yang Li et al. “Coordination and metalation bifunctionality of Cu with 5,10,15,20-tetra(4-pyridyl)porphyrin: Toward a mixed-valence two-dimensional coordination network”. In: *J. Am. Chem. Soc.* 134.14 (Apr. 2012), pp. 6401–6408. DOI: [10.1021/ja300593w](https://doi.org/10.1021/ja300593w).
- [135] Francesco Armillotta et al. “Single Metal Atom Catalysts and ORR: H-Bonding, Solvation, and the Elusive Hydroperoxyl Intermediate”. In: *ACS Catal.* 12.13 (July 2022), pp. 7950–7959. DOI: [10.1021/acscatal.2c02029](https://doi.org/10.1021/acscatal.2c02029).
- [136] Violeta Iancu et al. “Electron–phonon coupling in engineered magnetic molecules”. In: *Chem. Commun.* 52.76 (2016), pp. 11359–11362. DOI: [10.1039/c6cc03847f](https://doi.org/10.1039/c6cc03847f).
- [137] Mattia Scardamaglia et al. “Spectroscopic observation of oxygen dissociation on nitrogen-doped graphene”. In: *Sci. Rep.* 7.1 (Dec. 2017), p. 7960. DOI: [10.1038/s41598-017-08651-1](https://doi.org/10.1038/s41598-017-08651-1).
- [138] Fuping Pan et al. “Identification of champion transition metals centers in metal and nitrogen-codoped carbon catalysts for CO₂ reduction”. In: *Appl. Catal. B Environ.* 226.November 2017 (2018), pp. 463–472. DOI: [10.1016/j.apcatb.2018.01.001](https://doi.org/10.1016/j.apcatb.2018.01.001).
- [139] Gerson Mette et al. “From porphyrins to pyrphyrins: Adsorption study and metalation of a molecular catalyst on Au(111)”. In: *Nanoscale* 8.15 (2016), pp. 7958–7968. DOI: [10.1039/c5nr08953k](https://doi.org/10.1039/c5nr08953k).
- [140] Yun Bai. “Photoelectron Spectroscopic Investigations of Porphyrins and Phthalocyanines on Ag(111) and Au(111): Adsorption and Reactivity.” PhD Thesis. Friedrich-Alexander-Universität Erlangen-Nürnberg, 2010.
- [141] O. Gunnarsson and K. Schönhammer. “CO on Cu(100)—Explanation of the Three-Peak Structure in the X-Ray-Photoemission-Spectroscopy Core Spectrum”. In: *Phys. Rev. Lett.* 41.23 (Dec. 1978), pp. 1608–1612. DOI: [10.1103/PhysRevLett.41.1608](https://doi.org/10.1103/PhysRevLett.41.1608).

- [142] C. Isvoranu et al. "Tuning the spin state of iron phthalocyanine by ligand adsorption". In: *J. Phys. Condens. Matter* 22.47 (2010), pp. 20–24. DOI: [10.1088/0953-8984/22/47/472002](https://doi.org/10.1088/0953-8984/22/47/472002).
- [143] M. P. De Jong et al. "Orbital-specific dynamic charge transfer from Fe(II)-tetraphenylporphyrin molecules to molybdenum disulfide substrates". In: *Phys. Rev. B - Condens. Matter Mater. Phys.* 72.3 (2005), pp. 1–8. DOI: [10.1103/PhysRevB.72.035448](https://doi.org/10.1103/PhysRevB.72.035448).
- [144] C. Kolczewski et al. "Detailed study of pyridine at the C 1s and N 1s ionization thresholds: The influence of the vibrational fine structure". In: *J. Chem. Phys.* 115.14 (2001), pp. 6426–6437. DOI: [10.1063/1.1397797](https://doi.org/10.1063/1.1397797).
- [145] Norman Schmidt, Rainer Fink, and Wolfgang Hieringer. "Assignment of near-edge x-ray absorption fine structure spectra of metalloporphyrins by means of time-dependent density-functional calculations". In: *J. Chem. Phys.* 133.5 (2010). DOI: [10.1063/1.3435349](https://doi.org/10.1063/1.3435349).
- [146] Anthoula C. Papageorgiou et al. "Self-terminating protocol for an interfacial complexation reaction in vacuo by metal-organic chemical vapor deposition". In: *ACS Nano* 7.5 (2013), pp. 4520–4526. DOI: [10.1021/nn401171z](https://doi.org/10.1021/nn401171z).
- [147] Stefan Müllegger et al. "Single-molecule chemical reduction induced by low-temperature scanning tunneling microscopy: A case study of gold-porphyrin on Au(111)". In: *Surf. Sci.* 678. February (2018), pp. 157–162. DOI: [10.1016/j.susc.2018.04.018](https://doi.org/10.1016/j.susc.2018.04.018).
- [148] Rong Lu et al. "Vibrational polarization spectroscopy of CH stretching modes of the methylene group at the vapor/liquid interfaces with sum frequency generation". In: *J. Phys. Chem. B* 108.22 (2004), pp. 7297–7306. DOI: [10.1021/jp036674o](https://doi.org/10.1021/jp036674o).
- [149] Jana Hudecová et al. "CH stretching region: Computational modeling of vibrational optical activity". In: *J. Chem. Theory Comput.* 9.7 (2013), pp. 3096–3108. DOI: [10.1021/ct400285n](https://doi.org/10.1021/ct400285n).
- [150] F. Partal Ureña et al. "A new insight into the vibrational analysis of pyridine". In: *Spectrochim. Acta - Part A Mol. Biomol. Spectrosc.* 59.12 (2003), pp. 2815–2839. DOI: [10.1016/S1386-1425\(03\)00082-9](https://doi.org/10.1016/S1386-1425(03)00082-9).
- [151] Brian D. Baker Cortés et al. "Comparing Cyanophenyl and Pyridyl Ligands in the Formation of Porphyrin-Based Metal-Organic Coordination Networks". In: *J. Phys. Chem. C* 125.44 (2021), pp. 24557–24567. DOI: [10.1021/acs.jpcc.1c05360](https://doi.org/10.1021/acs.jpcc.1c05360).
- [152] Bing Liu et al. "Inspecting the nonbonding and antibonding orbitals in a surface-supported metal-organic framework". In: *Chem. Commun.* 57.37 (2021), pp. 4580–4583. DOI: [10.1039/d1cc00506e](https://doi.org/10.1039/d1cc00506e).
- [153] Chi Vo-Van et al. "Magnetism of cobalt nanoclusters on graphene on iridium". In: *Appl. Phys. Lett.* 99.14 (2011), pp. 2012–2015. DOI: [10.1063/1.3646480](https://doi.org/10.1063/1.3646480).

- [154] Tao Lin et al. “Two-dimensional lattice of out-of-plane dinuclear iron centers exhibiting Kondo resonance”. In: *ACS Nano* 8.8 (2014), pp. 8310–8316. DOI: [10.1021/nn502765g](https://doi.org/10.1021/nn502765g).
- [155] Travis Marshall-Roth et al. “A pyridinic Fe-N₄ macrocycle models the active sites in Fe/N-doped carbon electrocatalysts”. In: *Nat. Commun.* 11.1 (2020), pp. 1–14. DOI: [10.1038/s41467-020-18969-6](https://doi.org/10.1038/s41467-020-18969-6).
- [156] Thomas Lukasczyk et al. “Interaction of Cobalt(II) Tetraarylporphyrins with a Ag(111) Surface Studied with Photoelectron Spectroscopy”. In: *J. Phys. Chem. C* 111.7 (Feb. 2007), pp. 3090–3098. DOI: [10.1021/jp0652345](https://doi.org/10.1021/jp0652345).
- [157] Giovanni Zamborlini et al. “Multi-orbital charge transfer at highly oriented organic/metal interfaces”. In: *Nat. Commun.* 8.1 (2017), pp. 1–7. DOI: [10.1038/s41467-017-00402-0](https://doi.org/10.1038/s41467-017-00402-0).
- [158] Matteo Jugovac et al. “Clarifying the apparent flattening of the graphene band near the van Hove singularity”. In: *Phys. Rev. B* 105.24 (2022), pp. 1–6. DOI: [10.1103/PhysRevB.105.L241107](https://doi.org/10.1103/PhysRevB.105.L241107).
- [159] Christian Tusche et al. “Nonlocal electron correlations in an itinerant ferromagnet”. In: *Nat. Commun.* 9.1 (2018). DOI: [10.1038/s41467-018-05960-5](https://doi.org/10.1038/s41467-018-05960-5).
- [160] Ioannis Katsounaros et al. “Oxygen electrochemistry as a cornerstone for sustainable energy conversion”. In: *Angew. Chemie - Int. Ed.* 53.1 (2014), pp. 102–121. DOI: [10.1002/anie.201306588](https://doi.org/10.1002/anie.201306588).
- [161] Nan Wang et al. “Recent Progress of Electrochemical Production of Hydrogen Peroxide by Two-Electron Oxygen Reduction Reaction”. In: *Adv. Sci.* 8.15 (2021), pp. 1–26. DOI: [10.1002/advs.202100076](https://doi.org/10.1002/advs.202100076).
- [162] Jiajian Gao and Bin Liu. “Progress of Electrochemical Hydrogen Peroxide Synthesis over Single Atom Catalysts”. In: *ACS Mater. Lett.* 2.8 (Aug. 2020), pp. 1008–1024. DOI: [10.1021/acsmaterialslett.0c00189](https://doi.org/10.1021/acsmaterialslett.0c00189).
- [163] Benedetto Bozzini et al. “In situ near-ambient pressure X-ray photoelectron spectroscopy discloses the surface composition of operating NdBaCo₂O_{5+δ} solid oxide fuel cell cathodes”. In: *J. Power Sources* 436.June (Oct. 2019), p. 226815. DOI: [10.1016/j.jpowsour.2019.226815](https://doi.org/10.1016/j.jpowsour.2019.226815).
- [164] Chang Hyuck Choi et al. “Hydrogen peroxide synthesis via enhanced two-electron oxygen reduction pathway on carbon-coated pt surface”. In: *J. Phys. Chem. C* 118.51 (2014), pp. 30063–30070. DOI: [10.1021/jp5113894](https://doi.org/10.1021/jp5113894).
- [165] Xiaofeng Tang et al. “Threshold photoelectron spectroscopy of the HO₂radical”. In: *J. Chem. Phys.* 153.12 (2020). DOI: [10.1063/5.0022410](https://doi.org/10.1063/5.0022410).
- [166] Wei Sun et al. “A rechargeable zinc-air battery based on zinc peroxide chemistry”. In: *Science (80-.)*. 371.6524 (Jan. 2021), pp. 46–51. DOI: [10.1126/science.abb9554](https://doi.org/10.1126/science.abb9554).

- [167] Jiajian Gao et al. “Enabling Direct H₂O₂ Production in Acidic Media through Rational Design of Transition Metal Single Atom Catalyst”. In: *Chem* 6.3 (Mar. 2020), pp. 658–674. DOI: [10.1016/j.chempr.2019.12.008](https://doi.org/10.1016/j.chempr.2019.12.008).
- [168] Yi Xiao and Weibin Zhang. “High-Throughput Calculation Investigations on the Electrocatalytic Activity of Codoped Single Metal–Nitrogen Embedded in Graphene for ORR Mechanism”. In: *Electrocatalysis* 11.4 (July 2020), pp. 393–404. DOI: [10.1007/s12678-020-00598-8](https://doi.org/10.1007/s12678-020-00598-8).
- [169] Kohsuke Suma, Yoshihiro Sumiyoshi, and Yasuki Endo. “The Rotational Spectrum of the Water-Hydroperoxy Radical (H₂O–HO₂) Complex”. In: *Science* (80-.). 311.5765 (Mar. 2006), pp. 1278–1281. DOI: [10.1126/science.1124022](https://doi.org/10.1126/science.1124022).
- [170] S. Aloisio and J. S. Francisco. “Existence of a Hydroperoxy and Water (HO₂·H₂O) Radical Complex”. In: *J. Phys. Chem. A* 102.11 (Mar. 1998), pp. 1899–1902. DOI: [10.1021/jp972173p](https://doi.org/10.1021/jp972173p).
- [171] Srinivasan S. Iyengar. “Dynamical effects on vibrational and electronic spectra of hydroperoxyl radical water clusters”. In: *J. Chem. Phys.* 123.8 (Aug. 2005), p. 084310. DOI: [10.1063/1.2006674](https://doi.org/10.1063/1.2006674).
- [172] Heriberto Hernández-Soto, Frank Weinhold, and Joseph S. Francisco. “Radical hydrogen bonding: Origin of stability of radical-molecule complexes”. In: *J. Chem. Phys.* 127.16 (Oct. 2007), p. 164102. DOI: [10.1063/1.2784558](https://doi.org/10.1063/1.2784558).
- [173] Xin Xu, Richard P. Muller, and William A. Goddard. “The gas phase reaction of singlet dioxygen with water: A water-catalyzed mechanism”. In: *Proc. Natl. Acad. Sci.* 99.6 (Mar. 2002), pp. 3376–3381. DOI: [10.1073/pnas.052710099](https://doi.org/10.1073/pnas.052710099).
- [174] Jin-Chao Dong et al. “In situ Raman spectroscopic evidence for oxygen reduction reaction intermediates at platinum single-crystal surfaces”. In: *Nat. Energy* 4.1 (Jan. 2019), pp. 60–67. DOI: [10.1038/s41560-018-0292-z](https://doi.org/10.1038/s41560-018-0292-z).
- [175] Jin-Chao Dong et al. “Direct In Situ Raman Spectroscopic Evidence of Oxygen Reduction Reaction Intermediates at High-Index Pt(hkl) Surfaces”. In: *J. Am. Chem. Soc.* 142.2 (Jan. 2020), pp. 715–719. DOI: [10.1021/jacs.9b12803](https://doi.org/10.1021/jacs.9b12803).
- [176] N. A. Vinogradov et al. “Controllable p-doping of graphene on Ir(111) by chlorination with FeCl₃”. In: *J. Phys. Condens. Matter* 24.31 (2012). DOI: [10.1088/0953-8984/24/31/314202](https://doi.org/10.1088/0953-8984/24/31/314202).
- [177] Manuel Corva et al. “Carbon dioxide reduction on Ir(111): stable hydrocarbon surface species at near-ambient pressure”. In: *Phys. Chem. Chem. Phys.* 18.9 (2016), pp. 6763–6772. DOI: [10.1039/C5CP07906C](https://doi.org/10.1039/C5CP07906C).
- [178] Sampsa K. Hämäläinen et al. “Self-Assembly of Cobalt-Phthalocyanine Molecules on Epitaxial Graphene on Ir(111)”. In: *J. Phys. Chem. C* 116.38 (Sept. 2012), pp. 20433–20437. DOI: [10.1021/jp306439h](https://doi.org/10.1021/jp306439h).

- [179] Jing-Ying Gu et al. “Single-Molecule Imaging of Iron-Phthalocyanine-Catalyzed Oxygen Reduction Reaction by in Situ Scanning Tunneling Microscopy”. In: *ACS Nano* 10.9 (Sept. 2016), pp. 8746–8750. DOI: [10.1021/acsnano.6b04281](https://doi.org/10.1021/acsnano.6b04281).
- [180] Nils Blom et al. “Resonance Raman studies of metal tetrakis (4-N-methylpyridyl) porphine: band assignments, structure-sensitive bands, and species equilibria”. In: *J. Phys. Chem.* 90.13 (June 1986), pp. 2847–2852. DOI: [10.1021/j100404a015](https://doi.org/10.1021/j100404a015).
- [181] Koiti Araki et al. “Resonance Raman spectra of a supramolecular species containing four ruthenium(II)-bipyridine complexes attached to zinc-tetrapyrrolyl porphyrinate”. In: *Spectrosc. Lett.* 28.1 (Jan. 1995), pp. 119–126. DOI: [10.1080/00387019508011660](https://doi.org/10.1080/00387019508011660).
- [182] James R Kincaid et al. “Resonance Raman spectra of oxygen adducts of cobalt porphyrins. Enhancement of solvent and solute bands via resonance vibrational coupling”. In: *J. Am. Chem. Soc.* 107.24 (Nov. 1985), pp. 6775–6781. DOI: [10.1021/ja00310a005](https://doi.org/10.1021/ja00310a005).
- [183] Verena Streibel et al. “In Situ Electrochemical Cells to Study the Oxygen Evolution Reaction by Near Ambient Pressure X-ray Photoelectron Spectroscopy”. In: *Top. Catal.* 61.20 (Dec. 2018), pp. 2064–2084. DOI: [10.1007/s11244-018-1061-8](https://doi.org/10.1007/s11244-018-1061-8).
- [184] Rosa Arrigo et al. “In Situ Study of the Gas-Phase Electrolysis of Water on Platinum by NAP-XPS”. In: *Angew. Chemie Int. Ed.* 52.44 (Oct. 2013), pp. 11660–11664. DOI: [10.1002/anie.201304765](https://doi.org/10.1002/anie.201304765).
- [185] Marco Favaro et al. “Understanding the Oxygen Evolution Reaction Mechanism on CoO_x using Operando Ambient-Pressure X-ray Photoelectron Spectroscopy”. In: *J. Am. Chem. Soc.* 139.26 (July 2017), pp. 8960–8970. DOI: [10.1021/jacs.7b03211](https://doi.org/10.1021/jacs.7b03211).
- [186] Xiaowei Cai et al. “Understanding the Evolution of Cobalt-Based Metal-Organic Frameworks in Electrocatalysis for the Oxygen Evolution Reaction”. In: *ChemSusChem* 14.15 (Aug. 2021), pp. 3163–3173. DOI: [10.1002/cssc.202100851](https://doi.org/10.1002/cssc.202100851).
- [187] Yun Bai et al. “Interfacial coordination interactions studied on cobalt octaethylporphyrin and cobalt tetraphenylporphyrin monolayers on Au(111)”. In: *Phys. Chem. Chem. Phys.* 12.17 (2010), p. 4336. DOI: [10.1039/b924974p](https://doi.org/10.1039/b924974p).
- [188] Mark C. Biesinger et al. “Resolving surface chemical states in XPS analysis of first row transition metals, oxides and hydroxides: Cr, Mn, Fe, Co and Ni”. In: *Appl. Surf. Sci.* 257.7 (Jan. 2011), pp. 2717–2730. DOI: [10.1016/j.apsusc.2010.10.051](https://doi.org/10.1016/j.apsusc.2010.10.051).
- [189] Christopher S. Goldenstein et al. “SpectraPlot.com: Integrated spectroscopic modeling of atomic and molecular gases”. In: *J. Quant. Spectrosc. Radiat. Transf.* 200 (Oct. 2017), pp. 249–257. DOI: [10.1016/j.jqsrt.2017.06.007](https://doi.org/10.1016/j.jqsrt.2017.06.007).
- [190] E. Vohringer-Martinez et al. “Water Catalysis of a Radical-Molecule Gas-Phase Reaction”. In: *Science (80-.)*. 315.5811 (Jan. 2007), pp. 497–501. DOI: [10.1126/science.1134494](https://doi.org/10.1126/science.1134494).

- [191] Lev Chuntonov, Revati Kumar, and Daniel G. Kuroda. “Non-linear infrared spectroscopy of the water bending mode: direct experimental evidence of hydration shell reorganization?” In: *Phys. Chem. Chem. Phys.* 16.26 (2014), pp. 13172–13181. DOI: [10.1039/C4CP00643G](https://doi.org/10.1039/C4CP00643G).
- [192] Jie Yang et al. “Direct Observation of Ultrafast Hydrogen Bond Strengthening in Liquid Water”. In: *Submitted* 596. September 2020 (2021). DOI: [10.1038/s41586-021-03793-9](https://doi.org/10.1038/s41586-021-03793-9).
- [193] Krupa Ramasesha et al. “Water vibrations have strongly mixed intra- and intermolecular character”. In: *Nat. Chem.* 5.11 (Nov. 2013), pp. 935–940. DOI: [10.1038/nchem.1757](https://doi.org/10.1038/nchem.1757).
- [194] Asmita Singha, Kaustuv Mittra, and Abhishek Dey. “Effect of hydrogen bonding on innocent and non-innocent axial ligands bound to iron porphyrins”. In: *Dalt. Trans.* 48.21 (2019), pp. 7179–7186. DOI: [10.1039/C8DT03852J](https://doi.org/10.1039/C8DT03852J).
- [195] Igor D. Petrik et al. “Spectroscopic and Crystallographic Evidence for the Role of a Water-Containing H-Bond Network in Oxidase Activity of an Engineered Myoglobin”. In: *J. Am. Chem. Soc.* 138.4 (Feb. 2016), pp. 1134–1137. DOI: [10.1021/jacs.5b12004](https://doi.org/10.1021/jacs.5b12004).
- [196] Perumandla Nagaraju et al. “The secondary coordination sphere controlled reactivity of a ferric-superoxo heme: unexpected conversion to a ferric hydroperoxo intermediate by reaction with a high-spin ferrous heme”. In: *Chem. Commun.* 52.45 (2016), pp. 7213–7216. DOI: [10.1039/C6CC02162J](https://doi.org/10.1039/C6CC02162J).
- [197] Christopher J. Chang, Leng Leng Chng, and Daniel G. Nocera. “Proton-Coupled O-O Activation on a Redox Platform Bearing a Hydrogen-Bonding Scaffold”. In: *J. Am. Chem. Soc.* 125.7 (Feb. 2003), pp. 1866–1876. DOI: [10.1021/ja028548o](https://doi.org/10.1021/ja028548o).
- [198] Per-Olov Löwdin. “Quantum Theory of Many-Particle Systems. I. Physical Interpretations by Means of Density Matrices, Natural Spin-Orbitals, and Convergence Problems in the Method of Configurational Interaction”. In: *Phys. Rev.* 97.6 (Mar. 1955), pp. 1474–1489. DOI: [10.1103/PhysRev.97.1474](https://doi.org/10.1103/PhysRev.97.1474).
- [199] Andreas Eichler. “CO adsorption on Ni(1 1 1) - A density functional theory study”. In: *Surf. Sci.* 526.3 (2003), pp. 332–340. DOI: [10.1016/S0039-6028\(02\)02682-1](https://doi.org/10.1016/S0039-6028(02)02682-1).
- [200] Vanessa L. Zhang, Heike Arnolds, and David A. King. “Hot band excitation of CO/Ir{1 1 1} studied by broadband sum frequency generation”. In: *Surf. Sci.* 587.1-2 (2005), pp. 102–109. DOI: [10.1016/j.susc.2005.04.039](https://doi.org/10.1016/j.susc.2005.04.039).
- [201] Ch Hess et al. “Hot-band excitation of CO chemisorbed on Ru(001) studied with broadband-IR sum-frequency generation”. In: *Chem. Phys. Lett.* 325.1-3 (2000), pp. 139–145. DOI: [10.1016/S0009-2614\(00\)00627-8](https://doi.org/10.1016/S0009-2614(00)00627-8).

- [202] Ch Hess, M. Wolf, and M. Bonn. "Direct observation of vibrational energy delocalization on surfaces: CO on Ru(001)". In: *Phys. Rev. Lett.* 85.20 (2000), pp. 4341–4344. DOI: [10.1103/PhysRevLett.85.4341](https://doi.org/10.1103/PhysRevLett.85.4341).
- [203] Mischa Bonn, Christian Hess, and Martin Wolf. "The dynamics of vibrational excitations on surfaces: CO on Ru(001)". In: *J. Chem. Phys.* 115.16 (2001), pp. 7725–7735. DOI: [10.1063/1.1404986](https://doi.org/10.1063/1.1404986).
- [204] Kristen N. Johnson et al. "Role of the Supporting Surface in the Thermodynamics and Cooperativity of Axial Ligand Binding to Metalloporphyrins at Interfaces". In: *Curr. Org. Chem.* 26.6 (2022), pp. 553–562. DOI: [10.2174/1385272826666220209122508](https://doi.org/10.2174/1385272826666220209122508).
- [205] Alison Crossley and David A. King. "Infrared spectra for co isotopes chemisorbed on Pt "111": Evidence for strong adsorbate coupling interactions". In: *Surf. Sci.* 68.C (1977), pp. 528–538. DOI: [10.1016/0039-6028\(77\)90245-X](https://doi.org/10.1016/0039-6028(77)90245-X).
- [206] Nicola Podda et al. "Experimental and theoretical investigation of the restructuring process induced by CO at near ambient pressure: Pt nanoclusters on graphene/Ir(111)". In: *ACS Nano* 11.1 (2017), pp. 1041–1053. DOI: [10.1021/acsnano.6b07876](https://doi.org/10.1021/acsnano.6b07876).
- [207] Richard C. Powell. "Energy Transfer between Chromium Ions in Nonequivalent Sites in Li₂Ge₇O₁₅". In: *Phys. Rev.* 173.2 (Sept. 1968), pp. 358–366. DOI: [10.1103/PhysRev.173.358](https://doi.org/10.1103/PhysRev.173.358).
- [208] Xia Li et al. "Coverage-Induced Orientation Change: CO on Ir(111) Monitored by Polarization-Dependent Sum Frequency Generation Spectroscopy and Density Functional Theory". In: *J. Phys. Chem. C* 124.33 (2020), pp. 18102–18111. DOI: [10.1021/acs.jpcc.0c04986](https://doi.org/10.1021/acs.jpcc.0c04986).
- [209] J. M. Burke et al. "Structure-Sensitive Resonance Raman Bands of Tetraphenyl and "Picket Fence" Porphyrin-Iron Complexes, Including an Oxyhemoglobin Analogue". In: *J. Am. Chem. Soc.* 100.19 (1978), pp. 6083–6088. DOI: [10.1021/ja00487a018](https://doi.org/10.1021/ja00487a018).
- [210] J. M. Burke, J. R. Kincaid, and T. G. Spiro. "Resonance Raman Spectra and Vibrational Modes of Iron(III) Tetraphenylporphine μ -Oxo Dimer. Evidence for Phenyl Interaction and Lack of Dimer Splitting". In: *J. Am. Chem. Soc.* 100.19 (1978), pp. 6077–6083. DOI: [10.1021/ja00487a017](https://doi.org/10.1021/ja00487a017).
- [211] S Popovici, W Leyffer, and R Holze. "The mechanism of dioxygen reduction at iron meso-tetrakis (pyridyl) porphyrin: a spectroelectrochemical study". In: *J. Porphy. Phthalocyanines* 2.3 (May 1998), pp. 249–260. DOI: [10.1002/\(SICI\)1099-1409\(199805/06\)2:3<249::AID-JPP77>3.3.CO;2-V](https://doi.org/10.1002/(SICI)1099-1409(199805/06)2:3<249::AID-JPP77>3.3.CO;2-V).
- [212] Thomas S. Rush et al. "Computational Modeling of Metalloporphyrin Structure and Vibrational Spectra: Porphyrin Ruffling in NiTPP". In: *J. Phys. Chem. B* 104.20 (May 2000), pp. 5020–5034. DOI: [10.1021/jp000266s](https://doi.org/10.1021/jp000266s).

- [213] Metin Aydin. “DFT and Raman spectroscopy of porphyrin derivatives: Tetraphenylporphine (TPP)”. In: *Vib. Spectrosc.* 68 (Sept. 2013), pp. 141–152. DOI: [10.1016/j.vibspec.2013.06.005](https://doi.org/10.1016/j.vibspec.2013.06.005).